

# Oligocene - Miocene Ice Sheet and Paleoceanographic Evolution of the Eastern Wilkes Land Margin

Ph.D. Thesis  
2020

**ARIADNA SALABARNADA ROSET**



UNIVERSIDAD  
DE GRANADA



# Oligocene - Miocene Ice Sheet and Paleoceanographic Evolution of the Eastern Wilkes Land Margin

Ariadna Salabarnada Roset

Ph.D. Thesis

2020

Departamento de Geociencias Marinas  
Instituto Andaluz de Ciencias de la Tierra (CSIC-UGR)



Programa Doctorado  
Ciencias de la Tierra

Editor: Universidad de Granada. Tesis Doctorales  
Autor: Ariadna Salabarnada Roset  
ISBN: 978-84-1306-515-1  
URI: <http://hdl.handle.net/10481/62873>





**UNIVERSIDAD  
DE GRANADA**



# **Oligocene - Miocene Ice Sheet and Paleoceanographic Evolution of the Eastern Wilkes Land Margin**

Ariadna Salabarnada Roset  
Supervisor Dr. Carlota Escutia Dotti

Departamento de Geociencias Marinas  
Instituto Andaluz de Ciencias de la Tierra (CSIC-UGR)

Ph.D. Thesis 2020



Programa Doctorado  
Ciencias de la Tierra

The front cover photography was taken during my trip to Antarctica in 2018 and is located close to the South Shetland Islands and looking towards the Antarctic Peninsula. In the foreground, several icebergs with blue ice are travelling with the antarctic currents until they will melt far away from its origin. One of them carries a big rock on it, that in the future will fall down to the seafloor. It is a dropstone to-be! In the background, we can see a thin white line that is the sea-ice from the Antarctic Peninsula.

This PhD thesis has been carried out in the Department of Marine Geosciences, at the Instituto Andaluz de Ciencias de la Tierra. Financial support was provided by a grant Formación de Personal Investigador FPI from the Spanish Ministerio de Economía y Competitividad with the grants CTM 2011-24079 and CTM2014-60451-C2-1-P.



*“A la meva mare i al meu pare,  
i a la insistència, al suport, a l’amor i a la vida  
que m’heu donat. Sense vosaltres dos mai hagués sigut  
possible”*





## Agradecimientos

Des de que empecé en Febrero de 2013 la tesis en Granada hasta este momento en que parece que se acaba he vivido mil aventuras, he trabajado en un sinfín de sitios diferentes y con un sinfín de científicos y gente maravillosa, y he aprendido, aprendido de la ciencia, de la paciencia y de la vida, y también de la muerte.

Y tanto aprendizaje y aventuras no hubieran sido posible sin mi gran maestra y directora, Carlota Escutia, que me has ayudado y dado todas las oportunidades y más, y me has acogido, y guiado, y enseñado la virtud del eterno optimismo, y de la perseverancia. También por aguantar siempre con una sonrisa mis desvaríos y que al hablar contigo todo parezca más fácil (aunque luego no lo sea tanto), y por confiar en mí. Pero sobretodo porque todo esto ha sido compatible con el disfrutar, el hablar y preocuparse, y con cuidarse. Y gracias por esta tesis, que sin tu ayuda nunca hubiera visto la luz. Y también a Hans, por tus sabias discusiones sobre sedimentología, turbiditas y contornitas, y por contarnos tantas historias y aventuras geológicas!

Esta tesis es también un trabajo colectivo a lo largo del tiempo en el que han participado y ayudado muchísimas personas, directa o indirectamente, y que a lo mejor no seré capaz de nombrar aquí, así que desde ya os doy mis más sinceras gracias!

Quiero agradecer a toda la gente del IACT, que me habéis acogido y ayudado siempre en todo, a Menchu Comas, Paqui Martínez Ruiz y Paco Lobo, Jesús Galindo, a Júlia y a Francis. Y a todos con los que hemos estado de campaña en el mar, y que nos lo hemos pasado tan bien haciendo ciencia, que no se hace sola! A todo el equipo EuroFleets Gateway cuando estuvimos de campaña en el mar de Alborán y el Atlántico. Y al equipo TASMANDRAKE destino a la Antártida, una experiencia difícil de olvidar, y a todos los que estábamos y a los que ya no están. Y al gran equipo que formamos con Meghan, Johan, Adri y Dimitris... que risas! Así da gusto irse al mar. Y los viajes a Texas para muestrear sondeos y nuestras incursiones en la cultura de los EEUU.

Sin olvidar a Juani, Ana y Carolina por el trabajo de gestión que hacéis cada día, que me ha ayudado a gestionar y a hacer más fácil la vida con mis múltiples viajes y las infinitas gestiones administrativas.

A mis grande compañeros de despacho en el IACT por las risas y la compañía, la amistad y las risas, y las grandes discusiones antárticas con Dimitris y Adri y Johan que sois lo más! Y a l'Enric, que vaig compartir amb tu els teus moments agònics tesils, de xerrar sense parar i escoltar música al despatx. Y muchos otros que han pasado y hemos compartido tanto, a Beny, Ahmed, Moha, y a Cecília que viene a dar el relevo con mucha alegría! Y todos los compis del IACT que habéis sido unos cuantos, con los que hemos compartido comidas y fiestas. Y a Nicole y a Manu y a Bob, por las magnificas escapadas a Sierra Nevada.

Y a mis favoritos granaínos, que ya son parte de mi familia, y han hecho que mis años en Granada hayan sido lo más. A Marga y a Patri (aunque te guste más Pa), porque me habéis acogido siempre a vuestro lado cuando he necesitado una casa (y no han sido pocas veces, y aún son y serán). Y a todas vosotras otra vez, a Mapi, a Mary, Marga, Patri, Enric, Mauri, JP, Dani, Chiara, Maria, Zita y Nono para que nos encontremos siempre más y podamos continuar haciendo nuestras tapillas cada diilla que sea posible.

I was lucky enough to stay for four months at the Antarctic Research Centre in Wellington (New Zealand) where I learned Antarctic sedimentology from the great Rob McKay and Tim Naish, and I had the opportunity to share nice moments and beers with the other students there. Y de encontrarme a Manuel i a la Maria, que nos acompañamos a conocer la isla y a descubrir todas las cervezas IPAs habidas y por haber.

Y luego mi aventura científica continuó en Japón, donde estuve en JAMTSEC aprendiendo geoquímica con Francis, y descubriendo costumbres distintas, de la cultura y de la comida japonesa. Y de mis compis de "Oppama des" Taka y Aya, y de Joaquín, de Carmen, Cristoph y Iona. Arigato gozaimasss.

Y fue gracias al máster en cambio climático, y a Blas Valero que me dirigió el trabajo final, y a la gente del IPE, que yo empecé mis andaduras en la ciencia. Y a todos mis compañeros del CO2 forever y sobre todo a Francesca y a Matías, y a Mallorca i ses seves gents.

I als meu amics de l'ànima, als geòlegs i no geòlegs que ens acompanyem des de fa tant de temps, que hem escalat i compartit muntanyes i muntanyes de tots tipus, perquè al final l'important és el camí i amb qui el fas el que conta. I que no importa si estem a prop o si estem lluny, perquè hi som i hi serem. A tots vosaltres que espero poder continuar donant-vos la vara durant molt més temps i viceversa. Marta, Iñigo, Cris, Muntsa, Elsa, Jaume, Carlota, Anna, Xavi, Jelena, Martí, Joana, Álvaro, Gemma, Aina, Olga, Berta, Ursu, a l'Esther, a les super Geonenes. I a tots vosaltres que no escric el nom, però que també heu deixat un trosset vostre dins meu, i m'heu fet créixer tant.

I tots aquets anys els he passat viatjant al cantó del Lluís, no sempre pels mateixos indrets però sempre pel mateix camí, tant feliços, que no es pot trobar millor xurri de vida.

I agrair infinitament a la meva mare i al meu pare, que sense ells jo no seria, ja que són ells que em van inculcar la curiositat per aprendre i descobrir. I la meva germaneta Estel·la, que és tan sabia i m'ha escoltat tant i m'ha fet tanta psicologia com ha pogut, i m'ha obert els ulls a la ment i de la ment, als seus enganys i paranys, i a que es poden entendre i canviar!

Y gracias a la birra que me ha dado tanto!

*“Y cuando la tormenta de arena haya pasado, tú no comprenderás cómo has logrado cruzarla con vida. ¡No! Ni siquiera estarás seguro de que la tormenta haya cesado de verdad. Pero una cosa sí quedará clara. Y es que la persona que surja de la tormenta no será la misma persona que penetró en ella”*

*Haruki Murakami - Kafka en la orilla*



## ABSTRACT

The Antarctic Ice sheet (AIS) and the Southern Ocean (SO) are major components of the Earth climate system. Changes in the AIS affect SO circulation, global sea levels, Earth's albedo, and marine nutrient distribution among other. In addition, Antarctic Bottom Water (AABW) and Circumpolar Deep Water (CDW) distribution in the Southern Ocean affect ice sheet dynamics, the Meridional Overturning Circulation and the global Earth's climate, among other. Little is known however, about ice sheet ocean configurations and interactions during past times warmer than today even though this knowledge is important in the current scenario of global warming. Intergovernmental Panel on Climate Change (IPCC) projections of atmospheric CO<sub>2</sub> concentrations within this century range from 400 to 750 ppm. A similar, albeit opposite shift in CO<sub>2</sub> concentrations was experienced by our Planet during the late Oligocene-early Miocene period. Therefore, the insights that we can gain from geological records from this period regarding ice sheet dynamics and ocean configurations can be relevant to inform models for future changes.

The overall objective of this thesis is to understand East Antarctic ice sheet (EAIS) and SO configuration and dynamics during the warm late Oligocene and the transient Mi-1 glaciation in the unexplored eastern Wilkes Land (WL) margin of East Antarctica. To achieve this objective, we have conducted sedimentological, geochemical mineralogical and cyclostratigraphic analyses in Oligocene-Miocene sediments recovered by the Integrated Ocean Drilling Program (IODP) Expedition 318 at Site U1356. In addition, we use the available grid of multichannel seismic reflection profiles to extend the results from drilling regionally and to study the distribution of water masses and their pathways.

This thesis shows that before 28 Ma a single water mass flowing westward, the proto-AABW, occupied the seafloor in the studied region. The first evidence for the onset of a current flowing eastward, the proto-CDW, is found at 28 Ma. Between 26 and 25 Ma ice sheets were mainly continental-based and an oceanic frontal system already existed and migrated during glacial-interglacial cycles that were paced by obliquity. The late Oligocene frontal system was however weaker than today's Polar Front because we find evidence for intrusion of warm north component waters close to the Antarctic margin. The latest Oligocene (24-23.4 Ma) witnessed at least eight times of ice sheet advancing into the continental shelf and retreats inland, pointing to a highly dynamic ice sheet during the cooling trend leading to the glacial Mi-1 event. During this period, we interpret that the EAIS in the WSB becomes marine-based as a consequence of the erosion and overdeepening of the Wilkes Subglacial Basin by the repeated advances and retreats of the EAIS since it was formed in the early Oligocene (33.6 Ma).



## RESUMEN

El casquete de hielos antártico (AIS) y el Océano Austral (SO) son unos componentes importantes del sistema climático de la Tierra. Cambios en el AIS afectan a la circulación del SO, los niveles del nivel del mar global, el albedo terrestre, y la distribución de nutrientes marinos, entre otros. Además, la distribución e interacción entre las Aguas Profundas Antárticas (AABW) y la Corriente Profunda Circumpolar (CDW) tiene un papel clave en la dinámica del AIS y la Circulación Termohalina, y por tanto en el clima global de la Tierra. Poco se sabe sin embargo sobre la configuración y la interacción de la AIS y el SO durante tiempos pasados más cálidos que el actual, aunque este conocimiento es importante ante el escenario de calentamiento global actual. El Panel Intergubernamental sobre el Cambio Climático (IPCC) sitúa las proyecciones de CO<sub>2</sub> a finales de este siglo entre 400 y 750 ppm. Un salto similar en las concentraciones de CO<sub>2</sub>, aunque en sentido inverso, tuvo lugar desde el Oligoceno tardío al Mioceno temprano. El estudio de este periodo, por lo tanto, constituye una oportunidad excelente para entender las relaciones entre la dinámica del AIS y los diferentes escenarios oceanográficos, y así contribuir a acotar los modelos ante futuros cambios en el clima de la Tierra.

El principal objetivo de esta tesis es comprender la dinámica del casquetes de hielo oriental (EAIS) y las diferentes configuraciones oceanográficas durante el Oligoceno superior y la transición hacia el Mioceno (conocida como Mi-1) en el inexplorado margen oriental de la Tierra de Wilkes. Para ello, hemos realizado análisis sedimentológicos, geoquímicos, mineralógicos y cicloestratigráficos en los sedimentos Oligocenos-Miocenos recuperados del pozo U1356 por la Expedición 318 del Integrated Ocean Drilling Program (IODP). Además, una malla de perfiles sísmicos de reflexión multicanal permite extender los resultados de los sondeos regionalmente y así estudiar la distribución de las masas de agua y sus trayectorias.

Los resultados derivados de esta tesis muestran que antes de los 28 Ma una masa de agua, la AABW, circulaba hacia el oeste y ocupaba todo el fondo marino en la región estudiada. La primera evidencia de una corriente de agua hacia el este, la proto-CDW, es al comienzo del Oligoceno superior. Entre 26 y 25 Ma, los casquetes de hielo fundamentalmente eran continentales, y los sistemas oceánicos frontales ya existían y migraban durante los ciclos glaciares-interglaciares forzados por la oblicuidad. Sin embargo, la intrusión de aguas cálidas de componente norte cerca del margen Antártico muestra que dichos frentes eran más débiles que el Frente Polar actual. A finales del Oligoceno (24-23.4 Ma) el registro muestra al menos ocho avances de la EAIS a la plataforma continental y retrocesos hacia tierra, evidenciando un casquete de hielo muy dinámico durante la fase de enfriamiento que culmina en el evento glacial Mi-1. Es en este periodo interpretamos que la EAIS pasa de estar anclado en tierra a estar anclado por debajo del nivel del mar (marine-based) como consecuencia de la erosión y la profundización de la Cuenca Subgacial de Wilkes durante avances repetidos de la EAIS desde su formación hace 33.6 Ma





## CONTENTS

|  |           |
|--|-----------|
| ABSTRACT .....   | i         |
| RESUMEN .....  | iii       |
| <b>CONTENTS .....</b>  | <b>01</b> |
| LIST OF FIGURES .....  | 05        |
| LIST OF TABLES .....   | 09        |
| ABBREVIATION INDEX.....  | 09        |
| <b>CONTEXT AND MOTIVATION .....</b>  | <b>3</b>  |
| <b>OBJECTIVES AND HYPHOTESIS .....</b>   | <b>4</b>  |
| <b>THESIS LAYOUT .....</b>   | <b>5</b>  |
| <b>CHAPTER 1 - INTRODUCTION .....</b>  | <b>9</b>  |
| 1.1. Eocene to early Miocene global climate and Antarctic Ice Sheet evolution.....   | 9         |
| 1.2. Earth orbital parameters .....  | 12        |
| 1.3. Deep-water sedimentation on glaciated margins.....  | 14        |
| 1.4. The eastern Wilkes Land margin .....  | 16        |
| 1.4.1. Tectonic and Seismic Stratigraphic Evolution of the Wilkes Land.....  | 16        |
| 1.4.2. The Wilkes Subglacial Basin .....   | 17        |
| 1.4.3. Physiography Offshore the Eastern Wilkes Land Margin.....   | 18        |
| 1.5. Modern and past configurations of the Southern Ocean in the Wilkes Land margin .....  | 18        |
| <b>CHAPTER 2 - MATERIALS AND METHODS .....</b>   | <b>25</b> |
| 2.1. IODP Site U1356.....  | 25        |
| 2.2. Methods.....  | 27        |
| <b>CHAPTER 3 - PALEOCEANOGRAPHY AND ICE SHEET VARIABILITY OFFSHORE WILKES LAND, ANTARCTICA:<br/>INSIGHTS FROM LATE OLIGOCENE ASTRONOMICALLY PACED CONTOURITE SEDIMENTATION .....</b> | <b>31</b> |
| 3.1. Introduction.....   | 32        |
| 3.2. Materials and Methods.....  | 34        |
| 3.2.1. Site U1356 Description .....  | 34        |
| 3.2.2. Age Model.....  | 35        |
| 3.2.3. Facies Analyses.....  | 36        |
| 3.2.4. X-Ray Fluorescence (XRF) Analyses .....   | 36        |
| 3.2.5. Spectral Analyses .....   | 37        |
| 3.3. Results.....  | 38        |
| 3.3.1. Sedimentary Facies .....  | 38        |
| 3.3.2. Geochemistry .....  | 40        |

|   |           |
|---|-----------|
| 3.3.4. Spectral Analysis.....   | 45        |
| 3.4. Discussion.....  | 47        |
| 3.4.1. Glacial and Interglacial Contourite Sedimentation off Wilkes Land .....  | 47        |
| 3.4.2. Ice Sheet Configuration During The Warm Late Oligocene .....   | 49        |
| 3.4.3. Paleoceanographic Implications.....  | 50        |
| 3.4.3.1. Glacial Paleoceanographic Configuration .....  | 50        |
| 3.4.3.2. Interglacial Paleoceanographic Configurations .....  | 51        |
| 3.4.4. Orbital Forcing and Glacial and Interglacial Cyclicality .....   | 54        |
| 3.5. Conclusions .....  | 55        |
| <b>SUPPLEMENTS TO CHAPTER 3.....</b>  | <b>57</b> |
| S3.1.    Lithostratigraphy For Site U1356.....  | 57        |
| S3.2.    Astrochronologic analysis .....  | 63        |
| S3.3.    R_analysis code created to produce the astronomical analysis in the late Oligocene.....  | 72        |
| <b>CHAPTER 4 - ICE SHEET AND OCEANIC CONFIGURATIONS IN THE EASTERN WILKES LAND MARGIN DURING THE LATE OLIGOCENE TO MIOCENE TRANSITION .....</b> | <b>79</b> |
| 4.1. Introduction .....   | 79        |
| 4.2. Materials and Methods.....   | 80        |
| 4.2.1. IODP Site U1356.....   | 80        |
| 4.2.2. Facies Analyses.....   | 82        |
| 4.2.3. Geochemical Analyses .....   | 83        |
| 4.2.4. Linking Site U1356 with Seismic Reflection Profiles .....  | 83        |
| 4.3. Results.....   | 84        |
| 4.3.1. Sediment Facies Analysis and Sedimentary Processes .....   | 84        |
| 4.3.1.1. Unit V .....   | 84        |
| 4.3.1.2. Unit IV .....  | 84        |
| 4.3.1.3. Unit III .....   | 87        |
| 4.3.2. Geochemical Results .....  | 88        |
| 4.3.3. Wilkes Land Margin Regional Evolution based on Seismic Reflection Data .....   | 91        |
| 4.4. Discussion .....   | 94        |
| 4.4.1. Late Oligocene to Early Middle Miocene Ice Sheet History and Paleoceanography Through Depositional Settings and Environments .....       | 94        |
| 4.4.2. Long Term Changes in the Paleoceanography and Their Role in Triggering the Glaciation in the OMT .....                                   | 98        |
| 4.5. Conclusions .....  | 100       |

|  |                |
|--|----------------|
| <b>CHAPTER 5 - OLIGOCENE TO MIOCENE BOTTOM CURRENT DEPOSITION AND CIRCULATION OFF THE EASTERN WILKES LAND MARGIN .....</b>               | <b>105</b>     |
| 5.1. Introduction .....  | 105            |
| 5.2. Geologic framework of Wilkes Land and Site U1356.....   | 107            |
| 5.3. Methods.....  | 109            |
| 5.4. Ocean circulation in the Wilkes Land margin .....   | 110            |
| 5.5. Results.....  | 111            |
| 5.5.1. Paleosurface Reconstructions.....   | 111            |
| 5.5.2. Contouritic Depositional and Erosional Features: .....  | 114            |
| 5.5.3. Evolution of Contourite Deposition Off the Wilkes Land Margin .....   | 119            |
| 5.5.3.1. Phase 1 .....   | 120            |
| 5.5.3.2. Phase 2 .....   | 120            |
| 5.5.3.3. Phase 3 .....   | 122            |
| 5.6. Discussion .....  | 124            |
| 5.6.1. Topographic Controls in Contourite Deposition.....  | 124            |
| 5.6.2. Contouritic Bodies and Current Paths: Insights into Water Masses .....  | 125            |
| 5.7. Conclusions .....   | 126            |
| <br><b>CHAPTER 6 - GENERAL DISCUSSION - OLIGOCENE-MIOCENE ICE SHEET AND PALEOCEANOGRAPHIC EVOLUTION OFF THE WILKES LAND MARGIN .....</b> | <br><b>131</b> |
| 6.1. Phase 1 - early Oligocene (33.6 To 28 ma) .....   | 131            |
| 6.2. Phase 2 - late Oligocene (28 to ~23.4 Ma) .....   | 131            |
| 6.3. Phase 3 - the Oligocene Miocene transition (~23.4 To >17 ma) .....  | 133            |
| <br><b>SUMMARY AND CONCLUSIONS .....</b>   | <br><b>137</b> |
| <b>UNSETTLED ISSUES AND FUTURE PERSPECTIVES .....</b>  | <b>140</b>     |
| <br><b>REFERENCES .....</b>  | <br><b>145</b> |
| <br><b>APPENDIX 1 - Co-authored papers related to the topic of the thesis. ....</b>  | <br><b>169</b> |
| <b>APPENDIX 2 - Datasets from chapter 3 and 4 .....</b>  | <b>177</b>     |
| <br><b>Curriculum Vitae .....</b>  | <br><b>181</b> |



## LIST OF FIGURES

- Figure 1.1.** Cenozoic pCO<sub>2</sub> and stacked deep-sea benthic foraminifer oxygen isotope curve for 0 to 65 Ma, updated from Zachos et al. (2008) and converted to the “Gradstein timescale” (Gradstein et al., 2004); extracted from (Escutia et al., 2014). Mi-1 = Miocene isotope Event 1, Oi-1 = Oligocene isotope Event 1, ETM2 = Eocene Thermal Maximum 2, PETM = Paleocene/Eocene Thermal Maximum, ETM1 = Eocene Thermal Maximum 1. Antarctic ice sheet evolution (mostly inferred from low latitude records) under the different CO<sub>2</sub> scenarios is shown at the top of the figure. Shaded squares indicate future CO<sub>2</sub> (purple) and Temperature (blue) scenarios forecasted by the IPCC (2014). .....11
- Figure 1.2.** Components of Milankovitch cycles.....13
- Figure 1.3.** Standard facies models of a) Pelagites/hemipelagites, associated with settling through the water column; b) contourite sequence, linked to variations in contour current velocity (modified from Stow and Faugères, (2008), based on the original figure from Gonthier et al. (1984); and c) Turbidite with Bouma sequence, linked to density currents (Lowe, 1982). .....15
- Figure 1.4.** Multichannel seismic reflection profile across Site U1356 showing the regional unconformities WL-U3, WL-U4, WL-U5 extracted from Escutia et al., 2011). Site U1356 penetration is marked with the red rectangle. ....16
- Figure 1.5.** Antarctic ice sheet surface grid and bed elevation grid (Bedmap2) modified from Fretwell et al. (2013). Wilkes Subglacial basin (WSB) and study area are pointed. ....17
- Figure 1.6.** Maps from Paxman et al., (2019) of reconstructed Antarctic continental paleotopographies for a) the Eocene-Oligocene boundary (ca. 34 Ma), b) the Oligocene–Miocene boundary (ca. 23 Ma), and c) the mid-Miocene climate transition (ca. 14 Ma). .....18
- Figure 1.7.** Bathymetric map from Escutia et al. (2011) of the eastern Wilkes Land margin with the location of Site U1356 and other Expedition 318 drill sites. Contour interval=250 m. ....19
- Figure 1.8.** Southern Ocean circulation and Antarctic circumpolar oceanic fronts. Antarctic Circumpolar Current (ACC) marked by blue arrows and main oceanic fronts from north to south are the sub-Tropical Front (STF), Sub-antartic Front (SAF), the Polar Front (PF), and the Southern ACC front (SACC) figure from Rintoul et al. (2001). .....20
- Figure 1.9.** Schematic drawing of the modern Southern Ocean Antarctic bottom water masses and the Antarctic Circumpolar Current (ACC), with the associated Polar Fronts and the Antarctic divergence. ....21
- Figure 2.1.** Location of IODP 318 Site U1356 (Escutia et al., 2010) on the Adélie coast continental rise. Bed topography from IBSCO2 (Arndt, JE et al., 2013). .....25
- Figure 2.2.** Age-depth plot for U1356A from Tauxe et al., (2012). Lithostratigraphic summary from Escutia et al. (2011). Biostratigraphic constraints from Escutia et al. (2011) and paleomagnetic tie point from Tauxe et al., (2012). Seismic regional unconformities WL-U3, WL-U4, and WL-U5 from the Wilkes Land (Escutia et al. 2011). LO=Last occurrence, FO=First occurrence, LCO=Last common occurrence, LAO=last abundant occurrence, FCO=First common occurrence, FAO=First abundant occurrence.....26
- Figure 2.3.** Seismic sequence-internal-reflection terminations. Brown and Fisher, (1979).....28
- Figure 3.1.** Location of IODP 318 Site U1356 (Escutia et al., 2010) on the Adélie coast continental rise. Bed topography from IBSCO2 (Arndt, JE et al., 2013). Schematic position of the different water masses at present and locations of Antarctic Bottom Water formation (Orsi, 1995) are indicated. The position of the Oligocene Polar Front (Scher et al., 2015) is also shown. ASF: Antarctic Slope Front; SB: Southern Boundary; SACCF: Southern

|   |    |
|---|----|
| Antarctic Counter Current Front; ARB: Adélie Rift Block.....  | 32 |
| <b>Figure 3.2.</b> Magnetic susceptibility (MS) and natural gamma radiation (NGR) physical properties, and selected X-Ray Fluorescence (XRF) data (in total counts) and elemental ratios plotted against the new detailed U1356 facies log between 689.4 and 641.4 mbsf .....   | 39 |
| <b>Figure 3.3.</b> Detailed images, CT-scans and HRSEM from Facies 1 (F1) and Facies 2 (F2). (a) Example of F1 taken from Core 71R-2 119/146 cm, showing faint laminations (fl) and bioturbation by <i>Planolites</i> (p) (b) CT-scan 3D image of the same core interval, note the pyritized burrows (py). (c) Example of F2 taken from core 72R-1 18/53 cm). (d-f) Close-ups of laminations from F1: ripples (r), planar lamination (pl), and faint laminations (fl), with mud offshoots (mo). (d) <i>Chondrites</i> (Ch) bioturbation inside F1. (g) HRSEM image of F1 (68R-4-86/88 cm) with detritic aspect and a mudstone clay matrix, Quartz grains (Qz), diagenetic calcite (arrows), and dissolved coccoliths (circles); (h) HR-SEM image of F2 (71R-2 140/142 cm) silt sized matrix and reworked calcareous nannofossils, and conchoidal quartz grain (C-Qz); (i) Detail of dissolved coccoliths and diagenetic calcite mineral; (j) Detail of a dissolved and reworked calcareous nannofossils and a fractured conchoidal quartz (C-Qz)..... | 41 |
| <b>Figure 3.4.</b> Detailed facies characterization of two representative sections using: (a) Interpreted facies F1 and F2; a high-resolution digital image of the core sections (b), facies log (c), Magnetic susceptibility (MS) (d), XRF Zr/Ba ratio (e), and XRF calcium counts (f). .....  | 42 |
| <b>Figure 3.5.</b> Linear correlation between CaO% (discrete XRF) and $\ln(\text{Ca}/\text{Ti})$ (XRF scanner) values in order to estimate carbonate contents ( $\text{CaCO}_3$ est. %).....  | 43 |
| <b>Figure 3.6.</b> Spectral analysis results of the Zr/Ba obliquity tuned and anchored data. (a) Zr/Ba ratio tuned with Astrochron (Meyers, 2014) and anchored to the top of the C8n.2n (o) chron. (b) EHA and (c) MTM spectral analysis on Zr/Ba tuned data. EHA normalized power with 300-kyr window with 3DPSS tapers. (d) EHA amplitude for the eccentricity-obliquity-precession ETP solution (Laskar et al., 2004) calculated for the same period of time with 3DPSS tapers and 200-kyr window. ....  | 46 |
| <b>Figure 3.7.</b> Paleooceanographic reconstructions based on our interpretations for Facies 1 and 2. (a) Modelled ice thickness for the mid-Miocene ice sheet by Gasson et al., (2016). (b) Glacial periods with low obliquity configuration. Westerlies and Polar Front (PF) move northwards. There is enhanced proto-AABW formation. Low ventilation conditions occur at the ocean/sediment interface and mixing of waters masses is diminished. Bottom currents are weak and fluctuating, producing laminated sediments. (b) Interglacials occur during high obliquity configuration. Westerlies and the PF move southwards, close to the Site U1356. Proto-AABW formation is reduced. Intrusions of proto-CDW/NADW-like reach southernmost positions. (c) During warm Interglacials, NADW-like is enhanced and $\text{CaCO}_3$ sedimentation is more abundant. (b,c) Bottom water ventilation and upwelling are more vigorous, with stronger bottom currents that result in fully bioturbated and silty-sized sediments.....                    | 53 |
| <b>Figure S3.1.</b> Detailed sedimentary log from IODP U1356 Site U1356 exp. 318 from 11R to 95R (95.4 to 896 mbsf). .....  | 59 |
| <b>Figure S3.2.</b> IODP Site U1356 Exp. 318 from 11R to 95R (95.4 to 896 mbsf). Schematic Facies Log with plotted Magnetic Susceptibility (MS). Paleomagnetic tie points are also present. Ages from Tauxe et al. (2012) are updated to GPTS 2012.....   | 62 |
| <b>Figure S3.3.</b> Tuning of Zr/Ba to the obliquity solution. Zr/Ba (in the depth domain) is tuned to the obliquity solution cycle by cycle. Tuning of Zr/Ba record (in depth scale) and bandpass filtering were done in Analyseries (Paillard et al., 1996). (a) Magnetostratigraphic chrons (Tauxe et al., 2012); (b) schematic stratigraphic log; (c) Zr/Ba data in depth scale with the envelope filter centred at 2m (in red); (d) Zr/Ba data in time scale using paleomagnetic tie points and a linear sedimentation rate, with the envelope filter centred at 40 Kyr (in red); (e) Eccentricity and   |    |

obliquity solutions (Laskar et al., 2004); (f) Polarity chrons from the GPTS2012; (g) Blakmann-Tukey in the Zr/Ba data in time domain (not tuned), with statistical (>90%) periodic peaks in the 40 Kyr and 20 Kyr periodicities; (g) Blakmann-Tukey in the Zr/Ba data in depth domain, with statistical (>90%) periodic peaks. ....65

**Figure S3.4.** Evolutive Harmonic Analysis (EHA) in depth scale Zr/Ba data. The detrended Zr/Ba data is linearly interpolated to a constant sample spacing of 2 cm prior to analysis. EHA employs with 3DSDP tapers and a 15 window. ....66

**Figure S3.5.** Astrochronologic testing using evolutive ASM analysis. (a) Evolutive ASM plot, displaying Ho-SL values (90% confidence level), across sedimentation rates spanning 3 to 10 cm/kyr. (b-c) Summary of evolutive ASM results, using a threshold Ho-SL value of 0.1 to identify optimal sedimentation rates. (b) displays each sedimentation rate, and (c) displays the associated Ho-SL. ....66

**Figure S3.6.** Frequency tracking for minimal tuning. The obliquity cyclicity (41 Kyr) can be tracked in the EHA harmonic F-test confidence level results by setting the  $f_{min}=0.01$  and  $f_{max}=0.4$  based on the spatial frequencies calculated by EASM results. Calculated sedimentation rates based on spatial frequency tracking. ....67

**Figure S3.7.** Tuned record and depth-time plot derived by frequency domain minimal tuning to the obliquity cycle. The grey dotted lines show the correlated depth and time. ....68

**Figure S3.8.** MTM results of the tuned data with the major periods in kyr. These peaks achieve the 95% confidence level for both the MTM harmonic F-test and the AR1 red noise model or the AR1 noise model only. ....69

**Figure S3.9.** Following Zr/Ba tuning (a), MS (b), Zr/Ti (c), Ba (d), and Ca/Ti (e) have been tuned. EHA analysis was applied in order to depict the frequencies. EHA on the ETP solution is also added in order to compare the resulting frequencies (f). ....70

**Figure S3.10.** Spectral analysis over individual core sections for the Zr/Ba dataset on the depth scale. The 0.5 cycle/m (that counts for obliquity) achieve >90% significance in all cores except for core 70 where smaller frequencies seem to dominate. Changes in peak frequency seem to be dominated by slightly changes in sedimentation rate. Each core was analysed by a) MTM and b) EHA with a 5 m window. ....71

**Figure 4.1.** Location of IODP 318 Site U1356 (Escutia et al., 2010) on the Adélie coast continental rise. Bed topography from IBSCO (Arndt, JE et al., 2013). Schematic position of the different water masses at present and locations of Antarctic Bottom Water formation (Orsi, 1995) are indicated. Seismic reflection profiles used in this work are shown. ASF: Antarctic Slope Front; SB: Southern Boundary; SACCF: Southern Antarctic Contour Current Front; ARB: Adélie Rift Block. ....81

**Figure 4.2.** Lithological log from site U1356 with their summarised facies and sequences. High resolution images, CT-Scans, HR\_SEM. ....85

**Figure 4.3.** Mass Transport Deposit (MTDs) types studied at site U1356. ....86

**Figure 4.4.** Correlation matrix for (a) Miocene and (b) Oligocene in situ sediments. Elements are ordered in hierarchical ordination to identify groups of similar affinity within XRF data set. Colors refer to the correlation coefficient, where blue (red) are positively (inversely) correlated. Crossed squares have significance level < 0.95. R corrplot package. ....89

**Figure 4.5.** Discrete XRF geochemical proxies Ba/Ti, Si/Ti, Zr/Ba, Zr/Ti, CaO%, and TEX86 extracted from Hartman et al., 2018., plotted against core U1356. ....90

**Figure 4.6.** Formation tops used in the Kingdome project to correlate seismic profiles against core sediments from U1356. Time velocity depth calculations are selected based in sedimentary units described in this study. .91

**Figure 4.7.** Seismic reflection profiles that provide a regional setting for Site U1356 in the Wilkes Land Margin. .... 93



|  |     |
|--|-----|
| <b>Figure 4.8.</b> Summary figure showing schematic representations of the variability and evolution of the depositional settings and the paleoceanography of the Wilkes Land margin during the studied phases. ....   | 97  |
| <b>Figure 5.1.</b> Location of IODP 318 Site U1356 (Escutia et al., 2010) on the Adélie coast continental rise. Bed topography from IBSCO2 (Arndt, JE et al., 2013). Schematic position of the different water masses at present and locations of Antarctic Bottom Water formation (Orsi, 1995) are indicated. The position of the Oligocene Polar Front (Scher et al., 2015) is also shown. ASF: Antarctic Slope Front; SB: Southern Boundary; SACCF: Southern Antarctic Counter Current Front; ARB: Adélie Rift Block. ....  | 108 |
| <b>Figure 5.2.</b> Hydrographic profile dataset extracted from WOCE ( <a href="https://www.nodc.noaa.gov">https://www.nodc.noaa.gov</a> ) along a transect at 140°E from the Wilkes Land Margin. (a) Temperature profile with a schematic view of the meridional overturning circulation in the Southern Ocean, adapted from Rintoul et al. (2001). Dotted lines in panel (a) show approximate major frontal locations. (b) Oxygen and (c) salinity. AASW = Antarctic Surface Water; AAIW = Antarctic Intermediate Water; UCDW = Upper Circumpolar Deep Water; LCDW = Lower-CDW; AABW = Antarctic Bottom Water; PF-S = southern branch of the PF; SACCF-N = northern branch of the Southern ACC Front; SACCFS = southern branch of the Southern ACC Front; SB = Southern Boundary of the ACC. Sections were created using ODV software (Schlitzer, 2012). Profile respresented is RAE53-06. .... | 111 |
| <b>Figure 5.3.</b> Paleosurfaces maps of three major regional unconformities previously defined in the study area: a) WL-U3, b) WL-U4, and c) WL-U5 from the eastern Wilkes Land margin. ....  | 112 |
| <b>Figure 5.4.</b> Main seismic facies identified on the multichannel seismic data with their reflection characteristics (internal geometries, continuity, amplitude, shape). Their identification and interpretation is based on a contourite deposition based in Rebesco et al., (2014). ....  | 114 |
| <b>Figure 5.5.</b> Interpreted (left) and un-interpreted (right) selected regional multichannel seismic profiles, with a location map on the center. Profiles show main seismic unconformities (WL-U3, WL-U4, and WL-U5), and their correlative seismic units. ....  | 116 |
| <b>Figure 5.6.</b> Sketch map showing main contouritic morphological features of Wilkes Land for the Oligocene modified by the Coriolis force. Sections are done as an example of contourite and drift interpretation. ....  | 119 |
| <b>Figure 5.7.</b> Regional major contourites features distribution presented in this work off the Wilkes Land Margin with superimposed schematic drawing of the water mass circulation in plan view for the a) early Oligocene, b) the late Oligocene, and c) the Oligocene-Miocene transition. ....  | 122 |
| <b>Figure 6.1.</b> Long term and schematic evolution of the ice sheet, the paleoceanography, and the drift formation off the Wilkes Land margin. We separated three evolutive phases, coincident with the regional seismic unconformities in the Wilkes Land margin. 3-D bathymetries are based on the paleosurface reconstruction of Phase 1 and phase 3 (Chapter 5). The profile reconstructs an idealized section where all the processes occur linearly. ....  | 134 |

## LIST OF TABLES

|   |    |
|---|----|
| <b>Table 3.1.</b> Age model by Tauxe et al., (2012) and transformed ages to GPTS 2012.....  | 35 |
| <b>Table 3.2.</b> R Pearson Linear correlation between XRF-scanner elements.....  | 43 |
| <b>Table 3.3.</b> Types of facies differentiated by physical, geochemical, and biological character and their interpretation in terms of sedimentary processes and paleoclimate.....  | 44 |
| <b>Table 4.1.</b> Time-depth conversion for the regional unconformities previously defined in the Wilkes Land margin (WL-U3, WL-U4, WL-U5) and to the reflectors separating lithostratigraphic units/subunits defined in this study (reflectors rA and rB). Calculated P-wave velocities for eastern Wilkes Land regional unconformities reflectors. TWTs: two way travel time in seconds; MD m: measured depth in meters; mbsf: meters below sea floor. .... | 92 |

## ABBREVIATION INDEX

|                 |  |
|-----------------|--|
| AABW            | Antarctic Bottom Water                       |
| AASW            | Antarctic Surface Water                      |
| ACC             | Antarctic Circumpolar Current                |
| AD              | Antarctic Divergence                         |
| AIS             | Antarctic Ice Sheet                          |
| ALBW            | Adélie Land Bottom Water                     |
| ASC             | Antarctic Slope Current                      |
| ASM             | Average Spectral Misfit                      |
| CDW             | Circumpolar Deep Water                       |
| CO <sub>2</sub> | Carbon Dioxide                               |
| CT-Scan         | Computed Tomography scanner                  |
| CRP             | Cape Roberts Project                         |
| DSDP            | Deep Sea Drilling Project                    |
| EAIS            | East Antarctic Ice Sheet                     |
| EHA             | Evolutionary Harmonic Analysis               |
| EOT             | Eocene Oligocene Transition                  |
| IODP            | Integrated Ocean Drilling Program            |
| IPCC            | Intergovernmental Panel on Climate Change    |
| IRD             | Iceberg Rafted Debris                        |
| L/UCDW          | Lower/Upper Circumpolar Deep Water           |
| LSR             | Linear Sedimentation Rate                    |
| Ma/myr          | million years ago / million years (duration) |
| mbsf            | meters below sea floor                       |
| mbsl            | meters below sea level                       |

|       |  |
|-------|--|
| mCDW  | Modified Circumpolar Deep Water          |
| MCS   | Multi Channel Seismic                    |
| Mi-1  | Miocene isotope event 1                  |
| MS    | Magnetic Susceptibility                  |
| MTM   | Multi Taper Method                       |
| ODV   | Ocean Data View                          |
| Oi-1  | Oligocene isotope event 1                |
| OMT   | Oligocene Miocene Transition             |
| PF    | Polar Front                              |
| RSDW  | Ross Sea Deep Water                      |
| SACCF | Southern Antarctic Contour Current Front |
| SB    | Southern Boundary                        |
| SLE   | Sea level equivalent                     |
| SO    | Southern Ocean                           |
| SST   | Sea Surface Temperature                  |
| TWTT  | Two way travel time                      |
| UPS   | Universal Polar Stereographic            |
| WAIS  | West Antarctic Ice Sheet                 |
| WL    | Wilkes Land                              |
| WL-S  | Wilkes Land Seismic unit                 |
| WL-U  | Wilkes Land Unconformity                 |
| WSB   | Wilkes Subglacial Basin                  |
| XRD   | X-ray Diffraction                        |
| XRF   | X-ray Fluorescence                       |

# Context and Motivation

---



## CONTEXT AND MOTIVATION

The Antarctic Ice Sheet (AIS) and surrounding sea ice cover are one of the most important components of the Earth system affecting global changes in sea level, the global thermohaline oceanic circulation, Earth's albedo, atmosphere-ocean CO<sub>2</sub> exchange and marine ecosystems, among other.

The Antarctic ice sheet developed at ~34 million years ago (Ma) and from that time onwards its volume fluctuated considerably. The spatial and temporal scale of these ice sheet fluctuations is still mostly unknown. A better understanding of past AIS dynamics and stability is however especially important in the current scenario of global warming. At present, CO<sub>2</sub> global mean annual concentrations recorded at the Mauna Loa Observatory in Hawaii are as high as 408 ppm in 2018. These CO<sub>2</sub> concentrations have not been recorded on Earth since the last 3-5 Ma. The Intergovernmental Panel on Climate Change (IPCC) forecasts for the next century include an increase in greenhouse gases between 500 and 1000 ppm of CO<sub>2</sub>, and an increase in global temperature between 1.8° to 4°C, depending if we follow a low-emission scenario (the Paris Agreement) or a business as usual scenario (IPCC, 2014). The forecasted ranges in CO<sub>2</sub> are similar to atmospheric CO<sub>2</sub> levels reported during the Oligocene (23.03–33.9 Ma) that fluctuated between 400 and 750–800 ppm (Pagani et al., 2005; Beerling and Royer, 2011; Zhang et al., 2013). Although the Earth's climate system was different during the Oligocene because different plate tectonics and ocean configurations, the insights that we can gain about ice sheet-oceanic interactions and the response of the ice sheet to this warm period are still valid to inform the models used by the IPCC for future changes.

The Integrated Oceanic Drilling Program (IODP) Expedition 318 to the Wilkes Land Margin (Escutia et al., 2011) intended to provide a long-term record of Cenozoic Antarctic glaciation and its close relationships with global climatic, oceanographic and sea level changes (Escutia et al., 2005, 2011). Expedition 318 recovered sediments from the East Antarctic Wilkes Land (WL) margin in front of the Wilkes Subglacial Basin (WSB). This location is relevant because in the WSB the East Antarctic Ice Sheet (EAIS) is grounded on land that is below sea level (marine-based). Because marine-based ice sheets are more sensitive to warming, the East Antarctic Wilkes Land margin was an ideal place to test the stability of the EAIS that until then was thought to be very stable.

IODP Expedition 318 was carried out between 4 January–9 March 2010 (Wellington, NZ- Hobart, AUS) and recovered ~2000 m of high quality middle Eocene–Holocene sediments at seven sites along shelf-to rise-transects. Together, the cores represent a near continuous ~53 m.y. record of Antarctic history. Sediments recovered at Site U1356 included Oligocene and Miocene sediments that provided a unique opportunity to study ice sheet and ocean dynamics under warmer than present conditions (within the range of future projections by the IPCC) in this potentially more sensitive sector of the East Antarctic margin. In addition, the available grid of multichannel seismic reflection profiles in this area provided the



possibility to extend the results from Ste U1356 regionally.

## OBJECTIVES AND HYPHOTESIS

The overarching aim of this thesis is to investigate East Antarctic Ice Sheet (EAIS) dynamics and paleoceanographic configurations during the Oligocene-Miocene with emphasis, when possible, in warmer than actual episodes of the Earth history (i.e., late Oligocene).

To achieve this overarching aim, this thesis has three main objectives:

1. *Determine ice sheet evolution and glacial-interglacial dynamics during the late Oligocene and the Oligocene-Miocene transition (OMT).*
2. *Determine the paleoceanographic evolution and polar front dynamics during the Oligocene - Miocene.*
3. *Investigate forcing mechanisms and thresholds that drive EAIS dynamics and paleoceanographic variability during the Oligocene and the Miocene.*

This thesis objectives aim to verify the following hypotheses:

### **Hypotheses related to objective 1:**

- After a continental-size ice sheet had developed by 33.6 Ma, ice sheets remained highly dynamic during the Oligocene.
- Large mass transport deposits recovered across the Oligocene-Miocene Transition (OMT, 23.03 Ma) at Site U1356 result from the major expansion of the East Antarctic Ice Sheet during the cooling trend to the isotopic Mi-1 event .

### **Hypotheses related to objective 2:**

- Paleoceanographic configurations similar to modern ones are not established until after the OMT (23.03 Ma).
- Polar fronts associated with a proto-Antarctic Circumpolar Current (ACC) underwent changes in latitudinal extent and current strength during glacial-interglacial cycles.

### **Hypotheses related to objective 3:**

- Large mass transport deposits mark a threshold in ice sheet dynamics in the Wilkes Land margin.
- Ice sheet and ocean dynamics during the Oligocene and the Miocene are driven by changes in the earth's orbit around the sun.

## THESIS LAYOUT

This thesis is organized into seven chapters:

Chapter 1 **Introduction.** This chapter provides an overview of global climate and Antarctic ice sheet evolution; the orbital cycles; the glaciomarine deep-water sedimentary processes; the tectonic and stratigraphic evolution of the margin; the onshore and offshore physiography of the Wilkes Subglacial Basin and offshore the eastern Wilkes Land; and modern and past configurations of the Southern Ocean.

Chapter 2 **Materials and methods.** We provide a broad introduction to the Integrated Ocean Drilling Program (IODP) Expedition 318 that recovered the sediments from Site U1356 that are the main focus of this study. In addition, a general introduction to the methodologies used for this thesis is also provided although detailed methodological explanations are given in chapters 3, 4 and 5.

Chapter 3 **Late Oligocene astronomically paced contourite sedimentation in the Wilkes Land margin of East Antarctica: insights into paleoceanographic and ice sheet configurations.**

*Salabarnada, A., Escutia, C., Röhl, U., Nelson, C. H., McKay, R., Jiménez-Espejo, F. J., Bijl, P. K., Hartman, J. D., Strother, S. L., Salzmann, U., Evangelinos, D., López-Quirós, A., Flores, J. A., Sangiorgi, F., Ikehara, M. and Brinkhuis, H.*

*Published in Climate of the Past, 14(7), 991–1014, doi:10.5194/cp-14-991-2018, 2018.*

Based on a detailed study of sediments from IODP Site U1356 we provide: 1) the first glacial–interglacial deep-water sedimentation model off the Wilkes Land margin during the late Oligocene (26 – 25 Ma); 2) insights into the configuration of the ice sheet and the Southern Ocean dynamics in this sector of the east Antarctic margin; and 3) insights into the astronomical forcing in late glacial-interglacial dynamics.

Chapter 4 **Ice sheet and oceanic configurations in the eastern Wilkes Land margin during the late Oligocene to Miocene transition.** Ice sheet and ocean dynamics across the Oligocene-Miocene transition (OMT) are determined based on sediments recovered from Site U1356. Our results point to a very dynamic East Antarctic Ice Sheet (EAIS) and ocean frontal systems at that time. In addition, we interpret the occurrence of large Mass Transport Deposits (MTDs) to result from the erosion and overdeepening of the Wilkes Subglacial Basin during repeated advances of the EAIS. This results on a shift from a continental-based to a marine-based EAIS in this margin sector that takes place during the latest Oligocene.

Chapter 5 **Oligocene to Miocene bottom current deposition and circulation off the eastern Wilkes Land margin.** The spatial and temporal evolution of the contourite drifts off the Wilkes Land margin is determined through correlation of Site U1356 findings with the grid of multichannel reflection seismic profiles. The results provide key insights to understand the inception and variability of two water masses, the proto-AABW and the proto-CDW. We provide a paleoceanographic evolution model, where during





the early Oligocene (33.6 - 28 Ma) a westward flowing AABW dominated off the WL margin, and an eastward flowing current interpreted to correspond with the deep proto-CDW is not evidenced until the late Oligocene (around 28 Ma).

**Chapter 6 General Discussion - Oligocene-Miocene Ice Sheet and Paleoceanographic Evolution off the Wilkes Land Margin:** This chapter aims to integrate the findings in chapters 2, 3 and 4 and to discuss them in comparison with findings by previous workers in this region regarding ice sheet dynamics-ocean dynamics.

**Chapter 7 Summary and Conclusions:** The conclusions of this thesis are hereby stated in relation to the initial thesis objectives. In addition, we briefly discuss remaining open questions and future perspectives.

# Chapter 1

Introduction

---



## CHAPTER 1

### INTRODUCTION

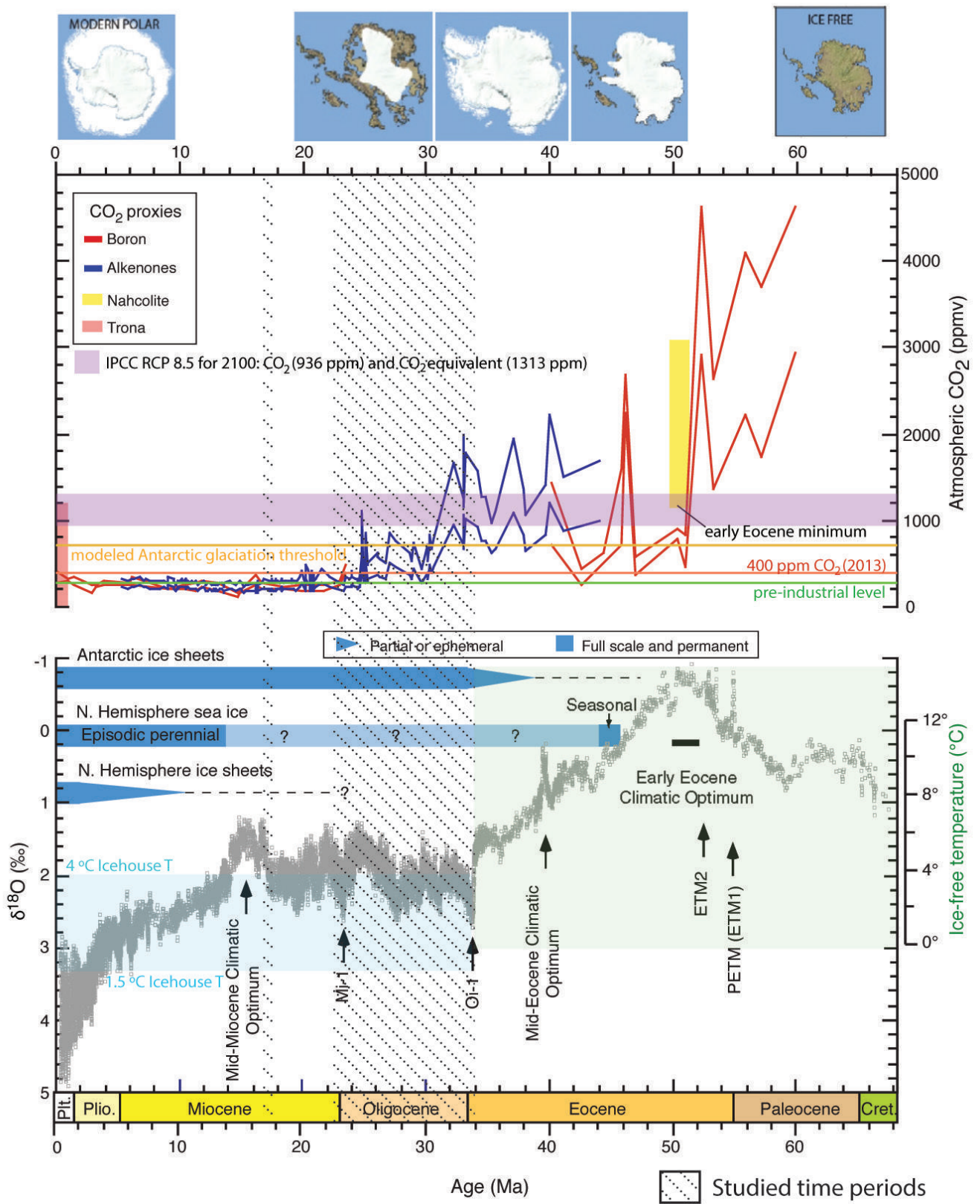
#### 1.1. EOCENE TO EARLY MIOCENE GLOBAL CLIMATE AND ANTARCTIC ICE SHEET EVOLUTION

The Antarctic Ice Sheets (AIS), sea ice and the Southern Ocean are key components of the Earth's climate system. The growth and decay of the AIS influence variations in the Earth's average albedo, sea ice extent, atmospheric and ocean circulation, global sea level, and marine nutrient distribution, among other. Despite the relevance of the AIS and the Southern Ocean on the global climate and sea levels, our knowledge regarding ice-ocean-atmosphere configurations and interactions controlling the variations and stability of the AIS is still rudimentary. Geological records from the Antarctic margins are key to understanding how the AIS has responded in the past to warming climates as those predicted for the future by the IPCC (2014).

Because geological records from around the margin are still limited, the history of the AIS has been largely reconstructed from low-latitude records, such as the oxygen isotope composition ( $\delta^{18}\text{O}$ ) obtained from benthic foraminifera recovered in deep-sea sediments. The  $\delta^{18}\text{O}$  has been long established as a proxy for global ice volume and seawater temperature (Shackleton and Kennett, 1976; Zachos et al., 2001). This data records peak greenhouse conditions during the early Eocene (around 55 Ma). Geological records from around Antarctica have shown that subtropical forests existed in the eastern Wilkes Land margin during peak greenhouse conditions at around 55 Ma (Pross et al., 2012; Contreras et al., 2012; Contreras et al., 2012). These authors also show that these forests were replaced by temperate forests during the middle Eocene in response to cooling. Sediments from the Ross Sea and Prydz Bay also record temperate conditions prior to the development of a continental ice sheet at around 34 Ma (Barrett et al., 2000; O'Brien et al., 2001).

Peak greenhouse conditions were followed by a cooling trend that is punctuated by several abrupt cooling/ice volume increase events (e.g., Zachos et al., 2001; Fig. 1.1). The first geologically speaking abrupt (spanning about 300,000 years) decrease in  $\delta^{18}\text{O}$  isotopes ( $>1.5\text{‰}$ , interpreted to represent a  $\sim 4\text{--}5^\circ\text{C}$  cooling of deep ocean temperatures), took place around 34 Ma (Zachos et al., 2001; Liu et al., 2009). This shift marked the transition from a greenhouse to an icehouse world that culminated with the growth of a continent-wide ice sheet by the Oi-1 isotopic event (Fig. 1.1; Zachos et al., 2001). Sediments recovered from the Antarctic continental shelf and rise have now provided ample evidence for ice sheets grounded at the shelf in the early Oligocene in the Ross Sea (Barrett, 1989, 2007), Prydz Bay (Barron et al., 1991; O'Brien et al., 2001; Passchier et al., 2017), Weddell Sea (Barker et al., 1988) and the eastern





Wilkes Land margin (Escutia et al., 2011, 2014). The development of this first ice sheet was originally linked to the tectonic and paleoceanographic reorganization that took place during the final opening and deepening of the Tasman and Drake gateways separating Antarctica from the American and Australian continents, respectively (Kennett, 1977). The final opening and deepening of the basins allowed the development of the Antarctic Circumpolar Current (ACC) that would result in the thermal isolation of Antarctica (Kennett, 1977). Models however, cannot reproduce the growth of a continent-wide ice sheet only accounting with the cooling caused by the opening of these gateways (Fig. 1.1.; DeConto and Pollard, 2003). Instead, models state that a rapid decline in atmospheric CO<sub>2</sub> is strongly implicated in the growth of the Antarctic Ice Sheet across a CO<sub>2</sub> threshold that was crossed (around 800 ppm; Fig. 1.1). That said, the timing of gradual cooling during the middle Eocene has been directly linked with the initial opening of the Tasman Gateway (Bijl et al., 2013; Houben et al., 2013) pointing to the opening of the Tasmanian Gateway as a pre-conditioning mechanism for Southern Ocean surface water and global deep ocean cooling, especially in the apparent absence of (sub-) equatorial cooling.

Oxygen isotopic records from the early Oligocene (28–26 Ma; Fig. 1.1) point to highly variable climate conditions and ice sheet dynamics (Pälike et al., 2006; Liebrand et al., 2016; 2017) that are forced by orbital variations (Liebrand et al., 2016). During the late Oligocene (~26–23.5 Ma) warmer conditions are inferred from the up to 1 ‰ long-term decrease in the benthic  $\delta^{18}\text{O}$  isotopic record (Zachos et al., 2001; Liebrand et al., 2016; Fig. 1.1). The significant warming trend interpreted from the decrease in the  $\delta^{18}\text{O}$  isotope records was thought to result in the deglaciation of large parts of the AIS (Zachos et al., 2001). However, there are important differences between  $\delta^{18}\text{O}$  records from Pacific, Indian, and Atlantic Ocean sites (e.g., Pälike et al., 2006; Cramer et al., 2009; Liebrand et al., 2011; Mudelsee et al., 2014; Hauptvogel et al., 2017) and Southern Ocean sites (Pekar et al., 2006; Mudelsee et al., 2014). Based on the study of the isotopic record in sediments from the Atlantic, the Indian, and the equatorial Pacific, Pekar et al. (2006) explained this conundrum of a glaciated Antarctica and varying intra-basinal  $\delta^{18}\text{O}$  values with the coeval existence of two deep-water masses, one sourced from Antarctica and another, warmer bottom water, sourced from lower latitudes. High  $\delta^{18}\text{O}$  values in the Southern Ocean sediments are in agreement with the ice proximal record recovered by the Cape Roberts Project (CRP) in the Ross Sea, which show the existence of glaciers/ice sheets at sea level (Barrett, 2007; Hauptvogel et al., 2017). However, additional geological records from close to Antarctica are needed to further evaluate these differences and to understand ice-ocean interaction.

← **Figure 1.1.** Cenozoic pCO<sub>2</sub> and stacked deep-sea benthic foraminifer oxygen isotope curve for 0 to 65 Ma, updated from Zachos et al. (2008) and converted to the “Gradstein timescale” (Gradstein et al., 2004); extracted from (Escutia et al., 2014). Mi-1 = Miocene isotope Event 1, Oi-1 = Oligocene isotope Event 1, ETM2 = Eocene Thermal Maximum 2, PETM = Paleocene/Eocene Thermal Maximum, ETM1 = Eocene Thermal Maximum 1. Antarctic ice sheet evolution (mostly inferred from low latitude records) under the different CO<sub>2</sub> scenarios is shown at the top of the figure. Shaded squares indicate future CO<sub>2</sub> (purple) and Temperature (blue) scenarios forecasted by the IPCC (2014).



The second abrupt shift in the oxygen isotopic record occurs at the Oligocene-Miocene transition (OMT) and is marked by a large expansion of the AIS (the Mi-1 event) identified by a positive oxygen isotope shift ( $\sim 0.6 - 1\%$ ) (Fig. 1.1; Kennett, 1977; Zachos et al., 2001, 2008). This event is attributed to declining  $\text{CO}_2$ , coinciding with a node in obliquity and a minimum in eccentricity, which are favourable conditions for ice sheet growth (Zachos et al., 2001b). In Antarctica, an erosional hiatus in the Cape Roberts Project drill core provided the first direct evidence for major cooling and ice sheet expansion of the EAIS outlet glaciers into the western Ross Sea at  $\sim 23.7$  Ma (Naish et al., 2001). Sediments collected from the Ross Sea indicate an ice sheet volume increase in the order of 20% greater than the present during the OMT (Shackleton and Kennett 1976).

After the Mi-1 event, marine palynomorphs indicate that coastal temperatures did not return to the warmth of the late Oligocene and that there was a reduced freshwater melt input to coastal regions (Salzmann et al., 2016). During the early and middle Miocene, marine deep-sea oxygen isotope records indicate a period of ice sheet instability superimposed on a long term warming trend that culminated in the mid-Miocene climatic optimum from  $\sim 17$  to 15 Ma (Zachos et al., 2001). This phase was followed by a time of significant ice sheet expansion on Antarctica (e.g. Miller et al., 1991; Lear et al., 2000; Shevenell et al., 2004).

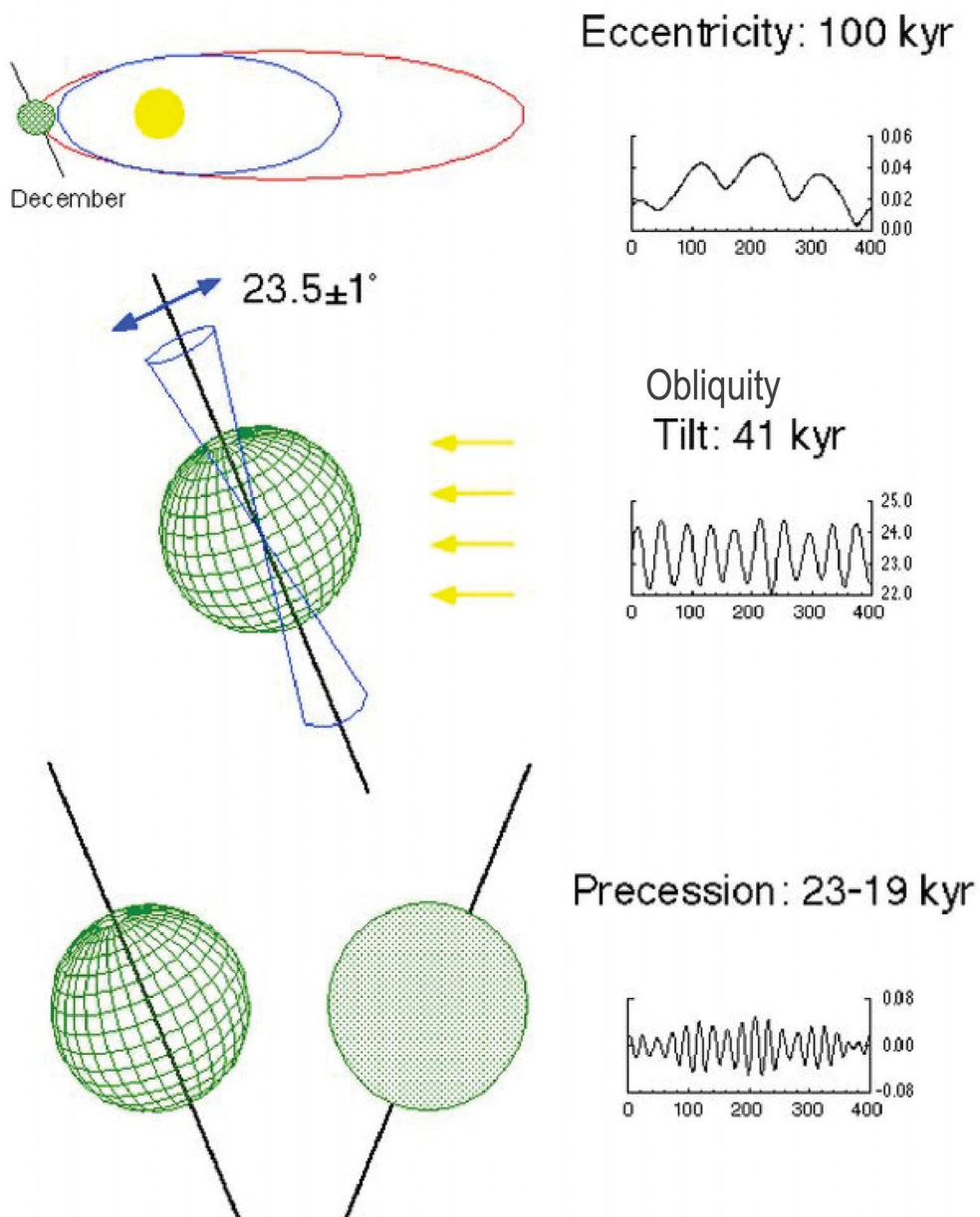
## 1.2. EARTH ORBITAL PARAMETERS

Quasi-periodic variations in Earth's orbital and rotational parameters relative to the Sun force changes in seasonal, latitudinal, and total insolation, leading to local and global climate cycles at  $10^4$  to  $10^6$  yr time scales (Hinnov, 2013). These climate cycles, or Milankovitch cycles (Milankovitch, 1941) initiate glacial-interglacial cycles that are recorded in sedimentary archives. Thus, one of the major interests in paleoclimatology is to recover continuous sedimentary sections that can provide insights to the response of Earth's climate system to orbital induced changes in insolation (Zeeden, 2013).

The astronomical parameters that affect insolation are (Fig.1.2): (1) Earth's orbital eccentricity, which determines Earth-Sun distance, and thus total insolation, which vary in periods of 413, 123 and 100 thousands of years (ka); (2) the precession of Earth's rotation axis, or precession of the equinoxes, which determines the timing and location of the seasons with respect to Earth's orbit and has dominant periods at 24, 22 and 19 ka; and (3) Earth's axial tilt, or obliquity of the ecliptic, which determines the angle of incidence of insolation and has dominant periods of 54 and 41 ka (Milankovitch, 1941; Hinnov, 2013). Obliquity-forced changes in the meridional temperature gradient impact on ice-sheet development, evidenced in deep-sea records, which show a strong axial tilt signal controlling ice-sheet evolution. A paradigmatic example can be found during the Pliocene, in the northwest part of the Ross ice shelf, where the ANDRILL program revealed the link between well-dated  $\sim 40$ -kyr cyclic variations in ice-sheet extent and cycles in insolation influenced by changes in the Earth's obliquity (Naish et al., 2009). Recently,

this link has been extended towards past, where it has been shown that sensitivity to obliquity forcing increases when ice-sheet margins extend into marine environments (Levy et al., 2019). More specifically the influence of obliquity-driven changes in ocean dynamics is amplified when marine ice sheets are extensive, and sea ice is limited (Levy et al., 2019).

### Milankovitch Cycles



**Figure 1.2.** Components of Milankovitch cycles.





### 1.3. DEEP-WATER SEDIMENTATION ON GLACIATED MARGINS

Sedimentation in glaciated margins is strongly influenced by ice sheet growth and decay and by the circulation of water masses. Sediments around the Antarctic margin are therefore key to obtain proximal records of ice sheet behaviour and ocean-ice sheet dynamics. Sediments from around the Antarctic continental shelves provide key information regarding advances and retreats of the ice sheet grounding lines, but these deposits are discontinuous because of erosion and hard to date (e.g., Escutia et al 2019).

Deep-water deposits provide a more continuous and datable records of ice sheet (albeit indirect) and ocean configurations during glacial and interglacial cycles. This thesis focuses on sediments deposited on the limit between the continental rise and the abyssal plain of the eastern Wilkes Land margin. The dominant processes in this setting are similar to any other deep-water setting around the world with the difference that some processes are glacially-influenced. The main processes involved in glaciated deep-water settings are pelagic/hemipelagic settling, turbidity currents, mass transport deposits (MTDs), ice rafting and reworking by bottom currents (Fig. 1.3).

During interglacial times, when the ice sheet retreats closer to the coast, the outer shelf, slope and deep-water setting receive a rain of hemipelagic sediments (i.e., Andreson 1999; O'Brien et al., 2001; Escutia et al., 2003). Hemipelagic deposits consist of fine-grained sediments that result from slow settling through the water column of terrigenous and/or biogenic remains of organisms.

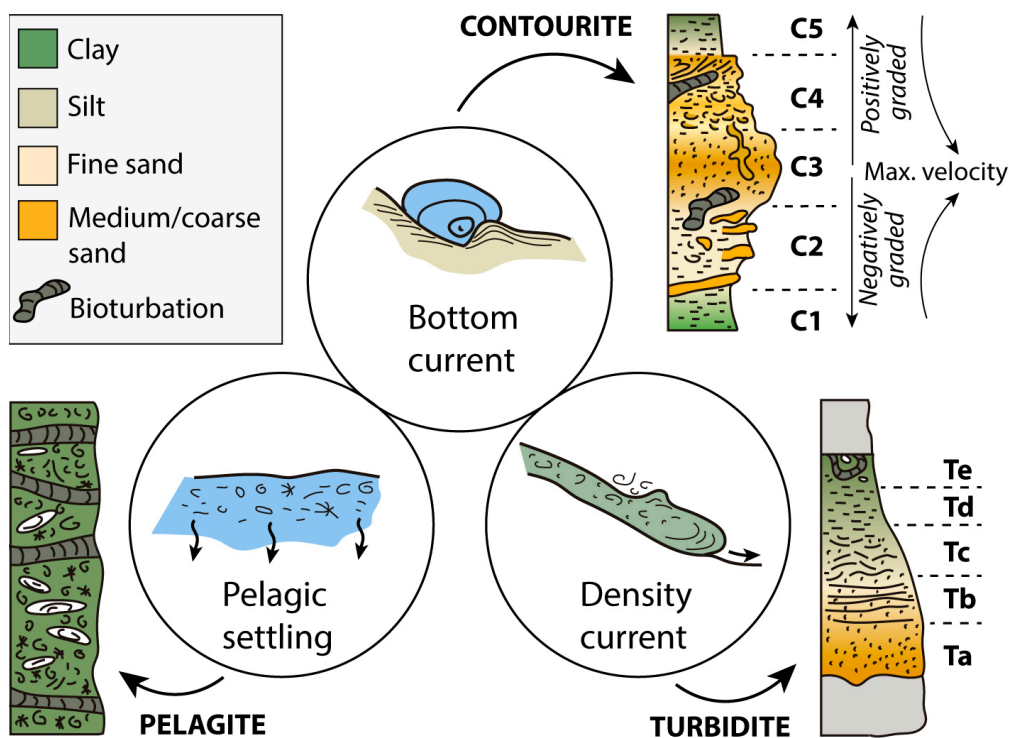
During glacial times when ice advances across the continental shelf, large volumes of sediment is delivered to the outer shelf and slope by the ice streams causing slope instability and the generation of mass transport deposits and/or turbidity currents. On the continental rise, these turbidity currents develop the channel and levee complexes characteristic of deep-sea fans (Eittrheim and Smith, 1987; Hampton et al., 1987; Escutia et al., 1997, 2000). Turbidites are deep-water deposits generated by turbidity currents. Turbidites commonly show predictable changes in bedding from coarse layers at the bottom to finer laminations at the top, known as Bouma sequences (Fig. 1.3), which result from different settling velocities of the particle sizes present. Turbidite deposits are a “member” of an evolutionary trend of vertically associated sediments that accumulate from debris flows, hyper-concentrated to concentrated density flows, and turbidity flows (Mulder and Alexander, 2001).

Mass transport deposits are grouped as cohesive flows that include debris flows and clay-rich and silty mud flows by Mulder & Alexander (2001). MTDs are typically structureless sediments that can form deposits with many different shapes, from sheets, lobes, mounds, channel fills or trench fills, for example. They can be several tens to hundreds of meters thick, several km across and stretch down slope for hundreds of kilometers (Nelson et al., 2011)

Ice rafted debris (IRD) deposition and reworking by slumping and/or oceanic currents can occur coevally to the deposition of hemipelagic, turbidite or MTDs.

Iceberg rafting is a common process involving grain of all sizes within and iceberg being dispersed and released into the water column. This takes place either because the iceberg is melting in the sea or the iceberg rotates due to instabilities and dumps loose material accumulated on the surface. Recognition of IRD can provide valuable information as for example to recognize the arrival of an ice sheet into the sea, the onset of a glaciation, ice sheet melting events, and information regarding ice sheet underlain terrains (e.g., Domack and Powell, 2017).

Contourites are sediments deposited or substantially reworked by the action of bottom currents (mainly thermohaline and wind-driven) that have an overall alongslope flow (Heezen et al. 1966). Contourites show a wide range of grain-sizes, composition, and preserved sedimentary structures. This process commonly results in well-sorted sediment, due to the reworking behaviour and the winnowing of the finer grained material (Rebesco et al., 2014). The common contourite facies model has been separated into 5 divisions by Stow and Faugères (2008) (Fig. 1.3), although it is common that in the geological record only partial base or top sequences are preserved (Stow and Faugères, 2008).



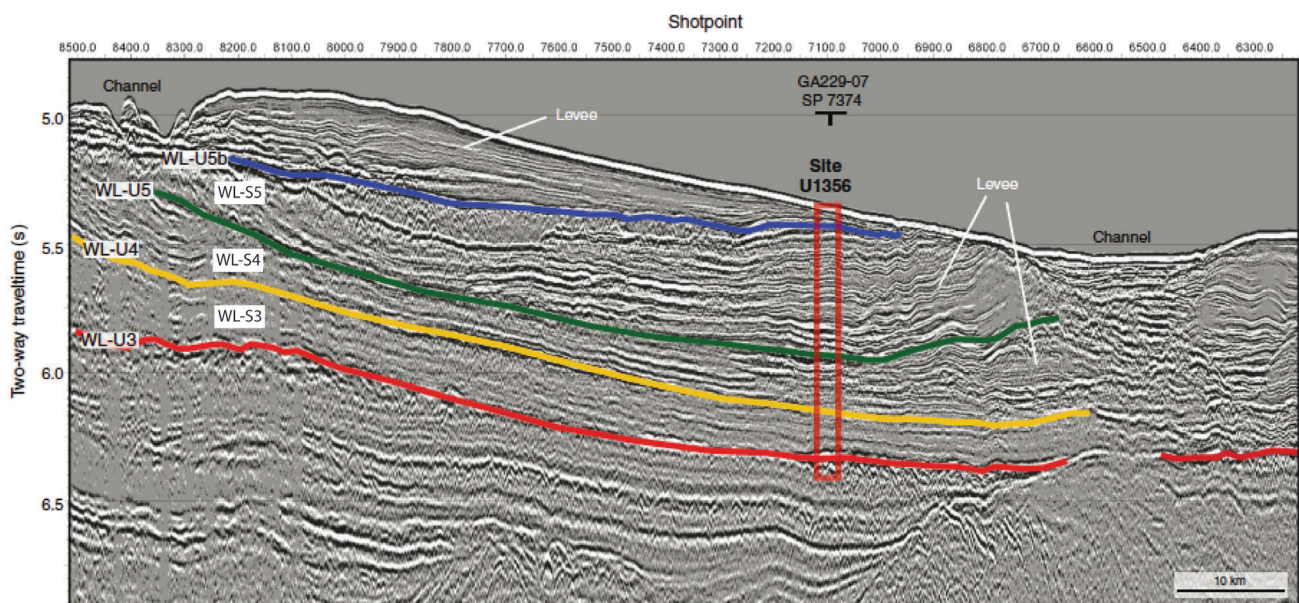
**Figure 1.3.** Standard facies models of a) Pelagites/hemipelagites, associated with settling through the water column; b) contourite sequence, linked to variations in contour current velocity (modified from Stow and Faugères, (2008), based on the original figure from Gonthier et al. (1984); and c) Turbidite with Bouma sequence, linked to density currents (Lowe, 1982).

## 1.4. THE EASTERN WILKES LAND MARGIN

### 1.4.1. TECTONIC AND SEISMIC STRATIGRAPHIC EVOLUTION OF THE WILKES LAND

The Wilkes Land continental margin is formed by the separation of Australia from Antarctica. Breakup propagated west to east starting at 83–75 Ma in the central Bight region and likely as late as about 50 Ma in the Terre Adélie-Otway region (e.g., Colwell, et al., 2006; Close, et al., 2009; Direen et al., 2013). The basement rock consists of blocks of faulted continental and oceanic crust, with deep marginal rift basins that contain >8 km sediment accumulation and areas of anomalously shallow bathymetry (Escutia et al., 1997; 2005; Donda et al., 2007). During middle Eocene times, continental blocks contained in the Tasmanian sill started to drown gradually (Röhl et al., 2004).

Cenozoic post rift sequences in the Wilkes Land have been widely studied from seismic surveys (e.g., Eittreim et al., 1995; Escutia et al., 1997, 2000, 2002, 2003, 2005; Donda et al., 2003). The main regional unconformities defined on the continental rise in this segment of the Wilkes Land margin and that are relevant for the objectives of this thesis are named, from older to younger: WL-U3, WL-U4, WL-U5 and WL-U6 (Fig. 1.4; Escutia et al., 1997, 2005, 2011; De Santis et al., 2003). These unconformities bound seismic units WL-S4 to WL-S6 (Fig 1.4). Unconformity WL-U3 was interpreted as a regressive surface inferred to represent the first arrival of an ice sheet on the Wilkes Land continental shelf during the Cenozoic (Eittreim and Smith, 1987; Escutia et al., 1997, 2005; De Santis et al., 2003). Drilling by the IODP Expedition 318 confirmed WL-U3 as the unconformity separating pre-glacial from glacial deposits in this margin (Escutia et al., 2011). The two deepest units above the WL-U3 and WL-U4 unconformities, WL-S4 and WL-S5, respectively, consist of stratified and continuous reflectors that generally terminate against the base of the slope (Escutia et al., 1997; 2005; Donda et al., 2003). Isolated channel-levee complexes were first observed up-section within unit WL-S5 (Escutia et al., 1997; Escutia et al., 2000;

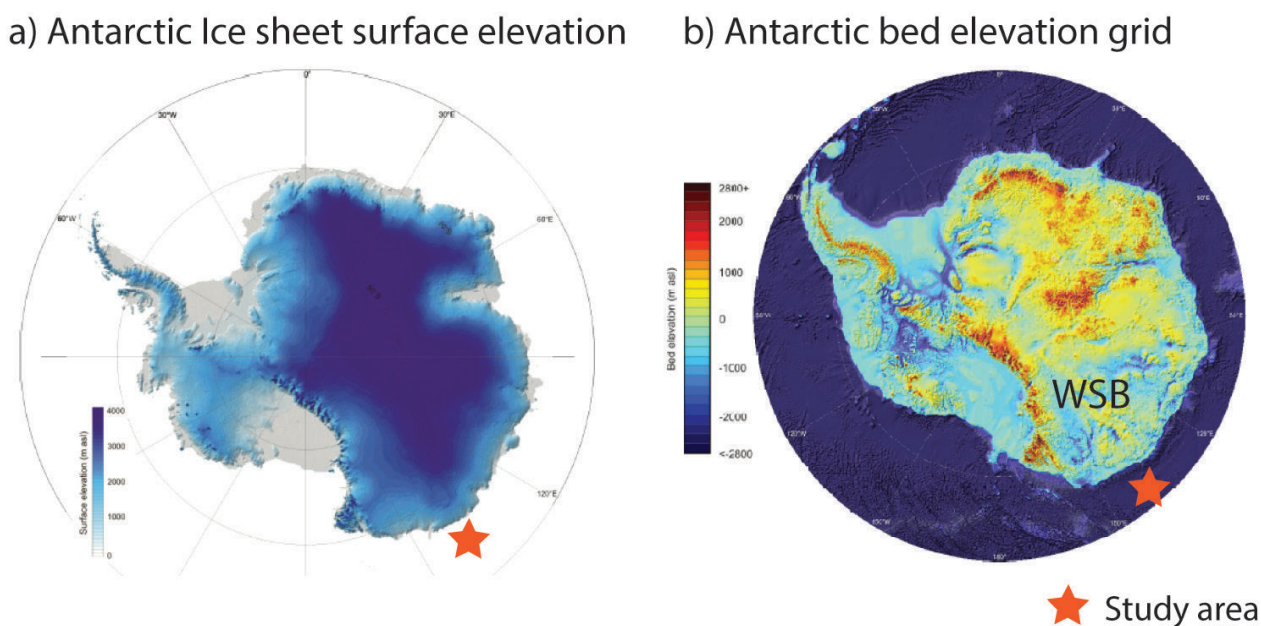


**Figure 1.4.** Multichannel seismic reflection profile across Site U1356 showing the regional unconformities WL-U3, WL-U4, WL-U5 and the seismic units they bound, extracted from Escutia et al., (2011). Site U1356 penetration is marked with the red rectangle.

Escutia et al., 2002; Donda et al., 2003). During deposition of units WL-S6 and WL-S7, channel-levee complexes became widespread and turbidity flows were interpreted to be the dominant process building the sedimentary ridges on the rise. However, sedimentary ridges and wavy reflectors that characterize bottom contour-current deposition occur on the lower rise above the WL-U5 unconformity (Escutia et al., 2000; 2002, 2005; Donda et al., 2003).

#### 1.4.2. THE WILKES SUBGLACIAL BASIN

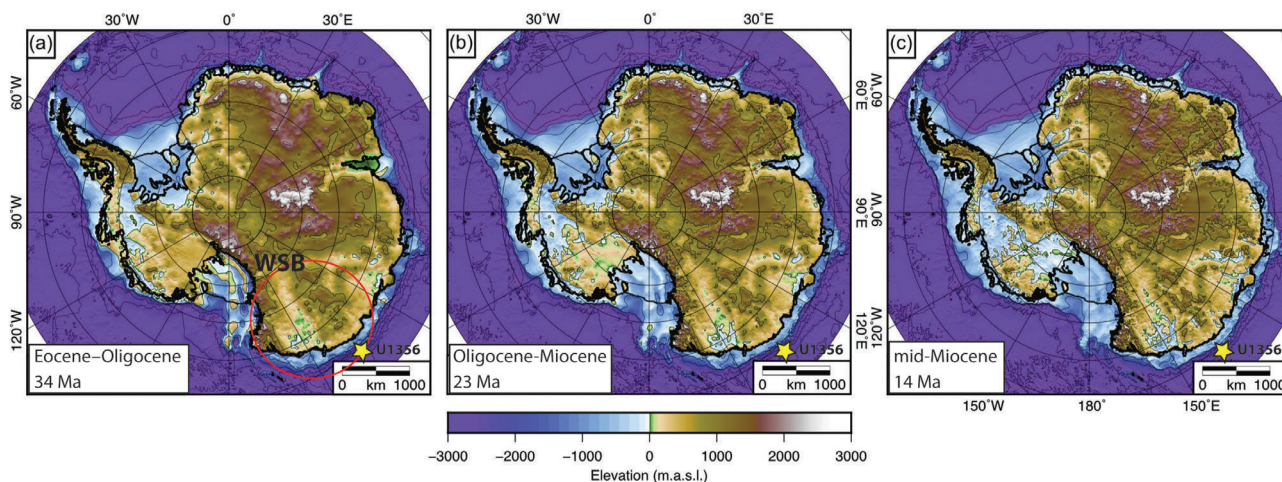
The study area is located off the eastern Wilkes Land margin at the seaward termination of the Wilkes Subglacial Basin (WSB; Drewry, 1983; Ferraccioli et al., 2001; 2009). Based on aeromagnetic investigations, the WSB is ~1400 km long and up to ~600 km wide (Ferraccioli et al., 2001, 2009) and is buried beneath a 3 km thick EAIS (Fig. 1.5a). The Bedmap2 bed elevation grid in Figure 1.5b shows how in the WSB the EAIS is largely grounded on land that is below sea level (mean bedrock elevation ~500 m below sea level; Fertwell et al., 2013). This makes this sector of the EAIS more vulnerable to warming which is of relevance considering that the WSB holds an ice mass equivalent to a 19m sea level rise that drains through marginal glaciers (e.g., Cook and Ninnis ice streams) near George V Land (e.g., Fretwell et al., 2013).



**Figure 1.5.** Antarctic ice sheet surface grid and bed elevation grid (Bedmap2) modified from Fretwell et al. (2013). Wilkes Subglacial basin (WSB) and study area are pointed.

Modelled reconstructions for the latest Eocene Antarctic elevations (34 Ma) show the WSB to be mostly occupied by low-lying lands largely above sea level (Fig. 1.6; Wilson and Luyendik, 2009; Paxman et al., 2019). 3-D flexural modelling conducted by Paxman et al. (2018; 2019) shows that an over-deepened WSB similar to today's occupied with a marine-based ice sheet was already in place by the Miocene. These authors suggest the main erosion of the WSB likely took place during the Oligocene (Fig. 1.6).





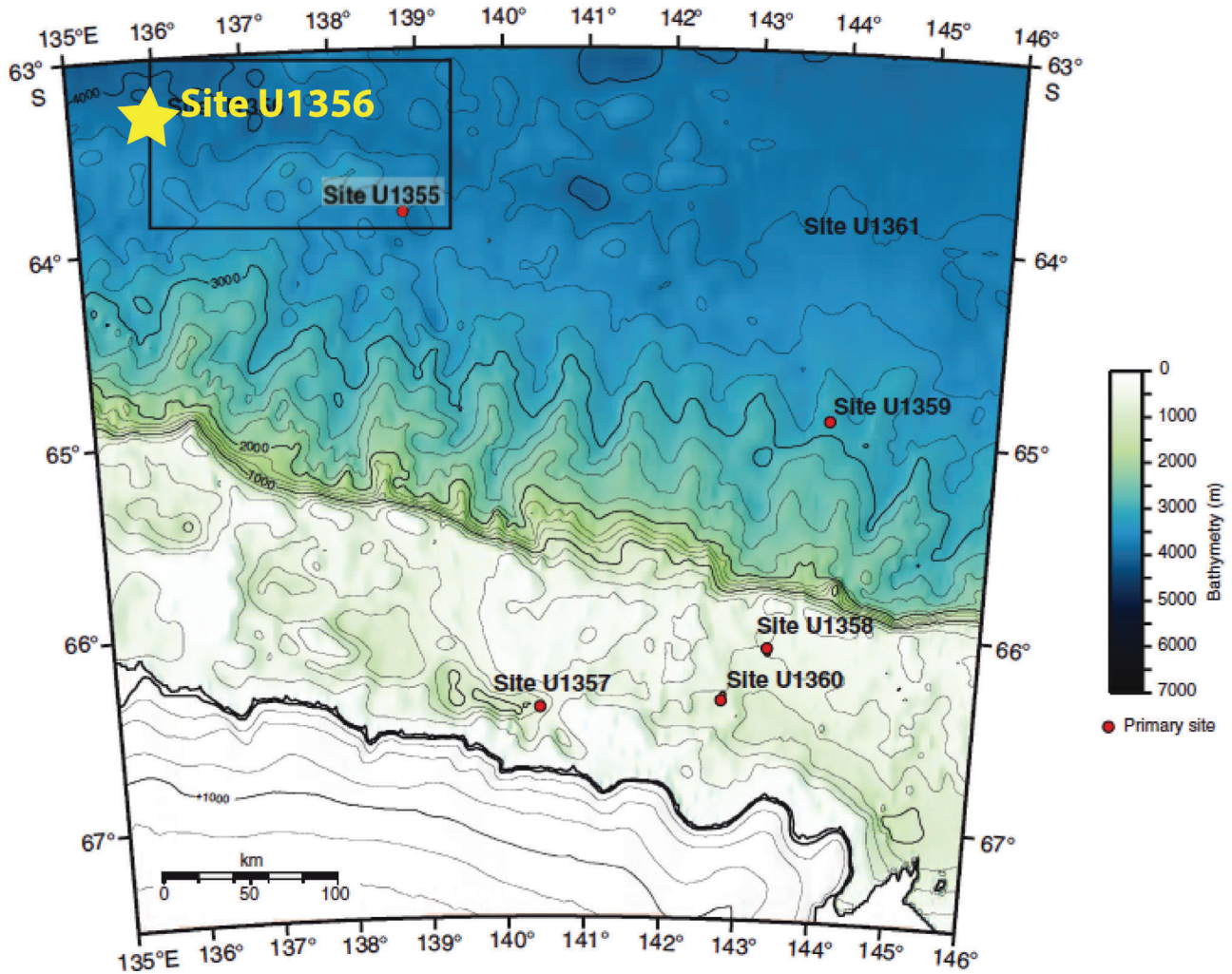
**Figure 1.6.** Maps from Paxman et al., (2019) of reconstructed Antarctic continental paleotopographies for a) the Eocene–Oligocene boundary (ca. 34 Ma), b) the Oligocene–Miocene boundary (ca. 23 Ma), and c) the mid-Miocene climate transition (ca. 14 Ma).

#### 1.4.3. PHYSIOGRAPHY OFFSHORE THE EASTERN WILKES LAND MARGIN

The offshore bathymetry of the studied sectors of the Wilkes Land margin is characterized by an irregular continental shelf ranging in depths from 200 m on outer-shelf banks to 1000 m in shelf troughs (Escutia et al., 1997, 2000) (Fig. 1.7). The troughs are deeper in the inner shelf and become shallower towards the outer shelf. These deep troughs have been eroded by ice streams extending into the continental shelf at times of glacial maxima. The shelf banks are the areas that have been bypassed by the most recent ice streams (Fig. 1.7) (Eittrheim et al., 1987). The continental slope extends from the shelf break to about 2000 m water depth, and is steep (gradient 1:9–1:30) and narrow (15 km average, but up to 25 km) (Escutia et al., 2000). The lower slope and upper continental rise also exhibit a rugged morphology because of a complex network of tributary slope canyons, rise channels and contourite mounds (Fig. 1.7; Escutia et al., 2000, 2002). The upper continental rise extends from approximately 2000 m to 3000 m water depth and is also steep (average gradients greater than 1:100), whereas gradients in the lower rise (from about 3000 m to 4000 m water depth) is less steep (average gradients less than 1:150) (Chase et al. 1987; Hampton et al. 1987).

### 1.5. MODERN AND PAST CONFIGURATIONS OF THE SOUTHERN OCEAN IN THE WILKES LAND MARGIN

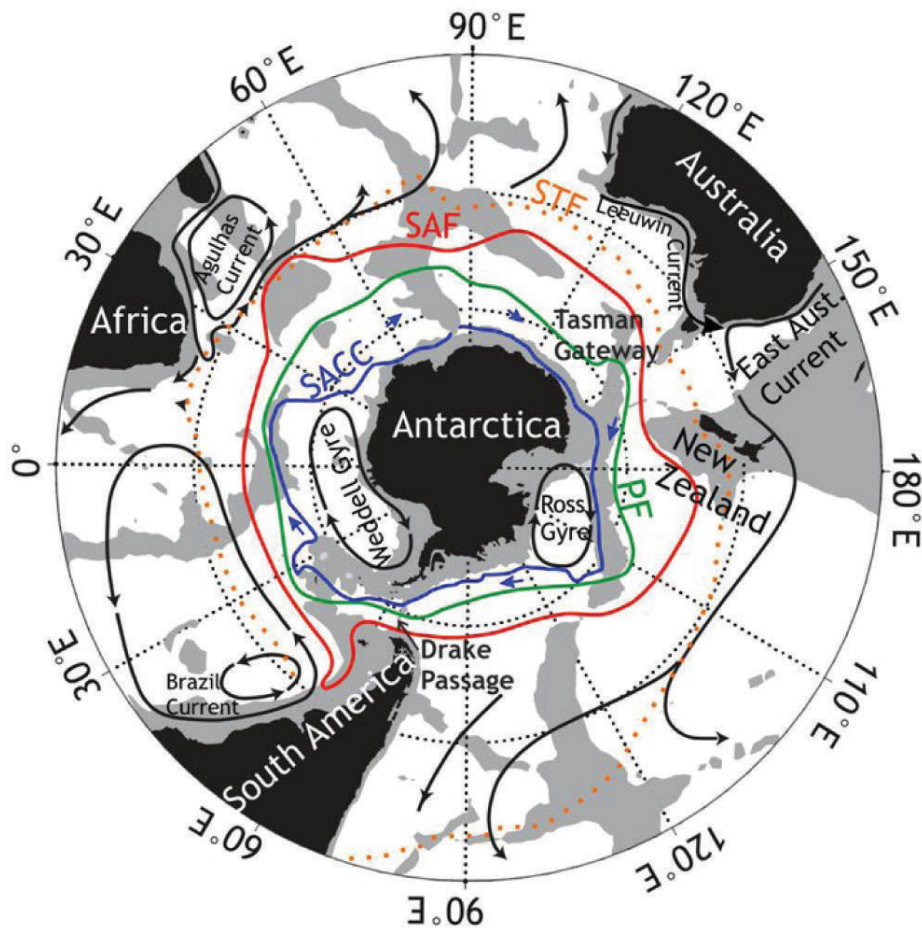
Today, the Southern Ocean (SO) strongly influences Earth’s climate through heat and carbon storage, and the formation of bottom water currents that regulate global atmospheric temperatures. SO circulation is dominated by the wind-driven Antarctic Circumpolar Current (ACC; Rintoul et al., 2018; Fig. 1.8), which connects all major oceanic basins and prevents the north-south exchange of  $\text{CO}_2$ , heat and moisture, isolating Antarctica from the influence of warmer waters to the north (Rintoul et al., 2001). The ACC



**Figure 1.7.** Bathymetric map from Escutia et al. (2011) of the eastern Wilkes Land margin with the location of Site U1356 and other Expedition 318 drill sites. Contour interval=250 m.

consist in multiple fronts (Fig. 1.8) that are greatly influenced by the topography at the seafloor that can be identified as the locations where jet-like currents are associated with a steep rise of isopycnals toward the south throughout the water column (Rintoul et al., 2001). The circumpolar fronts extend from the sea surface to the seafloor and mark zones with distinct physical, chemical, and ecological characteristics. The strong eastward flow of the ACC is highly connected to an overturning circulation that is composed of two counter-rotating cells. The fronts of the ACC are also circumpolar and existent on any north-south transect of the Southern Ocean. The different fronts are: the Subantarctic front (SAF), the Polar front (PF), and the Southern ACC front (SACC; Fig. 1.8). Within each zone, the water properties tend to be similar at each. The zones delimited by the fronts of the ACC also define biogeographic zones occupied by distinct species assemblages. For example, waters south of the Polar Front tend to be dominated by large phytoplankton such as diatoms (who need silicic acid) and large zooplankton, while coccolithophores and small zooplankton dominate north of the Subantarctic Front (Rintoul and Silva, 2019 and references therein).





**Figure 1.8.** Southern Ocean circulation and Antarctic circumpolar oceanic fronts. Antarctic Circumpolar Current (ACC) marked by blue arrows and main oceanic fronts from north to south are the sub-Tropical Front (STF), Sub-antarctic Front (SAF), the Polar Front (PF), and the Southern ACC front (SACC) figure from Rintoul et al. (2001).

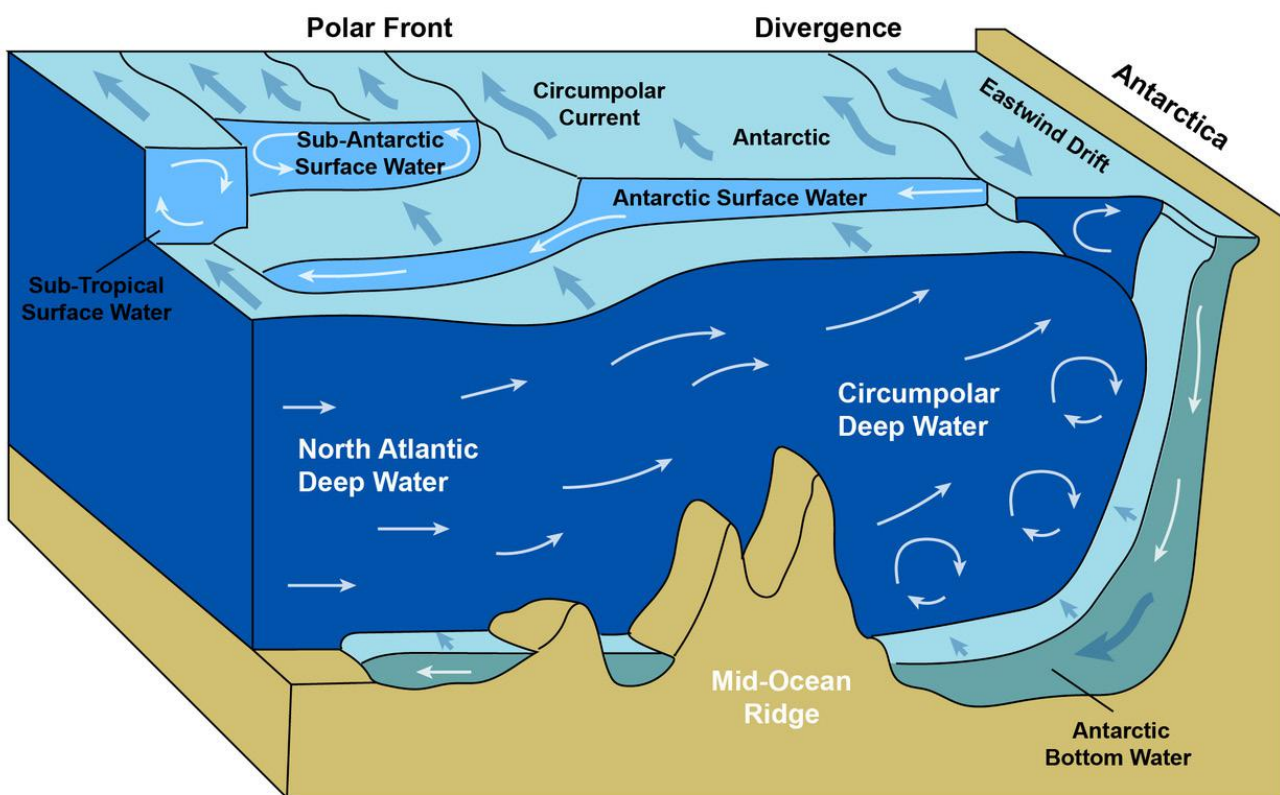
The deep Circumpolar Deep Water (CDW) originates from and circulates along the ACC (Rintoul and Silva, 2019). The Adélie Land at the eastern limit of the Wilkes Land margin is one of the three major sources for Antarctic Bottom Water (Rintoul et al., 2000) together with the Weddell and the Ross Sea (Rintoul et al., 2001). The AABW is the coldest and densest water mass of the global ocean circulation (Fig. 1.9). The ABBW is produced by strong heat loss into the atmosphere, brine rejection from sea ice formation in coastal polynyas and ice/ocean interaction (e.g., Orsi et al., 1999; Bindoff et al., 2000).

Observations over last several decades indicate the SO waters are warming, freshening and decreasing in oxygen (Shimada et al., 2012; Rintoul and Silva, 2019). A decrease in the production of Antarctic Bottom Waters has also been reported (Rintoul, 2007; Wijk and Rintoul, 2014). In addition, several studies have emphasized the role that the SO plays in determining how Antarctic ice sheets melt (Jacobs et al., 2011; Pritchard et al., 2012; Rignot et al., 2013).

The geological record provides insights into past SO configurations that allow us to learn about ice-ocean interactions. Based on available records, Scher and Martin (2008) and Scher et al. (2015) reconstructed

the position of the early Oligocene Antarctic Divergence to be located around 60°S. This was based on the distribution of terrigenous and biogenic (calcareous and siliceous microfossils) sedimentation, Nd isotopes, and Al/Ti ratios through a core transect across the Australian–Antarctic basin in the Southern Ocean. According to these interpretations, Site U1356 lay far to the north of the Antarctic Divergence zone and was closer to the polar front during the Oligocene.

In the studied region, progressive subsidence of the site location occurred through the middle to late Eocene, as evidenced by lithological and dinocyst assemblage changes (Bijl et al., 2013; Escutia et al., 2011). Existing paleo-depth reconstructions suggest deepening from a shallow marine setting (~500 m paleo-depth) in the early-middle Eocene to a more hemipelagic slope setting (>1000 m) by the earliest Oligocene. However, there is a significant level of uncertainty associated with these estimates (Escutia et al., 2011). The first incursion of water from the Pacific Ocean into the Indian Ocean through shallow opening of the Tasman gateway close to the Antarctic margin is during the middle Eocene (Bijl et al., 2013). Around 32 Ma, warm waters circulating to the east from the Pacific close to Australia have been reported by Stickley et al. (2004), and a cold current circulating towards the west close to Antarctica has been modelled by Huber et al. (2004). In addition, seawater neodymium (Nd) isotope records from fish debris in sediments recovered at Site U1356 identified the Wilkes–Adélie Land margin as a site of persistent deep-water formation from the Early Eocene to the Oligocene (Huck et al., 2017).



**Figure 1.9.** Schematic drawing of the modern Southern Ocean Antarctic bottom water masses and the Antarctic Circumpolar Current (ACC), with the associated Polar Fronts and the Antarctic divergence.





The timing of the deepening, allowing through flow of deep (3000 km) water masses, precedes the timing of glaciation (e.g., Coxall et al., 2005; Lear et al., 2008), which indeed precludes a direct link between rifting and the onset of glaciation. Moreover, numerical model evidence suggests that the Eocene Southern Ocean (with closed ocean gateways) featured large clockwise gyres, which prevented the influence of warm, low-latitude surface waters to reach the Antarctic shoreline (Huber, 2001; Huber et al., 2004; Sijp et al., 2011). This physics-based oceanographic reconstruction is consistent with biogeographic patterns of organic-walled dinoflagellate cysts (Bijl et al., 2013; Huber et al., 2004).

The first evidence of an eastward deep water interoceanic connection between the Indian and Pacific sectors of the Southern Ocean driven by the ACC appear when the Tasmanian Gateway aligned within the latitudinal band of the westerlies ~30 million years ago, as shown in neodymium (Nd) records (Scher et al., 2015).

# Chapter 2

Materials and methods

---

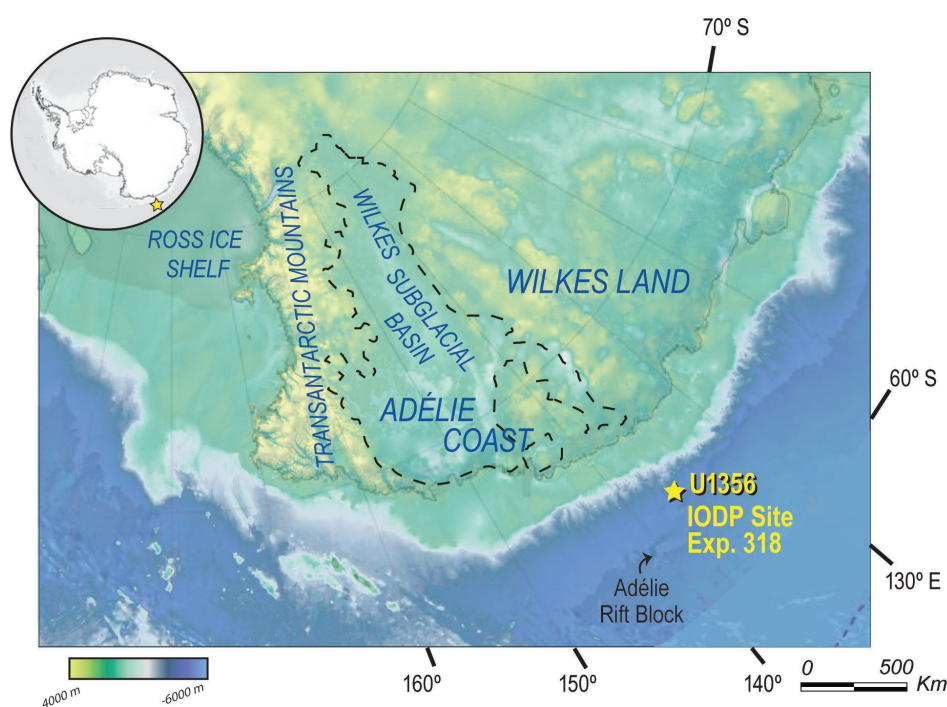


## CHAPTER 2

### MATERIALS AND METHODS

#### 2.1. IODP SITE U1356

The Integrated Ocean Drilling Program (IODP) Expedition 318, drilled Site U1356 ( $63^{\circ} 18.61380' S$ ,  $135^{\circ} 59.9376' E$ ) offshore from the glaciated East Antarctic Wilkes Land Coast, at 3992 m water depth (Fig. 2.1). The drilling penetrated 1006.4 mbsf (meters below sea floor) into a levee of a submarine channel on the lower continental rise (Escutia et al., 2011). Total core recovery was 35% and recovered sediments were dated between the early Eocene and the Pliocene (Fig. 2.2), with relatively high-recovery of nearly 80% for the late Oligocene section (640 - 690 mbsf). Sediments from site U1356 were described and analysed shipboard on the basis of lithofacies characterization, physical properties, geochemistry, biostratigraphy, and paleomagnetism (Escutia et al., 2011).

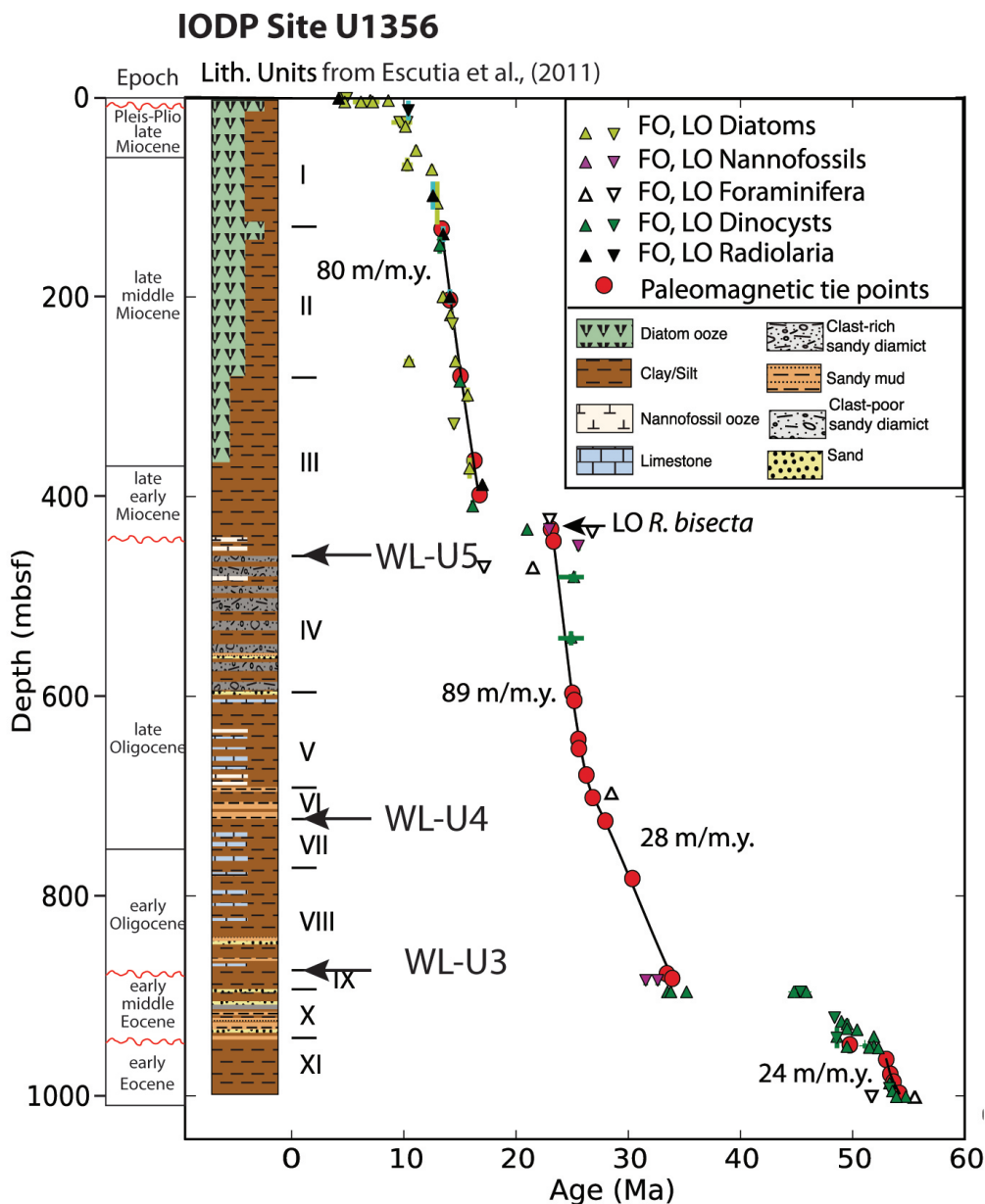


**Figure 2.1.** Location of IODP 318 Site U1356 (Escutia et al., 2010) on the Adélie coast continental rise. Bed topography from IBSCO2 (Arndt, JE et al., 2013).

Lithofacies at site U1356 consist of bioturbated siltstones and claystones with variable carbonate content, that are interbedded with laminated silty claystones, sandstones and siltstones with cross laminations, chaotic deposits, and mudstones and sandstones with dispersed clasts of different sizes. These facies result from hemipelagic settling and gravity flows with variable bottom current reworking (Escutia et al., 2011).



Today, Site U1356 lies close to the southern boundary of the Antarctic Circumpolar Current, near the Antarctic Divergence at 63° S (Orsi et al., 1995; Bindoff et al., 2000). A large polynya to the west of the Mertz Glacier is responsible for the formation of Antarctic Bottom Water (AABW) (Bindoff et al., 2000) that sink off the continental shelf, passing down to the continental slope and rise canyon system. However, the paleo-latitude of Site U1356 was around 58.5° +/- 2.5°S (van Hinsbergen et al., 2015) during the late Oligocene, i.e., more northerly than today.



**Figure 2.2.** Age-depth plot for U1356A from Tauxe et al., (2012). Lithostratigraphic summary from Escutia et al. (2011). Biostratigraphic constraints from Escutia et al. (2011) and paleomagnetic tie point from Tauxe et al., (2012). Seismic regional unconformities WL-U3, WL-U4, and WL-U5 from the Wilkes Land (Escutia et al. 2011). LO=Last occurrence, FO=First occurrence, LCO=Last common occurrence, LAO=last abundant occurrence, FCO=First common occurrence, FAO=First abundant occurrence..

## 2.2. METHODS

To address the overall objective of this thesis, to increase our understanding of Oligocene-Miocene ice sheet and ocean configurations off the Wilkes Land, we integrate detailed sedimentological studies with geochemical, mineralogical, cyclostratigraphy, and seismic stratigraphic analysis at different spatial (from cm to thousand of km) and temporal (from thousand years to million years) scales.

Chapters 3, 4, and 5 provide detailed information in the specific methods used for each chapter. In addition, the full dataset for Chapter 3 related to the late Oligocene X-Ray Fluorescence (XRF) scanner from IODP Site 318-U1356 Wilkes Land Margin, Antarctica is published in the open Access scientific repository of PANGAEA<sup>1</sup> (<https://doi.org/10.1594/PANGAEA.892208>). The full dataset for the discrete XRF used for Chapter 3 is included in Appendix 2.

In this chapter we provide the general information for the methods used in this thesis:

Facies characterization is conducted in sediments from IODP site U1356 to determine sedimentary processes and to conduct paleoenvironmental interpretations. Facies characterization is achieved through: 1) a detailed description of the lithology; 2) the identification of sedimentary structures (i.e., laminations, bedding) and textures (i.e., grain size, clast morphology); and 3) the determination of the type of contacts between beds (e.g., erosional vs gradational).

High-resolution scanning electron microscope (HR-SEM) is used in order to characterize the type and composition of biogenic and terrigenous particles, particle size, and morphology of each lithofacies. X-ray diffraction. X-ray diffraction (XRD) analysis is used to study the mineralogy of the bulk sediments and the detrital clay minerals.

X-Ray computed tomography scans (CT-Scan) were obtained to determine variations in sediment density, sedimentary internal structures, facies contacts, internal distribution of clasts and bioturbation, without the need of destroying the sediments. For detailed methods regarding CT-scans see chapters 3 and 4.

Magnetic susceptibility (MS) and grain density (GRA) were obtained on shipboard during IODP Expedition 318 (Escutia et al., 2011). MS provides information of the ferromagnetic content in sediments and is also used as a proxy for grain size and for the presence of heavy minerals (Evans et al., 1997). GRA provides estimated bulk densities of sediments (Escutia et al., 2011). For detailed methods regarding MS and GRA see chapter 3.

Detailed bulk-chemical composition records acquired by XRF core scanning allow accurate determination

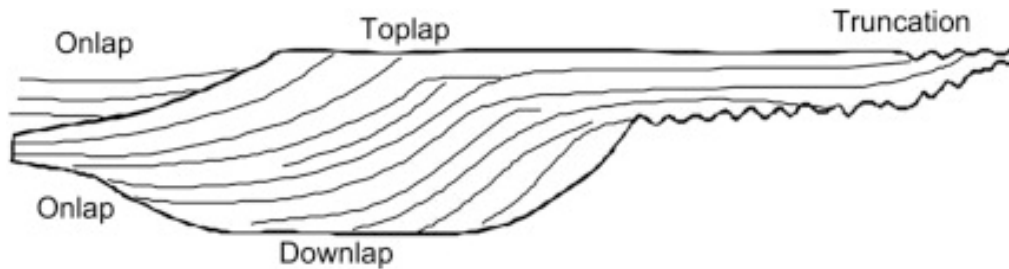
<sup>1</sup> Salabarnada, A.; Escutia, C.; Röhl, U.; Nelson, C. H.; McKay, R.; Jiménez-Espejo, F.J.; Bijl, P.K.; Hartman, J.D.; Ikehara, M.; Strother, S.L.; Salzmann, U.; Evangelinos, D.; López-Quirós, A.; Flores, J.A.; Sangiorgi, F.; Brinkhuis, H. (2018): Late Oligocene XRF scanner data from IODP Site 318-U1356 Wilkes Land Margin, Antarctica. Uploaded in PANGAEA, <https://doi.org/10.1594/PANGAEA.892208>.



of downcore changes and the assessment of the contribution of the various elemental components in the biogenic and lithogenic fraction in marine sediments (Croudace et al., 2006). For detailed methods regarding XRF see chapters 3 for and 4 for discrete XRF.

Spectral analyses applied to selected continuous XRF proxies are useful in order to detect nonstationary spectral variability and test the presence of spectral cycles (Meyers, 2014). For detailed methods regarding spectral analyses see chapter 3 and the supplements to chapter 3.

Multichannel seismic reflection lines, across site U1356 and nearby, were used to provide a regional context to the interpretations based on sediments obtained from site U1356 (see Chapter 4 and 5). In addition, analysis of the available multichannel seismic reflection (MCS) profiles in the region allowed for the morphosedimentary and seismic stratigraphic study in Chapter 5. Seismic stratigraphic provides indirect information regarding the depositional processes that were active when the margin was filled. For the analysis and interpretation of MCS, basic seismic stratigraphic techniques were used, which include: 1) identification of unconformities by the identification of reflector terminations (i.e., truncation, toplap, onlap, and downlap) (Figure 2.3) and their correlative conformable surfaces; 2) determination of external geometries of depositional bodies; and 3) seismic facies analysis based on the internal character of the reflections. For detailed methods see chapter 5.



**Figure 2.3.** Seismic sequence-internal-reflection terminations. Brown and Fisher, (1979).

# Chapter 3

Late Oligocene astronomically paced  
contourite sedimentation in the Wilkes  
Land margin of East Antarctica:  
insights into paleoceanographic and  
ice sheet configurations

---





## CHAPTER 3

PALEOCEANOGRAPHY AND ICE SHEET VARIABILITY OFFSHORE  
WILKES LAND, ANTARCTICA: INSIGHTS FROM LATE OLIGOCENE  
ASTRONOMICALLY PACED CONTOURITE SEDIMENTATION

*Co-authors to this chapter: Escutia, C., Röhl, U., Nelson, C. H., McKay, R., Jiménez-Espejo, F. J., Bijl, P. K., Hartman, J. D., Strother, S. L., Salzmann, U., Evangelinos, D., López-Quirós, A., Flores, J. A., Sangiorgi, F., Ikehara, M. and Brinkhuis, H.*

*Published in *Climate of the Past*, 14(7), 991–1014, doi:10.5194/cp-14-991-2018, 2018.*

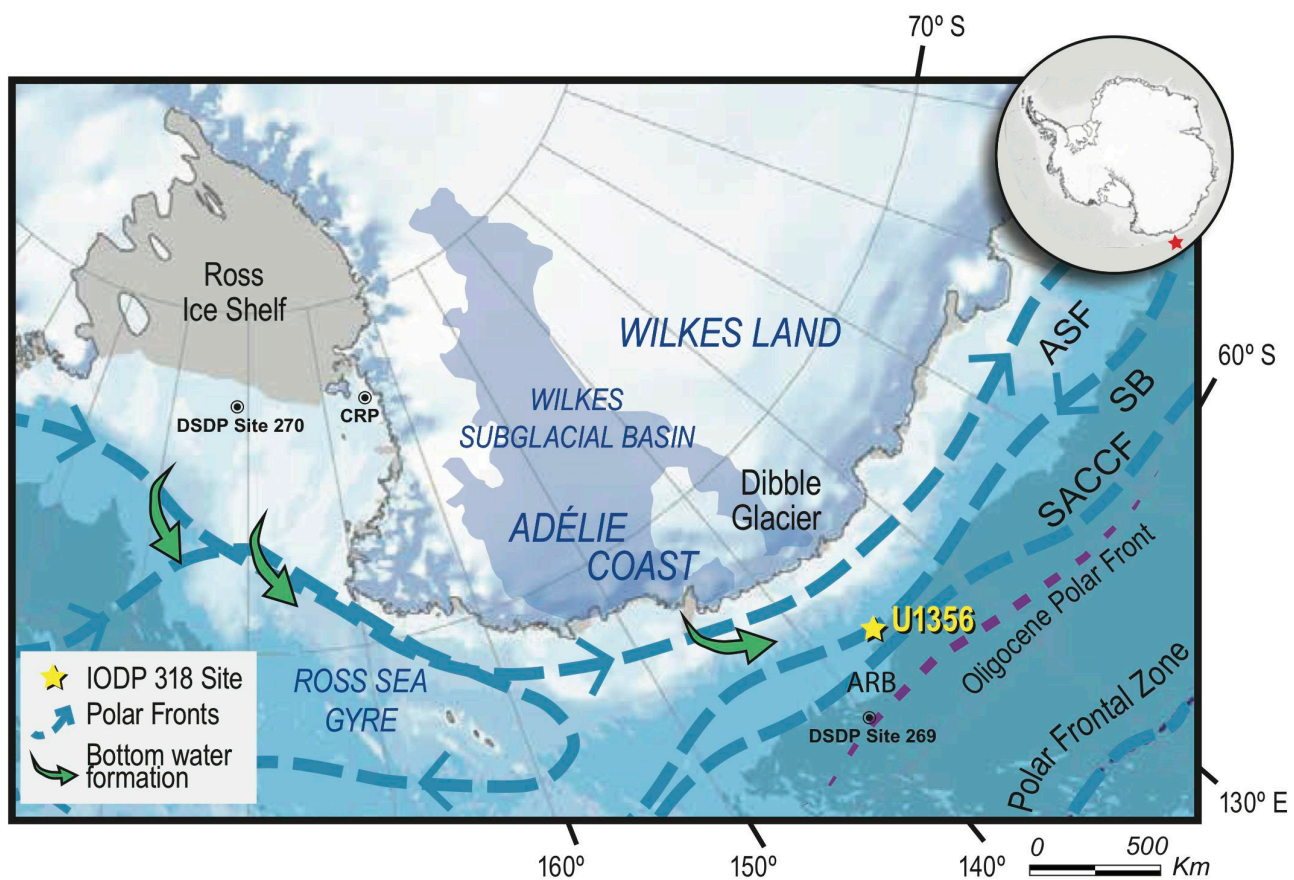
## ABSTRACT

*Antarctic ice sheet and Southern Ocean paleoceanographic configurations during the late Oligocene are not well resolved. They are however important to understand the influence of high-latitude Southern Hemisphere feedbacks on global climate under CO<sub>2</sub> scenarios (between 400 and 750 ppm) projected by the IPCC for this century, assuming unabated CO<sub>2</sub> emissions. Sediments recovered by the Integrated Ocean Drilling Program (IODP) at Site U1356, offshore of the Wilkes Land margin in East Antarctica, provide an opportunity to study ice sheet and paleoceanographic configurations during the late Oligocene (26–25 Ma). Our study, based on a combination of sediment facies analysis, magnetic susceptibility, density, and X-Ray Fluorescence geochemical data, shows that glacial and interglacial sediments are continuously reworked by bottom-currents, with maximum velocities occurring during the interglacial periods. Glacial sediments record poorly ventilated, low-oxygenation bottom water conditions, interpreted to result from a northward shift of westerly winds and surface oceanic fronts. Interglacial sediments record more oxygenated and ventilated bottom water conditions and strong current velocities, which suggests enhanced mixing of the water masses as a result of a southward shift of the Polar Front. Intervals with preserved carbonated nannofossils within some of the interglacial facies are interpreted to form under warmer paleoclimatic conditions when less corrosive warmer northern component water (e.g. North Atlantic sourced deep water) had a greater influence on the Site. Spectral analysis on the late Oligocene sediment interval show that the glacial-interglacial cyclicity and related displacements of the Southern Ocean frontal systems between 26–25 Ma were forced mainly by obliquity. The paucity of iceberg rafted debris (IRD) throughout the studied interval contrasts with earlier Oligocene and post-Miocene Climate Optimum sections from Site U1356 and with late Oligocene strata from the Ross Sea, which contain IRD and evidence for coastal glaciers and sea ice. These observations, supported by elevated sea surface paleotemperatures, the absence of sea-ice, and reconstructions of fossil pollen between 26 and 25 Ma at Site U1356, suggest that open ocean water conditions prevailed. Combined, these evidences suggest that glaciers or ice caps likely occupied the topographic highs and lowlands of the now marine Wilkes Subglacial Basin (WSB). Unlike today, the continental shelf was not over-deepened and thus ice sheets in the WSB were likely land-based and marine-based ice sheet expansion was likely limited to coastal regions.*



### 3.1. INTRODUCTION

Today, ice sheets on Antarctica contain about 26.5 million cubic kilometres of ice, which has the potential for raising global average sea level by 58 m, with the East Antarctic Ice Sheet constituting 53.3 m of this sea level equivalent (Fretwell et al., 2013). Satellite observations indicate significant rates of change in most of the West Antarctic Ice Sheet (WAIS) and some sectors of the East Antarctic Ice Sheet (EAIS). These include thinning at their seaward margins (Pritchard et al., 2012) and accelerating ice shelves basal melt rates (Rignot et al., 2013; Shen et al., 2018). Given the uncertainties in projections of future ice sheet melt, there has been a growing number of studies of sedimentary sections from the surrounding margins of Antarctica targeting records of past warm intervals (i.e., high-CO<sub>2</sub> and elevated temperature climates) in order to better understand ice sheets and Southern Ocean configurations under these conditions. For example, the early Pliocene (5-3 Ma) has been targeted because atmospheric CO<sub>2</sub> concentrations were similar to today's 400 ppmv concentrations (Foster and Rohling, 2013; Zhang et al., 2013). These studies have shown that early Pliocene Southern Ocean surface waters were warmer (i.e., between 2.5- > 4 °C) than present and that the summer sea ice cover was greatly reduced, or even absent (Bohaty and Hard-



**Figure 3.1.** Location of IODP 318 Site U1356 (Escutia et al., 2010) on the Adélie coast continental rise. Bed topography from IBSCO2 (Arndt, JE et al., 2013). Schematic position of the different water masses at present and locations of Antarctic Bottom Water formation (Orsi, 1995) are indicated. The position of the Oligocene Polar Front (Scher et al., 2015) is also shown. ASF: Antarctic Slope Front; SB: Southern Boundary; SACCF: Southern Antarctic Counter Current Front; ARB: Adélie Rift Block.

wood, 1998; Whitehead and Bohaty, 2003; Escutia et al., 2009; Cook et al., 2013). They also record the periodic collapse of both the WAIS and EAIS marine-based margins (Naish et al., 2009; Pollard and DeConto, 2009; Cook et al., 2013; Reinardy et al., 2015; DeConto and Pollard, 2016). Foster and Rohling (2013) provide a sigmoidal relationship between eustatic sea-level and atmospheric CO<sub>2</sub> levels whereby sea levels stabilise at ~22 +/-12 m above present-day level, between about 400 ppm and 650 ppm, suggesting loss of the Greenland Ice Sheet (6-7 m s.l.e.) and the marine-based West Antarctic Ice Sheet (+7 m s.l.e.). This implies that continental EAIS volumes remained relatively stable during these times, but experienced mass loss of some (or all) its marine-based margins, relative to the present day. With CO<sub>2</sub> concentrations at > 650 ppm they infer further increases in sea level, suggesting this as a threshold for initiating retreat of the terrestrial margins of EAIS. With sustained warming, CO<sub>2</sub> concentrations of more than 650 ppmv are within the projections for this century (Solomon, 2007; Field et al., 2014). The last time the atmosphere is thought to have experienced CO<sub>2</sub> concentrations above 650 ppmv was during the Oligocene (23.03-33.9 Ma), when CO<sub>2</sub> values remained between 400 to ~750-800 ppm (Pagani et al., 2005; Beerling and Royer, 2011; Zhang et al., 2013).

Geological records of heavy isotope values ~2.5 ‰ and far field sea level records from passive margins during the Oligocene suggest that, following the continental-wide expansion of ice during the Eocene-Oligocene transition that culminated at the Oi-1 event (33.6 Ma), the Antarctic ice cover was at least ~50 % of the current volume (e.g., Kominz and Pekar, 2001; Zachos et al., 2001; Coxall et al., 2005; Pekar et al., 2006; Liebrand et al., 2011, 2017; Mudelsee et al., 2014). The early part of the Oligocene records a significant  $\delta^{18}\text{O}$  decreasing slope with high-latitude sites exhibiting a strong deglaciation/warming that persisted until ~32 Ma (Mudelsee et al., 2014). This was followed by seemingly stable conditions on Antarctica as evidenced by minimal  $\delta^{18}\text{O}$  and Mg/Ca changes (Billups and Schrag, 2003; Lear et al., 2004; Mudelsee et al., 2014). A slight glaciation/cooling is recorded before 28 to ~27 Ma, which was followed by an up to 1 ‰ long-term decrease in the  $\delta^{18}\text{O}$  isotope records that was interpreted to result from the deglaciation of large parts of the Antarctic ice sheets during a significant warming trend in the late Oligocene (27-26 Ma) (Zachos et al., 2001a). Nevertheless, there are marked differences between the late Oligocene low  $\delta^{18}\text{O}$  values recorded in Pacific, Indian and Atlantic Ocean sites (e.g., Pälike et al., 2006; Cramer et al., 2009; Liebrand et al., 2011; Mudelsee et al., 2014; Hauptvogel et al., 2017), and the sustained high  $\delta^{18}\text{O}$  values recorded in Southern Ocean sites (Pekar et al., 2006; Mudelsee et al., 2014). High  $\delta^{18}\text{O}$  values in the Southern Ocean sediments are in agreement with the ice proximal record recovered by the Cape Roberts Project (CRP) in the Ross Sea, which show the existence of glaciers/ice sheets at sea level (Barrett et al., 2007; Hauptvogel et al., 2017). Based on the study of the isotopic record in sediments from the Atlantic, the Indian and the equatorial Pacific, Pekar et al. (2006) explained this conundrum of a glaciated Antarctica, and varying intrabasinal  $\delta^{18}\text{O}$  values with the coeval existence of two deep-water masses, one sourced from Antarctica and another, warmer bottom-water, sourced from lower latitudes. Superimposed on the above long-term swings in the  $\delta^{18}\text{O}$  Oligocene record, fluctuations on timescales shorter than several Myr were identified in the high-resolution benthic  $\delta^{13}\text{C}$  record from ODP 1218 (Pälike et al., 2006). These fluctuations in periods of 405 kyr and 1.2 Myr are related to Earth's orbital



variations in eccentricity and obliquity, respectively and have been referred as the short-term “heartbeat” of the Oligocene climate (Pälike et al., 2006). Oligocene records close to Antarctica are needed to better resolve Antarctic ice sheet and paleoceanographic configurations at different time scales and under scenarios of increasing atmospheric CO<sub>2</sub> concentrations.

Integrated Ocean Drilling Program (IODP) Expedition 318 drilled a transect of sites across the eastern Wilkes Land margin at the seaward termination of the Wilkes Subglacial Basin (WSB) (Escutia et al., 2011; Escutia et al., 2014) (Fig. 3.1). Relatively good recovery (78.2 %) of late Oligocene (26–25 Ma) sediments from Site U1356 between 689.4 and 641.4 meters below sea floor (mbsf) provides an opportunity to study ice-sheet and ocean configurations during the late Oligocene and to relate them with other Antarctic and global records. In this paper, we present a new glacial-interglacial sedimentation and paleoceanographic model for the distal glaciomarine record of the Wilkes Land margin constructed on the basis of sedimentological data (visual core description, facies analysis, computed tomography images, and high-resolution scanning electron microscopy images), physical properties (i.e., magnetic susceptibility of the bulk sediment and grain density), and X-ray fluorescence data (XRF). We also provide insights into the configuration of the ice sheet in this sector of the east Antarctic margin and evidence for orbital forcing of the glaciomarine glacial-interglacial sedimentation at Site U1356.

## 3.2. MATERIALS AND METHODS

### 3.2.1. SITE U1356 DESCRIPTION

Site U1356 (63° 18.6138'S, 135° 59.9376'E) is located at 3992 m water depth in front of the glaciated margin of the eastern Wilkes Land Coast of East Antarctica, and penetrated 1006 meters into the flank of a levee deposit in the transition between the lower continental rise and the abyssal plain (Escutia et al., 2011; Fig. 3.1). Overall recovery was 35% with sediments dated between the early Eocene and Pliocene, but several intervals provide good stratigraphic control (Escutia et al., 2011; Tauxe et al., 2012). The Oligocene section was recovered between 895 and 430.8 mbsf, Cores U1356-95R-3 83 cm to U1356-46R. Our study focuses on the relatively high-recovery (78.2 %) interval within the late Oligocene, which spans from 689.4 to 641.4 mbsf (Cores U1356-72R to -68R). The sediments from this interval are part of shipboard lithostratigraphic Unit V, which is characterized by light greenish-grey, strongly bioturbated claystones and micritic limestones interbedded with dark brown, sparsely bioturbated, parallel- and ripple-laminated claystones with minor cross-laminated interbeds (Escutia et al., 2011). The bioturbated and calcareous claystones and limestones were broadly interpreted to represent pelagic sedimentation superimposed on the background hemipelagic sedimentary input (Escutia et al., 2011). The laminated claystones and ripple cross-laminated sandstones were interpreted to likely result from variations in bottom current strength and fine-grained terrigenous supply (Escutia et al., 2011). In addition, a notable absence of Ice Rafted Debris (IRD) (>250µm) in this interval relative to underlying and overlying strata was also recorded.

The late Oligocene depositional setting of Site U1356 was however different to that of today. The stratigraphic evolution of the region testifies the progradation of the continental shelf taking place after continental ice sheet build-up during the Eocene-Oligocene Transition (EOT, 33.6 Ma; Eitrem et al., 1995; Escutia et al., 2005; 2014), which resulted in: 1) seismic and sedimentary facies on the continental rise becoming more proximal up-section (Hayes and Frakes, 1975; Escutia et al., 2000; 2005; 2014), and 2) high sedimentation rates during the Oligocene (Escutia et al., 2011; Tauxe et al., 2012). In this context, the studied late Oligocene sediments from Site U1356 record distal continental rise deposition in an incipient/low-relief levee of a submarine channel. As progradation continued, a complex network of well-developed channels and high-relief levee systems developed on the continental rise (Escutia et al., 2000) from the latest Oligocene onwards.

Today, Site U1356 lies close to the Southern Boundary of the Antarctic Circumpolar Current, near the Antarctic Divergence at  $\sim 63^\circ\text{S}$  (Orsi, 1995; Bindoff, 2000) (Fig. 3.1). However, the paleolatitude of Site U1356 was around  $58.5 \pm 2.5^\circ\text{S}$  (van Hinsbergen et al., 2015) during the late Oligocene, more northerly than today. Scher et al. (2008, 2015) reconstructed the position of the early Oligocene Antarctic Divergence to be located around  $60^\circ\text{S}$  (Fig. 3.1), based on the distribution of terrigenous and biogenic (calcareous and siliceous microfossils) sedimentation, Nd isotopes, and Al/Ti ratios through a core transect across Australian-Antarctic basin in the Southern Ocean. According to these interpretations Site U1356 lay far to the north of the Antarctic Divergence zone, and was closer to the Polar Front, during the Oligocene.

### 3.2.2. AGE MODEL

The age model for Site U1356 was established on the basis of the magnetostratigraphic datums constrained by marine diatom, radiolaria, calcareous nannoplankton and dinocyst biostratigraphic control (Escutia et al., 2011; Tauxe et al., 2012; Bijl et al., 2018). The late Oligocene interval contains three magnetostratigraphic datums (Table 3.1): 1) Chron C8n.1n (o) between 643.70 and 643.65 mbsf (U1356-68R-2); 2) C8n.2n (y) between 652.60 and 652.55 mbsf (U1356-69R-2), and 3) C8n.2n (o) between 679.90 and 678.06 mbsf (U1356-71R). For this study, the age model by Tauxe et al. (2012), which was calibrated to the Gradstein 2004 Geological Time Scale, has been updated using the GPTS 2012 Astronomic Age Model (Vanderberghe et al. 2012). Based on this calibration, the age of sediments between 678.98 and 643.37 mbsf is 25.99 and 25.26 Ma, respectively (Fig. 3.2; Table 3.1).

**Table 3.1.** Age model by Tauxe et al., (2012) and transformed ages to GPTS 2012.

| Core Section<br>Site U1356<br>Exp. 318 | Top depth<br>(mbsf) | Bottom depth<br>(mbsf) | Depth used<br>(m) | GPTS 2004                        | GPTS 2012<br>(Myr) | Chron      |
|--|---------------------|------------------------|-------------------|----------------------------------|--------------------|------------|
|  |                     |                        |                   | (Myr)<br>(Tauxe et al.,<br>2012) |                    |            |
| 68R-2                                  | 643.10              | 643.65                 | 643.37            | 25.444                           | 25.260             | C8n.1n (o) |
| 69R-2                                  | 652.55              | 652.60                 | 652.57            | 25.492                           | 25.300             | C8n.2n (y) |
| 71R-6                                  | 678.06              | 679.90                 | 678.98            | 26.154                           | 25.990             | C8n.2n (o) |



### 3.2.3. FACIES ANALYSES

Detailed facies analyses provide a stratigraphic framework on which we base our sedimentary processes and paleoenvironmental interpretations. Lithofacies are determined on the basis of detailed visual logging of the core during a visit to the IODP-Gulf Coast Repository (GCR), expanding on the lower resolution preliminary descriptions in Escutia et al. (2011). We logged the lithology, sedimentary texture (i.e., shape, size and distribution of particles) and structures with a focus on the contacts between the beds and on bioturbation at a mm to cm-scale resolution in cores expanding from 896 to 95.4 mbsf (Cores U1356-95R to -11R) (see Supplementary material at the end of Chapter 3, S1 Fig. 3.S1, S2). Physical properties data were measured during IODP Exp. 318 using the Whole-Round Multisensor Logger. Magnetic susceptibility measurements were taken at 2.5 cm intervals, and Natural gamma radiation (NGR) was measured every 10 cm (Escutia et al., 2011). In this paper, we focus on the interval between 689.4 and 641.4 mbsf that comprise cores 72R to 68R (Fig. 3.2).

X-ray Computed Tomography scans (CT-scans) measure changes in density and allow for analysis of fine-scale stratigraphic changes and internal structures of sedimentary deposits in a non-destructive manner (e.g., Dulu, 1999; St-Onge and Long, 2009; Van Daele et al., 2014; Fouinat et al., 2017). To further characterize the different facies in our cores, selected intervals of Core U1356-71R-6 (678.11 to 676.91 mbsf) and Core U1356-71R-2 (672.8 to 671.35 mbsf) were CT-scanned at the Kochi Core Center (KCC) (Japan), with the GE Medical systems LightSpeed Ultra 16. 2D scout (shooting conditions at 120Kv with 100mA, and 3D Helical image with 120Kv and 100mA and FOV=22.0). Image spatial resolution consists of 0.42 mm/pixel with 0.625 mm of slice thickness (voxel spatial resolution of 0.42 x 0.42 x 0.625 mm).

The type and composition of biogenic and terrigenous particles, particle size, and morphology of each lithofacies was characterized with a high-resolution scanning electron microscope (HR-SEM) at the Centro de Instrumentación Científica (University of Granada, Spain).

### 3.2.4. X-RAY FLUORESCENCE (XRF) ANALYSES

Detailed bulk-chemical composition records acquired by XRF core scanning allow accurate determination of sedimentological changes and the assessment of the contribution of the various components in the biogenic and lithogenic fraction in marine sediments (Croudace et al., 2006). This non-destructive method yields element intensities on the surface of split sediment cores and provides statistically significant data for major and minor elements (Richter et al., 2006; O'Regan et al. 2010, Wilhelms-Dick et al., 2012). The data are given as element intensities in total counts.

XRF core scanning measurements were collected every 2 cm down-core over a 1 cm<sup>2</sup> area with split size of 10 mm, a current of 0.2 mA (Al - Fe) and 1.5 mA (all other elements) respectively, and a sampling time of 20 seconds, directly at the split core surface of the archive half with XRF Core Scanner III at the MARUM – Center for Marine Environmental Sciences, University of Bremen, Germany. Prior to the scanning, cores were thermally equilibrated to room temperature, the surface was cleaned, flattened, and

covered with 4  $\mu\text{m}$  thin SPEXCerti Prep Ultralene1 foil to protect the sensor and prevent contamination during the scanning procedure. Scans were collected during three separate runs using generator settings of 10 kV for the elements Al, Si, S, K, Ca, Ti, Mn, Fe; 30 kV for elements such as Br, Rb, Zr, Mo, Pb; and 50 kV for Ba. The here reported data have been acquired by a Canberra X-PIPS Silicon Drift Detector (SDD; Model SXD 15C-150-500) with 150eV X-ray resolution, the Canberra Digital Spectrum Analyzer DAS 1000 and an Oxford Instruments 100W Neptune X-ray tube with rhodium (Rh) target material. Raw data spectra were processed by the Analysis of X-ray spectra by Iterative Least square software (WIN AXIL) package from Canberra Eurisys. Data points from disturbed intervals in the core face (i.e., slight fractures and cracks) were removed.

The light elements Al, Si, and K show large element variations (intra-element variations of 1 order of magnitude or more, Fig. 3.2). Similar variations have been previously described in sediment cores to indicate substantial analytical deviations due to physical sedimentary properties (i.e. Tjallingü and Röhl et al., 2007; Hennekam and de Lange 2012). Accordingly, for this study we have discarded the continuous records of Al, Si, and K and concentrated our interpretations on Al, Si and K values from the XRF analyses in discrete samples (see below). As Titanium (Ti) is restricted to the terrigenous phase in sediments and is inert to diagenetic processes (Calvert and Pedersen, 2007), we utilized Ti to normalize other chemical elements for the terrigenous fraction. Linear correlation ( $r$  Pearson) above standardised values has been done in order to find statistical relationships among the variables.

In addition, we conducted measurements of a total of 50 major and minor trace elements in 25 discrete sediment samples collected at 0.4 and 1 m spacing to determine their chemical composition. For this, we used a Pioneer-Bruker X-Ray Fluorescence (XRF) spectrometer S4 at the Instituto Andaluz de Ciencias de la Tierra (CSIC-UGR) in Spain, equipped with a Rh tube (60 kV, 150 mA) using internal standards. The samples were prepared in a Vulcan 4Mfusion machine and the analyses performed using a standard-less spectrum sweep with the Spectraplus software.

### 3.2.5. SPECTRAL ANALYSES

We selected key environmental indicators from XRF core scanner data and elemental ratios (i.e., Zr/Ba, Ba, Zr/Ti, Ca/Ti, MS) to conduct spectral analyses on the data from the interval between 689.4 to 641.4 mbsf (Cores U1356-72R to 68R). We performed evolutionary spectral and harmonic analysis on each dataset using Astrochron toolkit on the R software (Meyers, 2014). Detailed methodology is provided as supplementary information following the Astrochron code of Wanlu Fu et al. (2016) at the end of chapter this chapter. This method allows the detection of non-stationary spectra variability within the time series. The time series were analysed on the depth scale and then, applying the Frequency domain minimal tuning (Meyers et al., 2001), we converted spatial frequencies to sedimentation rates using an average period of 41 kyr, to transform them to an age scale, with the basis of the already resolved age model. The Evolutionary Average Spectral Misfit method was then used to resolve unevenly sampled series and changing sedimentation rates (Meyers et al., 2012). This method is used to test a range of





plausible timescales and simultaneously evaluate the reliability of the presence of astronomical cycles (Supplemental material S2).

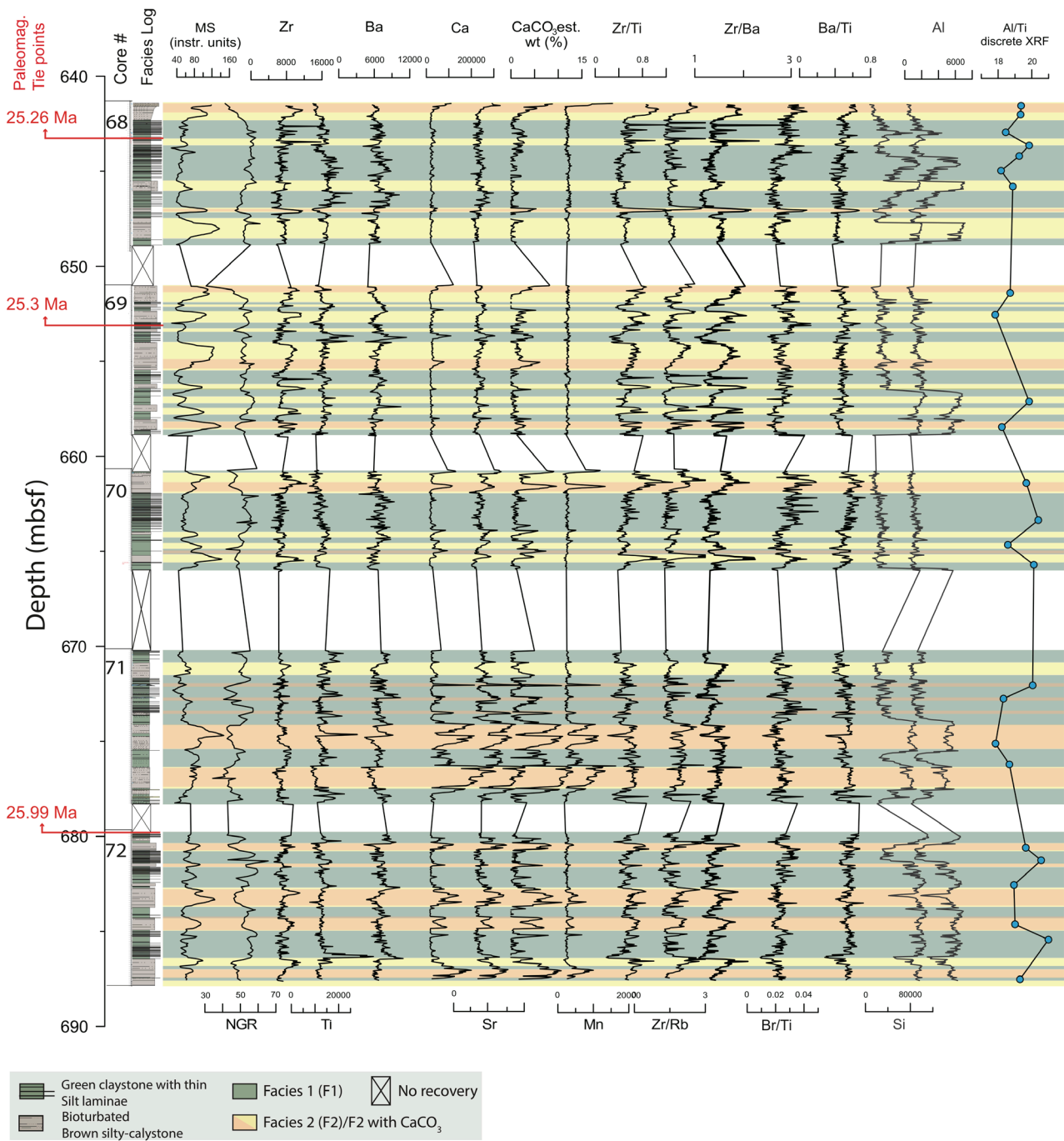
### 3.3. RESULTS

#### 3.3.1. SEDIMENTARY FACIES

The revised Oligocene facies log (Fig S1, S2), includes the high-recovery interval between 689.4 and 641.4 mbsf (Fig. 3.2). The integration of our lithofacies analyses, with physical properties (MS), CT-scans and HR-SEM analyses characterize an alternation between two main facies (Facies 1 and 2) (Figs. 3.2, 3.3, 3.4). Although these two facies were already visually identified shipboard, our analyses allow us a more detailed characterization and interpretation of the depositional environments and the processes involved in their development.

Facies 1 (F1) consists of slightly bioturbated greenish claystones with sparse (Fig. 3.3a) to common laminations (Figs. 3.2, 3.3a-f; Table 3.2). Laminae, as described on shipboard, vary from 0.1 to 1 cm thick and, based on non-quantitative smear slide observations, are composed of well-sorted silt to fine sand size quartz grains (Escutia et al., 2011). Laminations can be planar, wavy, with ripple-cross lamination structures (Escutia et al., 2011), and show faint internal truncation surfaces, mud offshoots, and internal erosional surfaces (Fig. 3.3a-f). HR-SEM analyses of the claystones show that the matrix is composed of clay-size particles and clay minerals (Fig. 3.3g, i). In addition, they show rare calcareous nanofossils that are partially dissolved (Fig. 3.3g, i). Authigenic carbonate crystals are also identified (Fig. 3.3i). Bioturbation in F1 is scarce, ichnofossils in the sediments are dominated mainly by *Chondrites* (Fig. 3.3d). CT-scans also show the presence of *Skolithos*, with their vertical thin tubes filled with high-density material suggesting they are pyritized (Fig. 3.3b). Pyrite was also observed in shipboard smear slides in small abundances from the laminated facies in the studied interval (Escutia et al., 2011). Magnetic susceptibility values within the laminated facies are low, between 40-70 MS instrumental units (iu), with higher values when silt laminations are more abundant (Figs. 3.2, 3.4). Natural Gamma Ray (NGR) is anti-correlated with MS, with high values in F1 varying between 50 - 65 counts per second (cps) (Fig. 3.2).

Facies 2 (F2) is composed by light greenish grey strongly bioturbated claystones and silty claystones (Figs, 3.2, 3.3; Table 3.2) with variable carbonate content varying between 5-16% based on our XRF analyses. No primary structures are preserved due to the pervasive bioturbation (Fig. 3.3a-c). Burrows are back-filled with homogeneous coarse material (silt/fine sand). Different types of ichnofossils are present with *Planolites* and *Zoophycos* being the most abundant (Fig. 3.3a, b). HR-SEM images show: 1) silt-size grains containing quartz grains with conchoidal fractures in the corners and impact marks on the crystal faces, indicative of high-energy environments; and 2) biogenic carbonate consisting of moderately to poorly preserved coccoliths, which exhibit dissolution of their borders, and to a minor degree detrital carbonate grains (Fig. 3.3h - j). A total of 13 carbonate-rich layers have been observed within the studied interval F2,



**Figure 3.2.** Magnetic susceptibility (MS) and natural gamma radiation (NGR) physical properties, and selected X-Ray Fluorescence (XRF) data (in total counts) and elemental ratios plotted against the new detailed U1356 facies log between 689.4 and 641.4 mbsf

and they range in thickness from 10 to 110 cm. Facies 2 CT-scans images show an increase in density (i.e., gradation towards lighter colours in the scan) towards the top of each bioturbated interval (Fig. 3.3b). MS values are higher in F2 compared to F1. Values vary from 50-150 instrumental units (iu) and exhibit an inverse grading or a bigradational-like morphology (Fig. 3.2, 4), while NGR is inversely correlated with minimum values occurring in F2 (between 35-55 cps) (Fig. 3.2).



Contacts between the two facies are sharp and apparently non-erosive, with minimal omission surfaces or lags (Figs. 3.3, 3.4). However, when bioturbation is present, gradual contacts in the transition from F1 to F2 also occur (Fig. 3.3b). Both sharp and transitional contacts are well imaged on the MS plots (Fig. 3.2).

In addition, where available, the CT-scan images confirm the shipboard and our own visual observations regarding the absence of outsized clasts and coarse sand grains in F1 and F2. Hauptvogel (2015) however, reports grains that are  $>150\mu\text{m}$  in size (fine sand fraction) as IRD. He argues that grains of that size could only reach Site U1356 through ice rafting given the distance of the site to shore, unless they were delivered by gravity flows. Thick and coarse-grained Mass Transport Deposits (MTDs) during the latest Oligocene at site U1356 (Escutia et al., 2011), argue for coarse material being delivered to the site by gravity flows. In addition, fine sand grains to gravel size clasts have been reported from channels on the lower continental rise off the Wilkes Land margin transported by gravity flows, including turbidity flows (Payne and Conolly, 1972; Escutia et al., 2000; Busetti et al., 2003). Given that during the late Oligocene, Site U1356 is located on a low-relief levee of a submarine channel, one can expect delivery of fine-grained sand and even coarser sediment to the site. In any case, even if some background IRD is present in our record, we argue it is minimal compared to elsewhere in the core.

### 3.3.2. GEOCHEMISTRY

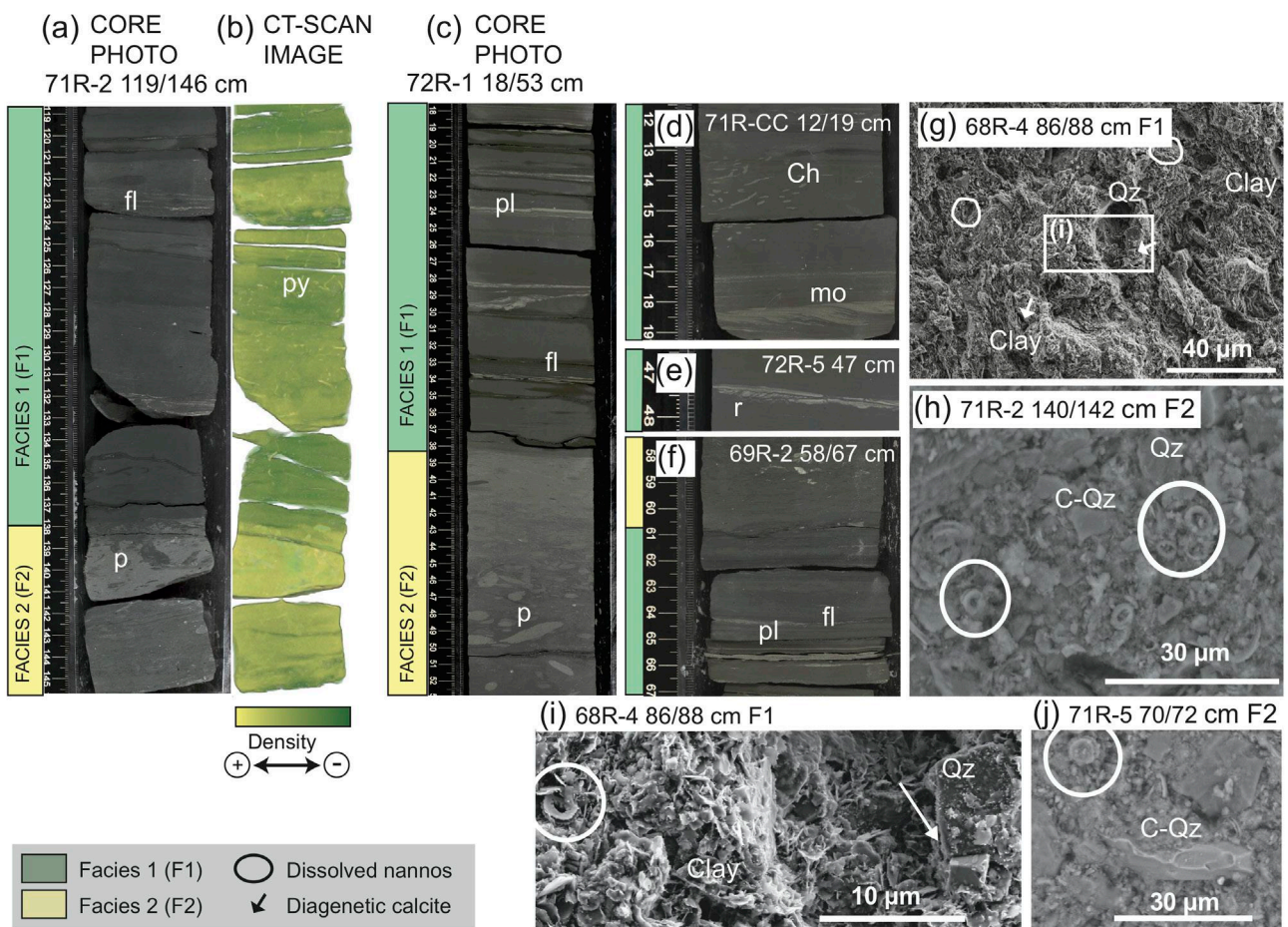
Down-core changes in the log ratios of various elements have been plotted against the facies log (Figs. 3.2, 3.4). In addition, in order to determine geochemical element associations we performed a Pearson correlation coefficient analysis of major elements on the whole XRF-scanner dataset (Table 3.3). This analysis highlights two main groups that are used as proxies for terrigenous (i.e., Zr, Ti, Rb, Ba) vs biogenic (i.e., Ca = carbonate) sedimentation.

Titanium (Ti), Zirconium (Zr), and Rubidium (Rb) are primarily derived from terrigenous sources, where Ti represents the background terrigenous input. During sediment transport Zr, Rb and Ti tend to become concentrated in particular grain-size fractions due to the varying resistance of the minerals in which these elements principally occur. Zr tends to become more concentrated in fine sand and coarse silt fractions, Ti in somewhat finer fractions and Rb principally in the clay-sized fraction (Veldkamp and Kroonenberg 1993; Dypvik and Harris 2001). The lack of correlation between Zr and Ti (Fig. 3.2; Table 3.3) implies that they are settled in different minerals and processes. The Zr/Rb ratio has been applied as a sediment grain-size proxy in marine records (Schneider, et al., 1997; Dypvik and Harris 2001; Croudace et al., 2006; Campagne et al., 2015). Zr/Al has been interpreted as an indicator for the accumulation of heavy minerals due to bottom currents (Bahr et al., 2014). In our cores, Zr/Rb and Zr/Ti ratios have a near identical variability downcore (Fig. 3.2). We utilize the high-amplitude Zr/Ti signal in our records as indicator for larger grain-size and current velocity (Fig. 3.2). The Zr/Ti ratio varies between 0.1 and 1 and exhibits maximum values within F2 showing an increasing upwards or bigradational patterns (Fig. 3.2). Although minimum Zr values (cps) are found in F1, laminations with coarser-grained sediment within

this claystone facies are also characterized by elevated Zr values similar to those in F2 (Figs. 3.3, 3.4; Table 3.3). The Zr/Ti pattern is positively correlated with magnetic susceptibility throughout the studied interval (Fig. 3.2).

The Zr/Ti, Zr/Rb and Zr/Ba ratios co-vary characterizing the laminations within F1 and the alternation between F1 and F2 by defining the contacts between them (Figs. 3.2, 3.4). They also mark the coarsening upwards or bigradational tendency in F2 (Fig. 3.4). Of the three ratios, the Zr/Ba ratio is the one that highlights these patterns best (Figs. 3.2, 3.4).

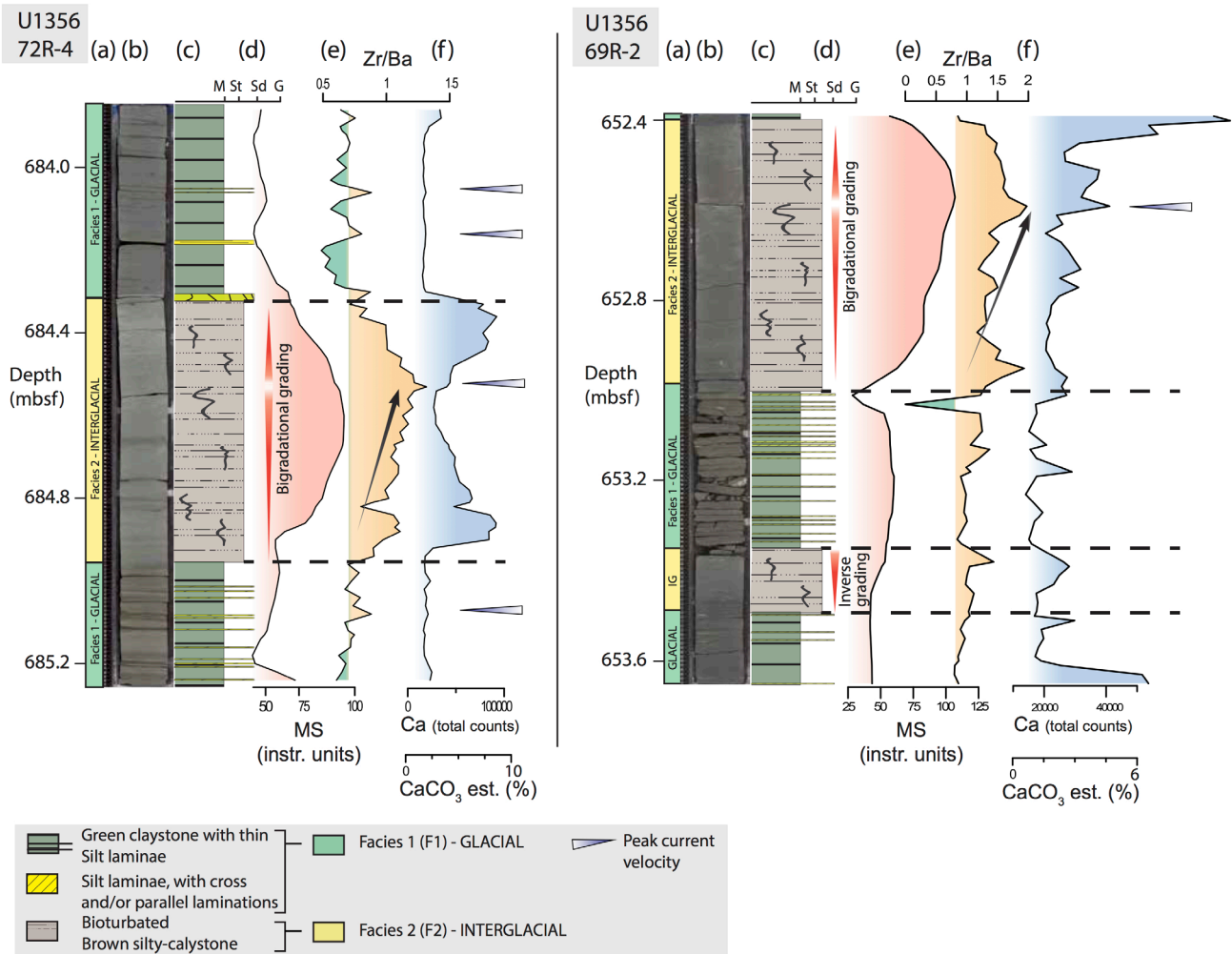
Barium (Ba) is present in marine sediments mainly in detrital plagioclase crystals and in the form of



**Figure 3.3.** Detailed images, CT-scans and HRSEM from Facies 1 (F1) and Facies 2 (F2). (a) Example of F1 taken from Core 71R-2 119/146 cm, showing faint laminations (fl) and bioturbation by *Planolites* (p) (b) CT-scan 3D image of the same core interval, note the pyritized burrows (py). (c) Example of F2 taken from core 72R-1 18/53 cm). (d-f) Close-ups of laminations from F1: ripples (r), planar lamination (pl), and faint laminations (fl), with mud offshoots (mo). (d) *Chondrites* (Ch) bioturbation inside F1. (g) HRSEM image of F1 (68R-4-86/88 cm) with detritic aspect and a mudstone clay matrix, Quartz grains (Qz), diagenetic calcite (arrows), and dissolved coccoliths (circles); (h) HR-SEM image of F2 (71R-2 140/142 cm) silt sized matrix and reworked calcareous nannofossils, and conchoidal quartz grain (C-Qz); (i) Detail of dissolved coccoliths and diagenetic calcite mineral; (j) Detail of a dissolved and reworked calcareous nannofossils and a fractured conchoidal quartz (C-Qz)



barite ( $\text{BaSO}_4$ ; Tribovillard et al., 2006). In the studied sediments, Ba and Ti have a correlation factor of  $r^2=0.66$  (Table 3.3), which is taken to indicate that Barium is predominantly present as a constituent of the continental terrigenous fraction and/or that biogenic barite was sorted by bottom currents. Ba has maximum values (10,000 total counts) at the base of F1 and decreases upwards in a saw-tooth pattern, reaching minimum concentrations within F2 (5,000 total counts) (Fig. 3.2; Table 3.3). The detrital fraction of Ba in the open ocean has been used in other studies as a tracer of shelf waters (Moore and Dymond, 1991; Abrahamsen et al., 2009; Roeske, 2011) and Ba record also is affected by current intensity in other



**Figure 3.4.** Detailed facies characterization of two representative sections using: (a) Interpreted facies F1 and F2; a high-resolution digital image of the core sections (b), facies log (c), Magnetic susceptibility (MS) (d), XRF Zr/Ba ratio (e), and XRF calcium counts (f).

depositional contourite systems (Bahr et al., 2014) preventing his use as paleoproductivity proxy in environments dominated by contour currents.

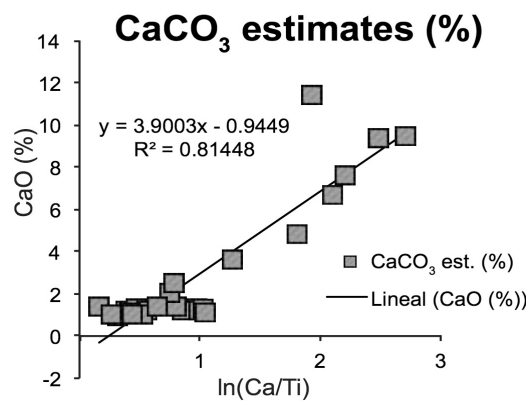
Variations in Ca, Mn, and Sr are strongly intercorrelated (Fig. 3.2) with  $r^2>0.87$  (Table 3.3). Biogenic calcite precipitated by coccoliths and foraminifera have greater Sr concentration than inorganically precipitated calcite or dolomite (Hodell et al., 2008). The positive Ca and Sr correlation could therefore

potentially be used to differentiate between terrigenous Ca sources (e.g. feldspars and clays) and biogenic carbonates (e.g. Richter et al., 2006, Foubert and Henriot, 2009, Rothwell and Croudace, 2015). Based on these observations, we interpret that Ca in our sediments is mainly of biogenic origin (CaCO<sub>3</sub>). This interpretation is supported by HR-SEM images taken from carbonate-rich intervals of F2, which show abundant coccoliths (Fig. 3.3d). Peaks in Ca in our record (Fig. 3.2) coincide with the carbonate-rich layers listed in the previous section. Additional peaks in the record may indicate carbonate-rich layers that we have been unable to identify visually.

**Table 3.2.** R Pearson Linear correlation between XRF-scanner elements

|    | MS     | S      | Ca     | Ti     | Mn     | Fe     | Br     | Rb     | Zr    | Sr    |
|----|--------|--------|--------|--------|--------|--------|--------|--------|-------|-------|
| S  | -0.214 |        |        |        |        |        |        |        |       |       |
| Ca | 0.226  | -0.122 |        |        |        |        |        |        |       |       |
| Ti | -0.212 | 0.620  | -0.290 |        |        |        |        |        |       |       |
| Mn | 0.151  | -0.121 | 0.858  | -0.246 |        |        |        |        |       |       |
| Fe | 0.0419 | 0.0449 | -0.396 | 0.510  | -0.324 |        |        |        |       |       |
| Br | -0.297 | 0.111  | -0.438 | 0.118  | -0.363 | 0.056  |        |        |       |       |
| Rb | -0.282 | 0.036  | -0.576 | 0.286  | -0.489 | 0.455  | 0.493  |        |       |       |
| Zr | 0.480  | -0.164 | -0.036 | -0.099 | -0.058 | -0.055 | 0.102  | 0.067  |       |       |
| Sr | 0.186  | 0.006  | 0.871  | -0.074 | 0.677  | -0.345 | -0.303 | -0.515 | 0.040 |       |
| Ba | -0.290 | 0.339  | -0.234 | 0.662  | -0.210 | 0.354  | 0.343  | 0.402  | 0.018 | 0.039 |

In order to estimate the CaCO<sub>3</sub> content continuously throughout the studied interval we use a calibration ( $r^2_{U1356}=0.81$ ) between natural logarithm (ln) of Ca/Ti ratio (ln(Ca/Ti)) from the XRF core scanner data and the XRF discrete CaCO<sub>3</sub> measurements (weight %) from Site U1356 as applied in other studies (Zachos et al., 2004; Liebrand et al., 2016) (Fig. 3.5). “CaCO<sub>3</sub> est.” is used throughout the text to refer to carbonate content estimated by ln(Ca/Ti) ratio. CaCO<sub>3</sub> est. concentrations are generally low (between 0-16%). Carbonates are mostly present in F2, varying between 5-16 %, although small contents (from 0 to 5 %) can be seen in the intervals of F1 with scarce laminations (Fig. 3.4). CaCO<sub>3</sub> est. peaks in some intervals have a particular morphology producing a double peak in the beginning and/or the end of bioturbated F2 (Figs. 3.2, 3.4).



**Figure 3.5.** Linear correlation between CaO% (discrete XRF) and ln(Ca/Ti) (XRF scanner) values in order to estimate carbonate contents (CaCO<sub>3</sub> est. %).



Mn(II) is soluble under anoxic conditions and precipitates as Mn(IV) oxyhydroxides under oxidising conditions (Tribovillard et al., 2006). Manganese is frequently remobilized to the sedimentary pore fluids under reducing conditions. Dissolved Mn can thus migrate in the sedimentary column and (re)precipitate when oxic conditions are encountered (Calvert and Pedersen, 1996). As such, large Mn enrichments primarily reflect changing oxygen levels at the sediment–water interface (Jaccard et al., 2016). The strong-correlated peaks of Mn and Ca (Fig. 3.2; Table 3.3) suggest that at least some of the Mn is present in the studied interval as Mn carbonates and/or Mn oxyhydroxides under oxic sediment-water interphase (Calvert and Pedersen, 1996; Calvert and Pedersen 2007; Tribovillard et al., 2006).

Br/Ti has been previously used as an indicator of organic matter in sediments (e.g., Agnihotri et al., 2008; Ziegler et al., 2008; Bahr et al., 2014). Br/Ti in our record shows generally low values (Fig. 3.2) most likely as the organic matter content in both facies types is relatively low (<0.5 %, Escutia et al., 2011). However, it exhibits some variability (0.01 to 0.05 Br/Ti ratio) within the two facies with higher ratio values in F1. Darker coloured sediments in F1 are in agreement with these higher Br/Ti values inside F1.

**Table 3.3.** Types of facies differentiated by physical, geochemical, and biological character and their interpretation in terms of sedimentary processes and paleoclimate

|   |               | <b>Facies 1 (F1)</b>   | <b>Facies 2 (F2)</b>  |
|---|---------------|--|---|
| <b>Lithological description</b>           |               | Bioturbated green claystones with thin silt laminae with planar and cross-bedded laminations | Highly bioturbated, thicker pale-brown, silty-claystones  |
| <b>Contacts</b>                           | <b>Top</b>    | Gradual, bioturbated   | Sharp   |
|   | <b>Bottom</b> | Sharp  | Gradual, bioturbated  |
| <b>Bioturbation</b>                       |               | Sparse bioturbation. Primary structures preserved  | Strong bioturbated. Massive. No primary structures preserved  |
| <b>Nannos</b>                             |               | Barren to rare   | Barren to variable abundance and preservation   |
| <b>IRD</b>                                |               | No   | No  |
| <b>Magnetic susceptibility (MS)</b>       |               | Low in claystones and high in silty laminations  | High  |
| <b>XRF-Scanner elements concentration</b> | <b>Zr</b>     | Low in claystones and high in silty laminations  | High, (max. values on top)  |
|   | <b>Ba</b>     | High, (max. values on bottom)  | Low   |
|   | <b>Ca</b>     | No   | Variable, low to high   |
| <b>Formation process</b>                  |               | Bottom currents of fluctuating intensities   | Bottom currents with higher velocity and constant flux  |
| <b>Facies interpretation</b>              |               | Cold periods. Supply of terrigenous by density current flows, reworked by bottom currents.   | Well-oxygenated deep-sea sedimentation. Warm periods with reworking of sediments by bottom currents |

In addition to the elemental analyses of the XRF-scanned data, we use the detrital Al/Ti ratio in discrete XRF bulk sediment samples to reflect changes in terrigenous provenance (Kuhn and Diekmann, 2002; Scher et al., 2015). Al/Ti ratio varies between 17-21, with the highest values found within F1 and the lowest in F2 (Fig. 3.2).

### 3.3.4. SPECTRAL ANALYSIS

To detect periodical signals, spectral analysis of time series was performed on the Zr/Ba and other elemental proxies (i.e., Ba, Zr/Ti, CaCO<sub>3</sub>, Magnetic Susceptibility) using Astrochron R software (Meyers, 2014; Figs. 3.6; S3-10).

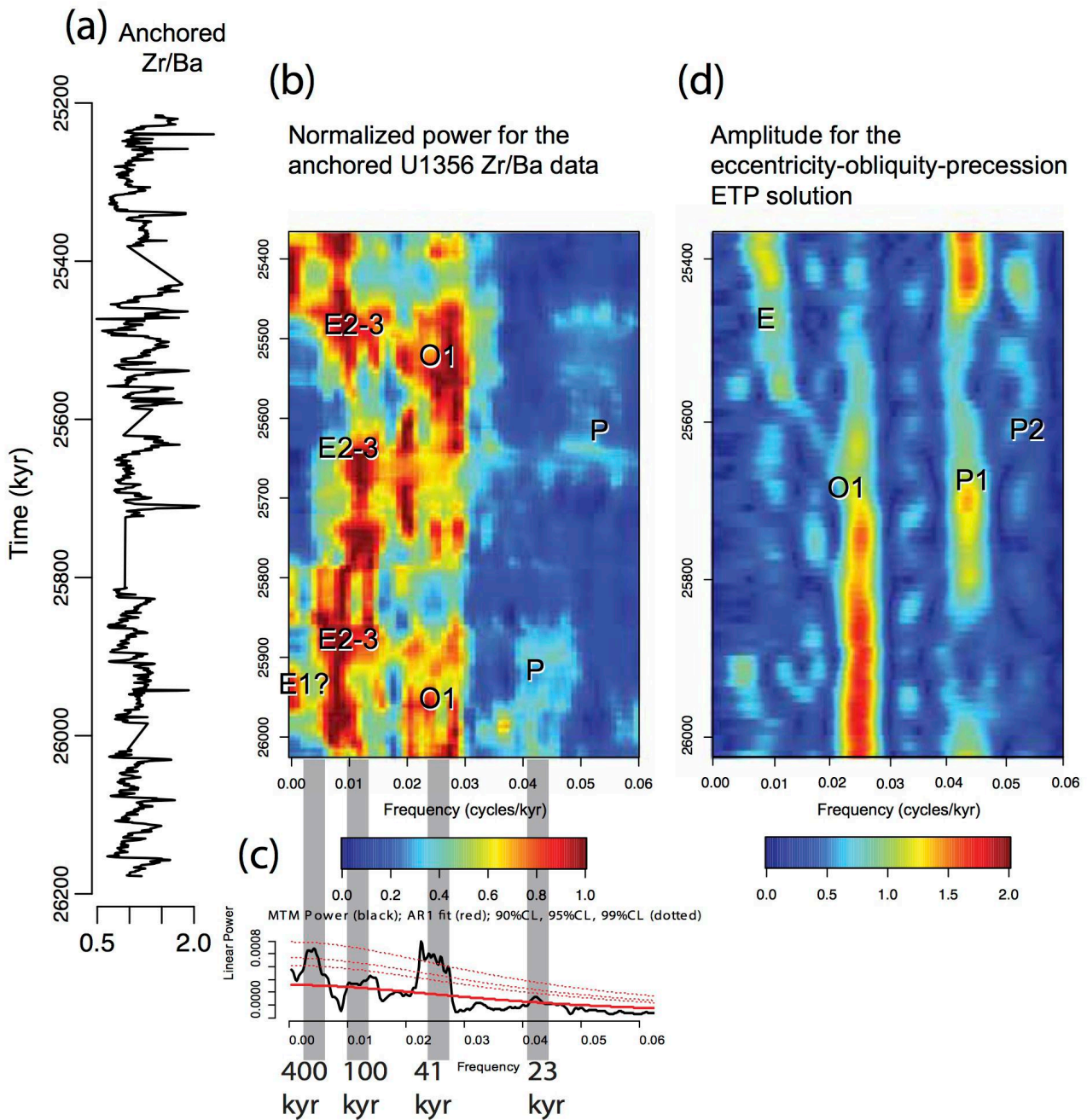
Multiple-taper spectral analysis (MTM) in Zr/Ba show a clear and statistically significant (>90%) cyclicity every 2m (0.5 cycles/m), and at 4.67m (0.21 cycles/m), and less significant one (>80%) at 1m (0.94 cycles/m) (Fig. 3.S3). On the basis of a linearly calculated sedimentation rate between the two extreme tie-points (Table 3.1), we obtained a sedimentation rate of approximately 5 cm/kyr. Within this sedimentation rate, the 0.5 cycles/m peak corresponds to the 41-kyr obliquity frequency; and the 0.21 and 0.94 cycles/m to the 95 and 21-kyr shorter eccentricity periods and precession frequencies, respectively.

After initial analysis, we ran an Evolutive Harmonic Analysis (EHA) (Astrochron (Meyers, 2014)) with 3 data tapers for the untuned Zr/Ba in depth domain with 2 cm resolution (Fig. 3.S3). The statistical significance of spectral peaks was tested relative to the null hypothesis of a robust red noise background, AR(1) modelling of median smoothing, at a confidence level of 95% (Mann and Lees, 1996). Despite a short core gap in the middle of the time series, obliquity (41 kyr) dominates throughout the time series (Fig. 3.6). The sedimentation rates obtained by this method vary between 4.6 and 5.4 cm/kyr for the studied section, similar to those obtained with linearly calculated sedimentation rates. Additionally, the Nyquist frequency for Zr/Ba data is 1 m<sup>-1</sup> (0.5 kyr), which implies the site is sampled sufficiently to resolve precessional scale variations however, core gaps prevent identification of long eccentricity cycles (Fig. 3.S6). Time series were anchored to the more robust paleomagnetic tie point in the U1356 age model, which is 25.99 Ma at 678.78 mbsf (Fig. 3.S7).

Apart from obliquity, spectral analyses of the tuned age model reveal an alignment of the eccentricity and precession bands (Fig. 3.6, S8). For example, a marked cyclicity at the obliquity periods of 41 Kyr is seen at Ba and Zr/Ti (99% confidence) and also eccentricity at 100 kyr, and precession at 20kyr (95% confidence) (Fig. 3.S9). We also observe coherent power above the 90% significance level at ~54 and ~29 ky periods, which are secondary components of obliquity. The anchored age model provides an unprecedented 500 yr resolution (2.5 cm sampling) of the data during the Late Oligocene. Orbital frequencies were tested in each core section individually in the Zr/Ba dataset in the depth scale in order to assure that cyclicity is not an artefact related to the gaps in the series (Fig. 3.S10).







**Figure 3.6.** Spectral analysis results of the Zr/Ba obliquity tuned and anchored data. (a) Zr/Ba ratio tuned with Astrochron (Meyers, 2014) and anchored to the top of the C8n.2n (o) chron. (b) EHA and (c) MTM spectral analysis on Zr/Ba tuned data. EHA normalized power with 300-kyr window with 3DPSS tapers. (d) EHA amplitude for the eccentricity-obliquity-precession ETP solution (Laskar et al., 2004) calculated for the same period of time with 3DPSS tapers and 200-kyr window.

### 3.4. DISCUSSION

Based on the integration of the facies characterized on the basis of sedimentological data (visual core description, facies analysis, CT-scans, HR-SEM), physical properties (magnetic susceptibility, NGR), and geochemical data (XRF), we provide for the late Oligocene interval (26 to 25 Ma): 1) a new glacial-interglacial sedimentation model for the distal glaciomarine record in the Wilkes Land margin dominated by bottom-current reworking of both, glacial and interglacial deposits; 2) insights into the configuration of the ice sheet in this sector of the east Antarctic margin; 3) changes in the paleoceanographic glacial-interglacial configuration; and 4) evidence for orbital forcing of the glaciomarine glacial-interglacial sedimentation at Site U1356.

#### 3.4.1. GLACIAL AND INTERGLACIAL CONTOURITE SEDIMENTATION OFF WILKES LAND

Laminated claystones (F1) from Site U1356 were originally interpreted by the shipboard science team to have formed during glacial times relating to variations in bottom current strength and fine-grained terrigenous supply. Conversely, the bioturbated claystones and micritic limestones (F2) were interpreted to result from mostly hemipelagic sedimentation during interglacial times (Escutia et al., 2011). Alternations between laminated deposits and bioturbated hemipelagic deposits, similar to those in F1 and F2, have been previously reported to characterize Pleistocene and Pliocene glacial-interglacial continental rise sedimentation, respectively, on this sector of the Wilkes Land margin (Escutia et al., 2003; Patterson et al., 2014). Gravity flows, mainly turbidity flows are the dominant process during glacial times resulting in laminated deposits. Interglacial sedimentation is dominated by hemipelagic deposition with higher opal and biogenic content (Escutia et al., 2003, Busetti et al., 2003). Erosion and re-deposition of fine-grained sediment by bottom contour currents has also been reported as another important process during Pleistocene and Plio-Quaternary interglacials (Escutia et al., 2002; Escutia et al., 2003, Busetti et al., 2003).

Despite being sparse, the occurrence of bioturbation in our laminated sediments in F1, which slightly affects both claystones and silt laminations, indicates slow and continuous sedimentation. This is not consistent with instantaneous turbidite deposition, which would be expected at the Site U1356 located on the left low-relief levee of a contiguous channel during the late Oligocene. It is however consistent with fine-grained turbidite overbank deposits being consequently entrained by bottom currents. Silt layer sedimentary structures similar to those described by Rebesco et al. (2008, 2014) indicate that there is current reworking of the sediments. For example, silt layers can be continuous or discontinuous with wavy and irregular morphologies, and within layers, sedimentary structures such as cross-laminations are common (Fig. 3.3c-f). Within the cross laminae, mud offshoots and internal erosional surfaces are distinctive features of fluctuating currents where successive traction and suspension events are super-imposed, indicating bottom-currents sedimentation as the principal process for the F1 laminated claystones (Shanmugam et al., 1993; Stow et al., 2002). Based on these observations, we interpret F1 as glacial laminated muddy contourites following the classification of Stow and Faugères (2008). The F1 sedimentary structures suggest bottom-currents with fluctuating intensities, that result in laminations and internal structures forming during peak current velocities (Lucchi and Rebesco, 2007; Martín-Chivelet et al. 2008; Rebesco et al.,



2014). Laminated, fossil-barren, glaciogenic deposits, consistent with those of Facies F1, have been observed on younger sedimentary sections in glaciated margins and interpreted as contour current modified turbidite deposits and as muddy contourites (Anderson et al., 1979; Mackensen et al., 1989; Grobe and Mackensen, 1992; Pudsey, 1992; Gilbert et al., 1998; Pudsey and Howe, 1998; Pudsey and Camerlenghi, 1998; Anderson, 1999; Williams and Handwerger, 2005; Lucchi and Rebesco, 2007; Escutia et al., 2009). This particular type of contourite facies is associated with glaciomarine deposition during times of glacial advance, and has been interpreted to result from unusual, climate-related, environmental conditions of suppressed primary productivity and oxygen-poor deep-waters (Lucchi and Rebesco, 2007).

Bioturbated sediments in F2 were previously interpreted as interglacial hemipelagic deposits (Escutia et al., 2011). In this study, we interpret F2 as hemipelagic and overbank deposits reworked by bottom-currents. The coarser grain-size in F2 compared to F1 (silty-clay matrix as seen in HR-SEM Fig. 3.3g-j), the distribution of heavy minerals as indicated by the Zr/Ba, and the elevated values of the magnetic susceptibility record with a bigradational pattern within the facies (Figs. 3.2, 3.4), support the notion that interglacial sediments of F2 have been heavily modified by bottom currents. Hemipelagic sediments are expected to be homogeneous in terms of grain-size and grading is not expected. Current winnowing of hemipelagic deposits and removal of the fine-grained fraction can produce the higher accumulation of heavy (indicated by the Zr) and ferromagnetic (indicated by MS) minerals observed in F2 compared to F1 (Fig. 3.2; Table 3.2). High MS values result from stronger bottom currents deposition and/or increased terrigenous input (e.g., Pudsey et al., 2000; Hepp et al., 2007). Also, bigradational trends have been previously described in contourite sediments and interpreted to record an increase followed by a decrease in the current velocities (e.g., Martín-Chivelet et al., 2008). The bigradational patterns in the Zr/Ba and MS plots (Figs. 3.2, 3.4) are therefore interpreted to depict a constant and smooth increase followed by a decrease in current velocity with little gradual changes in flow strength. In addition, the presence of grains of quartz with conchoidal fractures and reworked coccolithophores with signs of dissolution (Fig., 3h,j) support the reworking of background hemipelagic and turbidite overbank sediments by bottom currents in a high-energy environment (Damiani et al., 2006). Following the classification by Stow and Faugères (2008), we interpret that F2 has more silty massive contourites resulting from higher and more constant bottom current velocity compared to F1.

Transitions between the F1 and F2 facies are characterized by glacial-to-interglacial contacts that may be sharp or diffuse due to bioturbation, and characterized by a gradual change in physical and geochemical sediment parameters (Figs., 3.3, 3.4; Table 3.3). Interglacial-to-glacial contacts (F2 to F1), on the other hand, are characterized by an apparently non-erosional sharp lithological boundary. The sharp lithological boundaries between interglacial to glacial transitions can be explained by maximum current intensities achieved at the end of the interglacials (Shanmugam, 2008; Rebesco et al., 2014).

### 3.4.2. ICE SHEET CONFIGURATION DURING THE WARM LATE OLIGOCENE

Early Oligocene and post-Mid Miocene climate transition sediments from Site U1356 contain granule and larger clasts (>2mm) interpreted as ice rafted debris (IRD; Escutia et al., 2011; Sangiorgi et al., 2018; Fig. 3.S1). In addition, dinocyst assemblages indicate the presence of sea ice (Houben et al., 2013). Based on this, one could expect the site to be within the reach of icebergs calving from an expanded ice sheet grounded at the coast or beyond in the late Oligocene. This is supported by Pliocene-Pleistocene sedimentary sections in adjacent continental rise sites containing IRD (Escutia et al., 2011; Patterson et al., 2014). In addition to the paucity of IRD in our studied interval, the absence of sea ice-loving species *Selenopemphix antarctica* and common to abundant gonyaulacoid phototrophic dinocysts, suggest warm-temperate surface waters (Bijl et al., 2018a). A sea ice-free scenario during the late Oligocene is also supported by elevated sea surface temperatures (i.e., average summer temperatures are ~19°C) based on biomarker sea surface temperatures (TEX<sub>86</sub> data in Hartman et al., submitted, this volume). Furthermore, the presence of *in situ* terrestrial palynomorphs suggests that during the late Oligocene margins nearby were in part free of ice sheets and covered by a cool-temperate vegetation with trees and shrubs (Salzmann et al., 2016, Strother et al., 2017). All these observations suggest a reduced ice sheet and partly ice-free margins in the Wilkes margin during the late Oligocene.

These observations are consistent with the iceberg survivability modelling in the Southern Ocean for the warm Pliocene intervals, which shows the distance that icebergs could travel before melting was significantly reduced (Cook et al., 2014). Warm Pliocene summer sea surface temperatures up to 6°C warmer than today during interglacials and prolonged Pliocene warm intervals have been reported in the Ross Sea (e.g., Naish et al., 2009; McKay et al., 2012) and other locations around Antarctica (Whitehead and Bohaty, 2003; Whitehead et al., 2005; Escutia et al., 2009; Bart and Iwai, 2012). Contrary to what we observe in our late Oligocene record and in the Miocene Climatic Optimum (Sangiorgi et al., 2018), abundant IRD were delivered to continental rise sites adjacent to Site U1356 during the warm Pliocene (Escutia et al., 2011; Patterson et al., 2014). This was interpreted by Cook et al. (2017) to suggest that a considerable number of icebergs (iceberg armadas) had to be produced in order to reach the site under these warm Pliocene conditions. We argue that the lack of IRD delivery to site U1356 during the studied warm late Oligocene interval can result from the different Wilkes Subglacial Basin (WSB) late Oligocene paleotopographic setting. Paleotopographic reconstructions from 34 Ma ago (Wilson et al., 2012) and the early Miocene (Gasson et al., 2016), show the WSB to be an area of lowlands and shallow seas in contrast to the over-deepened marine basin that it is today (Fretwell et al., 2013). This paleotopographic configuration would have precluded widespread marine ice sheet instability during the Oligocene. This difference is important, as an ice sheet grounded on an overdeepened continental shelf can experience marine ice sheet instability, a runaway process relating to ice sheet retreat across a reverse slope continental shelf (Weertman 1974), which is proposed to be a driver for retreat of the EAIS in the WSB during the warm Pliocene (Cook et al., 2013). Conversely, a shallower continental shelf allows for the potential expansion of grounded ice sheets into the marine margin during warmer-than-present climates (Wilson et al. 2012), and thus direct records are required to assess the climate threshold for such an advance.



In comparison to the distal U1356 Wilkes Land margin record, the Ross Sea Embayment ice proximal sediments obtained by the Cape Roberts Project (CRP) contain Oligocene to Early Miocene palynomorphs, foraminifera and clay assemblages that point to a progressive decrease in fresh meltwater, cooling and intensifying glacial conditions (Leckie and Webb, 1983; Hannah et al., 2000; 2001; Raine and Askin, 2001; Thorn, 2001; Ehrmann et al., 2005; Barrett, 2007). Therefore, the coastal CRP sediment record does not support a significant loss of ice or warming during the late Oligocene (Barrett, 2007). The high sedimentation rates during the late Oligocene-early Miocene recorded at Deep Sea Drilling Project (DSDP) Site 270 were interpreted to reflect turbid plumes of glaciomarine sediments derived from polythermal-style glaciers or ice sheets that were calving into an open Ross Sea, without an ice shelf (Kemp and Barrett, 1975). In addition, seismic data indicate that during the late-mid Oligocene widespread expansion of a marine-based ice sheet onto the outer Ross Sea shelf did not take place but instead glaciers and ice caps drained from local highs and advanced only into shallow marine areas, rather than whole-scale marine ice sheet advance (Brancolini et al., 1995; De Santis et al., 1995; Bart and De Santis, 2012).

Combined, these evidences suggest that during the late Oligocene marine-terminating glaciers, ice caps and glaciers persisted along the Transantarctic Mountain front reaching the Ross Sea coastal areas, but may have been more confined within a warmer WSB margin. This is also supported by vegetation reconstructions derived from fossil pollen from both margins, which indicate for the middle Miocene and Late Oligocene higher terrestrial temperatures and more tree taxa at Wilkes Land (Salzmann et al., 2016; Sangiorgi et al., 2018) than the Ross Sea (Askin and Raine, 2000; Prebble et al., 2006). This is consistent with the ice sheet modelled configuration for Miocene topographies with CO<sub>2</sub> scenarios of 500-840 ppm (Gasson et al., 2016; Levy et al 2016; Fig. 3.7).

### 3.4.3. PALEOCEANOGRAPHIC IMPLICATIONS

Sediment physical properties and geochemical signatures of F1 and F2 are here related to changes in bottom water-sediment interphase oxygenation/ventilation during successive glacial and interglacial periods (Table 3.2). We interpret that these changes are linked to shifts in water-masses driven by a north-south displacement of the position of the westerlies, and associated changes in the intensity of frontal mixing or location of the Polar Front and Antarctic Divergence (Fig. 3.7). Based on our observations, we propose a model to explain the interpreted changes in bottom-water conditions at Site U1356 during successive glacial and interglacial times (Fig. 3.7).

#### 3.4.3.1. GLACIAL PALEOCEANOGRAPHIC CONFIGURATION

The Chondrites-like bioturbation with pyrite infilling the tubes of Skolithos within F1 (Fig. 3.3b, d) has previously been reported to characterize low-oxygen conditions at the water-sediment interphase (Bromley and Ekdale, 1984). In addition, pyritized diatoms are present throughout the Oligocene section of this site, but are found preferentially inside F1. The presence of pyritized diatoms was interpreted during Expedition 318 to indicate a prolific production and syn-sedimentary diagenesis in a restricted circulation (low oxygen) environment, mainly during glacial periods (Escutia et al., 2011). Reducing conditions in

the sediment also help to preserve primary sedimentary structures of the silt layers in F1 because bioturbation is limited. Higher amounts of organic matter in F1 compared to F2 are suggested by increased values of the Br/Ti ratio (Fig. 3.2). The higher organic content most likely produces a poorly ventilated environment with near reducing conditions at the water-sediment interphase, where pyrite can precipitate (Tribovillard et al., 2006). In spite of this, total oxygen depletion did not occur as indicated by the palynomorphs good preservation within F1 (Bijl et al., 2018a).

Low MS values such as those recorded within F1 (Fig. 4; Table 3.2) have been reported around Antarctica and attributed to magnetic minerals dissolution caused by dilution and/or primary diagenesis effects on the sediments due to the higher concentration in organic matter or to changing redox conditions (Korff et al., 2016). Several authors have postulated that oxygen-depleted Antarctic Bottom Water (AABW) occupying the abyssal zones of the oceans can change the redox conditions in the sediment, trapping and preserving dissolved and particulate organic matter and, consequently reducing and dissolving both, biogenic and detrital magnetite (Florindo et al., 2003; Hepp et al., 2009; Korff et al., 2016). At present, Site U1356 is influenced by AABW forming in the adjacent Wilkes Land shelf (Orsi et al., 1999; Fukamachi et al., 2000) and in the Ross Sea spilling over to the Wilkes Land continental shelf (Fukamachi et al., 2010) (Fig. 3.1). Our records suggest a reduced continental ice-sheet in the eastern Wilkes Land margin and reduced sea ice presence compared to today (Bijl et al., 2018a). Under these conditions, bottom water formation and downwelling can still occur (with or without presence of sea ice) as a result of density contrasts related to seasonal changes in surface water temperature and salinity (Huber and Sloan, 2001; Otto-Bliesner et al., 2002). Moreover, stable Nd isotopic composition in Eocene-Oligocene sediments from Site U1356 is consistent with modern day formation of bottom water from Adélie Land, as reported by Huck et al (2017).

Our evidence above points to deposition of F1 during glacial cycles under poorly-ventilated, low-oxygenation conditions at the water-sediment interface (Fig. 3.7a). We postulate, that during glacial periods, westerly winds and surface oceanic fronts migrate towards the equator, generating a more stratified ocean and reduced upwelling closer to the margin, with sporadic and fluctuating currents (Fig. 3.7a). Records of the Last Glacial Maximum show that this northward migration results in a weakening of the upwelling of the Circumpolar Deep Water (CDW; Govin et al., 2009), increasing stratification and reduced mixing of water masses also due to an enhanced sea ice formation, not seen during the late Oligocene.

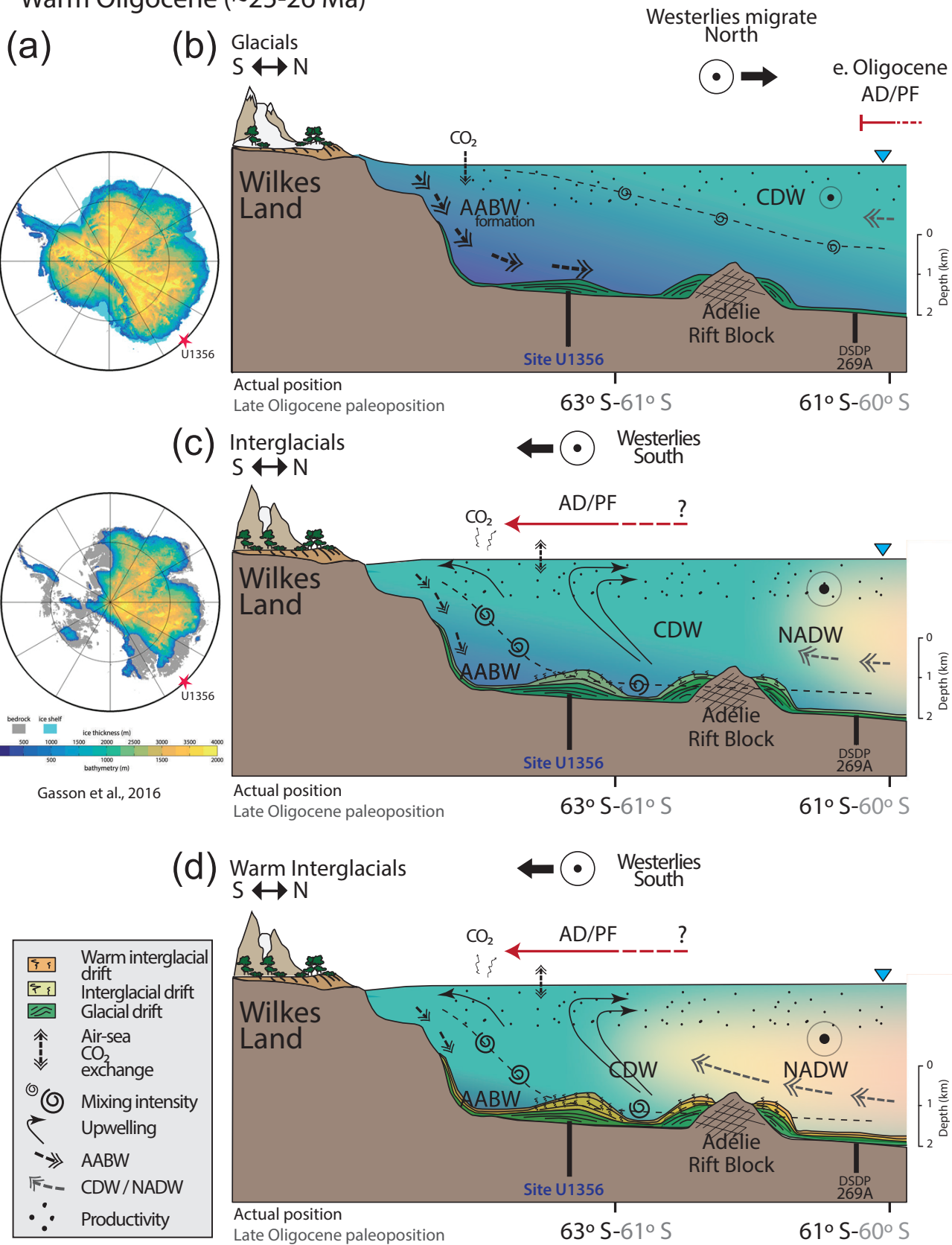
#### 3.4.3.2. INTERGLACIAL PALEOCEANOGRAPHIC CONFIGURATIONS

We differentiate two interglacial paleoceanographic configurations based on the presence of some intervals of micritic limestone with calcareous nannofossils.

In general, the higher degree of bioturbation in F2 with no primary structures preserved and the ichnofacies association (i.e., Planolites and Zoophycos), suggest a more oxygenated environment in comparison with F1. This is supported by the covariance of Mn and CaCO<sub>3</sub> est. (Fig. 3.4) where Mn enrichments



### Paleoceanographic configuration of Wilkes Land region during the Late Warm Oligocene (~25-26 Ma)



can be interpreted as redox changes variations (Calvert and Pedersen, 2007; Jaccard et al., 2016). More oxygenated conditions during interglacial periods can be achieved under more ventilated and mixed water masses, with enhanced current velocities. Enhanced currents during deposition of F2 are interpreted based on coarser grain size, and the increased accumulation of heavy and ferromagnetic minerals as indicated by the high values of the Zr/Ti ratio and MS within F2 (Figs. 3.2, 3.4). The bigradational pattern of the Zr/Ba and the MS (Fig. 3.4) is also interpreted to record an increase followed by a decrease in current velocities within F2.

The intervals of micritic limestone within F2 have calcareous nannofossils preserved (Fig. 3.3d). The productivity of calcareous nannofossils and the later preservation of these coccoliths in the sediment indicate specific geochemical conditions enabling carbonate deposition and preservation. Although today nanoplankton is abundant in surface waters at the Antarctic Divergence (Eynaud et al., 1999), these rarely deposit on the deep ocean floor because of corrosive bottom waters, which dissolve calcareous rain. A number of studies in other areas of the Antarctic margin and the Southern Ocean have correlated the presence of calcareous nannofossils with the presence of temperate north component water masses (North Atlantic Deep Water-like, NADW) that intrude close to the Antarctic continent and influence the Southern Ocean during the late Oligocene (e.g., Nelson and Cooke, 2001; Pekar et al., 2006; Villa and Persico, 2006; Scher and Martin, 2008), the Miocene (DeCesare et al., 2013; Sangiorgi et al., 2018), and during more recent times such as the Quaternary (Diekman, 2007; Kemp et al., 2010; Villa et al., 2012).

The more oxygenated and ventilated conditions in our records suggest enhanced mixing of the water masses (Fig. 3.7b-c). We postulate that during interglacials westerly winds and the Polar Front are shifted south and become more aligned. Under these conditions, upwelling of deep waters is likely promoted, facilitating the mixing and oxygenation of surface waters that form the precursor to bottom water. Similar process has been reported for the Holocene by Peck et al. (2015). Such a process would also generate increased geostrophic current velocities of the bottom water mass, supported by the coarser grain size and heavy mineral concentrations in the bioturbated F2 facies.

Similar to what is occurring under the present warming, bottom water formation during interglacials is likely fresher and less dense due to enhanced freshwater runoff from surface and subglacial melt

← **Figure 3.7.** Paleocceanographic reconstructions based on our interpretations for Facies 1 and 2. (a) Modelled ice thickness for the mid-Miocene ice sheet by Gasson et al., (2016). (b) Glacial periods with low obliquity configuration. Westerlies and Polar Front (PF) move northwards. There is enhanced proto-AABW formation. Low ventilation conditions occur at the ocean/sediment interface and mixing of waters masses is diminished. Bottom currents are weak and fluctuating, producing laminated sediments. (b) Interglacials occur during high obliquity configuration. Westerlies and the PF move southwards, close to the Site U1356. Proto-AABW formation is reduced. Intrusions of proto-CDW/NADW-like reach southernmost positions. (c) During warm Interglacials, NADW-like is enhanced and CaCO<sub>3</sub> sedimentation is more abundant. (b,c) Bottom water ventilation and upwelling are more vigorous, with stronger bottom currents that result in fully bioturbated and silty-sized sediments.





of the continental ice sheet (Wijk and Rintoul, 2104). Today, a reduction in the volume of the AABW is compensated by the expansion of the Circumpolar Deep Water (CDW) (Wijk and Rintoul, 2014), which forms by mixing of abyssal, deep, and intermediate water masses, including the AABW and the NADW (Johnson, 2008). We hypothesize, that during warmer interglacials, the influence of more northern-sourced water masses into the proto-CDW, relative to Antarctic-sourced (Fig. 3.7c), could enable carbonate productivity and preservation of coccolithophores remains, seen at least 13 occasions in our record. These data are also in agreement with the  $\delta^{13}\text{C}$  global isotopes oscillations between 26 and 25 Ma (Cramer et al., 2009; Liebrand et al., 2017), that suggest low values for an AABW and high  $\delta^{13}\text{C}$  values for a NADW, that may represent the different oceanic primary production and ventilation rates, as proposed in this work. In addition,  $\delta^{13}\text{C}$  records in the Atlantic show systematic offsets to lower values toward a North Atlantic signal for most of the late Oligocene to early Miocene. These data suggest the influence of two distinct deep-water sources: cooler southern component water and warmer northern component water (Billups et al., 2002; Pekar et al., 2006; Liebrand et al., 2011). In addition, the increased presence of North Component Deep waters influencing this sector of the eastern Wilkes Land margin could be related with a slowdown of the southern limb of the overturning circulation.

#### 3.4.4. ORBITAL FORCING AND GLACIAL AND INTERGLACIAL CYCLICITY

The first spectral analysis on late Oligocene sediments from the eastern Wilkes Land margin at Site U1356 shows that glacial-interglacial cycles, resulting in changes in the oceanic configuration off Wilkes Land, are paced with variations in Earth's orbit and seasonal insolation. Although the data is somewhat discontinuous due to gaps in our record, it clearly shows that the glacial-interglacial cyclicity (every 2 m or 41 kyr) discussed above has a persistent obliquity pacing throughout the studied late Oligocene interval (26-25 Ma) in the Wilkes Land. Consequently, this obliquity-paced cyclicity modulates the amount of deep-water production in the Southern Ocean, and exerts a major control on oceanic configuration and current strength. Bottom current velocity fluctuations and ventilation of bottom sediments respond to the forcings applied by the strength of the Southern Hemisphere westerlies, the position of the PF respect to the site, and consequently by the water mass occupying the bottom of the basin at each time. In addition to obliquity, precession is also present, which implies a dynamic response of the EAIS and offshore oceanic water masses to orbital forcing.

East Antarctic ice volume fluctuations at orbital periodicities in the obliquity band in the Wilkes Land margin have been previously reported from early warm Pliocene (3-5 Ma) sediments obtained from Site U1361 (Patterson et al., 2014). In the Ross Sea, cyclicity in sediments collected by the CRP from the late Oligocene, the late Miocene and the early warm Pliocene period was also paced by obliquity (Naish et al., 2001; McKay et al., 2009; Naish et al., 2009). Similar orbital variability in the deep-water circulation patterns have also been inferred to have occurred with the growth of the EAIS during the middle Miocene between 15.5 to 12.5 Ma (Hall et al., 2003). In addition, other studies have linked changes in Atlantic meridional overturning (Lisiecki et al., 2008; Scher et al., 2015) and Antarctic circumpolar ocean circulation (Toggweiler et al., 2008) to obliquity forcing. An interglacial mechanism has been proposed whereby the

southward expansion of westerly winds and associated Ekman transport is compensated for by enhanced upwelling of warmer, CO<sub>2</sub>-rich CDW (Toggweiler et al., 2008), which also promotes atmospheric warming. In the equatorial Pacific, Pälike et al. (2006) also report strong obliquity in the benthic  $\delta^{13}\text{C}$  isotopic record between 26–25 Myr, implying that changes in the carbon cycle (pacing glacial /interglacial periods) are triggered in the high southern latitudes and transferred to the global deep-ocean through the bottom water masses.

### 3.5. CONCLUSIONS

Our study provides new insights regarding Antarctic ice sheet and paleoceanographic configurations that prevailed in the eastern Wilkes Land margin between 26 and 25 Ma. Sediments at IODP Site U1356 during this interval are characterized by the alternation between two main facies (F1 and F2), that are dominated by reworking by bottom-currents with varying intensities of glacial-interglacial gravity flows and hemipelagic deposits. Claystones with silty laminations (F1) are interpreted to represent fluctuating bottom current intensities during glacial periods. Massive bioturbated silty clays and micritic limestones with coccoliths (F2) are interpreted as interglacial deposits and record maximum velocities of bottom-currents at this site. The lack of iceberg rafted debris (IRD), the absence of sea ice, elevated sea surface temperatures throughout the studied interval, and reconstructions of cool-temperate vegetation suggest that reduced glaciers or ice caps occupied the topographic highs and lowlands of the now overdeepened Wilkes Subglacial Basin between 26 and 25 Ma and that iceberg calving was only a background process during this time due to the lack of marine terminating ice sheets.

Glacial sediments record poorly ventilated, low-oxygenation conditions at the water-sediment interface that we postulate result when westerly winds and surface oceanic fronts migrate towards the equator and overturning is reduced near the Antarctic margin. During interglacial times, more oxygenated and better-ventilated conditions are inferred to have prevailed which would act to enhance mixing of the water masses with increased current velocities. We postulate that during interglacials, westerly winds shifted south and became more aligned with the Antarctic Divergence and Polar Fronts, which promoted upwelling of deep waters and facilitated the mixing and oxygenation of bottom waters. Micritic limestone intervals within interglacial F2, record warmer paleoclimatic conditions when the influence of more northern-sourced water masses into the proto-CDW, relative to Antarctic-sourced (Fig. 3.7c), could enable carbonate productivity and preservation of coccolithophores remains. Preservation of carbonate in some F2 intervals supports previous paleoceanographic studies that consider at least a two-layer ocean with an Antarctic Bottom Water (undersaturated with respect to calcium carbonate), and a proto-CDW with a greater influence of warmer Northern Component Water mass (NADW-like) to reconcile intra-basinal differences in  $\delta^{18}\text{O}$  values (Pekar et al., 2006). Based on the number of carbonate-rich layers, warmer NADW-like waters reached the site at least 13 times during the studied interval.



Spectral analysis on late Oligocene sediments from the eastern Wilkes Land margin reveal that glacial-interglacial paleoceanographic changes during the late Oligocene are regulated primarily by obliquity, although frequencies in the eccentricity and precession band are also recorded. However, as we do not have a measure of ice dynamics during this time (e.g. ice rafted debris), the orbital response of terrestrial ice in the Wilkes Land Basin remains ambiguous, beyond what is inferred from the deep-sea isotope record.

## SUPPLEMENTS TO CHAPTER 3

### S3.1. LITHOSTRATIGRAPHY FOR SITE U1356

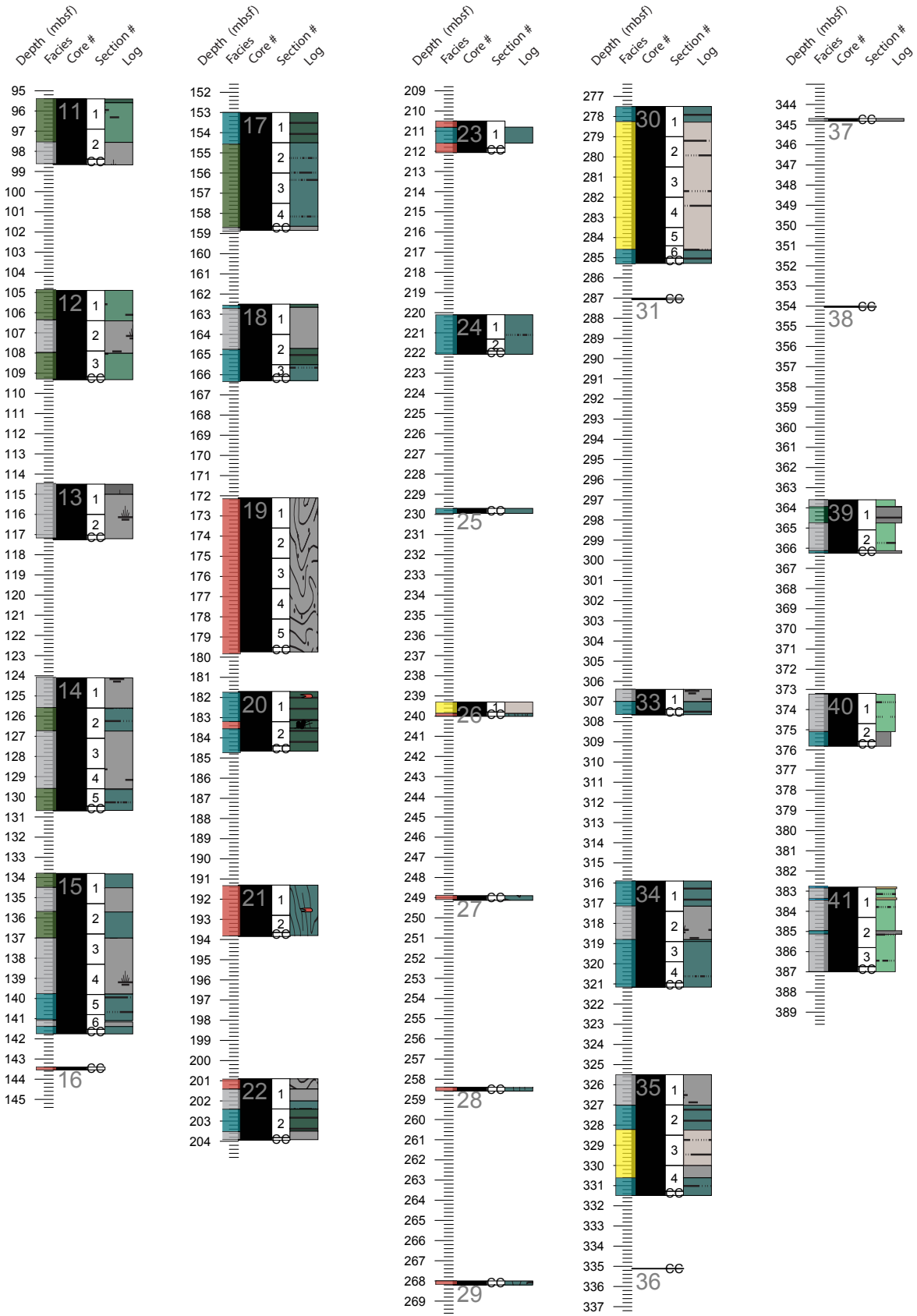
Site U1356 from 95.4 to 896 mbsf (Cores 11R to 95R) comprises lithostratigraphic Units I to IX described on shipboard during IODP Expedition 318 (Escutia et al., 2011). Here we present a revised and more detailed lithostratigraphic log (Fig. S3.3.1) and a schematic facies interpretation (Fig. S3.2). Facies are interpreted based on a detailed visual description of the cores during a visit to the IODP-Gulf Coast Repository (GCR) following IODP Proceedings methods in Escutia et al. (2011). We aided our interpretations with shipboard magnetic susceptibility data and high-resolution digital-images of the cores, both available from <http://web.iodp.tamu.edu>. In addition, the XRF core scanner data results obtained from the interval between 641.4 and 689.4 mbsf, which is the main focus of this paper, have been interpolated to other intervals down-core where sediments are “in situ.” The facies interpretation column in Figure S3.2, contains information on whether the sediments are deposited “in situ” or are deposited from allochthonous older materials.

Facies are here described briefly from top to bottom (Fig. S3.1-2). Early and middle Miocene section is recovered between 95.4 and 430.8 mbsf, Cores U1356-11R to U1356-45R. Sediments are comprised by an alternation between glacial laminated green silty clay and interglacial grey clay-rich diatom oozes. In addition, there are some intervals with Mass Transport deposits (i.e., debris flows). Miocene facies are dominated by mix sedimentary processes between turbidites, contourites and hemipelagites and are included within shipboard lithostratigraphic units I and II (Escutia et al., 2011). The Oligocene section is recovered between 430.8 and 895 mbsf, Cores U1356-46R to U1356-95R-3 83 cm. From 430.8 to 455 mbsf, turbidite facies dominate, with an alternation between dark grey claystones with *Nereites* ichnofacies and green claystones with silt laminae. Silt laminae have scours at the base, with cross lamination and planar laminations. These facies are included in shipboard lithostratigraphic Unit III. From 455 to 575 mbsf, sediments mostly comprise debris flow (DF) Facies, characterized by clast-rich/clast-poor contorted and chaotic sediments with a claystone to sandstone matrix. DF deposits exhibit scours at the base. DF events are locally separated by claystones with silt laminations that present cross and/or planar laminations. Shipboard this corresponded with lithostratigraphic Unit IV, which extended from 459.4-593.8 mbsf. The interval from 575 to 785 mbsf (which includes shipboard lithostratigraphic units V, VI and VII) is characterized by an alternation of two facies (F1 and F2). These facies are explained in detail in the main text of the article, and are composed of an alternation of glacial green claystones with thin silt laminae with planar and cross-bedded laminations presenting different traction and suspension structures (F1). These are interbedded with interglacial highly bioturbated, thicker pale-brown, silty-claystones (F2). This alternation is disrupted from 710 to 730 mbsf by a MTDs facies (i.e., slumps). From 785 to 879 mbsf (within shipboard lithostratigraphic unit VIII) slump facies prevail. Slump facies consist predominantly of



allochthonous stratified and chaotic sediments of similar lithology to F1 and F2. The interval from 879 to 895 corresponds with lithostratigraphic unit IX described on shipboard. This unit comprises sediments from the middle Eocene and the earliest Oligocene consisting of bioturbated purple silty claystones with some laminations. Erosion/non-deposition surfaces are present within this facies. They are intercalated with coarser green micaceous (very shiny) (sandy) silty-claystone. Laminations with ripples and pinstripe and cross-lamination are also observed. This facies are intercalated with MTD facies composed of these same sediments. The interval between 895 and 896 mbsf is within shipboard lithostratigraphic unit X and is characterized by a lithological change to Eocene green sands Facies.

Site U1356  
IODP Exp. 318  
Cores 11-41R



**Figure S3.1.** Detailed sedimentary log from IODP U1356 Site U1356 exp. 318 from 11R to 95R (95.4 to 896 mbsf).



Site U1356  
IODP Exp. 318  
Cores 42-95R

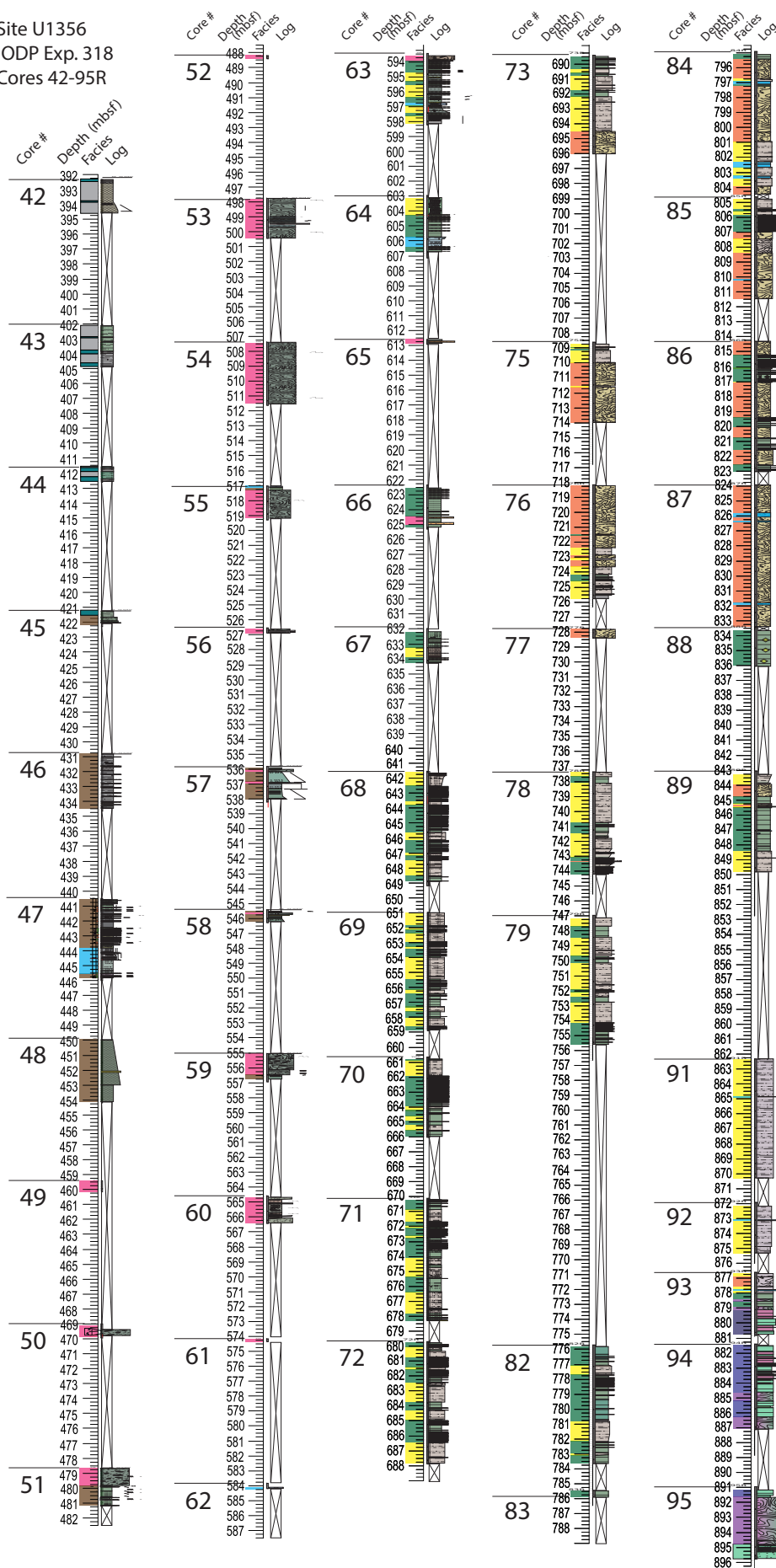


Figure S3.1. Cont.

## LEGEND U1356 CORES 11R-95R

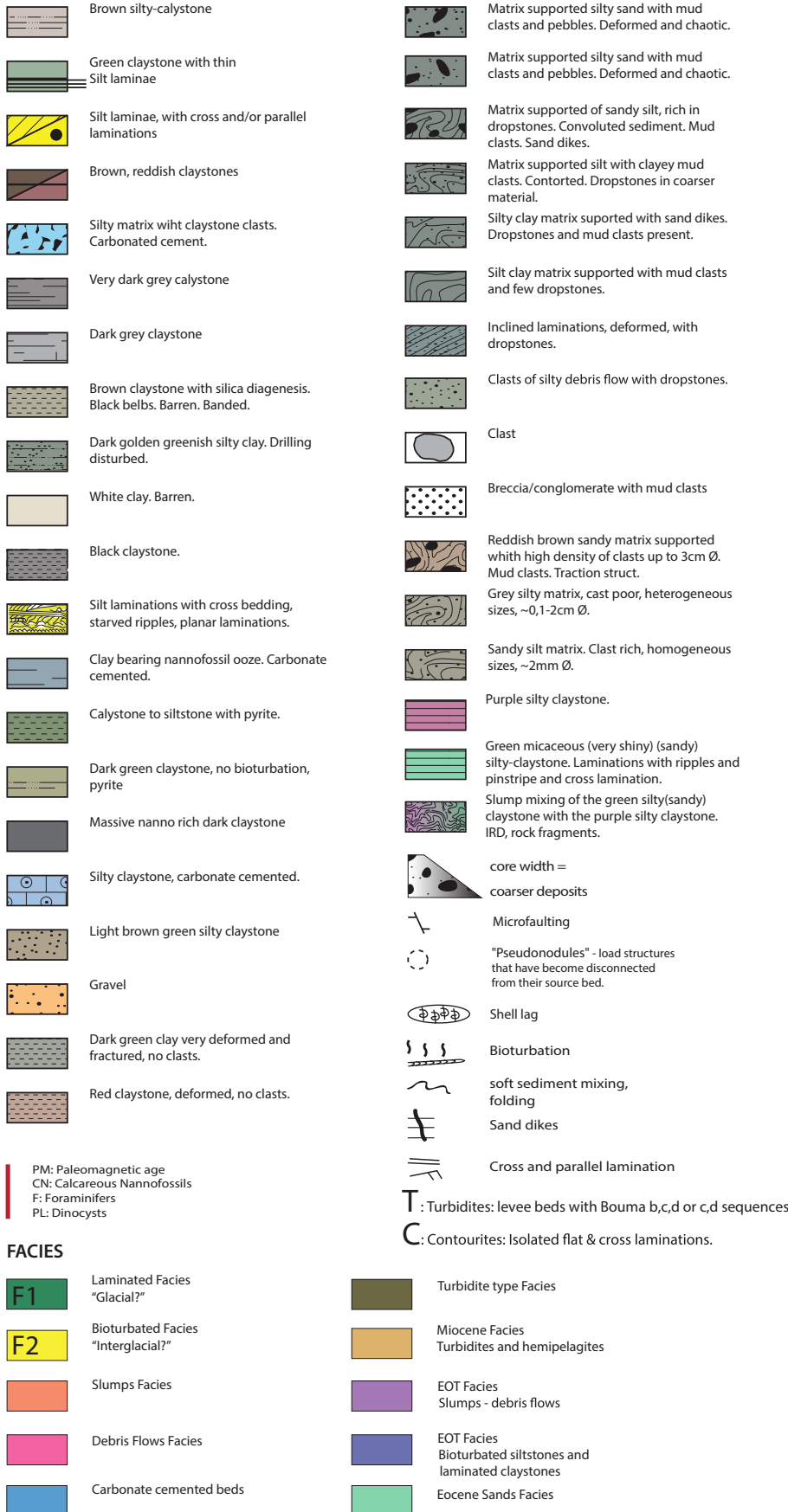
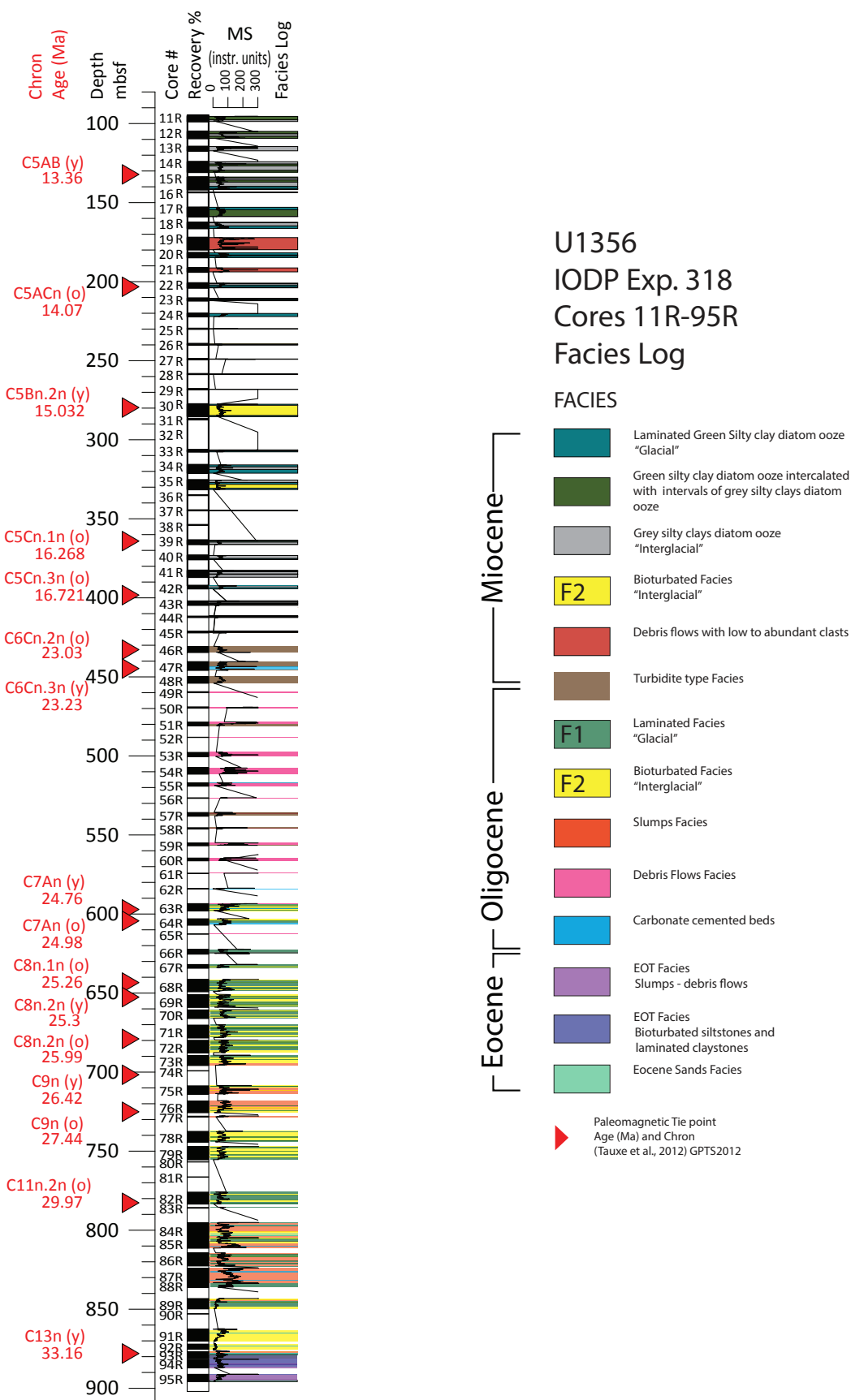


Figure S3.1. Cont.







**Figure S3.2.** IODP Site U1356 Exp. 318 from 11R to 95R (95.4 to 896 mbsf). Schematic Facies Log with plotted Magnetic Susceptibility (MS). Paleomagnetic tie points are also present. Ages from Tauxe et al. (2012) are updated to GPTS 2012.

### S3.2. ASTROCHRONOLOGIC ANALYSIS

We followed the procedures published by Meyers et al. (2012) and Wanlu Fu et al. (2016) in order to generate spectral analysis on our data.

We selected Zr/Ba ratio as we consider this ratio to integrate and summarize the processes shaping our facies model, showing clearly the marked cyclicity present.

Data preparation:

In order to remove the long-term trend data series were detrended, outliers were removed, and sampling interval was linearly interpolated in order to resample the dataset to an even spacing of 2cm. Average sedimentation rates between the two paleomagnetic tie end points were linearly interpolated and is 5cm/kyr for the investigated interval. Age model is calibrated to the Geologic Timescale 2012 (GPTS 2012, Table 3.1).

For initial cyclostratigraphic analyses, we used Anlyseries software (Paillard et al., 1996). We used B-Tukey method in order to preliminary assess the cyclicity on the record on a depth scale. A clear and statistically significant cyclicity is observed in Ba, Zr and Zr/Ti every 2m (0.5 cycles/m), and less significant ones but also reliable at 4.67m (0.21 cycles/m), and 1m (0.94 cycles/m) (Fig. S3.4). On the basis of the calculated sedimentation rate, the cycles above (0.5 cycles/m) account for 40 Kyr. After determining the significant frequency, we filtered the Zr/Ba dataset (at depth domain) at 0.5 frequency in order to extract the wavelet and compare it with the obliquity solution for that time-period (Laskar et al., 2004) and by improving the dissipative contributions, in particular in the evolution of the Earth-Moon System. The orbital solution has been used for the calibration of the Neogene period (Lourens et al. 2004). Cycles can be correlated one to one with a total of 23 cycles of obliquity (Fig. S3.4). After initial analysis we proceed with Astrochron Evolutive Average Spectral Misfit method (Meyers et al., 2012). Astrochron package is prepared to resolve unevenly sampled series, and changing sedimentation rates.

Time-frequency analysis:

Evolutive Harmonic Analysis (EHA; Fig. S3.4) of the prepared Zr/Ba (in depth scale) data provides an evaluation of changes in the spectral features through depth/time. EHA employs five  $3\pi$  DPSS tapers, and a moving window of 15 m. Significant frequencies are retrieved for further study.

Astrochronologic testing:

The Evolutive Average Spectral Misfit method (Meyers, 2014) (E-ASM; five  $3\pi$  tapers; searching to the mean Nyquist frequency of 1.504221 cycles/m) was used to test a range of plausible timescales and simultaneously evaluate the reliability of the presence of astronomical cycles. The ETP (eccentricity, obliquity and precession) target periods were determined from La04 (Laskar et al., 2004) using the interval from 25.0 – 26.4 Ma: 400.00 kyr (E1), 131.58 kyr (E2), 99.01 kyr (E3), 40.49 kyr (O1), 32.79 kyr (O2),



20.70 kyr (P1), 19.69 kyr (P2) and 17.06 kyr (P3).

The Zr/Ba MTM Harmonic F-test results of the EHA (Fig. 3.6) are evaluated using a grid of 100 sedimentation rates spanning 3 cm/Kyr to 10 cm/Kyr. This range of sedimentation rates encompasses the long-term average sedimentation rate for the section based on available paleomagnetic constraints with a total duration of 0.71 Ma and a total stratigraphic thickness between 30 – 40 m given the range of plausible correlation horizons for the section. We interpolate an average sedimentation rate of 5 cm/Kyr.

All spectral peaks above 90% F-test confidence level were evaluated using E-ASM, and Monte Carlo significance testing utilizing 10,000 simulations. Results with Null Hypothesis Significance Levels (Ho-SL) less than or equal to 0.1% were identified (Fig. S3.5).

Astronomical tuning:

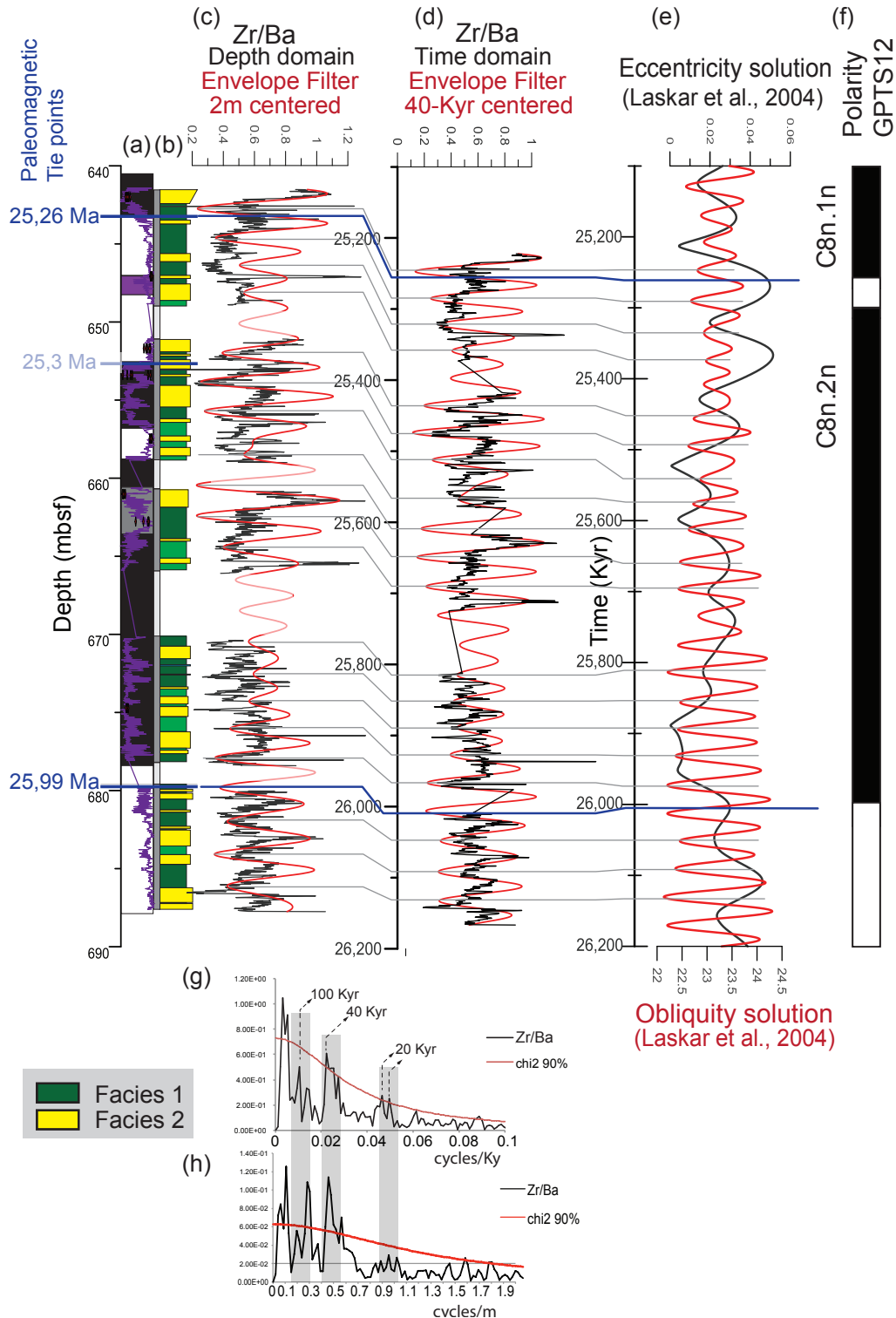
Frequency domain minimal tuning (Meyers et al., 2001) is used for tracking obliquity in EHA harmonic F-test for the calibrated periods and sedimentation rates. Spatial frequencies are afterwards converted to sedimentation rates using average period of 41 Kyr (Fig. S3.6) and a time-space map is created with a new calibrated time series. Time series is afterwards anchored to our paleomagnetic tie points (Fig. S3.7).

MTM and EHA results on the tuned data provide further evidence of the presence of precession, obliquity and eccentricity cycles, supporting the obliquity tuning (Fig. S3.8).

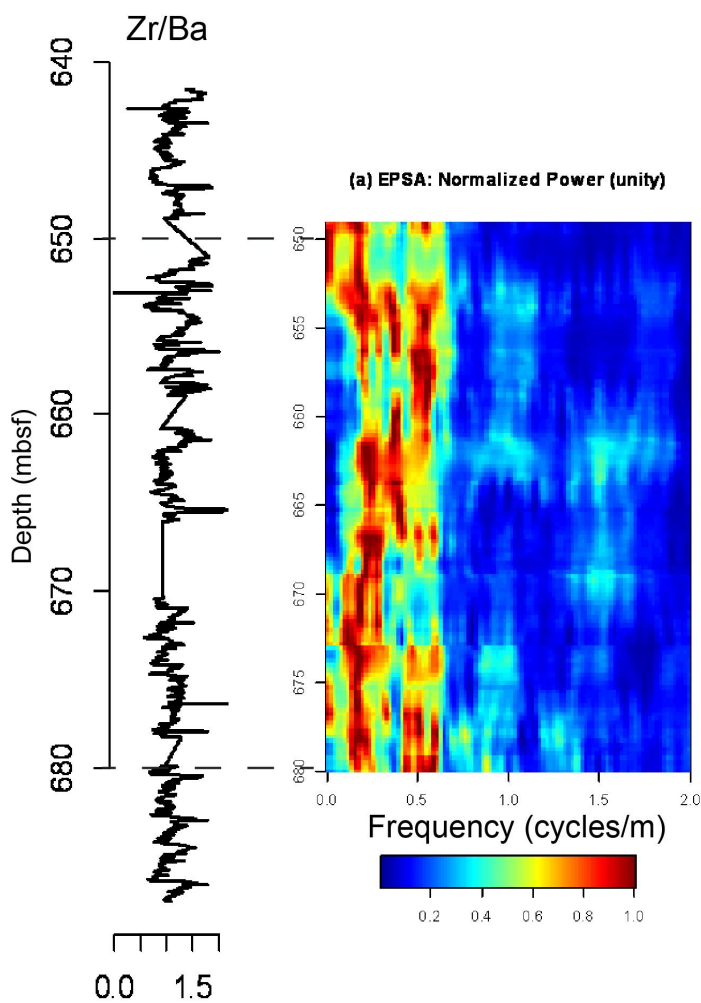
Significant Harmonic F-test peaks that achieve 95% CL are: 102.77 Kyr, 69.26 Kyr, 40.84 Kyr, 30.05 Kyr, 22.27 Kyr, 20.68 Kyr (Fig. S3.8).

The new time-scale is used to tune the other records (Zr/Ti; Ca/Ti; MS; Ba). EHA is then applied to tuned records in order to see the frequencies that appear (Fig. S3.9).

Orbital frequencies were tested in each core section individually in the Zr/Ba dataset in the depth scale in order to assure that cyclicity is not an artefact related to the gaps in the series (Fig. S3.10).

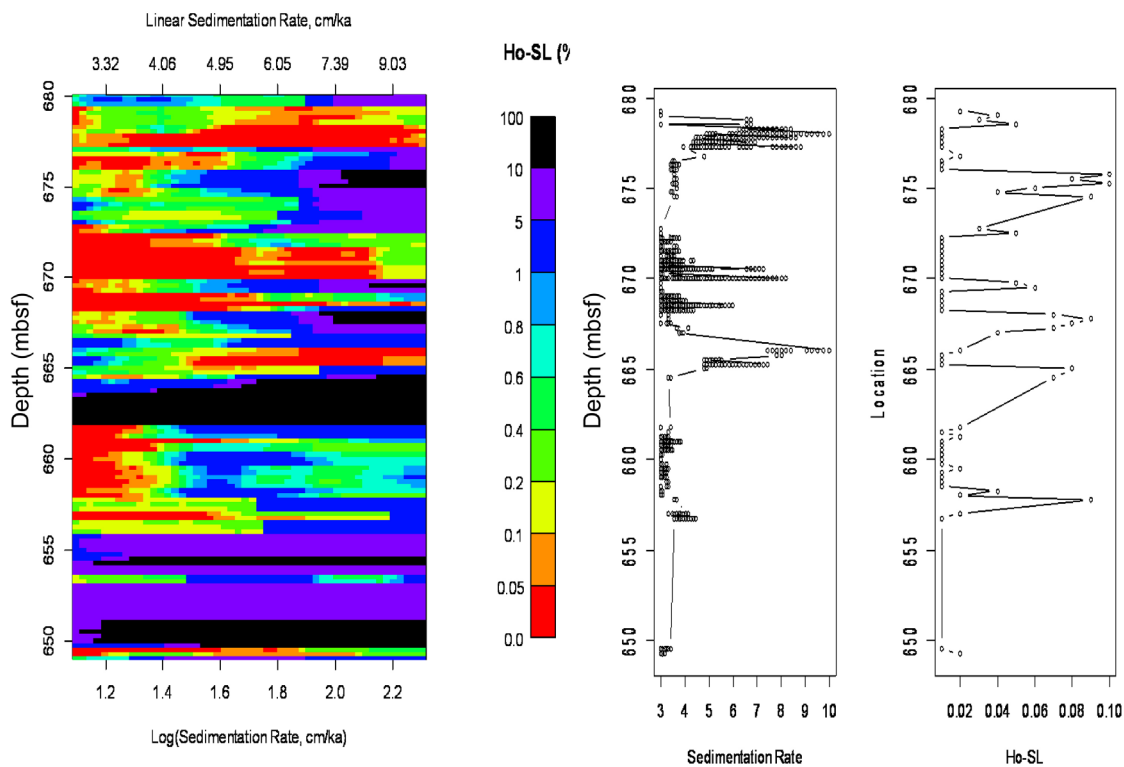


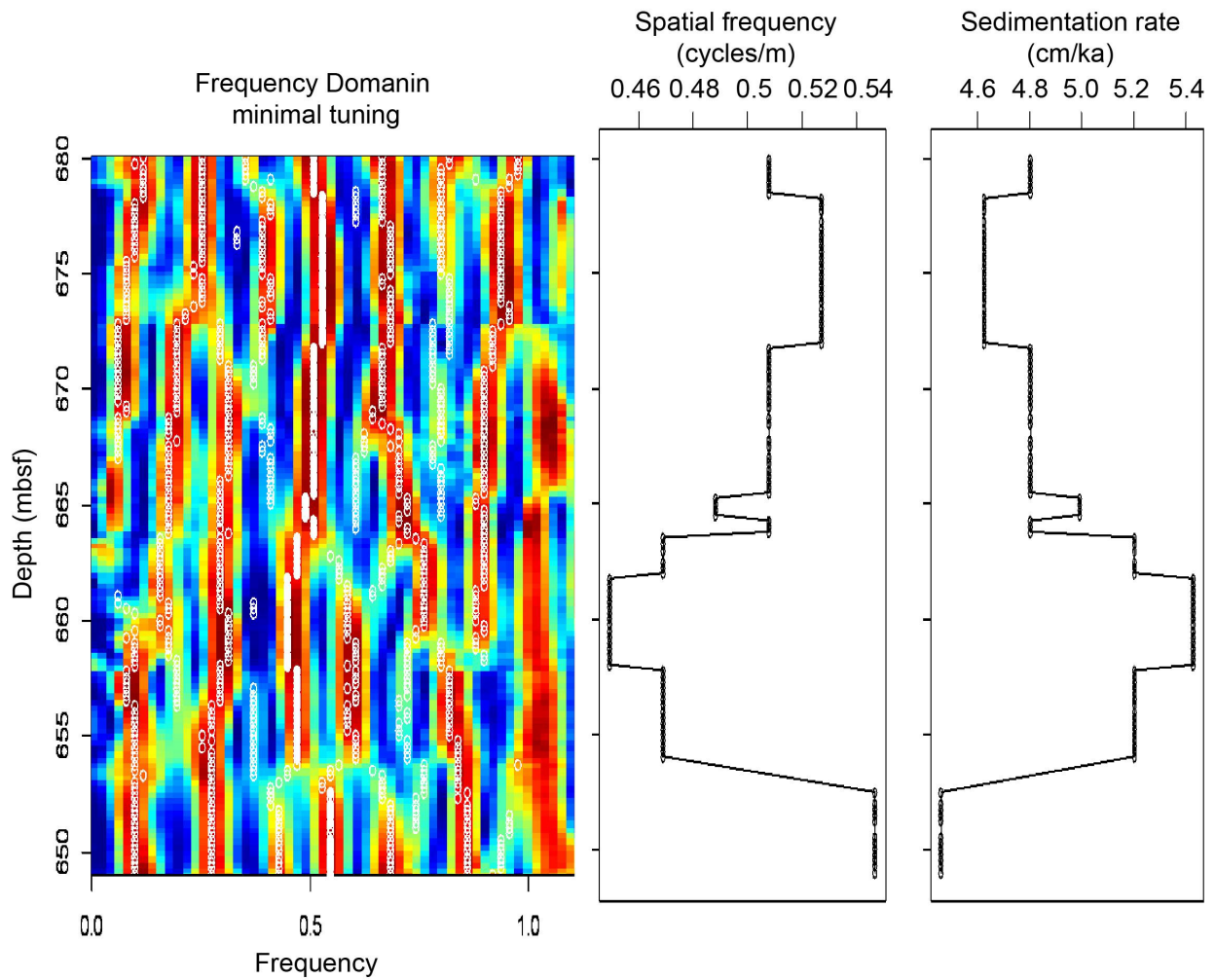
**Figure S3.3.** Tuning of Zr/Ba to the obliquity solution. Zr/Ba (in the depth domain) is tuned to the obliquity solution cycle by cycle. Tuning of Zr/Ba record (in depth scale) and bandpass filtering were done in Analseries (Paillard et al., 1996). (a) Magnetostratigraphic chrons (Tauxe et al., 2012); (b) schematic stratigraphic log; (c) Zr/Ba data in depth scale with the envelope filter centred at 2m (in red); (d) Zr/Ba data in time scale using paleomagnetic tie points and a linear sedimentation rate, with the envelope filter centred at 40 Kyr (in red); (e) Eccentricity and obliquity solutions (Laskar et al., 2004); (f) Polarity chrons from the GPTS2012; (g) Blakmann-Tukey in the Zr/Ba data in time domain (not tuned), with statistical (>90%) periodic peaks in the 40 Kyr and 20 Kyr periodicities; (h) Blakmann-Tukey in the Zr/Ba data in depth domain, with statistical (>90%) periodic peaks.



← **Figure S3.4.** Evolutive Harmonic Analysis (EHA) in depth scale Zr/Ba data. The detrended Zr/Ba data is linearly interpolated to a constant sample spacing of 2 cm prior to analysis. EHA employs with 3DSDP tapers and a 15 window.

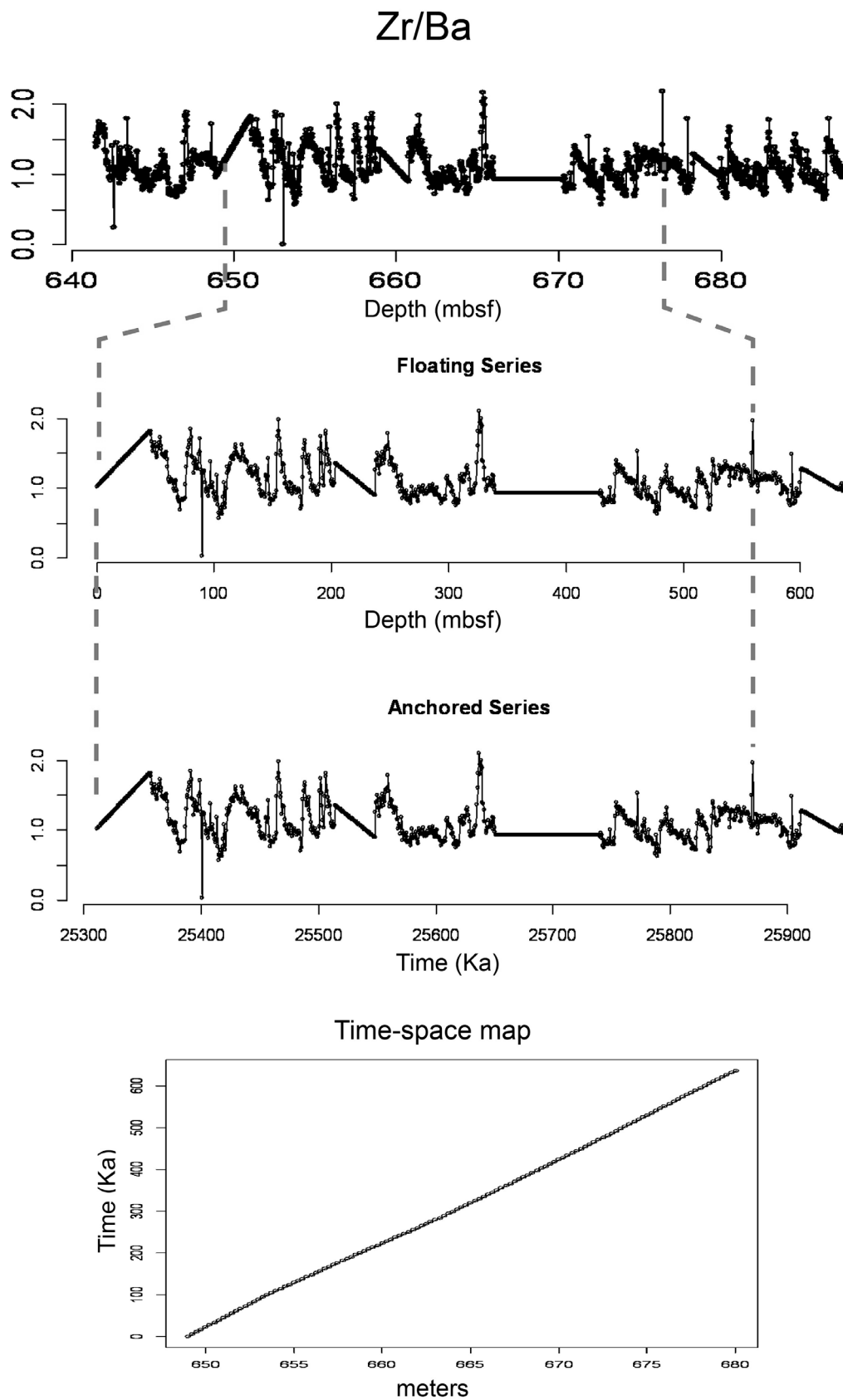
↙ **Figure S3.5.** Astrochronologic testing using evolutive ASM analysis. (a) Evolutive ASM plot, displaying Ho-SL values (90% confidence level), across sedimentation rates spanning 3 to 10 cm/kyr. (b-c) Summary of evolutive ASM results, using a threshold Ho-SL value of 0.1 to identify optimal sedimentation rates. (b) displays each sedimentation rate, and (c) displays the associated Ho-SL.



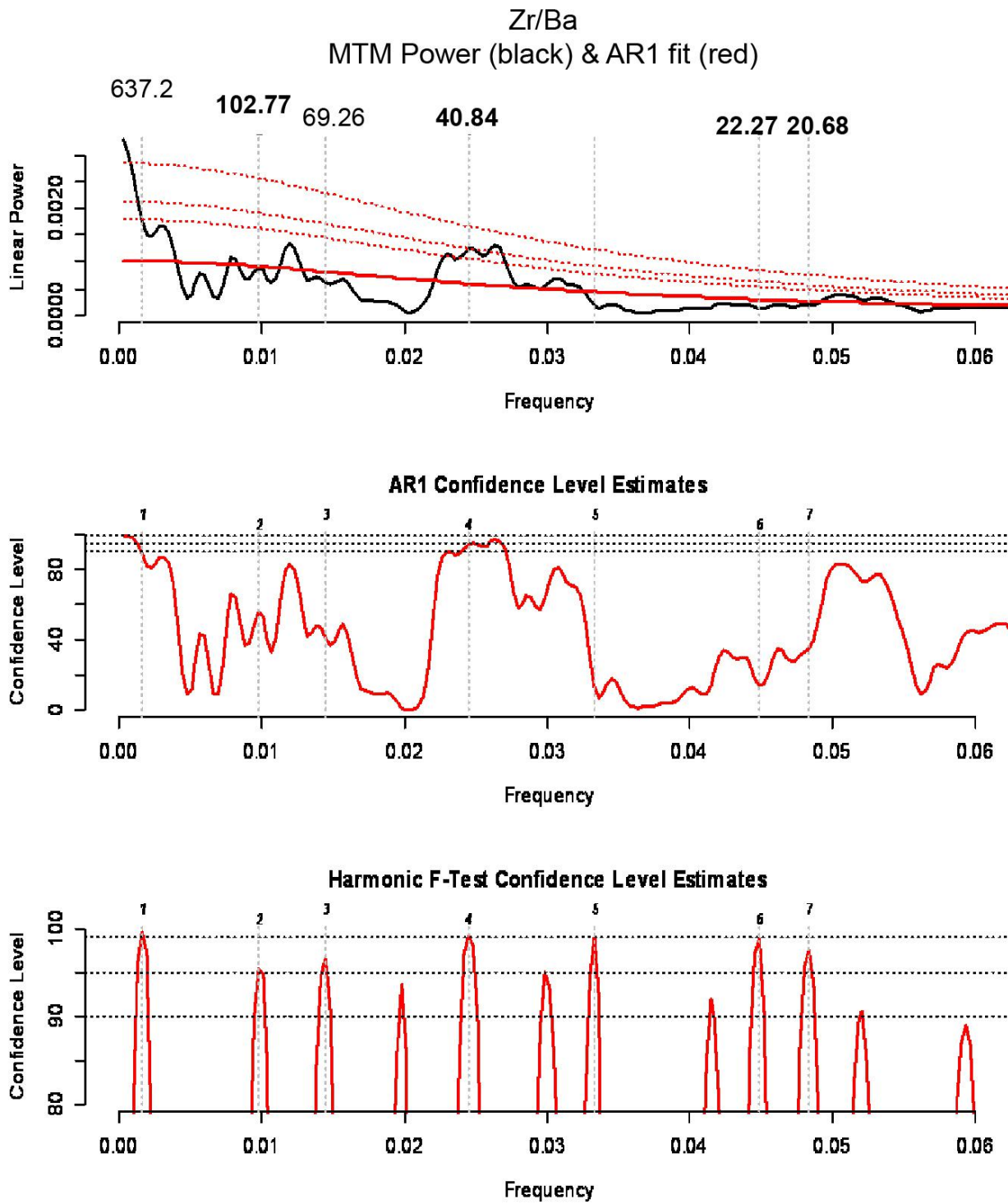


**Figure S3.6.** Frequency tracking for minimal tuning. The obliquity cyclicity (41 Kyr) can be tracked in the EHA harmonic F-test confidence level results by setting the  $f_{min}=0.01$  and  $f_{max}=0.4$  based on the spatial frequencies calculated by EASM results. Calculated sedimentation rates based on spatial frequency tracking.





**Figure S3.7.** Tuned record and depth-time plot derived by frequency domain minimal tuning to the obliquity cycle. The grey dotted lines show the correlated depth and time.

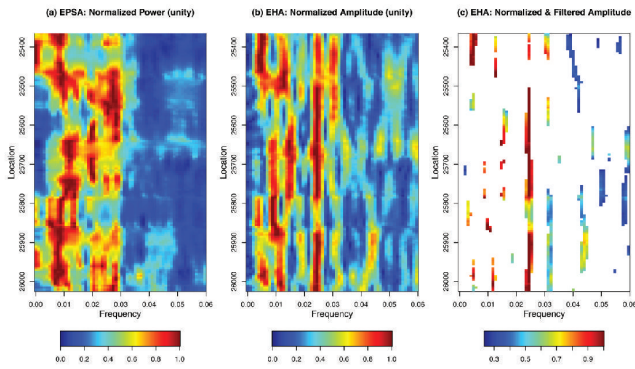


**Figure S3.8.** MTM results of the tuned data with the major periods in kyr. These peaks achieve the 95% confidence level for both the MTM harmonic F-test and the AR1 red noise model or the AR1 noise model only.

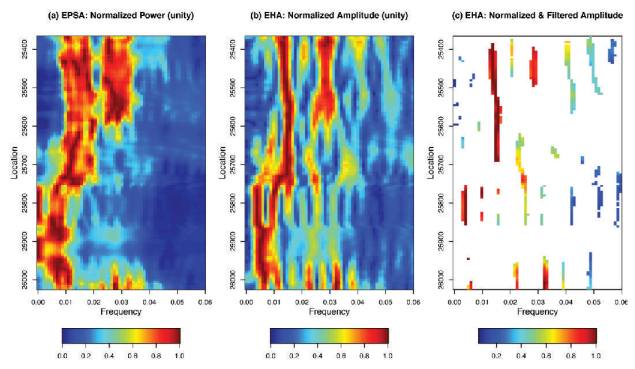




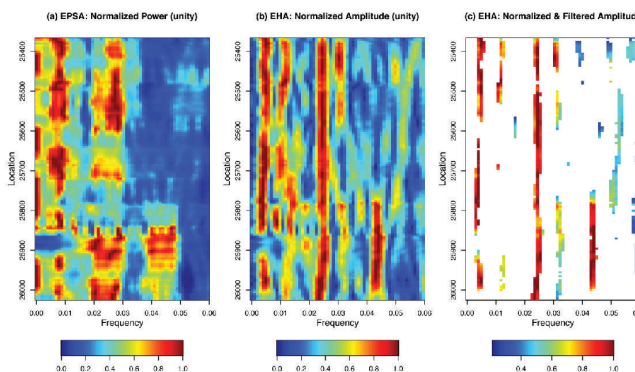
Zr/Ba Tuned  
EHA with 300win



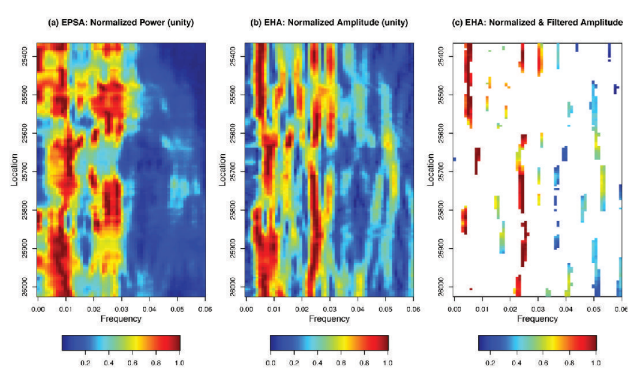
MS Tuned  
EHA with 300win



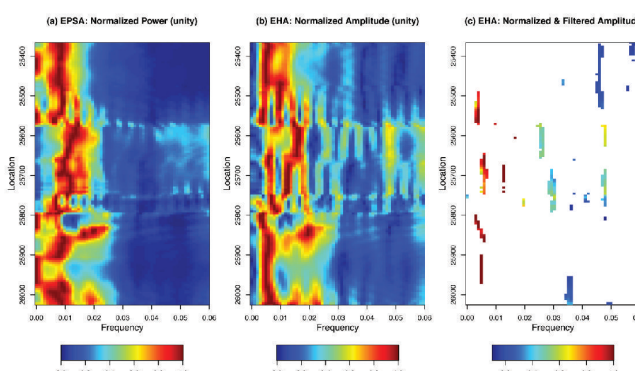
Zr/Ti Tuned  
EHA with 300win



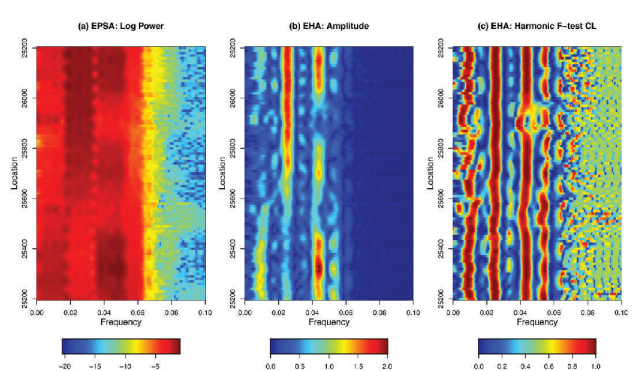
Ba Tuned  
EHA with 300win



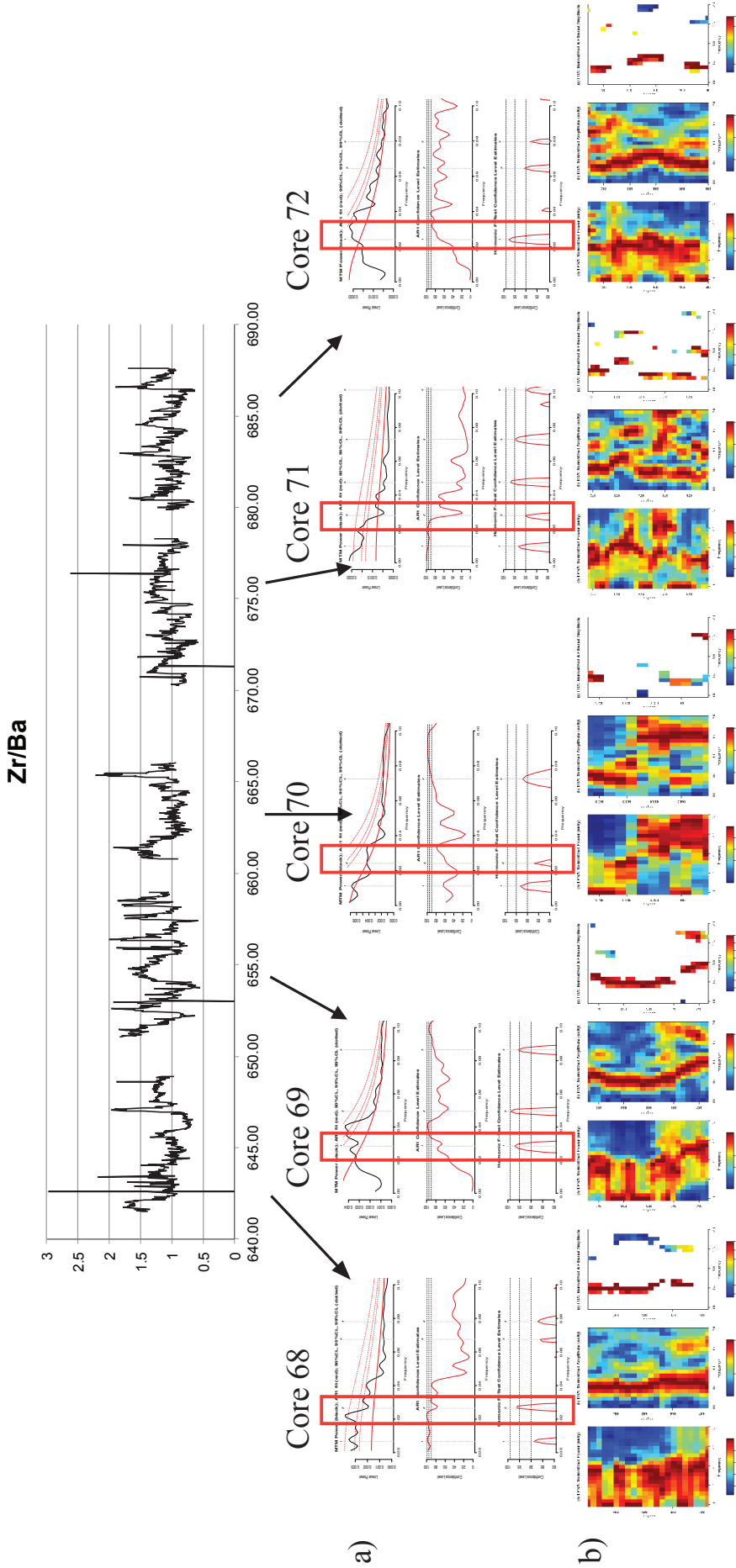
Ca/Ti Tuned  
EHA with 300win



ETP Solution  
EHA with 200win



**Figure S3.9.** Following Zr/Ba tuning (a), MS (b), Zr/Ti (c), Ba (d), and Ca/Ti (e) have been tuned. EHA analysis was applied in order to depict the frequencies. EHA on the ETP solution is also added in order to compare the resulting frequencies (f).



**Figure S3.10.** Spectral analysis over individual core sections for the Zr/Ba dataset on the depth scale. The 0.5 cycle/m (that counts for obliquity) achieve >90% significance in all cores except for core 70 where smaller frequencies seem to dominate. Changes in peak frequency seem to be dominated by slightly changes in sedimentation rate. Each core was analysed by a) MTM and b) EHA with a 5 m window.

### S3.3. R\_ANALYSIS CODE CREATED TO PRODUCE THE ASTRONOMICAL ANALYSIS IN THE LATE OLIGOCENE

```
#####
# (1) LOAD THE R-PACKAGE 'ASTROCHRON'
#####
library(astrochron)

#####
# (2) READ DATA FILE
#####
# Read the carbon isotope data from file 'CarbonIso.csv'
dat<-read(d=0)

#####
# (3) PREPARE TIME SERIES
#####
# The median sampling interval of the prepared data is 0.02 m, and the mean
sampling interval is 0.023 m
# Resample Zr/Ba data to 2.5 cm sampling grid, using piecewise linear
interpolation
ZrBa<- linterp(dat,dt=0.025)

#####
# (4) PERFORM EVOLUTIVE HARMONIC ANALYSIS
#####
mtmML96(ZrBa,xmax=2,pl=2,siglevel=.90,sigID='T')
mtm(ZrBa,xmax=2,pl=2,sigID='T')
# Use a 12 meter window, with five 3pi DPSS tapers.
# * Search up to the mean Nyquist frequency of 1.504221 cycle/m
# * Output F-test confidence level estimates for evolutive average spectral misfit (ASM) analysis.
prob=cha(ZrBa,fmax=2,output=4,genplot=4,pl=2,ydir=-1,win=15)

#####
# (5) IDENTIFY TARGET PERIODS FOR AVERAGE SPECTRAL MISFIT ANALYSIS
#####
# Obliquity and precession terms from Laskar et al. (2004)
```

```

model=etp(tmin=25000,tmax=26400)
cha(model,win=200,fmax=0.1,sigID='T',pad=10000)
mtm(model,xmax=0.1,pl=2,sigID='T')

#####
# (6) EVOLUTIVE AVERAGE SPECTRAL MISFIT ANALYSIS
#####
# Set up analysis parameters:
# * Astronomical target frequencies are determined from Laskar et al. (2004)
target=c(1/404,1/124,1/95,1/54,1/41,1/29,1/23,1/19)
#Ray=(1/N*Ax) on N= number of points in data series and Ax= sampling resolution of data series
# * Use average sampling interval to estimate the Nyquist frequency (for 1/(0.025m sampling * 2) Fny-
q=(1/2*Ax)
rayleigh=0.0217
nyquist=20
# * Average sedimentation rates is around 5cm/Kyr
# The total duration between the youngest and oldest age is 0.71 Ma +/- ? Ma.
# Given the range of plausible correlation horizons into the LO section,
# the total stratigraphic thickness can range from 30 m to 40 m.
# Execute evolutive ASM analysis. This will take 10-20 minutes to complete.
res1=eAsm(prob,target=target,rayleigh=rayleigh,nyquist=nyquist,sedmin=3,sedmax=10,num-
sed=100,siglevel=0.95,iter=10000,output=4)
# Track Ho-SL minima from evolutive ASM results
# * Identify those results with Ho-SL less than or equal to 0.1%
pl(1); eAsmTrack(res1[1],threshold=0.1,ydir=1)

#####
# (7) EXAMINE SELECTED SPECTRA AND ASM-CALIBRATED PERIODS
#####
# F-test CL spectrum from 43.965 m
# Calculate calibrated periods in kyr (observed)

prob_674.53=extract(prob,get=674.53)
1/(peak(prob_674.53,level=0.9)[2]*0.025)

prob_670.03=extract(prob,get=670.03)
1/(peak(prob_670.03,level=0.9)[2]*0.025)

prob_656.03=extract(prob,get=656.03)

```



```
1/(peak(prob_656.03,level=0.9)[2]*0.025)
```

```
prob_661.03=extract(prob,get=661.03)
```

```
1/(peak(prob_661.03,level=0.9)[2]*0.025)
```

```
#####
```

```
# (8) ASTRONOMICALLY-TUNE Zr/Ba DATA USING
```

```
# FREQUENCY-DOMAIN MINIMAL TUNING (Meyers et al., 2001)
```

```
#####
```

```
# Track obliquity in EHA harmonic F-test confidence level given the ASM-calibrated periods
```

```
# Track obl term on the basis of the ASM calibrated sedimentation rates
```

```
# Note that the Rayleigh frequency is 0.0217 cycles/m
```

```
freqs=trackFreq(prob,fmin=0.023,fmax=1,threshold=0.9)
```

```
# convert spatial frequencies to sedimentation rates using average period of 41 kyr
```

```
sedrate=freq2sedrate(freqs,period=41,ydir=-1)
```

```
sedrate
```

```
# View the calibrated sedimentation rates on depth sedrate
```

```
# Integrate the sedimentation rate curve to create a time-space map
```

```
time=sedrate2time(sedrate)
```

```
# View the calibrated time series
```

```
time
```

```
# The duration of specific interval can be calculated by the output of sedrate and time
```

```
# Tune the ZRBA series using the time-space map
```

```
tuned=tune(ZrBa,time)
```

```
#####
```

```
# (9) PREPARE TUNED SERIES AND EVALUATE SPECTRA
```

```
#####
```

```
# Interpolate the tuned series. Median sampling interval is 0.5 kyr and mean is 0.55 kyr.
```

```
# Will use AR1 test; use a conservative interpolation to avoid introducing serial correlation.
```

```
datatuned=linterp(tuned,dt=0.6)
```

```
# Perform MTM analysis on the tuned series
```

```
spec=mtm(datatuned,tbw=2,pl=2,siglevel=0.95,xmax=0.06,output=1,sigID=T)
```

```
# identify periods of AR1 CL peaks that acheive the 90% AR1 CL
```

```
1/peak(cb(spec,c(1,4)),level=95)[2]
```

```
# Perform EHA on the tuned series
```

```
ZrBa_final<-read(d=0)
```

```
pwr=eha(datatuned,fmax=0.06,output=2,ydir=-1,win=250)
```

```
plotEha(pwr,pl=1,ydir=-1)
```

```
#####
# (10) BANDPASS FILTERING AND ECCENTRICITY AMPLITUDE
MODULATION ANALYSIS
#####
# Perform bandpass-filtering on the tuned series to extract short eccentricity (E2+E3)
e23_data=bandpass(datatuned,flow=0.006,fhigh=0.011,xmax=0.02)
# Perform bandpass-filtering on the eccentricity terms from Laskar et al. (2011)
model=getLaskar("1a10d")
model=iso(model,xmin=25000,xmax=26400)
e23_model=bandpass(model,flow=0.006,fhigh=0.011,xmax=0.02) #short-term
eccentricity
# Evaluate the alignment between the amplitude envelope of the filtered short-term eccentricity and the
filtered long-term eccentricity
am_data=hilbert(bandpass(datatuned,flow=0.006,fhigh=0.011))
pl(1)
plot(s(am_data),type="l",ylim=c(-3,3))
lines(s(e1_data),col="red")

#Anchor the tuned data to a tie point from the time scale where 606.226 is equivalent to 678.78
ZrBa_tuned2=anchorTime(datatuned,606.2262,25990,flipOut=T,timeDir=2)

write.csv(ZrBa_tuned2,file="ZrBa_tuned_at_606.226to25990.csv") #Save data

Tune other data series and analyse with EHA:

Ba<-read(d=0)
Ba_tuned=tune(Ba,time)
cha(linterp(Ba_tuned,dt=0.5),fmax=0.06,output=2,ydir=-1,win=150)
Ba_tuned=anchorTime(datatuned,678.9,25990,flipOut=T,timeDir=2)

MS<-read(d=0)
MS_tuned=tune(MS,time)
cha(linterp(MS_tuned,dt=0.5),fmax=0.06,output=2,ydir=-1,win=150)
MS_tuned=anchorTime(datatuned,678.9,25990,flipOut=T,timeDir=2)
```





# Chapter 4

Ice sheet and oceanic configurations in the  
Eastern Wilkes Land margin during the  
late Oligocene to Miocene transition

---





## CHAPTER 4

# ICE SHEET AND OCEANIC CONFIGURATIONS IN THE EASTERN WILKES LAND MARGIN DURING THE LATE OLIGOCENE TO MIOCENE TRANSITION

### 4.1. INTRODUCTION

Today the section of the East Antarctic Ice Sheet (EAIS) that drains through the Wilkes Subglacial Basin (WSB) is grounded on land that is below sea level (marine-based) (e.g., Fretwell et al., 2013). This has important implications because marine-based ice sheets on a landward sloping continental shelf are more sensitive to changes in oceanic circulation and temperature (Colleoni et al., 2018; Morlinghem et al., 2019). A recent study summarizing four decades of Antarctic ice sheet mass balance cautions about enhanced glacier flow in areas of West and East Antarctica that are closest to warm, salty, subsurface circumpolar deep water (CDW) (Rignot et al., 2019). This evolution is consistent with the contraction of the westerlies winds in polar areas forcing more CDW on the continental shelf, which reaches the base of the ice sheet through deep troughs carved on the sea floor by former ice streams (Spence et al., 2017). Recent studies have now linked the intrusion of warm waters to past instabilities of the Antarctic cryosphere (e.g., Sangiorgi et al., 2018; Etourneau et al., 2019). Although loss of ice from the Antarctic Peninsula and West Antarctic Ice Sheets has been widely reported, recent studies point to sectors from the EAIS (i.e., in front of the Wilkes Subglacial Basin and Aurora Basin) as a potential major contributors to multi mm sea level rise (Rignot et al., 2019).

The geological records from vulnerable areas of the EAIS such as the Wilkes Subglacial Basin (WSB) are key to providing insights into the behavior of the cryosphere and coeval oceanographic configurations during past warm periods. Paleotopography reconstructions in WSB sector of the EAIS, show it to be above sea level around the Eocene-Oligocene boundary (34 Ma) and to have deepened some time before 14 Ma (Paxman et al., 2018; 2019). Moreover, based on the study of sedimentary accumulation offshore the WSB and 3-D flexural modeling, Paxman et al. (2019) hypothesize this deepening to have taken place sometime during the Oligocene. In the Ross Sea sector the transition from continental to marine-based ice sheets took place at around 24 Ma (Levy et al., 2019). At this time the ice sheet becomes subject to the influence of the ocean (Levy et al., 2019). Constraining the timing of the shift from continental-based to marine-based ice sheets in the eastern Wilkes Land margin is therefore relevant to better understand the response of the ice sheet to past warm intervals. The Oligocene-Miocene periods are in addition important to this discussion because atmospheric CO<sub>2</sub> concentrations also decreased during this period between 600 and around 400 parts per million (ppm) (Beerling et al., 2011).

Site U1356 drilled during the Integrated Ocean Drilling Program (IODP) Expedition 318 recovered



sediments from the continental rise dated from the Eocene to Pliocene (Escutia et al., 2011). We have integrated a detailed facies analyses with physical properties and XRF discrete geochemical data to reconstruct late Oligocene to early Miocene ice sheet and ocean dynamics. In addition, we provide insights into the timing when the EAIS in this sector became marine-based following erosion and over-deepening of the WSB.

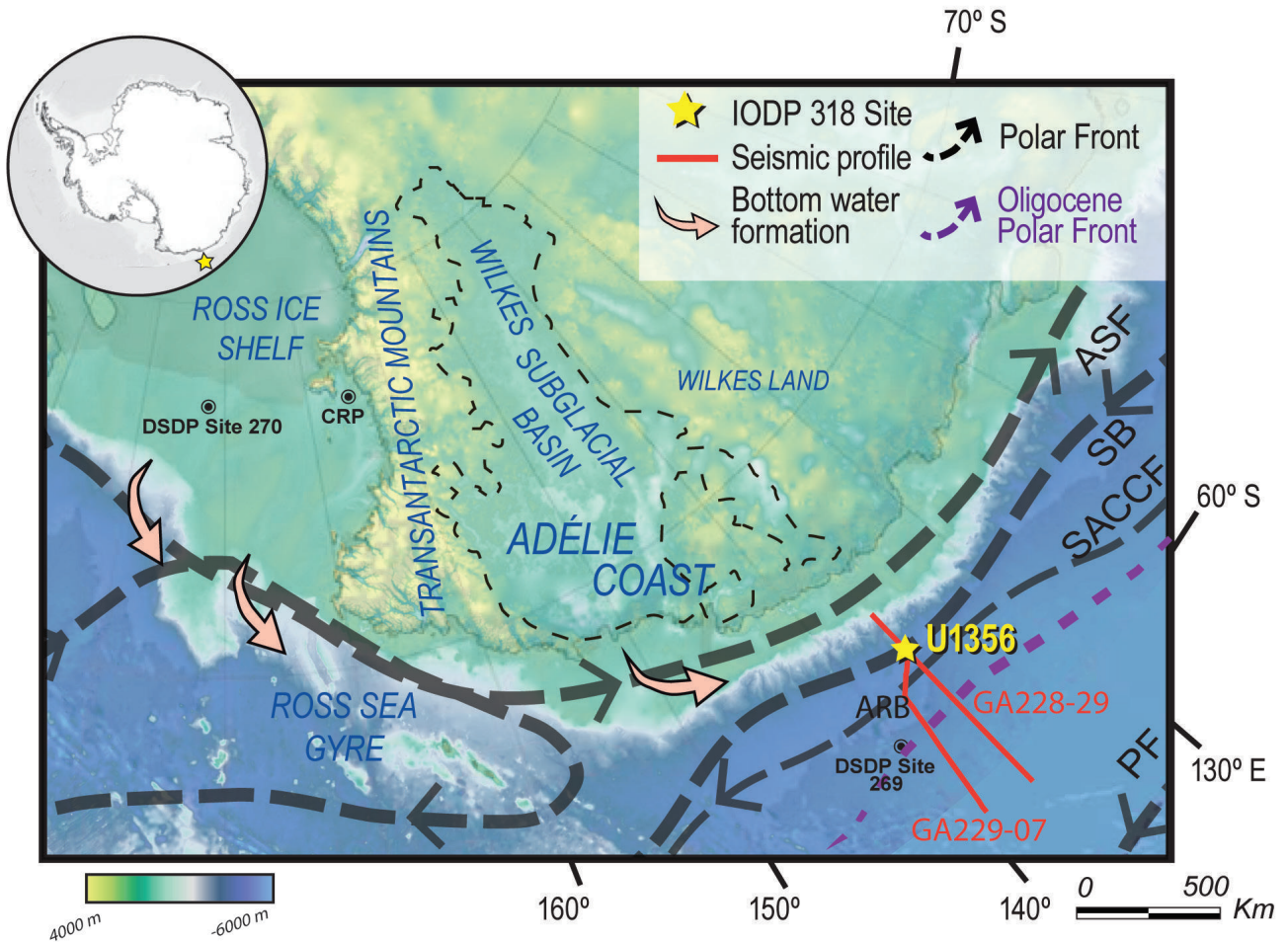
## 4.2. MATERIALS AND METHODS

### 4.2.1. IODP SITE U1356

Integrated Ocean Drilling Program (IODP) Expedition 318 Site U1356 (63° 18.61380'S, 135° 59.9376'E, 3992 m water depth) is located off the eastern Wilkes Land Coast. The drilling penetrated 1006.4 mbsf (meters below sea floor) into the flank of a levee deposit on the lower continental rise (Escutia et al., 2011, 2011b; Fig. 4.1). Total core recovery was 35% and recovered sediments were dated between the early Eocene and the Pliocene. Sediments from Site U1356 were described and analysed shipboard on the basis of lithofacies characterization, physical properties, geochemistry, biostratigraphy, and paleomagnetism (Escutia et al., 2011b).

The age model for Site U1356 was established on the basis of the magnetostratigraphic datums constrained by biostratigraphic control using marine diatom, radiolarian, calcareous nanoplankton, and dinocyst (Escutia et al., 2011b; Tauxe et al., 2012) updated to GPTS 2012 (Bijl et al., 2018). Based on this model, sediments in this study are dated between the late Oligocene and the early Middle Miocene. A hiatus spanning ~ 5.5 Myr is placed at core 45R-1 at 30 cm (421.7 m bsf) (Bijl et al., 2018; Escutia et al., 2011b; Tauxe et al., 2012).

In this study, we analyse the sediments between 690 and 392 mbsf that on shipboard were included within lithostratigraphic units V to III, spanning the late Oligocene to the middle Miocene (Escutia et al., 2011b). Since Expedition 318, the lower part of Unit V (690 to 640 mbsf) was studied at high-resolution by Salabarnada et al. (2018), who interpreted the facies in this interval to result from bottom-current reworking of the sediments deposited by gravity flows and hemipelagic settling during glacial and interglacial cycles, respectively. In addition, these sediments provided insights into changing paleoceanographic conditions linked to frontal zone migrations during glacial and interglacial cycles (Salabarnada et al., 2018; Bijl et al., 2018; Hartman et al., 2018). Furthermore, particle grain size analysis and major and trace elements analyses were conducted in the interval of our interest by Passchier et al. (2018). Passchier et al. (2018) proposed a new sequence stratigraphic model to explain high-latitude stratigraphy. They document that during the early Oligocene and the mid-Miocene large ice volumes were present in the Wilkes Land, recorded in the margin as cyclic sedimentation of hemipelagites and turbidites/contourites, and conclude that those indicate the onset of ice growth phases during high sea levels, due to GIA accommodation. During the late Oligocene, small ice volume phases or interglacials were composed by the presence of



**Figure 4.1.** Location of IODP 318 Site U1356 (Escutia et al., 2010) on the Adélie coast continental rise. Bed topography from IBSCO (Arndt, JE et al., 2013). Schematic position of the different water masses at present and locations of Antarctic Bottom Water formation (Orsi, 1995) are indicated. Seismic reflection profiles used in this work are shown. ASF: Antarctic Slope Front; SB: Southern Boundary; SACCF: Southern Antarctic Contour Current Front; ARB: Adélie Rift Block.

sandy debris flows in the Wilkes Land margin, and reported them to represent the onset of ice sheet minima under low sea levels (Passchier et al., 2018).

Sediments within Unit IV (459.4 to 593.8 mbsf) are characterised by multiple intervals of contorted diamictites and abundant gravel-bearing lithologies. Interbedded between the diamictite intervals are claystones, siltstones and also some carbonate-cemented beds. This unit was interpreted shipboard to result from extensive gravity flow deposition and ice rafting with intermittent hemipelagic deposition reworked by bottom currents. Units III (278.4 to 459.4 mbsf) and V (593.8 to 694.4 mbsf) are characterized by interbedded greenish-grey bioturbated claystones and brown laminated claystones with cross-laminated siltstones and sandstones. Some of the bioturbated claystones within these units are carbonate cemented. Preliminary interpretation on shipboard pointed out to cyclical changes in bottom oxygenation, bottom current strength, and fine-grained terrigenous supply. Rare gravel-sized clasts were taken to suggest minimal influence of ice rafting at the Site.

Site U1356 at the present is placed within the Antarctic Divergence (AD) Zone off the Adélie Coast, located at 63-64°S (Bindoff et al., 2000; Fig. 4.1). The AD has a very weak westward flow (Bindoff et al., 2000) and is bounded latitudinally between the southern boundary of Antarctic Contour Current Front (SACCF) and the Antarctic Slope Front (ASF; Orsi, 1995; Rintoul et al., 2001). This is a key location to evaluate the variations in the position of the Antarctic polar fronts as, in the transect between Antarctica and Tasmania around 140°, the ACC fronts are very close and together generate some of the largest temperature and salinity gradients in the world ocean (Rintoul et al., 2001 and cites therein). In addition, the Site is in close proximity to the source and pathway of Adélie Land Antarctic Bottom Waters (ALBW; van Wijk and Rintoul, 2014).

Site U1356 drifted approximately 3° south and 25° east between the Oligocene and the present day, calculated based on the paleomagnetic reference frame of Trosvisk et al. (2012) using [www.paleolatitide.org](http://www.paleolatitide.org) (van Hinsbergen et al., 2015). Since the early Oligocene Site U1356 has been in a deep-water setting landward from the continent-ocean boundary (COB) (Escutia et al., 2011, 2011b; 2014) Based on facies distribution across an Antarctic Australian transect Scher et al. (2015) placed the PF during the Oligocene to be at around 60°S. Recent studies in late Oligocene and middle Miocene sediments from Site U1356 report on latitudinal shifts in the position of the PF during glacial and interglacial periods (Bijl et al., 2018; Hartman et al., 2018; Salabarnada et al., 2018; Sangiorgi et al., 2018).

#### 4.2.2. FACIES ANALYSES

Detailed facies analyses provide a stratigraphic framework on which we base our interpretations regarding sedimentary processes and paleoenvironments. Lithofacies are determined on the basis of detailed visual logging of the core during a visit to the IODP Gulf Coast Repository (GCR), expanding on the lower-resolution preliminary descriptions in Escutia et al. (2011). Facies differentiation is done by using observations based on visual core description, high-resolution digital core imaging, magnetic susceptibility (MS), Computed Tomography X-Ray scans (CT-Scan), mineralogical analysis with X-Ray diffraction (XRD), geochemical analysis with discrete X-Ray Fluorescence (XRF), and High Resolution Scanning Electron Microscopy (HR-SEM) images. The complete detailed lithostratigraphic log for the Oligocene-Miocene sections is published in the supplementary material from Salabarnada et al., (2018, Supplementary Materials within chapter 3 of this thesis). Figure 4.2, shows the detailed log for the late Oligocene-Miocene cores that are the focus of this study.

To further characterize the different facies, magnetic susceptibility (MS) was measured every 2.5 cm during IODP Exp. 318 using the Whole Round Multisensor Logger (Escutia et al., 2011b). In addition, we obtained X-ray computed tomography scans (CT scans) of selected intervals at the Kochi Core Center (KCC) (Japan), with the GE Medical systems LightSpeed Ultra 16. 2-D scout (shooting conditions at 120 Kv with 100 mA; 3-D helical image with 120 Kv and 100mA and FOV=22.0). Image spatial resolution consists of 0.42 mm pixel<sup>-1</sup> with 0.625mm of slice thickness (voxel spatial resolution of 0.42x0.42x0.625 mm). CT-scans measure changes in density and allow for the analysis of fine-scale stratigraphic changes

and internal structures of sedimentary deposits in a non-destructive manner (e.g., Dulu, 1999; St-Onge and Long, 2009; Van Daele et al., 2014; Fouinat et al., 2017). CT-scans create 2D and 3d images of the cores, and permit a 3D interpretation of the sediments. Specifically, we can study the individual position of the different clasts in relation with the facies and their contacts that provides valuable spatial information, without destroying the core.

#### 4.2.3. GEOCHEMICAL ANALYSES

In order to determine the chemical composition of the sediments we acquired discrete X-Ray Fluorescence (XRF) major and trace elements from 104 sediment samples. For this, we used a Pioneer-Bruker XRF spectrometer S4 at the Instituto Andaluz de Ciencias de la Tierra (CSIC) in Granada, equipped with a Rh tube (60 kV, 150 mA) using internal standards. The samples were prepared in a Vulcan 4Mfusion machine and the analyses performed using a standard-less spectrum sweep with the Spectraplus software. Sediment samples were collected targeting to characterize the different lithologies.

Mineralogy of the bulk sediments and detrital clay minerals were studied using a representative and homogeneous part of each sample to perform X-ray diffraction (XRD) analysis. The XRD analysis was carried out using a PANalytical X'Pert Pro series diffractometer equipped with a cobalt-target tube, X'Celerator detector and operated at 45 kV and 40 mA. Scans were run from 4° to 69° 2θ for bulk-sample diffractograms and untreated clay preparations. For bulk mineralogy, samples were air dried, ground in an agate mortar to <2 μm, and packed in Al sample holders. Preparation of the samples for XRD was performed following the international recommendations compiled by Kisch (1991). XRD results are analysed using Profex Software (Doebelin and Kleeberg, 2015). XRD is a key method to differentiate biogenic opal transformed into Opal-CT (Hesse and Schacht, 2011) through the amorphous peak that is defined to represent biogenic silica (DeMaster, 2013).

Clustering is a common multivariate statistical method that is useful for grouping observations into homogeneous clusters (Penkrot et al., 2018). Hierarchical clustering is based on the multivariate distance between observations in order to make classifications through similarity indexes and correlations between elements. This analysis was performed in the R programming language using the “hclust” function (R Core Team, 2017).

#### 4.2.4. LINKING SITE U1356 WITH SEISMIC REFLECTION PROFILES

Multichannel seismic reflection (MCS) lines GA228-29 and GA229-07 cross U1356 and were used, together with other seismic data, to provide a regional context to the interpretations based on sediments obtained from Site U1356. MCS data are accessible through the Antarctic Seismic Data Library System SDLS (<http://sdls.ogs.trieste.it>). To integrate Site U1356 results with the multichannel seismic data, we conducted a depth-time conversion using the sonic velocity data obtained shipboard from discrete samples (Fig. 4.6; Escutia et al., 2011b) using the Kingdom Suite Software®. This allowed us to extend the results from Site U1356 through the grid of seismic regional profiles providing an age control to the



previously interpreted unconformities in this margin (Escutia et al., 1997, 2000; Donda et al., 2003, 2005; De Santis et al., 2003).

## 4.3. RESULTS

### 4.3.1. SEDIMENT FACIES ANALYSIS AND SEDIMENTARY PROCESSES

In this study, sediments within lithostratigraphic units V-III (690-392 mbsf) described by Escutia et al. (2011) have been further characterized and subdivided as described below.

#### 4.3.1.1. Unit V

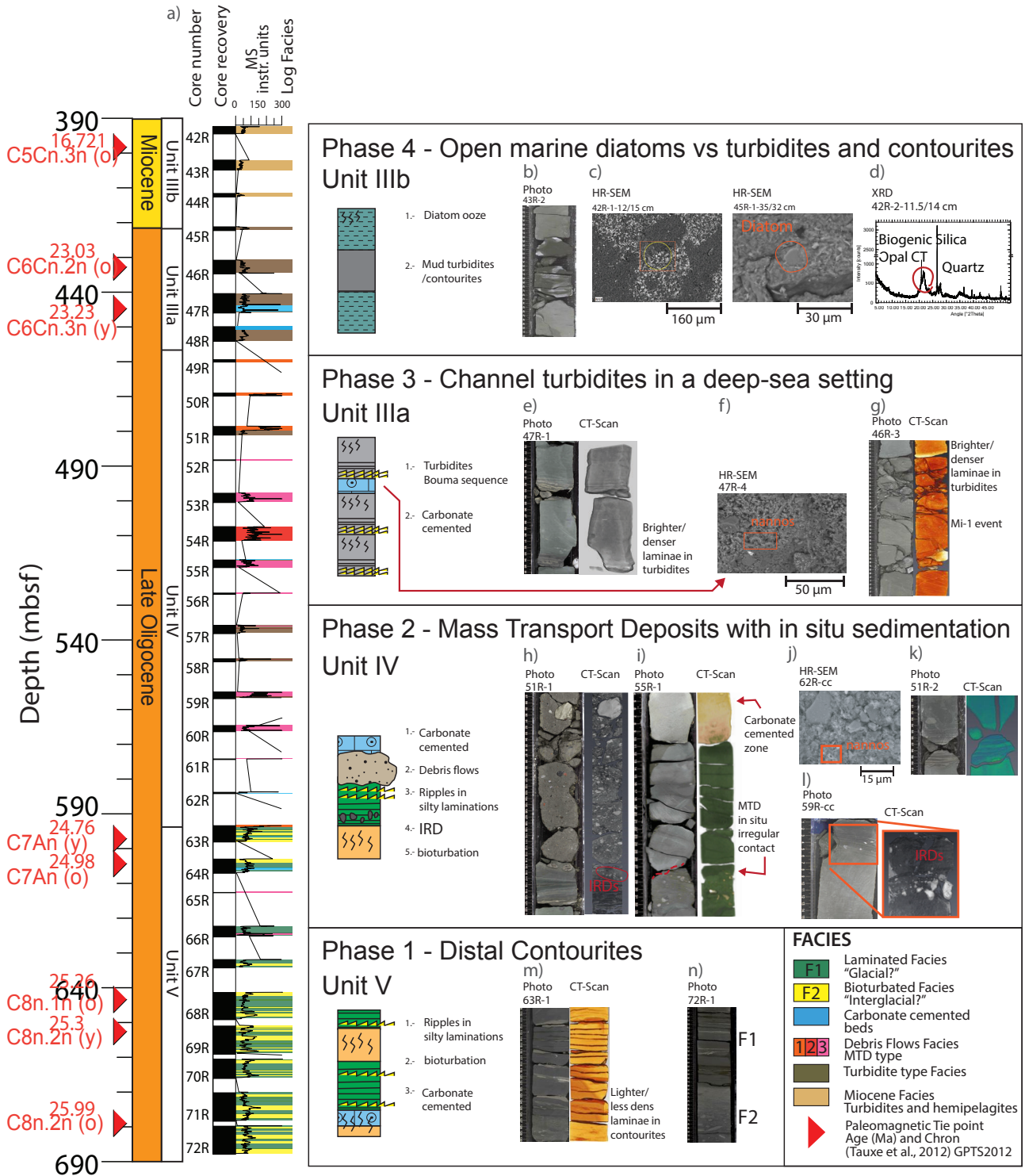
Unit V, spans from 690 to 593.8 mbsf and consists of cyclic alternations of claystones with thin silt laminae and bioturbated silty claystones, with interbedded carbonate cemented intervals containing reworked coccolithophores (Escutia et al., 2011b) (Fig. 4.2-m,n). These two facies were interpreted to form by reworking of sediment delivered to the Site by gravity flows and hemipelagic settling during glacial interglacial cycles (Escutia et al., 2011b). Sedimentary facies within an interval of relatively high-recovery (78.2%) between 690 and 640 mbsf were studied in detail by Salabarnada et al. (2018).

An interval within Unit V located at 624.5 mbsf exhibits finning upward gravels and sands, slightly disturbed due to the coring processes. Gravel clasts are unconsolidated and are polymictic and sub-rounded in nature.

In the upper 2 meters of Unit V (591-593.8 mbsf) the laminations inside the claystones become more frequent, thicker (up to 1 cm thick) and coarser grained (i.e., silty-sand beds). Sediment structures within the silty-sand beds include climbing ripples, and sinusoidal, planar, and lenticular bedding (Fig. 4.2-m). CT-Scans show these laminations to be less dense (darker colors in the CT-scans) than the muddy intervals (Fig. 4.2-m). The basal contacts of the laminations are sharp, with some flutes and scour marks. At the top, silty-sand beds transit sharply to dark claystones with fine laminations. CT-scan images, also show the differences in density between the current-reworked turbidites/contourites (lighter silty sands; Fig. 4.2-m) and the overlying turbidites (denser silty sands) (Fig. 4.2-e,g).

#### 4.3.1.2. Unit IV

Unit IV (from 593.8 – 459.4 mbsf) was described on shipboard to be matrix supported gravel-sized clasts interbedded with alternating bioturbated claystones, and cross-laminated and graded silty claystones (Escutia et al., 2011b). These deposits were interpreted to result from extensive gravity flow events (Escutia et al., 2011b, 2014). Based on continental slope-to-rise seismic reflection profiles crossing Site U1356, these debris flows were interpreted to be the distal reaches of a series of stacked MTDs at the base of the slope (Escutia et al., 2014; Passchier et al., 2018), delivered to the continental rise during advances of the ice sheet into the continental shelf (Escutia et al., 2011b; 2014). Interbedded between



**Figure 4.2.** Lithological log from site U1356 with their summarised facies and sequences. High resolution images, CT-Scans, HR\_SEM.

the MTDs are bioturbated claystones including occasional <1 m thick calcareous and rare nanofossil-bearing intervals.

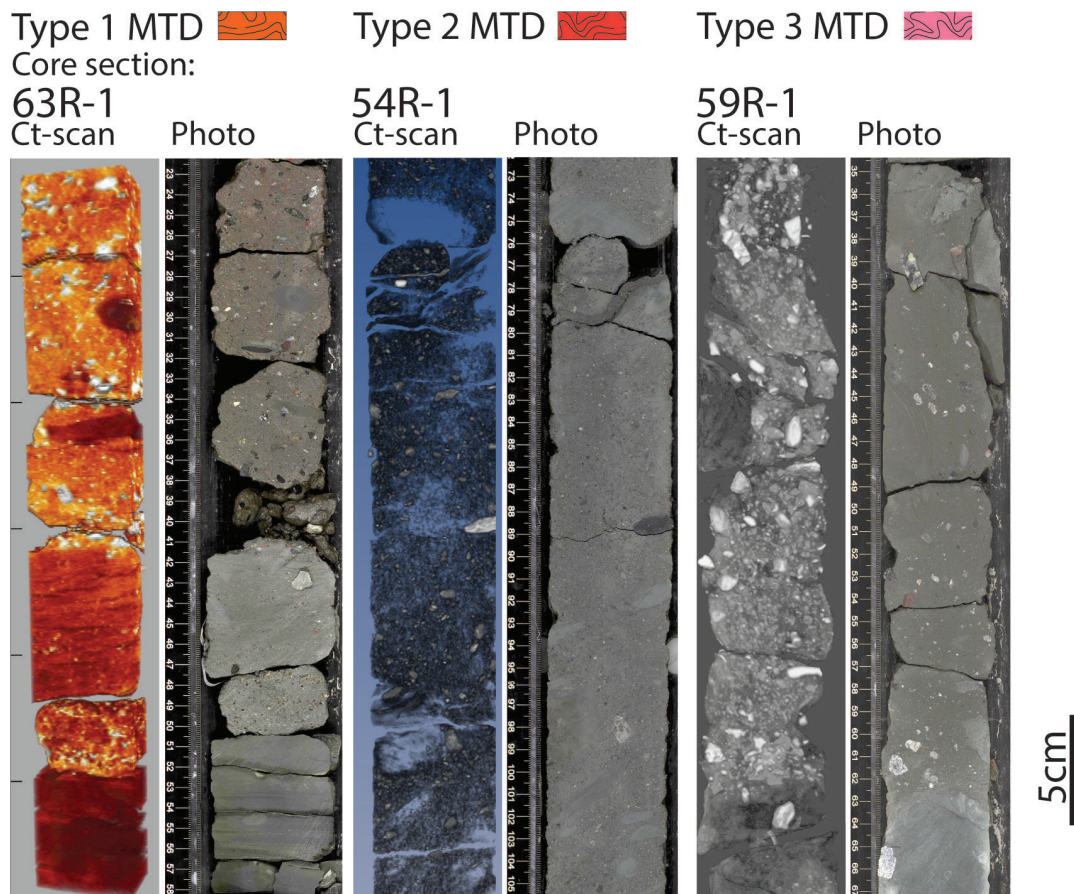
Both visual observation and CT-scan images clearly show the sharp contact between the sediments of Unit V and the Mass Transport Deposits (MTDs) that dominate Unit IV (Fig. 4.2-h,i). The irregular basal





contacts of the MTDs attest to erosion of the pre-existing sediments.

CT-scans and high-resolution core images allow us to differentiate 3 types of MTD facies (Fig. 4.3): Type 1) Homogeneous coarse sand matrix with abundant and heterogeneous clasts (from 0.5 to 3.5 cm) and random fabric. They exhibit some overpressure surfaces and alignments, and erosional and deformational structures at the base such as irregular bases and ball and pillow structures (i.e. cores 49R, 50R, 51R, 63R-1; Figs. 4.2-h, 4.3). Type 2) Very coarse sand matrix with dispersed heterogeneous size clasts (one reaching up to 5 cm). Type 2 MTDs are characterized by the presence of elongated mud clasts (2 cm long) that are aligned in a common orientation axis, and by some clast-to-clast contacts (i.e., core 54R; Fig. 4.3). Type 3) Include intercalated clast-poor mudstones and clast-rich sandstones (similar to Type 1) that are strongly contorted, and faulted laminated mudstones (i.e. cores 53R, 55R, 59R, 60R, 61R, e.g., Fig. 4.2-i, 4.3).



**Figure 4.3.** Mass Transport Deposit (MTDs) types studied at site U1356.

Interbedded between MTD facies are claystones, silty claystones, and/or carbonated facies, which exhibit contacts that are erosional at the base and irregular at the top (Fig. 4.2-i). We identify eight erosional basal surfaces that attest to erosion of the pre-existing sediments at 593.8, 574.2, 564.8, 556.4, 526.6, 511.5, 500.0, and 479.8 mbsf. Below two of these basal contacts and near the top of the underlying laminated claystones, we identified two zones with a cluster of clasts (placed at 556.5 and 479.87 mbsf; Fig. 4.2-h,l). CT-scan 3D images show how these clasts deform the underlying in situ laminations and are draped by

laminated sediments above. Based on these observations, we interpret these clusters of clasts as ice rafted debris (IRD) events.

Laminated claystones and siltstones interbedded between the MTDs are similar to those described for Unit V. We thus interpret these sediments to be in situ and to result from hemipelagic and gravity flow deposition reworked by bottom currents following the interpretation of Escutia et al. (2011b) and Salabarnada et al (2018). Among these in situ deposits, three carbonate-cemented siltstone beds were reported by Escutia et al. (2011b) at 584, 565.9, and 517.1 mbsf. HR-SEM images show these sediments to be coarse-grained and to contain rare- to abundant reworked coccolithophores and scarce planar barite crystals (Fig. 4.2-j), which point to strong bottom-currents reworking in these sediments.

At 480.75 mbsf there is an event that generated basal scour marks that are filled with silts exhibiting sedimentary structures (i.e., climbing ripples) and intercalated with mud offshoots and muddy layers (Fig. 4.2-k), that are consistent with deposition through current reworking of an erosive turbidite deposit. This erosive turbiditic event is also reported by Passchier et al. (2018).

#### 4.3.1.3. Unit III

Escutia et al. (2011b) described unit III (459.4 – 392 mbsf) to be comprised by interbedded bioturbated (silty) claystones and silt-laminated claystones, with some nannofossil bearing beds near the base of the unit. From 412.6 to 392 mbsf, silt laminations disappear and an alternation between green and dark claystones dominates. Throughout this unit, gravel-sized clasts are absent.

Here, we divide this unit in two sub-units: 1) Unit IIIa (459.4 to 421.5 mbsf), and 2) Unit IIIb (421.5 to 392 mbsf).

Unit IIIa consists of an alternation between burrowed dark grey claystones with nereites ichnofacies and green claystones with silt laminae at the bottom. Silt laminae exhibit scours at the base and an internal succession of structures (i.e., cross and planar laminations) characteristic of the Bouma b, c, d or c, d turbidite sequences (Bouma, 1962; Fig. 4.2-e). Within the claystones there are two highly bioturbated carbonate cemented intervals, one at 450 mbsf and another between 445.5 and 443.8 mbsf. HR-SEM images of these intervals show abundant coccolithophores with calcite cemented matrix, aluminosilicates and coarse silt quartz grains (Fig. 4.2-f). CT-Scans show that laminated silty intervals have higher density (lighter colour) than the claystones sediments (Fig. 4.2-e). This contrasts with contouritic laminations in Unit V (Fig. 4.2-l), which present less dense CT-scan values compared to the claystones. Bioturbation is observed mainly in the claystones, filled by a denser material, pyrite, similar as occurs in the bioturbated contourite facies from below (Fig. 3.3-b). From 434.5 to 434.1 mbsf, CT-scan images show a deformed/chaotic interval indicated by inclined ( $< 20^\circ$ ) laminated claystones with micro-faults in the laminations and weight striations (Fig. 4.2-g). These are mixed with a sandstone matrix with clasts up to 2 mm (Fig. 4.2-g).



Unit IIIb, consists of an alternation of bioturbated olive grey claystones with fine dark planar laminations and dark green claystones with silica cemented matrix. HR-SEM images confirm the cemented matrix to be fine-grained and to be composed mainly of silica, clay minerals and barite. Notably, barite minerals present a planar morphology and are arranged in circular patches around the surface of the sample (Fig 2-b,c). These patches appear to correspond to diatoms ghost that result from diagenesis and dissolution processes (Fig. 4.2-c). In addition, XRD analyses confirm that biogenic opal CT is present, as seen for the amorphous peak of the biogenic siliceous material (Fig. 4.2-d; DeMaster, 2013). In this unit there are also small concentrations of carbonate with rare coccolithophores.

### 4.3.2. GEOCHEMICAL RESULTS

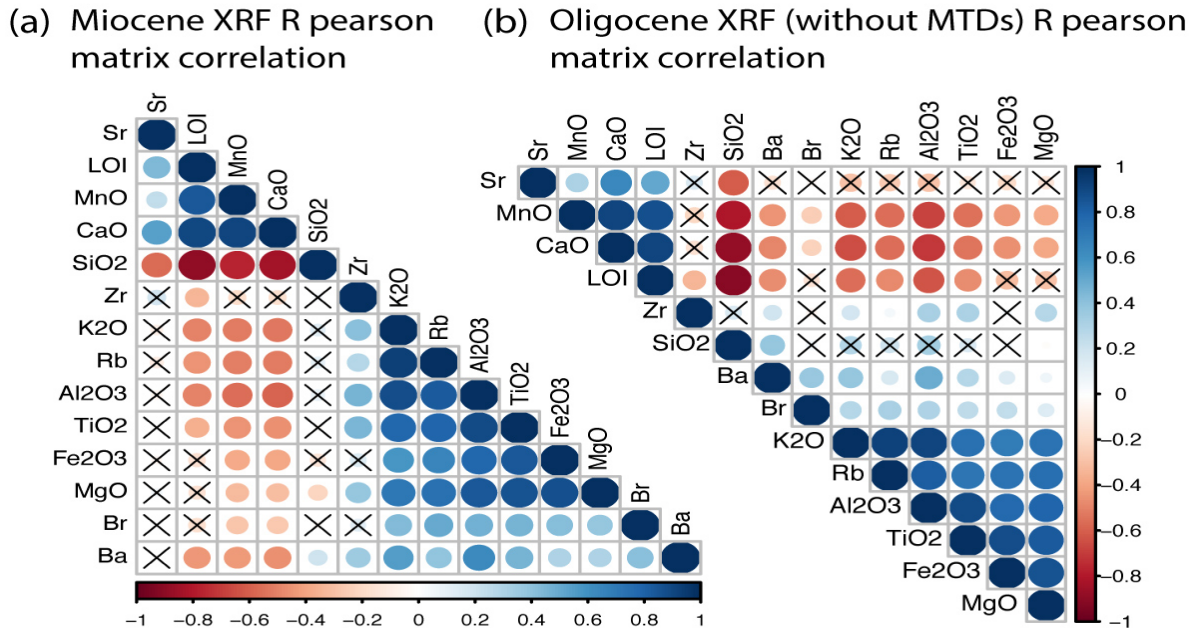
We use bulk XRF major and trace element geochemical compositions downcore to characterize the biogenic and detrital input, in order to investigate the imprint of past continental and oceanographic conditions in the sedimentary record.

XRF matrix correlation analyses describe two different elemental composition relationships for the Miocene and the Oligocene sediments from U1356 (Fig. 4.4). Interpretations of the XRF discrete data are based on samples taken from the in situ facies, and samples placed in the chaotic facies interpreted as MTDs where discarded for the correlation analysis. In the matrix correlation, elements were ordered by hierarchical ordination depending on their correlation coefficients and similarity distances (how much the different elements are equal) between them, which implies that the ordination in the correlation matrix is different for each time-period. Significant values  $< 0.95$  have been crossed.

For the Oligocene section (Fig. 4.4-b) four clusters describe the major element similarities. CaO is positively correlated with MnO, LOI, and Sr; and inversely correlated with SiO<sub>2</sub> and terrigenous elements such as K<sub>2</sub>O, Rb, TiO<sub>2</sub>, and Ba. Zr has low correlation with terrigenous elements as TiO<sub>2</sub>. Terrigenous elements are composed by TiO<sub>2</sub>, K<sub>2</sub>O, Rb, Al<sub>2</sub>O<sub>3</sub>, Fe<sub>2</sub>O<sub>3</sub>, MgO. SiO<sub>2</sub> is positively correlated with Ba.

For the Miocene section, three clusters describe the major element similarities (Fig. 4.4-a). SiO<sub>2</sub> significantly inversely correlated with CaO, MnO, LOI and Sr, and is not significantly correlated with the other elements analysed. CaO is correlated with LOI and Sr but also is inversely correlated with all the other elements including SiO<sub>2</sub>. The rest of elements are positively correlated altogether, representing a solid detrital behaviour, including Ba.

Element ratios to TiO<sub>2</sub> were used as a method for normalization to the terrigenous fraction, as Ti is limited to the terrigenous phase in sediments and is not affected by diagenesis (Calvert and Pedersen, 2007). Site U1356 geochemical variability is characterised by the following element depth ratios (Fig. 4.5): Ba/Ti, Si/Ti, Zr/Ti and CaO%. Samples within the MTDs were selected and plotted separately (i.e., orange dotted line, Fig. 4.5) from those collected on interpreted in situ sediments.



**Figure 4.4.** Correlation matrix for (a) Miocene and (b) Oligocene in situ sediments. Elements are ordered in hierarchical ordination to identify groups of similar affinity within XRF data set. Colors refer to the correlation coefficient, where blue (red) are positively (inversely) correlated. Crossed squares have significance level  $< 0.95$ . R corrpilot package.

Ba/Ti records an increasing tendency to higher values from the bottom of the studied section to 595 mbsf, although cyclical variations are also observed. From 590 to 480 mbsf Ba/Ti values are close to 0. Highest values on average are found between 480 and 422 mbsf. Miocene Ba/Ti values are anticorrelated with Si/Ti, and show cyclic variability. Ba/Ti minimum values coincide with carbonate layers at 585, 565, and 518 mbsf. In the MTDs, Ba/Ti values remain higher compared with in situ samples.

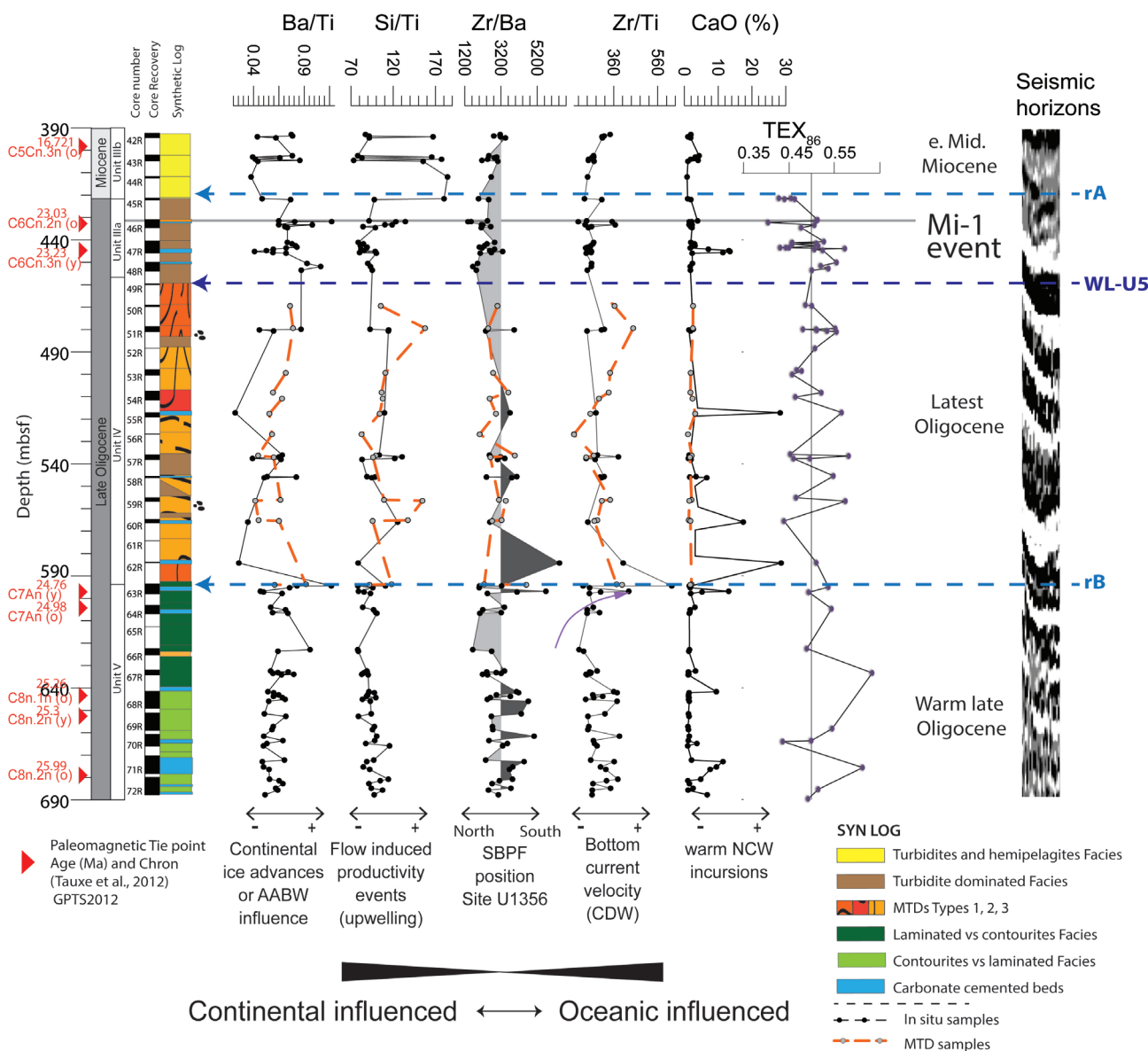
We differentiate between three intervals in the Si/Ti record (Fig. 4.5): late Oligocene values (690-590 mbsf) vary between 70 and 110 with a tendency to lower values towards the top of the interval. Between 590-460 mbsf (24.76-23.23 Ma) values in general increase and show higher variability. This is true for both, sediments that are in situ (80 and 130) and for the MTDs (80-160). A pronounced shift towards higher values (up to 190) is observed at 422 mbsf. From 422 to 390 mbsf, Si/Ti, is characterized by large amplitude cyclic variations (70-190). Two Si/Ti peaks inside the MTDs coincide with the clusters of dropstones interpreted as IRD at 556.5 and 479.87 mbsf. XRD analyses confirm that biogenic opal CT is present, coincident with the Si/Ti peaks.

Zr/Ti (Fig. 4.5) ratio is higher (360) coinciding with the bioturbated facies in the sedimentary column and decreases within the laminated facies (260). A sharp shift towards higher values (peaks up to 640) is observed at 595 mbsf, in sediments that are just below the first MTDs. Above 590 mbsf in situ sediments have values that remain around 260, except for four peaks at 538, 480, 432, 394 mbsf where values return to the ones similar on the interglacial bioturbated contourites (i.e., 360). Within this interval, samples



from the MTD intervals vary in the same range of amplitudes with maximum Zr/Ti values at 595, 556.5 and 480 mbsf, coincident with MTDs type 1 that have a coarser matrix and clustered dropstones.

CaCO<sub>3</sub> wt% is generally close to 0% throughout the studied section, with the exception of several peaks coinciding with the carbonated beds where concentrations range from 5% to nearly 30% (Fig. 4.5). HR-SEM images in these intervals show the presence of reworked coccolithophores (Fig. 4.2-j). CaCO<sub>3</sub> wt% values on the MTD samples display near zero values.

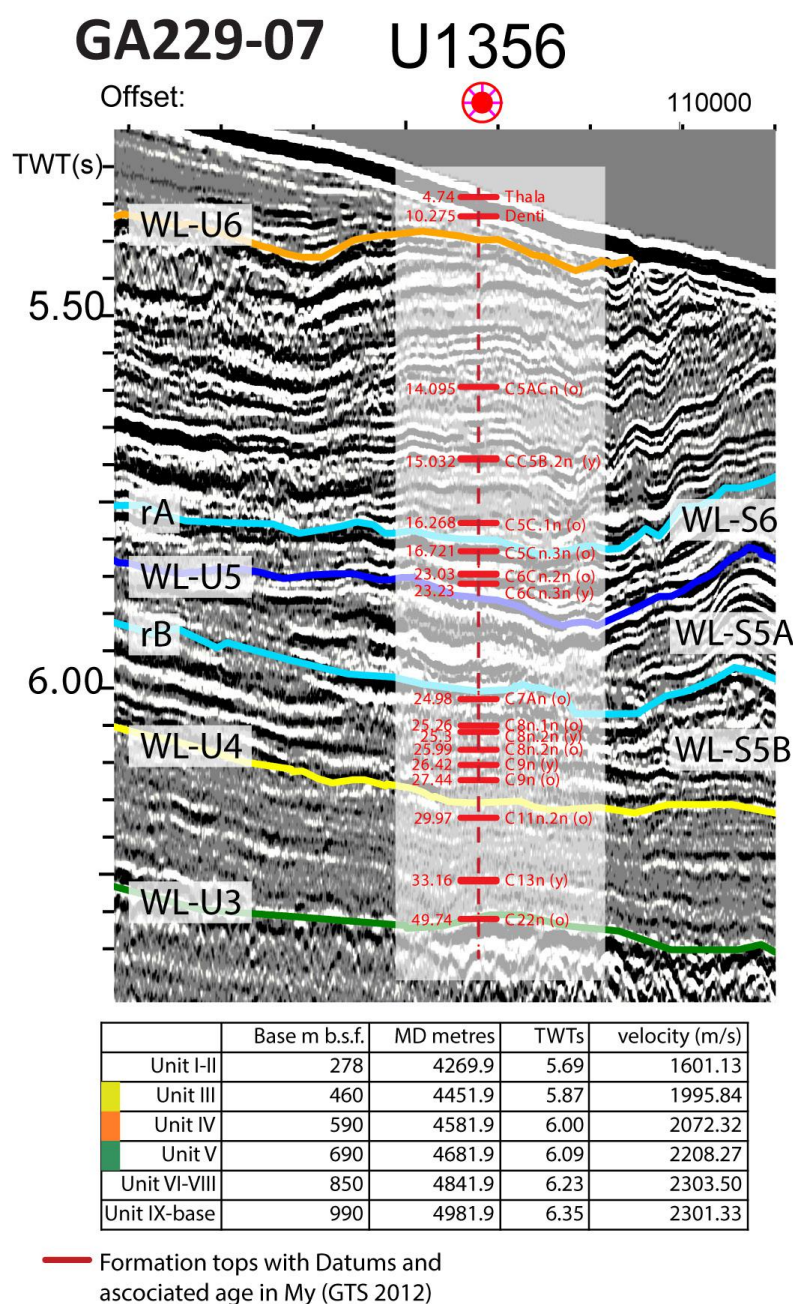


**Figure 4.5.** Discrete XRF geochemical proxies Ba/Ti, Si/Ti, Zr/Ba, Zr/Ti, CaO%, and TEX<sub>86</sub> extracted from Hartman et al., 2018., plotted against core U1356.

### 4.3.3. WILKES LAND MARGIN REGIONAL EVOLUTION BASED ON SEISMIC REFLECTION DATA

#### DATA

Results obtained from our studied interval at Site U1356 have been correlated with the two multichannel seismic lines that cross the Site, and from there with the grid of available seismic profiles in the region. Given that no sonic logs were obtained at Site U1356, the required depth to time conversion has been achieved by estimating the shipboard discrete xyz p-wave median velocity measured in sediments recovered at the Site (Fig. 4.6). The resulting range of velocities with depth are similar to those obtained by refraction/wide-angle reflection sonobuoy stations on the same line GA228/29 (Stagg et al., 2004).



**Figure 4.6.** Formation tops used in the Kingdome project to correlate seismic profiles against core sediments from U1356. Time velocity depth calculations are selected based in sedimentary units described in this study.



This correlation shows that sediments from 690 to 392 mbsf are within seismic units WL-S5 and WL-S6 (Escutia et al., 2000; DeSantis et al., 2003; Escutia et al., 2005; Escutia et al., 2011b). Seismic unit WL-S5 is bound at the base by unconformity WL-U4, which according to our time-depth conversion is placed at 732 mbsf (6.14, Two Way Travel Time-TWTT). Seismic unit WL-S6 is bound at the base by unconformity WL-U5, located at 512 mbsf (5.91 s TWTT) as seen in Table 4.1 (Fig. 4.6).

**Table 4.1.** Time-depth conversion for the regional unconformities previously defined in the Wilkes Land margin (WL-U3, WL-U4, WL-U5) and to the reflectors separating lithostratigraphic units/subunits defined in this study (reflectors rA and rB). Calculated P-wave velocities for eastern Wilkes Land regional unconformities reflectors. TWTTs: two way travel time in seconds; MD m: measured depth in meters; mbsf: meters below sea floor.

| Seismic horizons in U1356 | TWTTs | MD m    | mbsf   |
|---------------------------|-------|---------|--------|
| rA                        | 5.87  | 4465.17 | 473.27 |
| WL-U5                     | 5.91  | 4503.63 | 511.73 |
| rB                        | 6.02  | 4609.41 | 617.51 |
| WL-U4                     | 6.14  | 4724.80 | 732.90 |
| WL-U3                     | 6.29  | 4869.03 | 877.13 |

Seismic facies that characterize unit WL-S5 where Site U1356 is located are uniform with predominantly high amplitude continuous reflectors. Results from drilling allow us however to subdivide seismic unit WL-S5 in two sub units WL-S5A and WL-S5B (Fig. 4.6, 4.7). Contourite dominated deposits of lithostratigraphic Unit V are comprised within seismic subunit WL-S5B. The Mass Transport Deposits of lithostratigraphic Unit IV span seismic subunit WL-S5A that is bound between reflectors rB and unconformity WL-U5. The turbidites of lithostratigraphic Unit III are emplaced within seismic unit WL-S6, between unconformity WL-U5 and reflector rA. Above rA, deposition is dominated by hemipelagites and mud turbidites contourites.

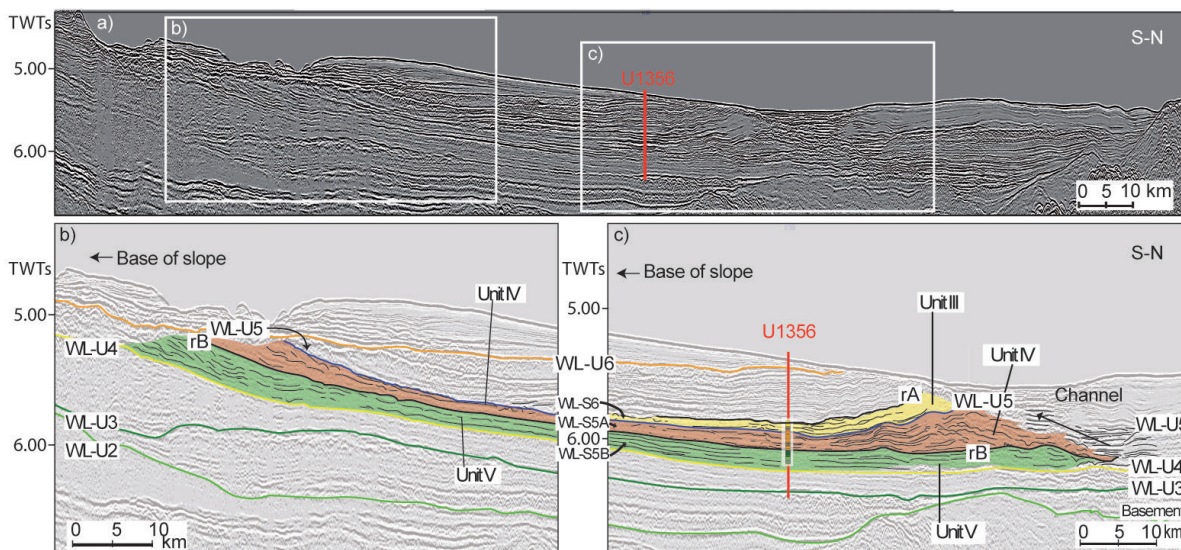
At the base of the slope/upper continental rise the external geometry between reflectors rB and WL-U5, is that of a series stacked wedges that thin seaward. The landward end of the wedge is truncated by a younger unconformity, WL-U6 of De Santis et al. (2003). At the base of the slope, reflectors within the wedge are semi-transparent and chaotic (Fig. 4.6). Basinwards, these facies transition from undulated to the sub-parallel reflectors of moderate to low amplitude observed where Site U1356 is located. Based on this correlation, Site U1356 sediments between reflectors rB and WL-U5 represent the distal ends of large MTDs deposits that originate at the outer shelf or the upper slope. To the north of Site U1356, reflector rB has an erosive character and marks the beginning of an erosive channel with low-relief levees. Calculation of the minimum thickness of the MTDs wedge in the base of the slope account for up to 150 m of sediments.

Unconformity WL-U5 separates the MTD deposits below from sup-parallel reflectors above the unconformity. Reflectors above WL-U5 where Site U1356 is located have a wedge shaped geometry,

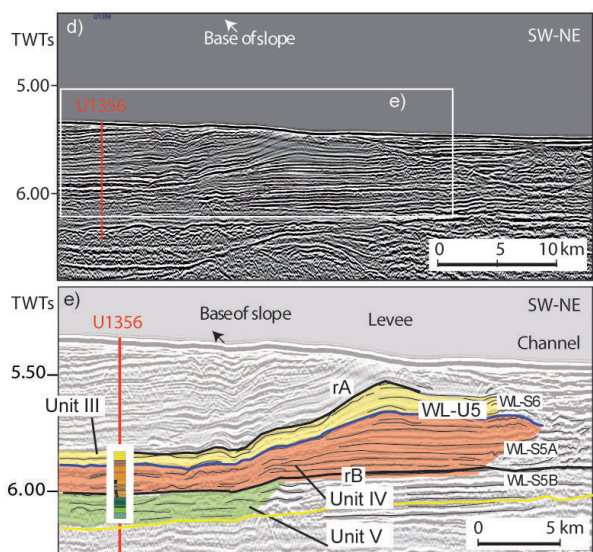
thinning landward and downlapping unconformity WL-U5. These geometries are characteristic of levee deposits suggesting that our Site records dominant turbidite deposition from the adjacent channel, that is more than 200 km long and 10 km wide in the continental rise section. We calculated the relief of the levee above reflector rA (that constitutes the initial stages on the formation of the channel levee) to be at least >200 m (without decompacting sediments; Fig. 4.7-c,e). Above rA seismic facies consist of laminated semi-continuous transparent reflectors that are interpreted as hemipelagites and mud turbidites reworked by bottom currents (Escutia et al., 2011b).

Site U1356 therefore records the interplay between downslope delivered material as base of slope debris flow deposits and turbidity currents that travel through the nearby channel and spill onto the levee, with the reworking of along-slope bottom currents. Both seismic and sediment facies are coherent with sedimentation in a distal setting influenced by contour currents (Escutia et al, 2011b).

**GA228-29**



**GA229-07**



**Figure 4.7.** Seismic reflection profiles that provide a regional setting for Site U1356 in the Wilkes Land Margin.





## 4.4. DISCUSSION

### 4.4.1. LATE OLIGOCENE TO EARLY MIDDLE MIOCENE ICE SHEET HISTORY AND PALEOCEANOGRAPHY THROUGH DEPOSITIONAL SETTINGS AND ENVIRONMENTS

Climate, ice sheet and ocean interactions controlled sedimentation on the basin during the Late Oligocene and Miocene. We differentiate four main shifts in sedimentation between 26.2 and 17 Ma (Figs. 4.2, 4.8): Phase 1) late Oligocene from 26.2 to ~24.5 Ma; Phase 2) the latest Oligocene, between 24.5 and 23.23 Ma; Phase 3) the Oligocene Miocene transition, between 23.23 and 22.9; and Phase 4) the early middle Miocene ~17 Ma.

**PHASE 1)** The late Oligocene from 26.2 to ~24.5 Ma (690 – 594 mbsf) at Site U1356 was already studied in detail by Salabarnada et al. (2018). These authors reported on glacial-interglacial deposition to be dominated by gravity flows and hemipelagic deposits, respectively, that were reworked by bottom contour currents. Laminated claystones were deposited under reduced oxygen conditions in the water sediment interface and under fluctuating bottom contour currents during glacial times. Bioturbated silty claystones, were interpreted as contourites formed under more oxygenated conditions during interglacial periods and under the influence of stronger and more continuous current velocities relative to those forming the laminated facies. In addition, carbonate cemented intervals were interpreted to result when Antarctic Bottom Water production weakened allowing a proto-CDW, influenced by warmer north component deep waters, to intrude closer to the continent (Salabarnada et al., 2018; Fig. 4.8).

The observed increased presence of thick laminated sediments starting around 24.9 Ma (591-593.8 mbsf) is here related to an intensification of the downslope processes at the Wilkes Land margin in form of turbidite or meltwater deposition combined with an strengthening of bottom contour currents that reworked these sediments. This bottom current intensification coincides with the start of a cooling trend in Summer Surface Temperatures (SST) reported at Site U1356 (Hartman et al., 2018) and with a global climate cooling trend in the oxygen isotope records (e.g., Zachos et al., 2008).

**PHASE 2)** The latest Oligocene (from 24.5 to 23.23 Ma; 594 – 459 mbsf) sediments recovered from Site U1356 are correlated with a series of stacked sediment wedges at the base of the continental slope, indicating that deposition is dominated by MTDs (Fig. 4.8). Glacial MTDs and debris flows have been interpret to result from ice sheet advance to the shelf edge (e.g., Ó Cofaigh et al., 2003; Dowdeswell et al., 2016). MTDs recovered at Site U1356 are similar to early Oligocene ice proximal diamictos recovered from the Wilkes Land continental shelf at Site U1360 (Escutia et al., 2011), the Prydz Bay continental shelf and slope (O'Brien et al, 2004; Passchier et al., 2003) and the Ross Sea continental shelf (McKay et al., 2009). We therefore imply that the MTDs recovered at Site U1356 result from sediment instability at the outer shelf and upper slope as ice sheets advanced into the outer continental Wilkes Land margin. Successive MTDs are accumulated as stacked wedges at the base of the slope (Fig. 4.7). Based on their recovery at Site U1356, we calculate minimum runout distances for these MTDs of approximately 200 Km. Runout distances however, may be even higher as an increase in coarse material input at ODP Site

269, 250 km seaward from Site U1356, has been reported to start at 24 Ma (Evangelinos et al., submitted). The start of glacial MTD deposition at 24 Ma is also correlated with the beginning of the Mi-1 isotopic event in the Southern Ocean (i.e. Zachos et al., 2001a, 2001b), coincident with the transient glacial advances and retreats described from the sediments in the Ross Sea (i.e., Cape Roberts; Naish et al., 2001; Barret et al., 2007).

The two high-energy MTD type 1 events (594 and 479.75 mbsf) have similar lithological characteristics as a diamicton deposited in an ice proximal/subglacial context on the continental shelf, that are after redeposited as glacial debris flows in the continental rise (Anderson, 1999). Debris flow activity can be interpreted as events of maximum ice sheet extent, close to the shelf edge and margin progradation (Ó Cofaigh et al., 2003; Dowdeswell et al., 2016) as seen in seismic lines. MTDs type 1 are also very similar early Oligocene diamictons recovered during Expedition 318 from the continental shelf at site U1360. This diamictons were interpreted to be deposited during the Eocene-Oligocene glacial expansion (Escutia et al., 2011; Passchier et al., 2018).

Within the MTDs, we identify eight erosional basal surfaces (at 593.8, 574.2, 564.8, 556.4, 526.6, 511.5, 500 and 479.8 mbsf) that attest to erosion of the pre-existing sediments by the MTDs and that we take to record eight times of glacial ice stream advance to or close to the shelf edge. Below two of these basal contacts and near the top of the underlying laminated claystones, we identified two zones with a cluster of clasts (placed at 556.5 and 479.87 mbsf; Fig. 4.2-h,l). CT-scan 3D images show how these clasts deform the underlying in situ laminations and are draped by sediments above. Based on these observations, we interpret these clusters of clasts as ice rafted debris (IRD) events.

In situ sediments preserved between MTD deposits represent an interruption in the delivery of MTDs to where Site U1356 is located. Based on their similar lithological and geochemical character to facies from the late warm Oligocene (Phase 1), we interpreted these sediments to represent glacial and interglacial sediments reworked by bottom currents recording times of open marine conditions with a distal continental ice terminus (Salabarnada et al., 2018). Importantly, interbedded with the MTDs are four carbonated cemented beds that record warm sea surface temperatures, based on  $TEX_{86}$ , around 17°C (Hartman et al., 2018), and open water conditions with the presence of warm water dinoflagellates cysts (Bijl et al., 2018). All these indicators imply warmer conditions during the deposition of the preserved sediments between the MTDs. Similar to Phase 1, these sediments provide evidence for a proto-CDW, influenced by north component warmer water masses saturated in carbonate, reaching the Site at different times during the deposition of Unit IV.

The alternation between MTDs and in situ sediments therefore speak of a very dynamic ice sheet during the late Oligocene with ice streams advancing into the continental shelf/shelf break and times of retreat to a continental position. These multiple advances and retreats of the ice sheet resulted in an important margin progradation (figs. 4.7, 4.8; Piper and Brisco; 1975; Eittrheim et al., 1995; Escutia et al., 2005) and



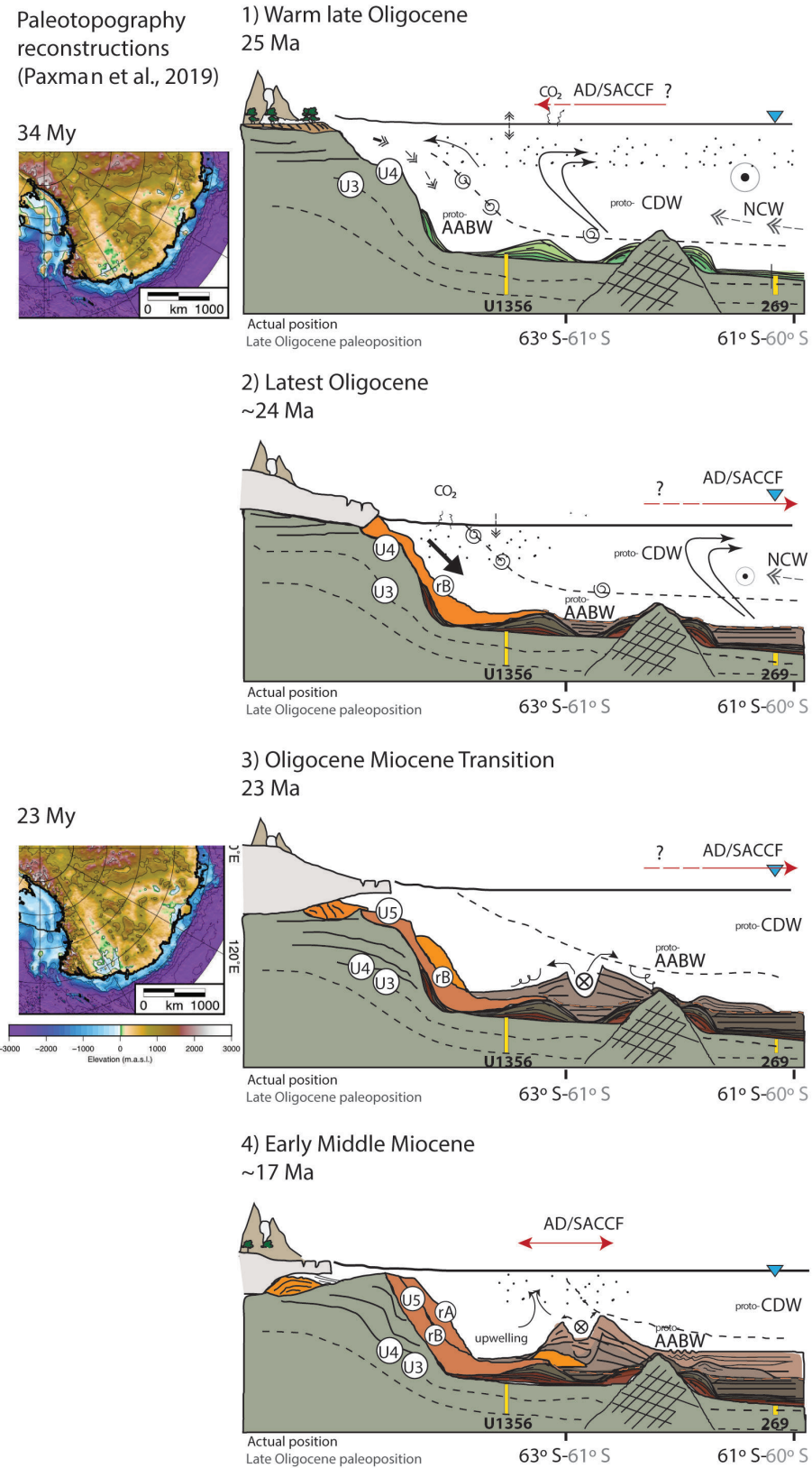
in the delivery of large volumes of sediment to the base of slope and the continental rise, such as those recorded at Site U1356 (Escutia et al., 2011; Tauxe et al., 2012). The MTDs sampled at Site U1356 do not represent local events because large glacial debris flow deposits have been previously reported regionally along the base of the slope in the Wilkes-Adèlie Land margin (Escutia et al., 2003, 2005; 2007; Donda et al., 2008). Based on multichannel seismic profiles, Escutia et al. (2007) described and mapped massive debris flow at the base of slope and upper continental rise deposited within two major regional unconformities WL-U3 (Eocene-Oligocene transition) and WL-U5 (Oligocene-Miocene transition). Thick MTD wedges at the base of the slope are unique depositional events that are not observed in younger sections (i.e., above the WL-U5 unconformity). MTDs therefore appear to be related to unconformities (WL-U3 and WL-U5) that are associated with two major Antarctic glaciations: the EOT and OMT, when a very dynamic ice sheet eroded large volumes of sediment in the continent and delivered them to deep-water settings where Site U1356 (Escutia et al., 2007; Donda et al., 2007).

**PHASE 3)** At the Oligocene-Miocene transition 23.23 to 23.03 Ma, seismic profiles and sediments from Site U1356 record a second drastic change in depositional style. Coarse-grained MTD deposition stops and turbidite deposits dominate the sedimentary record, accompanied by a drastic decrease in sedimentation rates compared with Phase 2 (Escutia et al., 2011; Tauxe et al., 2012). This change is also recorded regionally with channel-levee deposits overlying the MTD stacked wedges (Fig. 4.7, 4.8). This marked change in depositional style coincides with the cooling and ice sheet expansion leading to the Mi-1 event on the  $\delta^{18}\text{O}$  isotopic deep-sea records (e.g., Zachos et al., 2001; Beddow et al., 2016; Liebrand et al., 2011). It also coincides with a drop in SST values (from 12.5 °C to 9.5 °C) measured in sediments from Site U1356 (Hartman et al., 2018).

The above observations suggest that ice expansion related to Mi-1 event caused an irreversible change in the deep-water sedimentation at Site U1356. We hypothesize this change is linked to the deepening of the Wilkes Subglacial Basin due to elevated erosional rates during successive ice advances. Modelled bedrock topography reconstructions show the WSB to be mainly occupied by low lying lands at 34 Ma and below sea level by the Miocene (Gasson et al., 2016; Paxman et al., 2018; 2019). Paxman et al. (2018) analysed the flexural response to sediment loading and constrained the erosion estimates, with >1km of eroded material for the now over-deepened WSB since the latest Eocene but prior to the expansion of the EAIS in the Miocene. These authors propose that major erosion and deepening of the WSB took place in the Oligocene (Paxman et al., 2019). We therefore conclude that the shift from continental to marine based ice sheets in the WSB occurs during Phase 3. The IRDs observed in the laminated sediments support the presence of a marine terminating or a marine based ice sheet.

**PHASE 4)** Early middle Miocene (~17 Ma) is characterized by a period of very low sedimentary rates (Escutia et al., 2011; Tauxe et al., 2012). Deposition at Site U1356 of Unit IIIa is characterized by biosiliceous hemipelagic rain and muddy turbidites both reworked by bottom water currents. An interglacial diatom productive open marine environment is interpreted from the dissolution of silica in

### Variability and evolution of the depositional settings and the paleoceanography of Willkes Land Margin



**Figure 4.8.** Summary figure showing schematic representations of the variability and evolution of the depositional settings and the paleoceanography of the Wilkes Land margin during the studied phases.



the facies and the presence of ghost diatoms (Fig. 4.2). During glacials, terrigenous current reworked mud turbidites dominate the sedimentation. Both, sediments and seismic lines are indicative of a depositional environment consistent with a deep-water setting near a submarine channel. This is in agreement with the location of the Site in the south levee of a submarine channel-levee system (Fig. 5.7).

#### 4.4.2. LONG TERM CHANGES IN THE PALEOCEANOGRAPHY AND THEIR ROLE IN TRIGGERING THE GLACIATION IN THE OMT

At Site U1356, Barium input is correlated with the detrital fraction in the Wilkes Land, with minimum biogenic input. In addition, bottom currents present in the Wilkes Land margin during this time-period affect Ba deposition and prevent its use as a paleoproductivity proxy (Bahr et al., 2014; Salabarnada et al., 2018). Continental influence of Ba can be driven by the runoff of shelfal Antarctic waters (Moore and Dymond, 1991; Abrahamsen et al., 2009; Roeske, 2011), as dissolved Ba has more affinity with silicic waters south of the Southern Boundary of the Polar Front (SBPF; Pyle et al., 2016). Here, we interpret Ba to provide us with a continental signal related to the formation of downslope currents south of the SBPF (Fig. 4.5). Si/Ti is used as a biogenic opal silicic surface productivity marker (A.N. Meckler et al., 2013), as XRD analysis in the same samples confirm that biogenic opal CT is present in the Si/Ti peaks (Fig. 4.2; 5). Zr/Ti is applied as a sediment grain-size proxy in marine records (Schneider, et al., 1997; Dypvik and Harris 2001; Croudace et al., 2006; Campagne et al., 2015), and as an indicator of accumulation of heavy minerals due to bottom currents influenced by CDW in the Southern Ocean close to the Wilkes Land (Salabarnada et al., 2018; Evangelinos et al., submitted) (Fig. 4.5). After the previous considerations, we introduce Zr/Ba as the ratio between the signal of CDW (Zr) and AABW (Ba) that would mark a hypothetical position of the Polar Front at Site U1356 that separates the two water masses (Fig. 4.5) for the Wilkes Land Site U1356. CaCO<sub>3</sub> wt% peaks correspond with the presence of biogenic carbonates composed by reworked coccolithophores as seen from the HR-SEM images. Carbonate preservation depends on the bottom water geochemistry, so a warmer less corrosive water mass is interpreted to bath the Site in CaCO<sub>3</sub> peaks. CaCO<sub>3</sub> represents the influence of northern warmer waters to the CDW (Fig. 4.5) (Salabarnada et al., 2018; Bijl et al., 2018; Hartman et al., 2018; Sangiorgi et al., 2018).

In order to observe changes in the configuration bottom water masses we take into account not only the geochemistry but also the ongoing changes in the continent and the ice sheet in the WSB.

Punctually during the latest Oligocene, and permanently during the early middle Miocene, sedimentation exhibits an increase in biosiliceous sedimentation that coincides with the deposition of the first glaciogenic MTDs and in particular with IRD deposition (Fig. 4.5). Erosion of the WSB and continental shelf progradation due to successive ice sheet advances contributes to the increase of silicate weathering and therefore nutrient availability and fertilization of the Southern Ocean, as described in the South Atlantic margin by (Etourneau et al., 2012). This fertilization would favour biogenic productivity, which in the long term could act as a feedback for dropping CO<sub>2</sub> concentrations and producing a global cooling (Renaudie, 2016) leading to the Mi-1. It is at the early mid Miocene when an important change in the geochemistry

of the ocean occurs with the establishment of a “seasonal” silica deposition system (Fig. 4.5) that we relate here to the presence of the Antarctic Divergence close to the Site.

At 25 Ma approximately, the increase in the thickness and frequency of laminations and Ba/Ti concentrations together with the absence of carbonated deposits suggests an increase in continental inputs by ice sheet advance and an increase in dense water formation (AABW) with migration of the SBPF to the north (Fig. 4.5).

This shifts of the frontal systems are a consequence of the southerly migration of the Westerly Winds (Peck et al., 2015; Toggweiler, 2006) and a weak frontal system, and are corroborated by the several carbonate layers deposited throughout the entire late Oligocene until the middle Miocene at Site U1356 (Salabarnada et al., 2018) and DSDP 269 (Evangelinos et al., submitted), that demonstrate the high variability of this systems. Site DSDP 269 reinforces the presence of a different bottom water mass from Nd measurements (Evangelinos et al., 2019), with the shift from more AABW during the late Oligocene towards CDW with warm incursions, based in carbonates with foraminifer shells. Peaks of carbonates in the Site U1356 with presence of nannofossils (CaO%) and warm water taxa dyncist were reported recording warm water incursions over the Site during the late Oligocene (Salabarnada et al., 2018; Bijl et al., 2018; Hartman et al., 2018) and the middle Miocene (Sangiorgi et al., 2018).

During the latest Oligocene, and during the glacial MTD deposition, 5 carbonate events are recognized in the sediments. The last warm carbonate event preserved in the Site is placed at 23.2 Ma, marking the last shift towards warm conditions before the Mi-1 glaciation. This warm water incursions are interpreted as a positive feedback for the glaciation, as a relatively warm climate would increase the moisture transported into the continent resulting in a higher accumulation of snow in the ice sheet (Ehrmann and Mackensen, 1992) equally as in the Miocene, where different studies related Antarctic ice sheet growth with times when ocean temperatures were particularly warm (Hollburn et al., 2005; Shevenell et al., 2008). This, in combination with low obliquity and eccentricity modes (Liebrand et al., 2016), avoided melting ice in summers and favoured glacial growth.

The Southern boundary of the Polar Front and the Antarctic Divergence separate a terrigenous sedimentation (laminations and Ba accumulation) to the south from a siliceous ooze deposition zone in the north. The siliceous zone is associated with the region between the Antarctic divergence and the Southern Boundary of the Antarctic polar front, with high silicic waters that promote silica diagenesis, and cyclonic gyres and upwelling controlling surface circulation (Godell, 1973; Anderson, 1999). The Polar Front is placed north of the Antarctic Divergence, and is here characterised by bioturbated and oxygenated sedimentation that is reworked by bottom currents caused by the vigorous circulation of the CDW. While warm intrusions of warmer Northern waters into the CDW are recorded as carbonate cemented intervals in Site U1356.



With the combination of the detailed sedimentological study and the XRF proxies we can get insights on which factors and processes that helped triggering the Mi-1 glaciation. The ocean is one of the most important Earth systems in heat transport and accumulation. There are still a lot of doubts on which triggers were responsible for the thermal isolation of the Antarctic continent. The establishment of the ACC and the decreasing of CO<sub>2</sub> concentrations are believed to be the responsible processes. Here we demonstrate that a strong oceanic meridional transport existed, with a NCW invigorated during warm interglacials and an AABW invigorated during glacials. The growth of the EAIS was at least triggered by moisture inputs during interglacials, brought to the Antarctic continent by the NCW that arrived to a southerly position, at minimum to Site U136. Warm waters and humidity in combination with long term low eccentricity and obliquity orbital configurations (Liebrand et al., 2016) boosted the growth of an ice sheet with cold and humid interglacials that prevented snow melting, and cold glacials where ice sheet development.

#### 4.5. CONCLUSIONS

Site U1356 records the presence of in situ sediments interbedded between glacial mass transport deposits (MTDs) in the continental rise, that we interpret as at least 8 times of EAIS advancing into the continental shelf. However, the presence of calcareous nannofossils within the in situ sediments points to warm conditions prevailing during times of ice sheet retreat. The presence of more distal and hemipelagic sediments preserved in-between the MTD events indicates a highly dynamic EAIS with important fluctuations of the ice margin, and thus important ice volume changes during the latest Oligocene.

A sharp shift in sedimentation style on the continental rise (from dominant MTD deposition to turbidite and hemipelagic deposition) at around 23.4 Ma points to an important and irreversible change in the configuration of the EAIS in this margin sector. We interpreted the shift from MTD to turbidite dominated deposition at Site U1356 to represent a major threshold in the behaviour of the East Antarctic Ice Sheet in this sector of the east Antarctic margin. We interpret this threshold to correspond with the shift from a continental-based to a marine-based EAIS caused by erosion and overdeepening of the Wilkes Subglacial Basin during successive ice sheet expansions related to the Mi-1 cooling event.

At the early middle Miocene (> 17 Ma) a shift to overall finer-grained sediments is interpreted to imply a landward change in depositional depocenters. We cannot however know at this time if this shift is related to overdeepening of the continental shelf.

At 25 Ma approximately, AABW formation strengthens, as seen from the increase in laminated bare facies with elevated Ba/Ti concentrations. AABW can boost climate cooling being the precursor of the MTDs and thus the Antarctic glaciation.

The preservation of carbonated nannofossils in some of the interglacial sediments deposited throughout all the latest Oligocene, is taken to indicate that the proto-CDW bathing U1356 is modified by warmer north component waters (i.e., NADW-like) intruding closer to the Antarctic. A thick carbonate layer dated at 23.2 Ma precedes the final transition to the transient glaciation of the Mi-1 event.







# Chapter 5

Oligocene to Miocene bottom current  
deposition and circulation off the Eastern  
Wilkes Land margin

---



## CHAPTER 5

# OLIGOCENE TO MIOCENE BOTTOM CURRENT DEPOSITION AND CIRCULATION OFF THE EASTERN WILKES LAND MARGIN

### 5.1. INTRODUCTION

The early to middle Eocene warmth was followed by cooling, declining atmospheric CO<sub>2</sub>, and coeval tectonic reorganizations. These changes culminated in the development of a continental-scale ice sheet in Antarctica around the Eocene-Oligocene transition (around 34 Ma), and in a major reorganization of the Southern Ocean, including the formation of Antarctic Bottom Waters (AABW) and the initiation of the Antarctic Circumpolar Current (ACC).

Today, the Antarctic ice sheet and the Southern Ocean are key components of the global climate system. Cold and salty AABW form on the continental shelves of the Weddell Sea, the Ross Sea and Adélie Land, sink to the deepest depths of the oceans, and spread far north beyond the Equator to exchange with waters of the Northern Hemisphere. The ACC connects all major oceanic basins and prevents the north-south exchange of CO<sub>2</sub>, heat and moisture, isolating Antarctica from the influence of warmer waters to the north (Rintoul et al., 2001). The ACC consists of multiple jet-like fronts that are greatly influenced by the topography at the seafloor (Rintoul et al., 2018). The deep Circumpolar Deep Water (CDW) originates and circulates along the ACC.

Despite the relevance of the AABW and the ACC in the Earth Climate System, there are many unknowns regarding their origin and evolution towards modern conditions. This knowledge is however necessary because unabated climate warming is expected to have an effect in Southern Ocean circulation and ocean-ice sheet interactions, and thus, in the global ocean circulation. At present, satellite monitoring shows that the rate of marine basal melting (i.e., warm ocean water melting of marine-terminated ice sheets from below) has exceeded that of surface melting due to radiative forcing (Rignot et al., 2013, 2019; Wouters et al., 2015). In addition, in the last years, surface and deep waters of the Southern Ocean have freshened as a result of increases in melt from Antarctic ice shelves (Rintoul et al., 2009). To put these changes into perspective and in the context of climate warming predictions, it is critical to improve our understanding of past paleoceanographic configuration and their interaction with the Antarctic ice sheet.

The marine sediment record holds information about how the AABW, the ACC and the CDW have evolved from the early Oligocene (i.e., onset of continent-wide Antarctic glaciation) to present day. At this time, there is some controversy regarding the timing of the onset of the ACC. Neodymium (Nd) isotopes measured in sediments by Scher and Martin (2006), provided evidence for a middle Eocene



connection between the Atlantic and Pacific Oceans around 40–37 Ma. Other authors have argued that the beginning of the ACC took place between 33–28 Ma based on: 1) the temporal distribution of biogenic (i.e., shift from calcareous to siliceous microfossils in Southern Ocean sediments) sedimentation, Nd isotopes, and Al/Ti ratios through a core transect across the Australian–Antarctic basin in the Southern Ocean (Scher et al., 2015); and 2) the existence of regional erosional unconformities (the Marshall paraconformity) marking a shift from low- to high-energy environments (Carter et al., 2004). In contrast some studies argue for the onset of a deep ACC to occur at the Oligocene-Miocene boundary (around 24–23.03 Ma) based on erosional surfaces in the Tasman Gateway (Pfuhl and McCave, 2005) and in the South Pacific at the late Oligocene (Lyle et al., 2007). On the other hand, AABW formation has been reported since the Eocene in the eastern Wilkes Land margin (Huck et al., 2017), with widespread evidence for an important proto-AABW circulation since the Late Eocene (Gruetzner & Uenzelmann-Neben, 2016; Uenzelmann-Neben et al., 2007).

Seismic stratigraphic records can also be used to understand past and present bottom water circulation in oceanic basins that can then be correlated with global climate records (e.g., Stow et al., 2002). For example, using seismic reflection profiles Escutia et al. (2002) showed the formation of mixed turbidite-contourite deposits in the eastern Wilkes Land margin to be associated with westward flowing bottom current. Maldonado et al. (2005) used seismic reflection profiles and multibeam bathymetric data to provide information about the “exit” paths for the Weddell Sea bottom water towards the Scotia Sea. Lately, clockwise oceanic currents within the Antarctic-Australian basin were described to occur since the Paleogene/Eocene boundary ~58 Ma until the late Eocene. This current formed drifts along the continental slopes of Australia and Antarctica following the proto-Leewind current (Sauermilch et al., 2019) and that is totally disconnected from the Pacific Ocean (Huber et al., 2004; McGowran et al., 1997; Sijp et al., 2014).

Bottom-current sedimentation in the eastern Wilkes Land margin is evident since the early Oligocene but still needs to be determined if these currents are regional or if they can be tied to coeval bottom-contour current activity on the Pacific side of the gateway, and if they are truly circum-Antarctic. Seismic data shows a large build-up of levee deposits influenced by contour currents to take place above a regional unconformity related to the Oligocene-Miocene (OM) transition leading to glacial advance during the Mi-1 event (Escutia et al., 2000, 2002, 2011, 2014). Following the Mi-1 event, sedimentation is characterized by hemipelagic, turbidity-, and bottom-current deposition (Escutia et al., 2011). From ~17 Ma onward, progressive deepening and possible intensification of deep-water flow and circulation lead to a transition from a poorly oxygenated low-silica system to a well-ventilated silica-enriched system similar to the modern Southern Ocean (Escutia et al., 2011). That this transition is related to the development or intensification of the ACC and the variations of the ACC/CDW from that time to recent are little known.

Correlation between sediments recovered from site U1356 sediments and the regional grid of multichannel seismic reflection profiles allow us to differentiate a variety of contourite deposits resulting from the

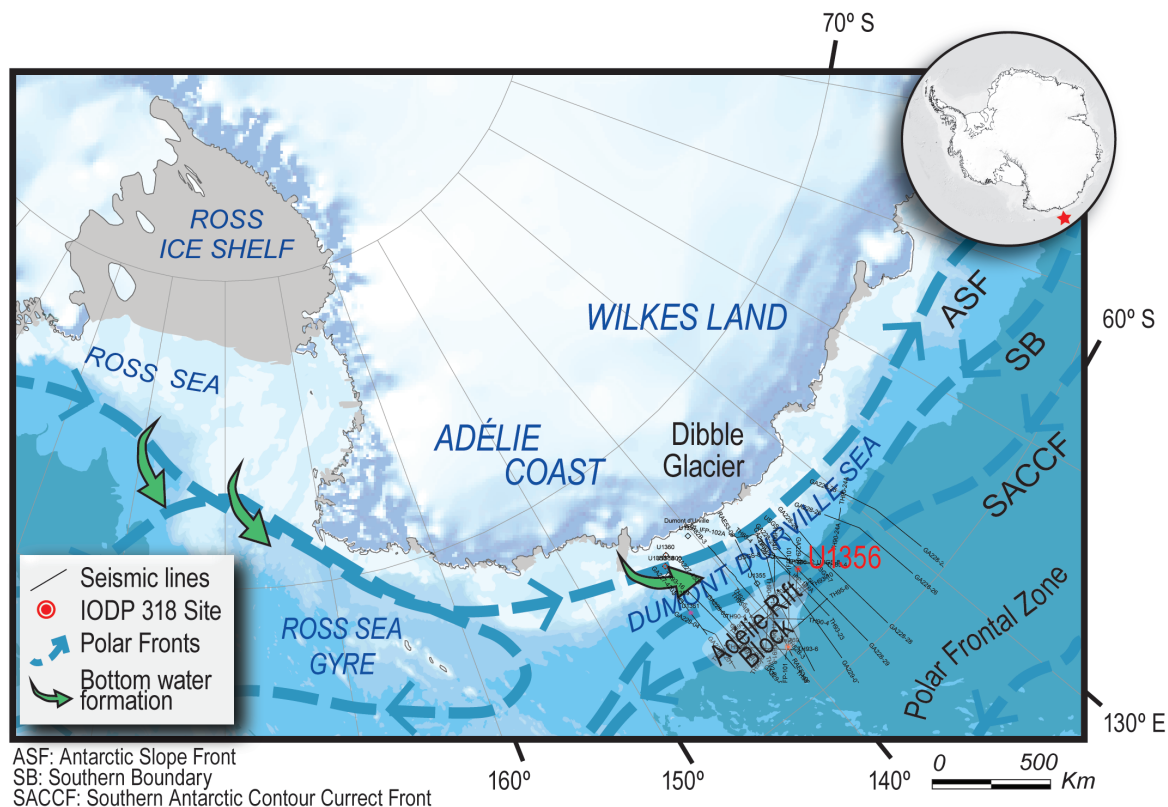
interaction between bottom currents and sea-floor paleomorphologies. In this paper we examine the Oligocene and Miocene evolution of Antarctic Bottom Water (AABW) and the Circumpolar Deep Water (CDW) circulation through a seismic-stratigraphic analysis of contourite drifts on the eastern Wilkes Land Margin and along the Adélie Rift Block (ARB). We use seismic-reflection profiles that are correlated with two cores, IODP Site U1356 (Escutia et al., 2011) and DSDP Site 269 (Hayes et al., 1975) that provide a sedimentary linkage. Our analysis focuses on sedimentary packages that have distinct internal architecture and mappable boundaries that are tied with an age control from Site U1356, which allows us to interpret the history of deep-ocean circulation in the Southern Ocean during transient climatic changes.

## 5.2. GEOLOGIC FRAMEWORK OF WILKES LAND AND SITE U1356

The Wilkes Land continental margin was formed by tectonic break-up of the Antarctic and Australian continents with a West to East propagation direction that started not later than the Early Eocene at the eastern Wilkes Land Margin (Colwell et al., 2006; Close et al. 2009; Direen et al., 2013). The final separation with the opening of the Tasman Gateway occurred during the middle Eocene with a rapid deepening at 35.5 Ma reported from the Tasman Rise region (Stickley et al., 2004). In the eastern Wilkes Land margin the record of the deepening of the Tasman gateway is masked by the WL-U3 regional unconformity. Sediments below and above the unconformity recovered at site U1356 record a hiatus of 13 million years (myr) between ~47 – 33.6 Ma (Escutia et al., 2011; Tauxe et al., 2012). Middle Eocene (~47 Ma) sediments were deposited in a shelf environment while earliest Oligocene (33.6 Ma) strata above the unconformity record deposition in a deep setting.

The studied segment of the east Antarctic Wilkes Land is located between 145° and 130°E longitude and between 60° and 65°S latitude (Fig. 5.1). The continental shelf is irregular with deep shelf troughs eroded during times of ice sheet advance and shallow shelf banks between them. The continental slope extends from the shelf break to about 2000-2500 m of water depth. The slope is steep (gradients between 1:9 and 1:30), narrow (15 Km average) and incised by numerous submarine canyons (Escutia et al., 2000). The continental rise is also relatively steep (average gradients greater than 1:100 in the upper rise to less than 1:150 in the lower rise) and rugged because of a complex network of tributary-like channels that continue from the slope canyons and the existence of high-relief levees and sediment ridges (Escutia et al., 2000; 2002). The lowermost continental rise and the abyssal plain off Wilkes Land is occupied by the Adélie Rift Block (ARB). The ARB is a faulted rifted continental crust block (Tanahashi et al., 1997; Close et al., 2007) consisting of an NW-SE trending horst and graben complex and isolated seamounts formed during the rifting of the Australian-Antarctic basin (Eittrheim, 1995; Colwell et al., 2006). The ARB is 130 km long with a maximum width of 66 km in the eastern side and a minimum width of 22 km towards the west. The highest point of the ARB is placed to the east of the study area with a depth of 3000 mbsl and exhibits a plateau-like irregular morphology. Post-rift strata lies above a major regional unconformity named WL-U3 (Escutia et al., 1997, 2000, 2005; De Santis 2003).





**Figure 5.1.** Location of IODP 318 Site U1356 (Escutia et al., 2010) on the Adélie coast continental rise. Bed topography from IBSCO2 (Arndt, JE et al., 2013). Schematic position of the different water masses at present and locations of Antarctic Bottom Water formation (Orsi, 1995) are indicated. The position of the Oligocene Polar Front (Scher et al., 2015) is also shown. ASF: Antarctic Slope Front; SB: Southern Boundary; SACCF: Southern Antarctic Counter Current Front; ARB: Adélie Rift Block.

The Integrated Ocean Drilling Program (IODP) Expedition 318 drilled Site U1356 ( $63^{\circ} 18.61380' S$ ,  $135^{\circ} 59.9376' E$ ) off the Eastern Wilkes Land Coast, at 3992 m water depth. The drilling penetrated 1006.4 mbsf (meters below sea floor) into the flank of a levee deposit on the lower continental rise (Fig. 5.1; Escutia et al., 2011). Sediments recovered from site U1356 are dated from the early Eocene to the Pliocene (Escutia et al., 2011). Drilling at IODP Site U1356 confirmed unconformity WL-U3 to be separating pre-glacial from glacial deposits, with the earliest glacial deposits recovered dated from the earliest Oligocene (33.6 Ma) (Escutia et al., 2011, 2014; Tauxe et al., 2012). Lithofacies consist dominantly of bioturbated siltstones and claystones with variable carbonate content, that are interbedded with laminated silty claystones sandstones and siltstones with cross laminations, mass transport deposits, and mudstones, and sandstones with dispersed clasts of different sizes. These sediments result from hemipelagic settling, gravity flows and bottom current reworking (Escutia et al., 2011).

Correlations of the stratigraphic record obtained from Site U1356 with the grid of multichannel seismic reflection profiles in the studied area have been conducted and are explained in detail in Chapter 4 of this thesis. Oligocene and Miocene strata are comprised between unconformities WL-U3 and WL-U6 (Fig. 1.6 from Chapter 1) that are bounding seismic units WL-S4, WL-S5, and WL-S6, respectively (Fig. 4.6

from chapter 4) (Escutia et al., 2002, 2005, 2011, 2011b; De Santis et al., 2003).

The regional grid of seismic reflection profiles also crosses Deep Sea Drilling Project (DSDP) Leg 28 Site 269 ( $61^{\circ}40.57'S$ ,  $140^{\circ}04.21'E$ , 4282 m water depth), located on the abyssal plain, 350 km to the NNE seaward from site U1356 (Fig. 5.1; Hayes et al., 1975). Sediments from Site 269 have been dated earliest Oligocene to Miocene (Hayes et al., 1975). And are mostly comprised by a mixtures of turbidites and contourites, with strong winnowing by bottom currents (Hayes et al., 1975).

Site U1356 has a paleolatitude history that changed from between  $59.8^{\circ}S \pm 4.8^{\circ}$  and  $61.5^{\circ} \pm 3.3^{\circ}S$  between 34 and 13 Ma, respectively (Bijl et al., 2018), based in the paleolatitude calculator of van Hisbergen et al. (2015). Site 269A has a paleolatitude of around  $60^{\circ}$  during the Oligocene-Miocene Transition (OMT) (Nelson and Cook, 2001).

### 5.3. METHODS

For this study we use the available multichannel reflection (MCS) seismic lines in the study area that are accessible through the Antarctic Seismic Data Library System SDLS (<http://sdls.ogs.trieste.it>). The analysis of the seismic profiles and the mapping of bottom current related deposits were achieved using the IHS Kingdom Software.

Using the MCS profiles, we generated paleosurfaces maps of the three major regional unconformities previously defined in the study area and comprised within the studied sediment cores. From older to younger these unconformities are named WL-U3, WL-U4, and WL-U5 (Eittrheim et al., 1995; Escutia et al., 1997, 2000, 2002, 2005, 2007; Donda et al., 2003, 2007; De Santis et al., 2003; 2010). We mapped each unconformity and through simple gridding interpolation we obtained paleosurface maps for each chosen period of time. It is important to note that our paleosurface reconstructions are not decompacted for the effect of thermal and sediment loading subsidence. Therefore, these reconstructions are not true topographic reconstructions but they are generated to help in understanding the distribution of relieves and depocenters that controlled the paths of currents and sediment deposition in the margin, respectively. All maps are plotted in Two Way Travel Time (TTWT) below sea level. We use the universal polar stereographic coordinate system (UPS) South Zone and the geodetic datum and ellipsoid WGS 1984.

We then conducted a morphosedimentary and seismic stratigraphic study of the seismic units that are bound by each of these paleobathymetric surfaces/unconformities. These seismic units have been previously named from older to younger WL-S4, WL-S5, and WL-S6, and characterized by several authors (Escutia et al., 1997, 2000, 2002, 2005, 2007; Donda et al., 2003, 2007; De Santis et al., 2003). The morphosedimentary study is focused in the analysis of the external morphologies of sedimentary deposits and their internal seismic facies following Mitchum et al. (1977). Because this study focuses on the study



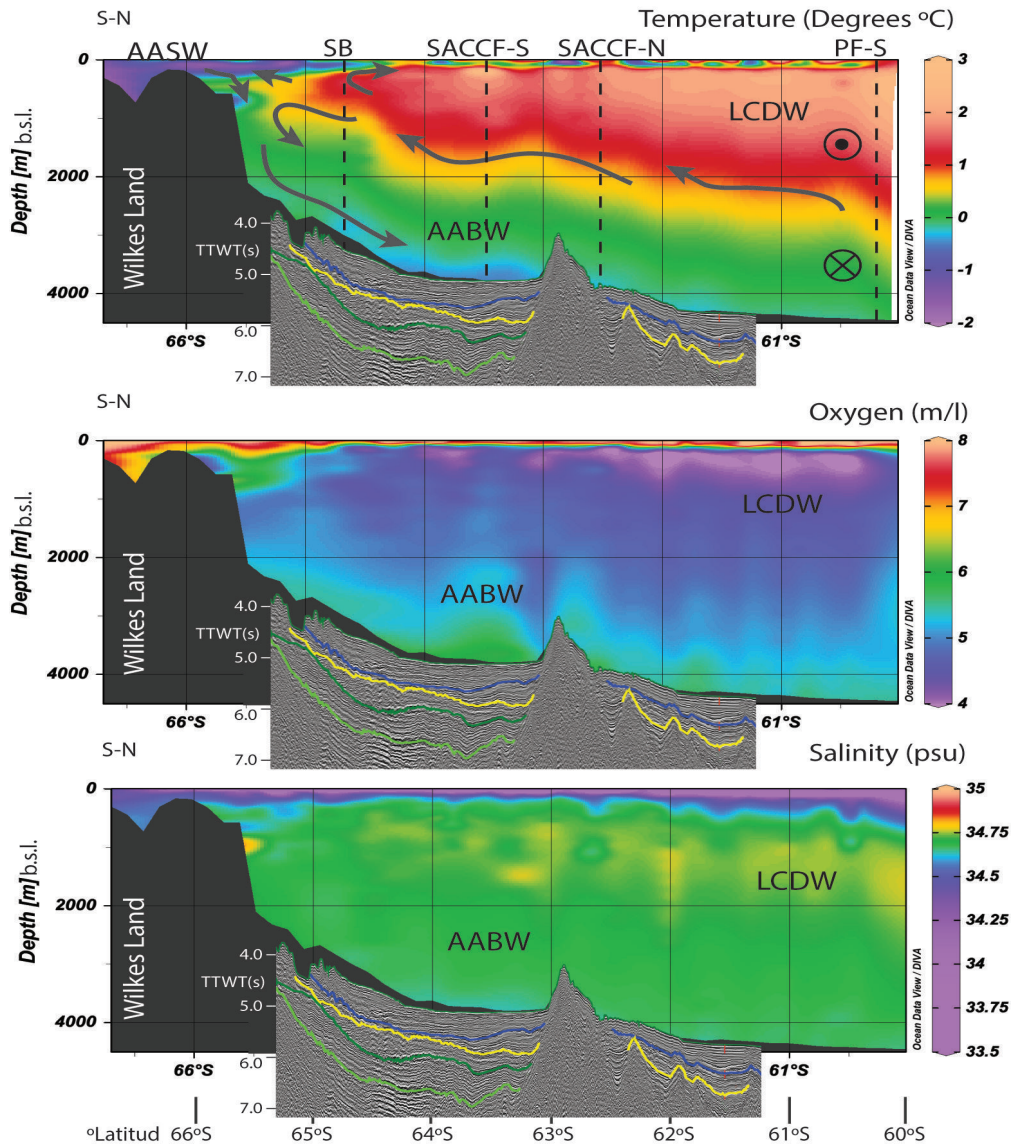


of bottom current deposits, we follow the contourite facies descriptions of Faugères et al. (1999) and Faugères and Stow (2008), later modified by Rebesco et al. (2014) to define the morphosedimentary features identified in our data.

#### 5.4. OCEAN CIRCULATION IN THE WILKES LAND MARGIN

Today, the Southern Ocean consists of three deep-water masses that are distinguished based in the potential temperature and salinity (Fig. 5.2; Rintoul et al., 2001; Pardo et al., 2012): 1) The Circumpolar Deep Water (CDW) being the most voluminous water mass in the Southern Ocean (53%); 2) the Antarctic Bottom Water (AABW, 17%); and 3) the North Atlantic Deep Water (NADW; 13%). The CDW is comprised by a mixture of 65% AABW, 30% NADW and 5% Antarctic Intermediate Water, and is divided into Lower CDW (LCDW) and Upper CDW (UCDW). The main flow direction of the CDW is towards the East being part of the deep reaches of the Antarctic Contour Current (ACC). The AABW, which is a key contributor of the oceanic Thermohaline circulation, is generated due to temperature and density changes produced by brine rejection and cooling of the water masses under floating ice shelves and polynyas (e.g., Fukamachi et al., 2000). The ABBW is a combination of three distinctive deep-water masses: the Weddell Sea Bottom Water (WSBW) (77%), Ross Sea Bottom Water (RSBW) (20%), and the Adélie Land Bottom Water (ALBW) (3%) (see review by Pardo et al., 2012 and references therein). In the eastern Wilkes Land region, around 140°E (Fig. 5.2), the AABW is composed mainly by ALBW (Bindoff et al., 2000). The ALBW occupies the deepest zones of the margin between 2000 and 6000 meters depth although its distribution is influenced by the topography of the slope and the presence of the ARB. Antarctic Surface Waters (AASW; Fig. 5.2) have a westward flow with near-freezing temperatures and low salinity, and mixes with the upwelled CDW forming the modified CDW (mCDW).

Hydrographic data from the World Ocean Database (<http://www.nodc.noaa.gov>) WOD13 is used to provide contextual oceanography for the observed seafloor morphologies in the Wilkes Land Margin. Water masses within the studied sector of the Wilkes Land Margin were identified (Lambelet et al., 2018) using Ocean Data View (ODV) software (Schlitzer, 2017, <https://odv.awi.de>). Figure 2 shows hydrographic profiles of potential temperature, oxygen, and salinity cross-section along 140°E longitude and 66°S to 60°S latitude off the Wilkes Land. Three different water masses can be identified along this transect: the AABW, LCDW, and the AASW based in their properties (Rintoul et al., 2001). The AABW occupies the lower zone of the basin below 2000 m and is characterised by cold ( $<0^{\circ}$ ), high dissolved oxygen (6.31 m/l), and saline (34.6 psu). Above, relatively warm (2.06°C), low oxygenated (4.47 m/l), and more saline (34.77 psu) is the LCDW (Fig. 5.2). The Antarctic Slope Front separates fresh and cold Antarctic shelf waters (AASW) from warmer, more saline waters of the CDW (Carter et al., 2009). The contact between AABW and LCDW is inclined towards the north following the topography of the seafloor. Several bumps or eddies are present with the seafloor inclination changes, in particularly around the ARB and in the transition from the continental rise to the abyssal plain.



**Figure 5.2.** Hydrographic profile dataset extracted from WOCE (<https://www.nodc.noaa.gov>) along a transect at 140°E from the Wilkes Land Margin. (a) Temperature profile with a schematic view of the meridional overturning circulation in the Southern Ocean, adapted from Rintoul et al. (2001). Dotted lines in panel (a) show approximate major frontal locations. (b) Oxygen and (c) salinity. AASW = Antarctic Surface Water; AAIW = Antarctic Intermediate Water; UCDW = Upper Circumpolar Deep Water; LCDW = Lower-CDW; AABW = Antarctic Bottom Water; PF-S = southern branch of the PF; SACCF-N = northern branch of the Southern ACC Front; SACCF-S = southern branch of the Southern ACC Front; SB = Southern Boundary of the ACC. Sections were created using ODV software (Schlitzer, 2012). Profile represented is RAE53-06.

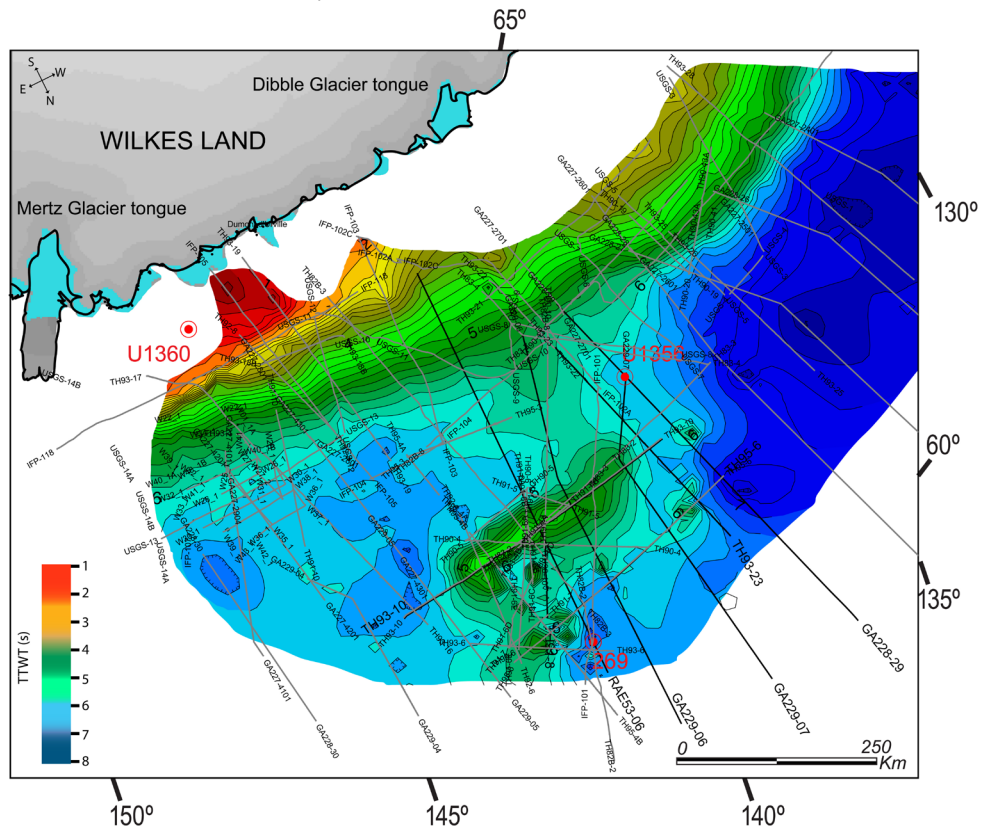
## 5.5. RESULTS

### 5.5.1. PALEOSURFACE RECONSTRUCTIONS

We conducted paleosurface reconstructions for the three major regional seismic unconformities previously described in the eastern Wilkes Land margin: WL-U3, WL-U4 and WL-U5 (Escutia et al., 1997, 2002, 2005; De Santis et al., 2003). These reconstructions comprise the lower slope, rise and abyssal plain because unconformities WL-U4 and WL-U5 generally onlap or downlap strata at the base of the slope



a) WL-U3 unconformity



b) WL-U4 unconformity

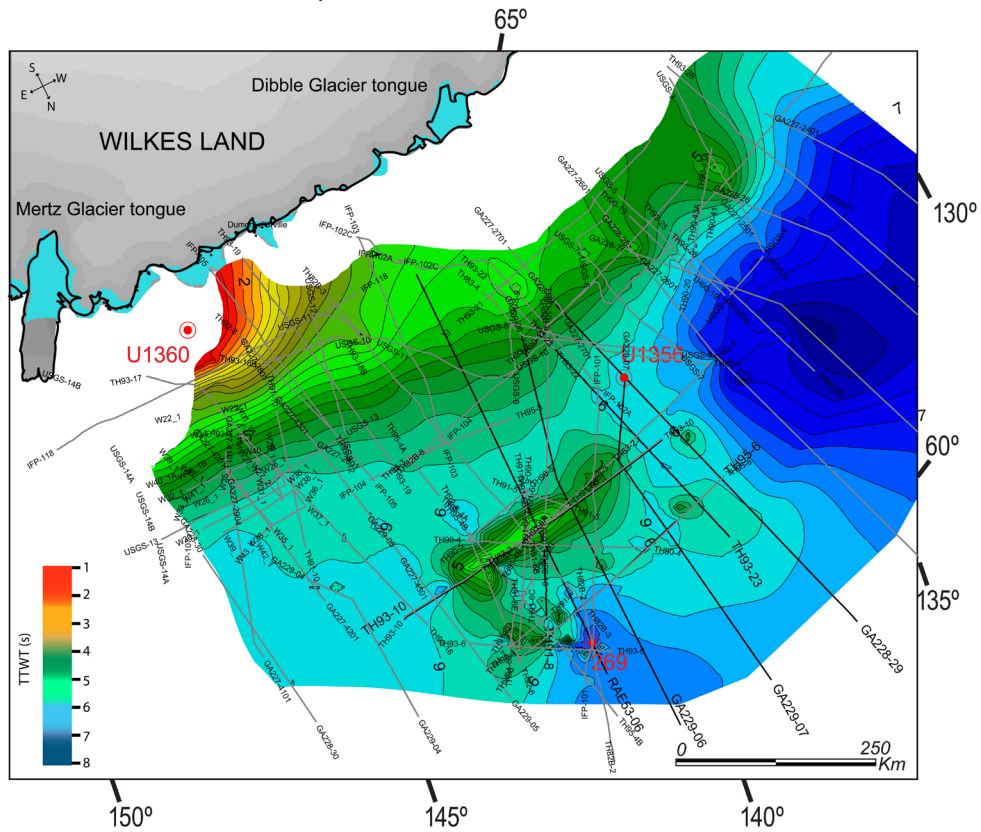


Figure 5.3. Paleosurfaces maps of three major regional unconformities previously defined in the study area: a) WL-U3, b) WL-U4, and c) WL-U5 from the eastern Wilkes Land margin.

## c) WL-U5 unconformity

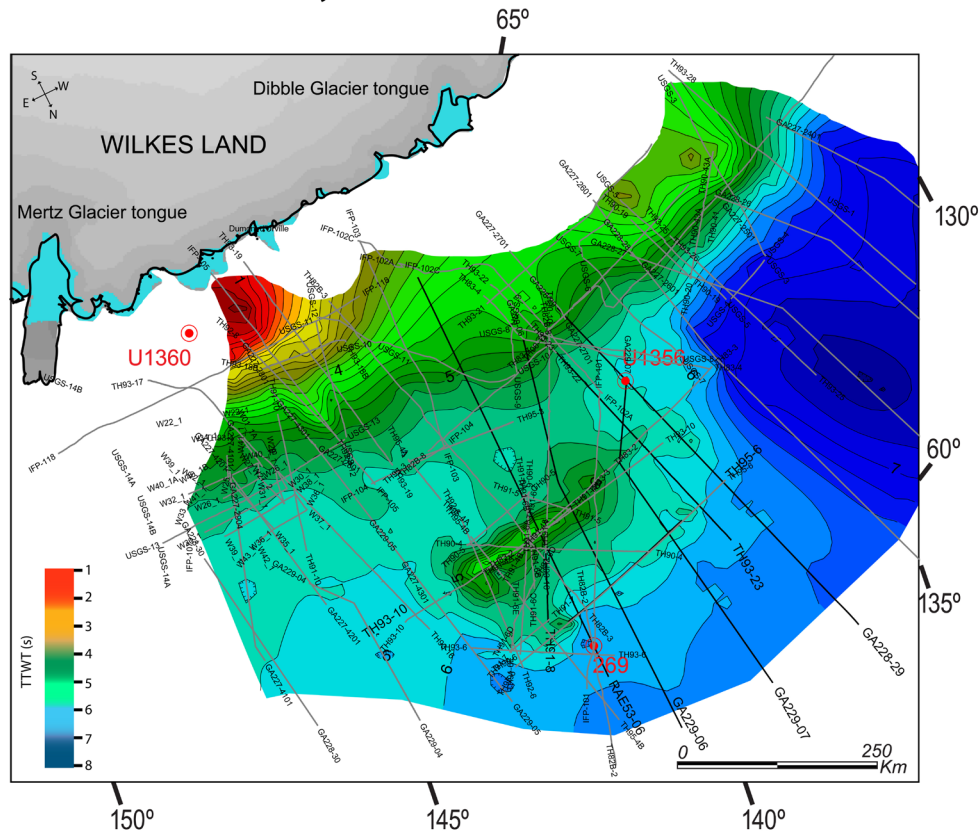


Figure 5.3. Continued.

(Escutia et al., 1997, 2002, 2005; De Santis et al., 2003) and don't provide information on the continental shelf.

Reconstructed WL-U3 paleosurface (Fig. 5.3a) shows a rather smooth slope with a steep gradient. Two deep basins occupy the continental rise. The basin to the east is shallower (i.e., between 6 to 6.6s TWT), while the one to the west is deeper reaching depths of 7s TWT, in the area of the Australian-Antarctic basin. The lower continental rise and the abyssal plain have a rough surface inherited from buried horst and grabens that are the structural remnants from the opening of the Australian-Antarctic basin (Close et al., 2009). These horst and grabens create a relief that is up to 0.8s TWT (Fig. 5.5.3a) with the ARB walls starting at 6s TWT.

The WL-U4 paleosurface reconstruction (Fig. 5.3b) shows the beginning of the development of small gullies and channels in the slope. In the continental rise landward of the ARB, the eastern basin has filled and the topography becomes smoother while the basin to the west is still deep. Structural highs around the ARB are still protruding, although the maximum relief decreases to up to 0.5 TWTs with the ARB walls starting at 5.8s TWT. Basins seaward of the ARB still have an irregular topography.

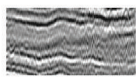
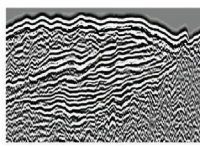
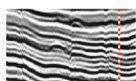
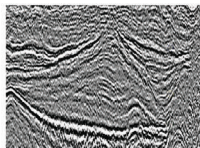

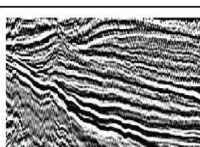
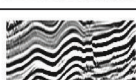
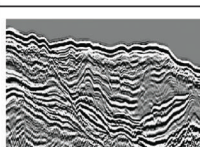
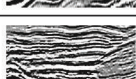
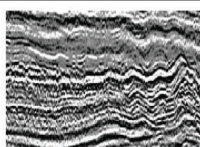
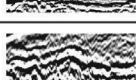
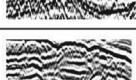

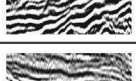
WL-U5 paleobathymetry (Fig. 5.3c) shows a slope that is steeper and more incised in the western zone. At the continental rise a landward migration of the main channel system is observed. The ARB steeper

walls are placed at 5.2s TWT. The eastern basin is completely filled up and exhibits a smooth morphology, while the eastern basin is still deep. The zones seawards of the ARB sector become smoother than before due to sediment filling, although big remnant reliefs from previous basement morphologies are still present. The abyssal plain has a nearly flat surface (Fig. 5.7c).

To the east of the western basin a channel descends perpendicular to the slope, and turns towards the West in the continental rise, acquiring a slope parallel direction (Fig. 5.7b). The channel starts forming at WL-U3, but it is not until after WL-U5 where channel development is clearly identified in the topography.

**5.5.2. CONTOURITIC DEPOSITIONAL AND EROSIONAL FEATURES:**

In this work we describe deposits associated with bottom current circulation on the basis of their setting in the margin and on their seismic facies and external morphology following the updated classification of Rebesco et al. (2014, and references therein). Based on this classification the following types of depositional and erosional features have been observed in the studied area (Fig. 5.4): Sheeted, plastered, elongated, mounded and separated drifts, channel-related patch drifts, and mixed drifts, contouritic moats and

| Seismic Facies and geometries   | Characterization  | Seismic external morphologies  | Contourite deposits                             |
|---|---|--|---|
|  | Semi transparent, non-continuous reflectors, of low amplitude.  |  | Plastered drift                                 |
|  | Parallel continuous reflectors of high and medium amplitude. Lenticular small mounds interpreted as sand dunes can be seen at top of some reflectors. |  | Giant mounded drift                             |
|  | Parallel reflectors. Medium amplitude. Reflectors onlap the ridge   |  | Contouritic moat with separated elongated drift |
|  | Parallel and continuous wavy parallel reflectors. Sediment waves with wedge morphology.   |  | Contourite channel and related drifts           |
|  | High amplitude semiparallel reflectors, onlap fill of a channel   |  | Sediment waves                                  |
|  | Semi chaotic lenticular reflectors of high amplitude  |  |   |
|  | chaotic reflectors of medium amplitude  |  |   |
|  | Hummocky and lenticular reflectors of medium amplitude  |  |   |
|  | Divergent wavy reflectors   |  |   |

**Figure 5.4.** Main seismic facies identified on the multichannel seismic data with their reflection characteristics (internal geometries, continuity, amplitude, shape). Their identification and interpretation is based on a contourite deposition based in Rebesco et al., (2014).

contouritic channels, and mixed contouritic turbiditic drifts.

Sheeted morphologies present planar to subparallel reflectors with an aggrading pattern. These morphologies are commonly observed on the abyssal plains and can be produced by hemipelagic, distal turbidite and mass transport deposits, contourites or the interaction of all these processes (Rebesco et al., 1997, 2014; Kuvaas and Leitchenkov 1992; Escutia et al., 2002). In the absence of sediment cores, we interpret these morphologies as mixed sheeted drifts.

Plastered drifts are characterized by parallel to subparallel and mounded reflectors (Figs. 5.4, 5.5; Faugères and Stow, 2008). Plastered drifts are observed climbing against the continental slope and at the walls of the ARB (Fig. 5.5).

Giant elongated mounded drifts form convex asymmetrical morphologies that are observed aligned parallel to the slope (Figs. 5.4, 5.5) as a result of the action of a high velocity flux (Miramontes et al., 2019) and develop in areas with a steep topography within the ARB (Fig. 5.5). Giant elongated mounded drifts are generally associated with a contourite moat located in one or both of its lateral margins (Figs. 5.4, 5.5).

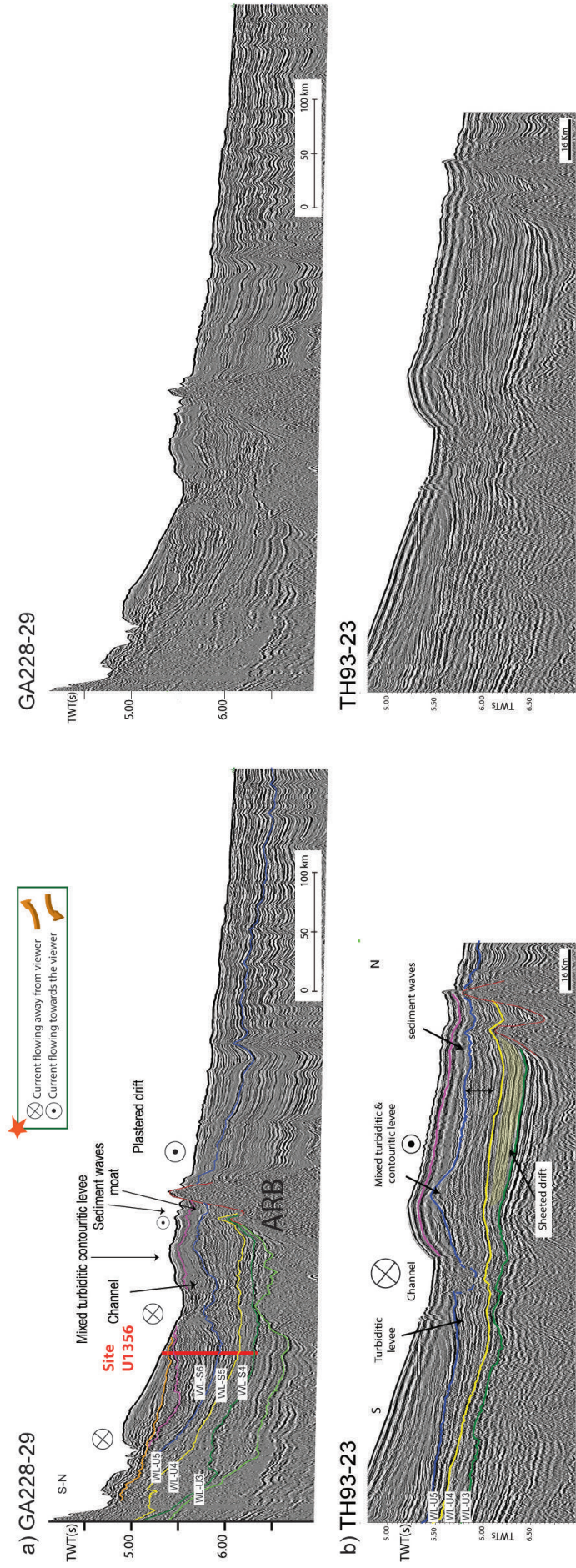
Irregular and small-mounded discontinuous sediment bodies with wavy bedforms are observed in the floors and walls of erosional depressions within the ARB, and are classified as channel patch drifts (Figs. 5.4, 5.5b; Rebesco et al., 2014). Channel patch-drifts are deposited inside the contouritic channel and also at the down current exit of it (Rebesco et al., 2014).

Contouritic moats are channels that originate beneath the flow path of a bottom current. In the study area they are generally non-erosive and are associated with elongated mounded separated drifts (Figs. 5.4, 5.5). Contourite channels are erosional and have complex morphologies with truncated reflectors (Fig. 5.4) and are observed associated to the patched drifts (Fig. 5.4).

Sediment waves are composed of parallel to subparallel aggrading undulating reflectors (Figs. 5.4, 5.5). They are commonly related to a topographic perturbation such as the ARB or associated to plastered or elongated drifts.

Levee deposits associated to submarine channels on the continental rise can present a displacement of the levee crest away from the channel caused by the interaction between overbank flows and bottom currents (Fig. 5.5a,b). In addition, sediment waves are also common in turbiditic channel levees (Fig. 5.5a,c) and are identified as they migrate upslope and decrease in amplitude downslope (Wynn and Stow, 2002) implying high sediment supply (Migeon et al., 2000).





**Figure 5.5.** Interpreted (left) and un-interpreted (right) selected regional multichannel seismic profiles, with a location map on the center. Profiles show main seismic unconformities (WL-U3, WL-U4, and WL-U5), and their correlative seismic units.

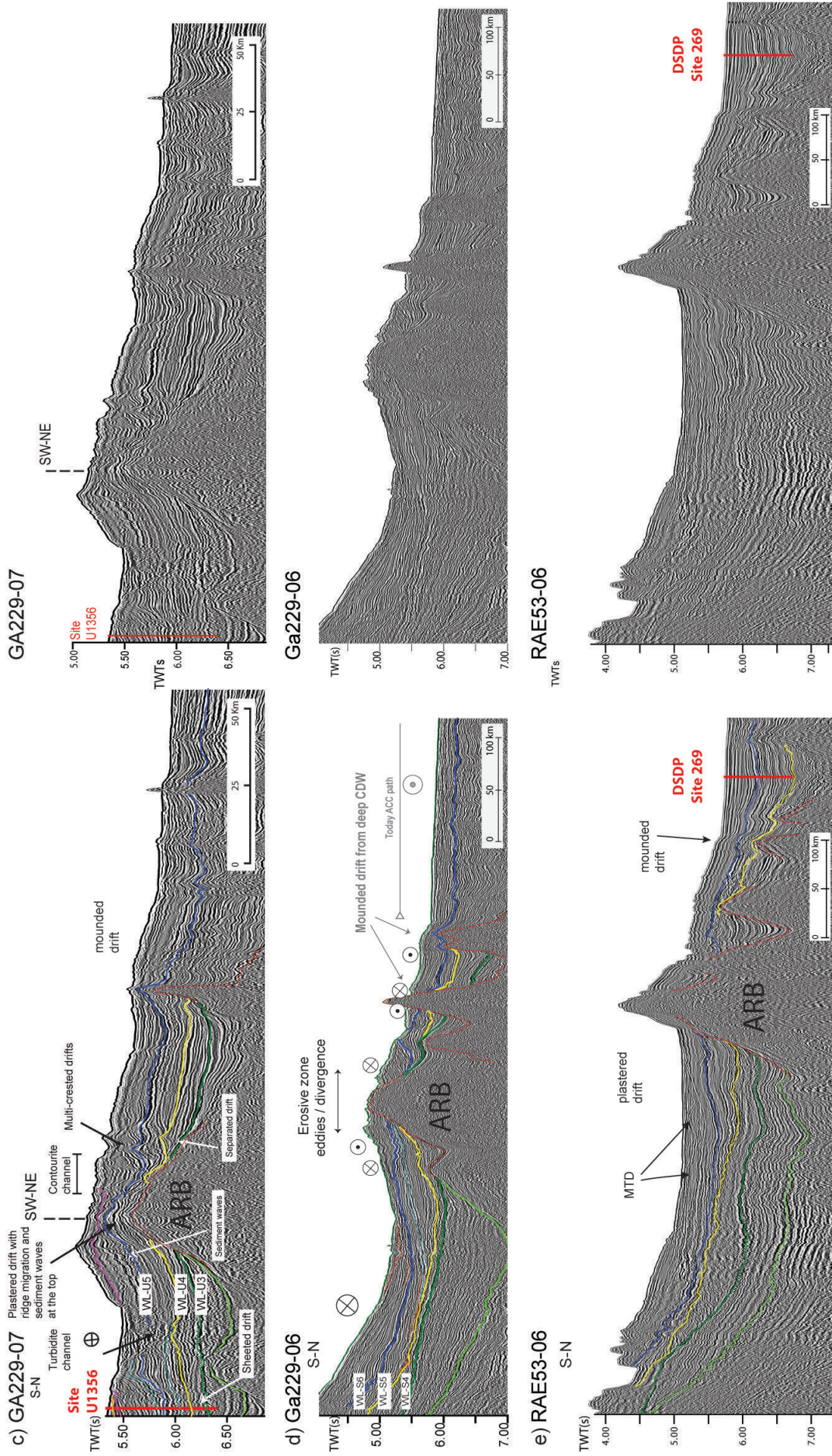


Figure 5.5. Continued





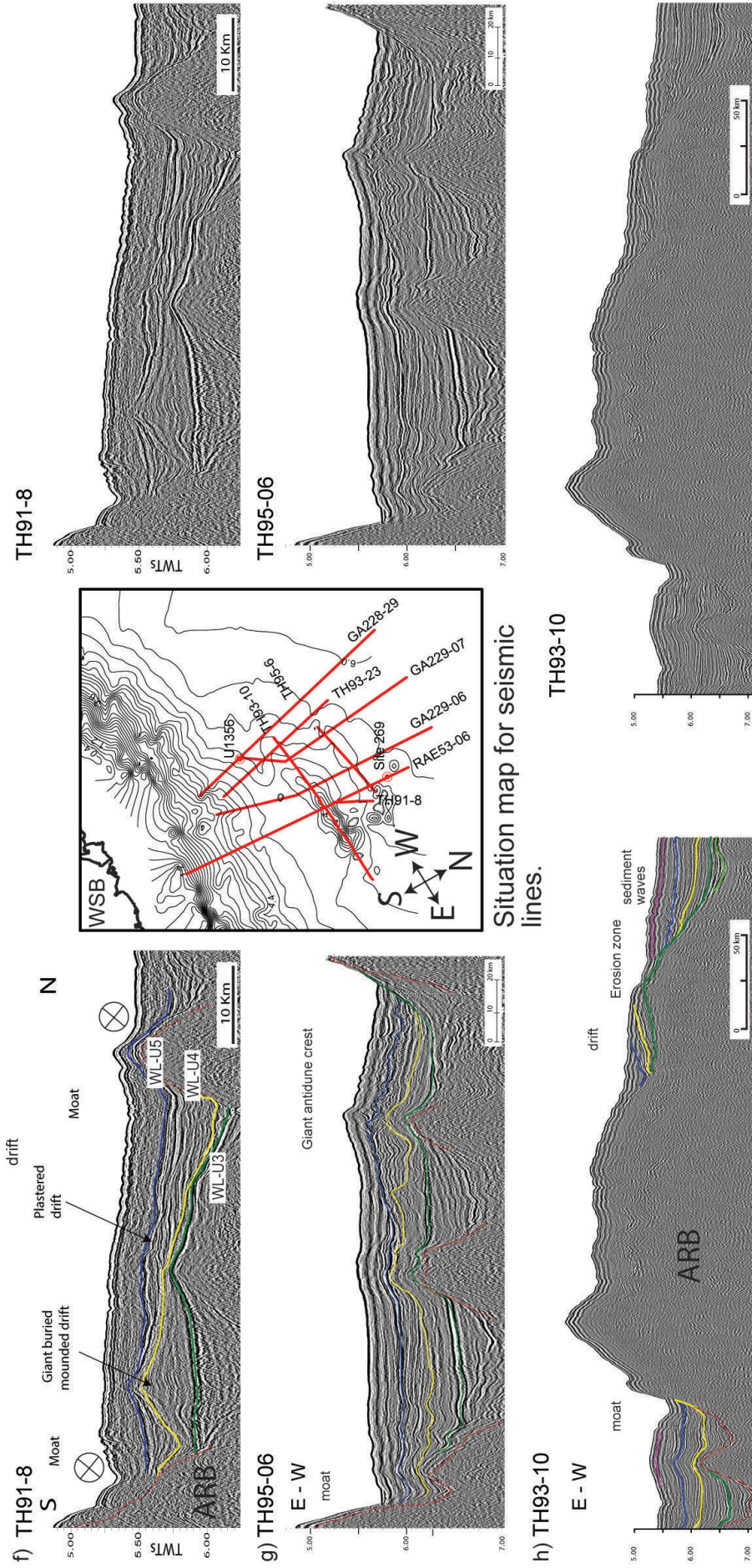


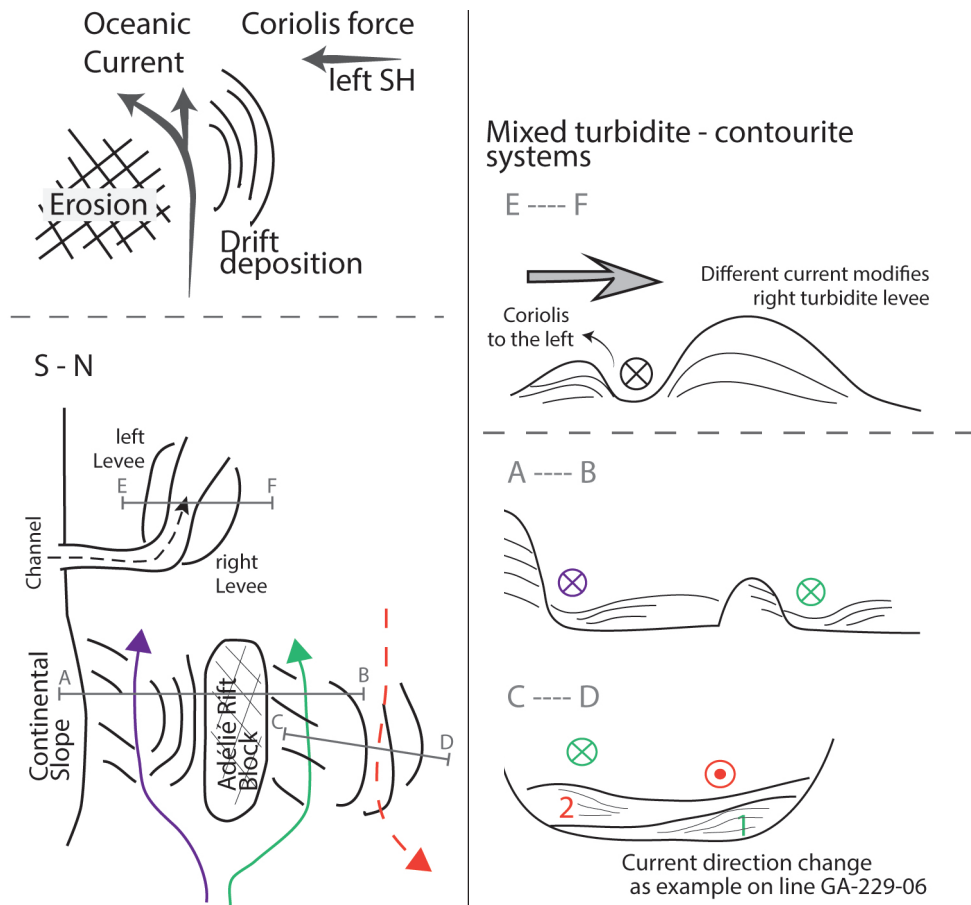
Figure 5.5. Continued

**5.5.3. EVOLUTION OF CONTOURITE DEPOSITION OFF THE WILKES LAND MARGIN**

The seismic stratigraphic analysis allowed us to determine the spatial and temporal distribution of contourite deposits and to provide insights into the bottom water masses in the eastern Wilkes Land margin.

In order to infer current flow directions from the contouritic mounds we take into account that, in the Southern Ocean, Coriolis force deflects bottom currents towards the left, which generates higher energy/velocity at this side, eroding the sediments, and depositing them to the right as the velocity of the flow diminishes (Fig. 5.6; Faugères et al., 1999). Also, when the flow interacts with obstacles the main core of the flux divides in branches, and, in the Southern Ocean, the right branch will have more erosive strength, generating a moat bigger than in the left side (Fig. 5.6; Hernández-Molina et al., 2006). In addition, over-bank deposition from gravity flows traveling along submarine channels, will be forced to the left and as a result the left levee will exhibit a higher relief than the right levee (e.g., Escutia et al., 2000; Carter et al., 2004; Miramontes et al., 2020).

We differentiate three major phases in the paleoceanographic evolution of this margin: Phase 1) Starts above unconformity WL-U3 and comprises unit WL-S4 dated early Oligocene; Phase 2) Starts above un-



**Figure 5.6.** Sketch map showing main contouritic morphological features of Wilkes Land for the Oligocene modified by the Coriolis force. Sections are done as an example of contourite and drift interpretation.



conformity WL-U4 and includes seismic unit WL-S5 dated late Oligocene; and Phase 3) that starts above unconformity WL-U5 and comprises seismic unit WL-S6 dated early Miocene and more recent seismic units above WL-S6.

### 5.5.3.1. Phase 1

Seismic unit WL-S4 reflectors onlap against the smooth topography of the lower slope. In some instances they exhibit divergent reflectors towards the slope forming small and low relief-mounded morphologies that are classified as separated mounded drifts that provide a westward flux direction (Fig. 7a).

On the continental rise landward of the ARB, seismic unit WL-S4 infills the eastern and western deep basins shown in the unconformity WL-U3 paleosurface reconstruction (Fig. 5.3a). Site U1356 recovered sediments from seismic unit WL-S4 and showed these sediments to be dominated by gravity flow and hemipelagic deposits reworked by bottom currents (Escutia et al., 2011; Salabarnada et al., 2018). In the lower part of seismic unit WL-S4 contouritic deposits are intercalated with deformed claystones interpreted as MTDs (Escutia et al., 2011). Based on the correlation between the recovered sediments and the seismic profiles we interpret seismic unit WL-S4 infilling the basin depressions as mixed sheeted drifts. Against the southeastern limit of the ARB, seismic unit WL-S4 reflectors terminate against the basement walls forming a plastered drift (drift 1; Fig. 5.7a). The absence of mounded morphologies points towards a westward flux direction creating this morphology. In the northern side of ARB a moat is mapped following the contours of the outcropping ARB (Fig. 5.7a). Seaward from the moat, the current produces a giant elongated mounded drift (drift 2) with its crest running parallel to the moat (Fig. 5.7a). When drift 2 develops in confined basins delimited by the structural highs of the ARB, a double moat is observed on both extremes of the drift (Figs. 5.7a, 5.5c). In this later case, current flux directions extrapolated from these morphologies point to a double westward current (Fig. 5.7a). In the northern side of the ARB the westwards flux is more erosive due to Coriolis force (Fig. 5.5).

During deposition of seismic unit WL-S4, the top of the ARB shows erosion or little sediment deposition (Fig. 5.5a,d,e,f,g,h).

Both drift 1 and 2 follow a similar evolution. They originate as small morphologies that gradually become bigger and migrate towards the south (landwards) (Fig. 5.5c,d,f). In the confined basins within the ARB, mounded morphologies tend to originate against the relieves of the northern walls and migrate gradually towards the southern limits of the basins.

Sediment wave field is mapped at the lee side of the elongate mounded and separated drift (Fig. 5.7a), and are generally formed when the topography becomes smooth away from the ARB (Figs. 5.7a, 5.5a,d).

### 5.5.3.2. Phase 2

Above unconformity WL-U4, at the base of the slope and in front of a shelf trough, there is an area with

a series of stacked wedges that exhibit internal chaotic reflectors. These deposits are interpreted as MTDs (Fig. 5.7b) and occupy an area of 40,000 km<sup>2</sup>. Plastered and slope separated drifts are common in other areas of the slope and provide an eastward flux direction (Fig. 5.7b).

In addition, the slope is dissected by a submarine channel that runs perpendicular to the slope (Figs. 5.5a, 5.7b). In the continental rise the channel path is forced to the west (i.e., towards the Australian-Antarctic basin) due to the presence of the ARB in the vicinity (Fig. 5.7b). Where the channel is crossed by our seismic profiles, it exhibits levees at both sides, with the crest of the northern levee being displaced towards the north (Fig. 5.5a,b,c). Contrary to what it would be expected due to the effect of the Coriolis force, the overall relief of the north levee is higher than the right levee. This suggests that bottom currents entrain sediments delivered to the continental rise by gravity flows and that these currents come from an opposite or oblique direction to the one of the downslope turbidite flux. These levee transition laterally into a plastered drift that is mapped against the southeastern face of the ARB (drift 1; Fig. 5.5b,c; 5.7b). Compared to Phase 1, the plastered drift 1 that develops during Phase 2 occupies a larger area that is up to 1.6 km N-S and 80 km long E-W (Fig. 5.7b). In the SE part of this plastered drift, reflectors start to climb above the ARB, and incipient sediment waves develop on this flank (Fig. 5.5b,d).

The giant elongated mounded drift (drift 2) from Phase 1 and the structural highs in this zone condition the topography in the northern part of the ARB during Phase 2 (Fig. 5.7b). In the northern side of the ARB, the contouritic moat developed during phase 1 continues to be active but narrows towards the NW (Fig. 5.5d, 5.7b). To the NE of the ARB, this moat becomes erosive and complex morphologies develop (Fig. 5.5c,d). We interpret this erosive zone as a contouritic channel that results from strong circulation and likely sediment reworking by eddies, which promotes the transformation of the elongated mounded drift 2 into a multi-crested mounded drift. This drift transitions towards the north into a small-mounded drift (drift 3) that is connected to a moat at the foot of the southern wall of the ARB. Drift 3 develops parallel to drift 2, and provides evidence for an eastward bottom current direction not recorded during Phase 1 (Fig. 5.5d). Drift 3 transitions from a mounded into a symmetric mounded morphology towards the NE with depicted opposite flux directions, when confined between highs of the ARB (Fig. 5.5d). In this phase we see the same tendency that in Phase 1 whit mounded morphologies growing gradually from small to bigger and with a clear southward migration.

In the NW area of the map (at the bottom right), very complex reflector morphologies arise (Fig. 5.5g). and the decreased thickness of seismic unit WL-S5 compared to its lateral continuation (Fig. 5.5g) in this area suggest to us the effect of erosional processes. Reflectors are continuous and onlap in several zones of the unconformity. Consecutive mounded bodies of different size configure a triangular shape morphology (Fig. 5.5g). Grid spacing of our seismic profiles doesn't allow us to fully understand the nature and origin of these morphologies. The fact that reflectors are continuous and aggrading leads us to interpret these morphologies are the result of bottom currents mixed with turbiditic deposition. We find similarities with sediment waves cut by the seismic line in an oblique perpendicular transect.

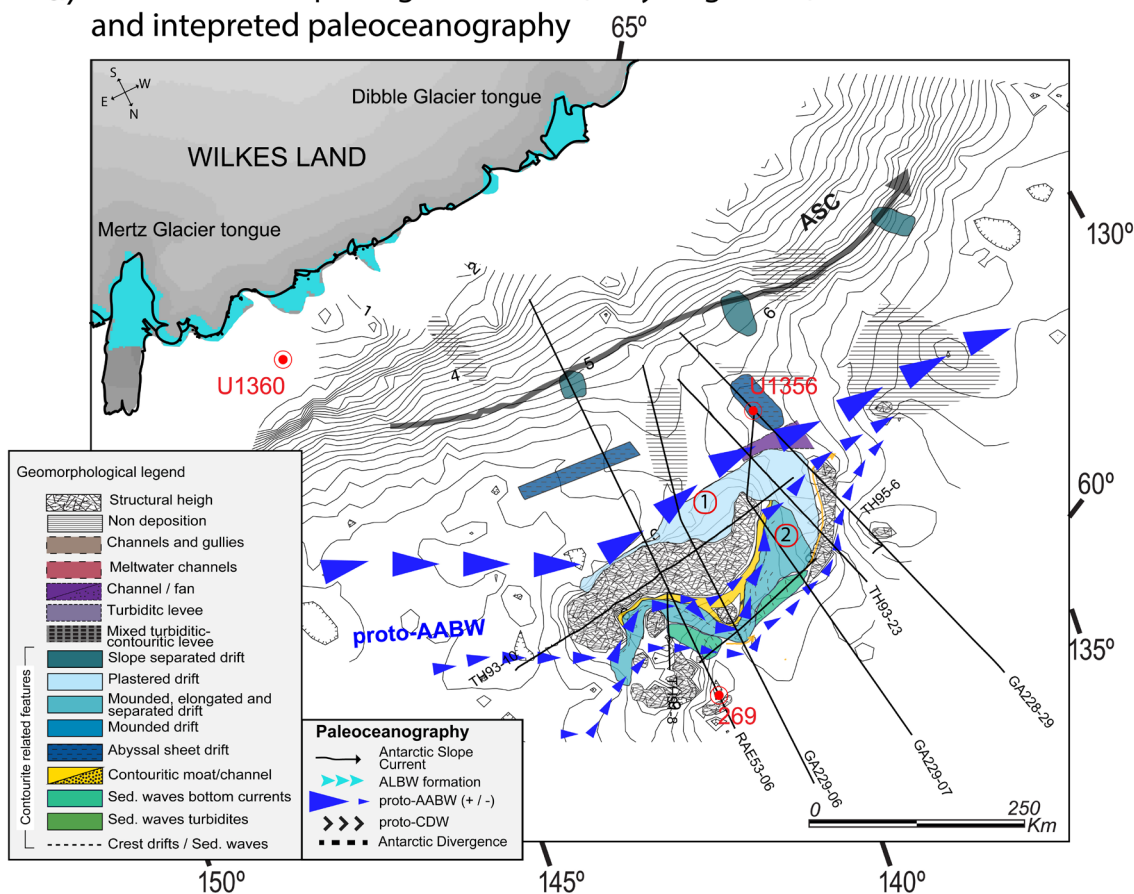


Available evidence points towards a high-energy system with several current cores that flow towards the N-NE. This sediment waves are also recognised in the surrounding seismic lines, with an estimated area of 2800 km<sup>2</sup>.

### 5.5.3.3. Phase 3

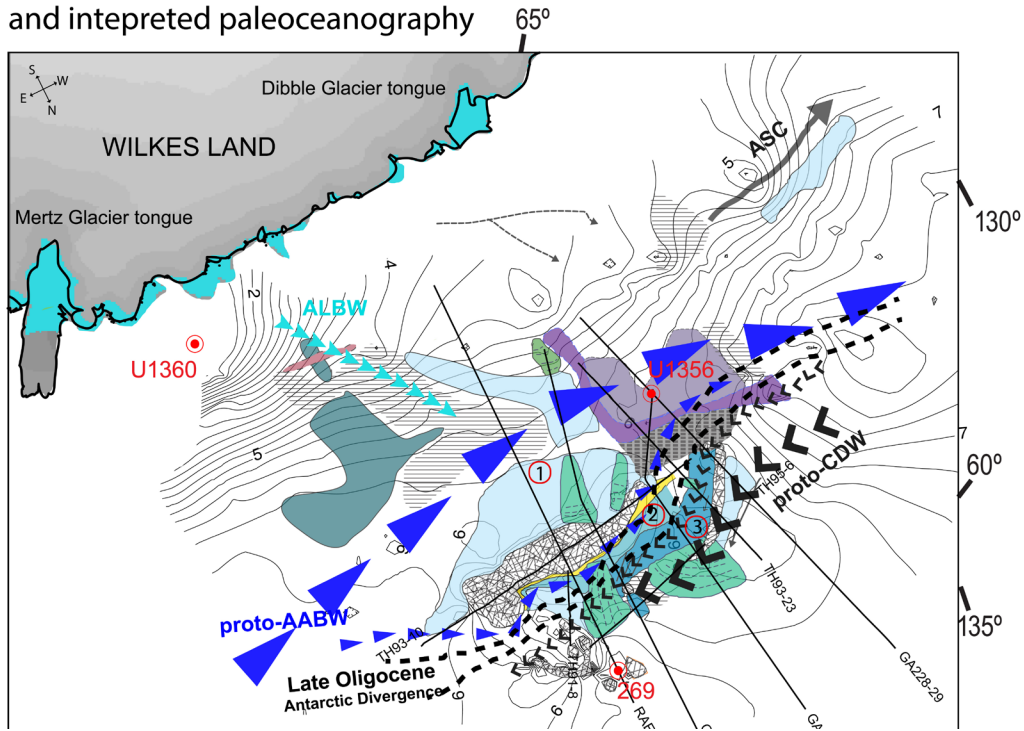
After unconformity WL-U5, gullies develop in the slope that evolve into channels (Fig. 5.7c). At the base of the slope, and at the right side of the main channel, we observe a field of sediment waves (Fig. 5.7c). Also at the base of slope, chaotic and non-continuous undulated reflectors with lensed morphologies are observed, and are interpreted as isolated MTDs (see Chapter 4). Phase 3 MTDs are distributed along channels and they originate to the west compared to the source for the MTDs reported at Phase 2. At the continental rise, the main channel migrates landward and the associated levees reach maximum growth (Fig. 5.7c). The southern (left) levee presents sediments waves with decreasing amplitude towards the south, away from the channel, which suggests a turbiditic origin for the sediment waves. The northern (right) levee is strongly modified with its crest aggrading or migrating landward, and with abundant sediment waves on the lee side. An eastward current is here interpreted in order to explain the complex morphologies of this mixed turbidite-contourite system. During Phase 3, the infilling of the basin de-

#### a) Contouritic morphologies after U3 (Early Oligocene) and interpreted paleoceanography



**Figure 5.7.** Regional major contourites features distribution presented in this work off the Wilkes Land Margin with superimposed schematic drawing of the water mass circulation in plan view for the a) early Oligocene, b) the late Oligocene, and c) the Oligocene-Miocene transition.

b) Contouritic morphologies after U4 (Late Oligocene) and interpreted paleoceanography



c) Contouritic morphologies after U5 (Miocene) and interpreted paleoceanography

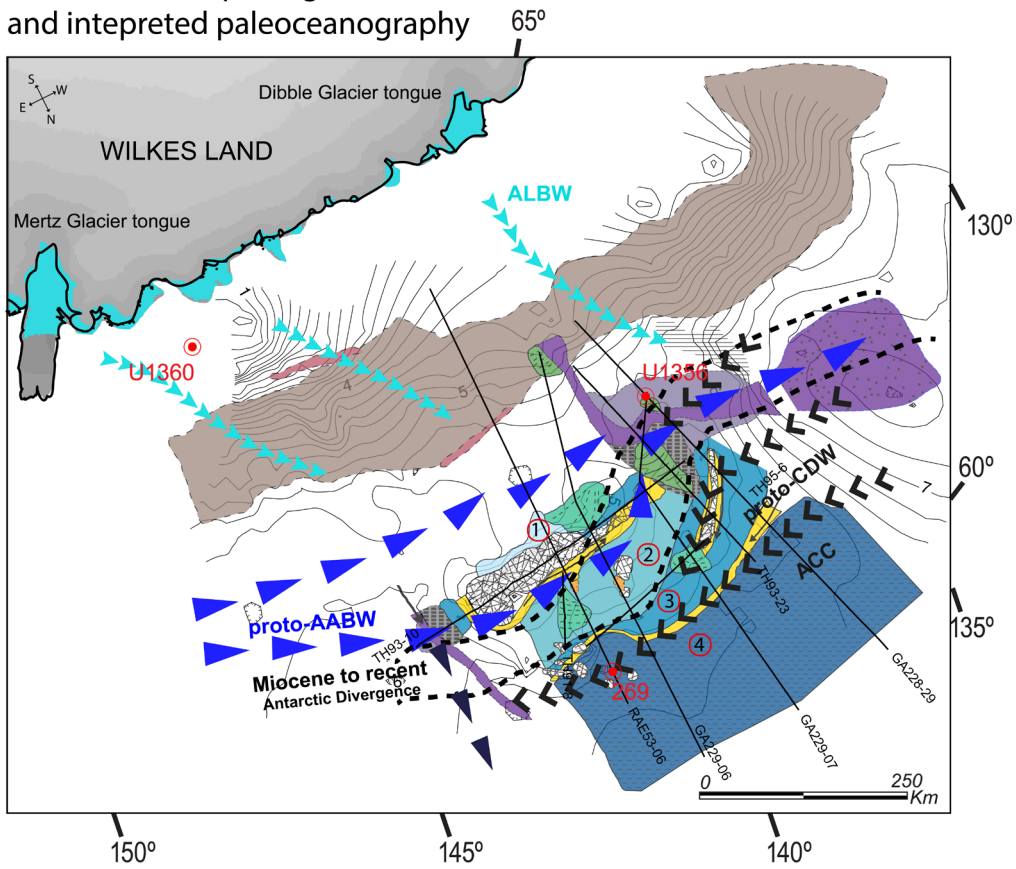


Figure 5.7. Continued.

pressions consists of parallel and continuous reflectors that are draping previous deposits and the topographic irregularities in the deeper parts of the Australian-Antarctic Basin.

In the SW area of the study zone a small channel develops (Fig. 5.5h, 5.7c). Levee systems develop at both sides of the channel, with the left levee exhibiting a higher relief due to the Coriolis force acting in a downslope (north) flux. The left levee transitions laterally into a mounded drift connected to a moat at the western foot of the ARB. This suggests that the mounded drift formed as a result of a downslope flux with direction towards the northeast.

During Phase 3, drift 1 diminishes its areal extension (<1 km wide) at the same time that the seafloor topography becomes smooth due to sediment infilling. In the eastern part of the ARB, the crests of drift 1 migrate landwards changing to higher frequency sediment waves (Fig. 5.5c). In the NE limit of the ARB, the contouritic channel erosive zone from phase 2 persists but is limited to the higher reliefs of the ARB (5.9 s TWT) and is identified by no-deposition in the channel, and very wavy reflectors present at the sides. (i.e. Fig. 5.5d).

Drift 2 grows in size during phase 3 compared with phase 2, especially towards the northwest and drift 3, occupies now a large area at the northeastern part of the ARB. The seismic profile in Figure 5.5g shows an oblique transect between these two drifts that allows us to interpret opposite current directions. The seismic lines also show a giant mound separating different seismic facies, from continuous high amplitude reflectors in the southern side to undulated and semi continuous reflectors like sediment waves (Fig. 5.5g).

Between 61°5' and 62° latitude and towards the North, reflectors become planar parallel and are infilling the basin depressions, including the depression where Ocean Drilling Program Site 269 was drilled (Figs. 5.5, 5.7). Sedimentation at Site 269 during the Oligocene and Miocene consists of coarse laminated siltstones that have been interpreted as contourites intercalated with turbidites (Hayes and Frakes, 1975). The transition between the rough into the planar surfaces occurs through a small moat connected to a mounded drift (drift 3) to the south.

## 5.6. DISCUSSION

### 5.6.1. TOPOGRAPHIC CONTROLS IN CONTOURITE DEPOSITION

In the Wilkes Land margin the reconstruction of the paleosurfaces of three major regional unconformities shows they played a key role in the distribution of bottom current deposits and bottom-water circulation during the Oligocene and the Miocene. Outcropping tectonic structures as the ARB and the other ridges around it control the distribution in space and time of contourite drifts in this margin. The existence of confined basins within the ARB generated an irregular topography that acted as barrier to

along slope bottom currents paths. In addition, obstacles along a current flow accelerate bottom current (Maldonado et al., 2005), as it is observed in the different Phases just described in this margin. High velocity fluxes generate erosive morphologies such as moats and contouritic channels along the walls of the ARB structural highs. Elongated mounded drifts are deposited parallel and on the right-hand side (in the Southern Hemisphere) as kinetic energy decreases related to the Coriolis force (Faugères and Stow, 1993; Rebesco et al., 2014).

### 5.6.2. CONTOURITIC BODIES AND CURRENT PATHS: INSIGHTS INTO WATER MASSES

In comparison to the actual hydrography of the WL and the paleoceanographic configuration of the Oligocene known at the moment (Rintoul et al., 2001; Scher et al., 2015), we associate the westward direction mounds to be formed under the AABW and the eastward direction mounds to be formed under the action of the CDW and the proto-ACC. In addition, we interpret the small-mounded drifts placed at the continental slope to be associated with westward flowing Antarctic Slope Current impinged by the Easterlies winds close to the Antarctic continent (Sokolov & Rintoul, 2002).

Clockwise oceanic currents within the Antarctic-Australian basin were previously described to occur since the Paleogene/Eocene boundary ~58 Ma until the late Eocene. This current formed drifts along the continental slopes of Australia and Antarctica following the surface-water proto-Lewin current (Sauerlich et al., 2019).

Current directions inferred from the stratigraphic analyses and mapping of depositional and erosional contourite morphologies in the eastern Wilkes Land margin (Fig. 5.6) provide insights into the presence of two opposed water flux directions from the late Oligocene onwards.

Based on this, we determine that during Phase 1 sedimentation of drifts 1 and 2 deposition was dominated by a westward flowing current (Figs., 5.6 and 5.7). We infer this current to be part of a proto-AABW spilling from the margin into the basin as does today (Fig. 5.2). The existence of the AABW in this margin was already reported by Huck et al. (2017) based on neodymium isotopic compositions similar to the AABW of today.

During Phase 2 and 3, the westward flowing AABW continues to influence the morphologies in the margin south and around the ARB (Fig. 5.7). In addition, starting with Phase 2 an eastward flowing current is determined by the distribution of the drifts within the confined basins of the ARB (Fig. 5.7). During the late Oligocene drift 3 develops to the south of a moat implying an eastward flux that we interpret to correspond with a proto-CDW (Fig. 5.6 and 5.7). This is in agreement with sedimentological studies of carbonated sediments that point to a proto-CDW intruding closer to the continental margin during the late Oligocene (Salabarnada et al., 2018). This contrasts with modern hydrography in this area where the AABW is the main water mass bathing this area of the Antarctic Divergence (Fig. 5.2). Phase 3, witnesses the development of two main cores in the eastward flowing proto-CDW shown by the





presence of drift 4 to the north of the ARB (Fig. 5.7).

Contouritic sediment waves developed in the area are usually associated with eastward bottom currents, which suggest they are formed under the influence of a proto-CDW, and here are found related to the interference zone between the proto-CDW and the underlying proto-AABW. The contact zone between these two water masses is tilted towards the north seaward. A pycnocline and thermocline is the zone where two water masses with different density and temperature get in contact, creating a high gradient interference zone. Interphase zones with strong gradients are associated with turbulent processes, such as waves and eddies (Reid et al., 1977) that can shape the seafloor by erosion and resuspension of sediments at the seafloor (Rebesco et al., 2014). In the eastern Wilkes Land margin, the zones where water masses converge coincide with deposits characterized by chaotic reflectors, associated with contouritic channels, eroded zones (as the top of the ARB) and a series of channel patch drifts.

We interpret the interphase zone of the proto-AABW and the proto-CDW based in the presence of opposite current flux indicators, the chaotic morphologies in the contouritic channel, and the contouritic sediment waves (Fig. 5.7). Based in this, we estimate an interphase zone in the WL margin placed at around 5.5 s TWTT at the ARB during the Oligocene and at 5.0 s TWTT at the Miocene. If we consider these TWTT mainly as water column distances, we could propose a depth of 4125 mbsl for the Oligocene and 3750 mbsl for the Miocene to recent times. Nowadays, interphase between AABW and CDW above the ARB is placed at a depth of aprox. 2000 mbsl, therefore the thickness of AABW in the Southern ocean during the Oligocene was inferior to present times. In addition, Site 269 neodymium data proves that the zone of the core during the latest Oligocene and the early Miocene was occupied by proto-CDW (Evangelinos et al., submitted).

Surrounding Indian (Pfhul and McCave, 2005) and Pacific (Carter et al., 2004) basins have also the imprint of the onset and evolution of the AABW. Oligocene drifts and associated erosive surfaces and hiatus interpreted to result from the action of ABWW have been recorded in Eastern New Zealand (Carter and McCave, 2002), Argentinian basin, Brasil (Vema drift; Faugères et al., 2002), Africa (Agulhas drift; Dingle et al., 1987; Niemi et al., 2000; Uenzelmann-Neben, 2001, 2002).

## 5.7. CONCLUSIONS

Oligocene and early Miocene contourite sedimentation in the eastern Wilkes Land margin is controlled by the basin topography. Based on the spatial and temporal distribution of erosional and depositional contourite morphologies, we determine three phases in paleoceanographic evolution of this margin:

- 1) Phase 1, early Oligocene (33.6 – 28 Ma) is dominated by westward flowing currents that we interpret to be associated to the action of a proto-AABW.

Phase 2, late Oligocene (28 – 23.4 Ma), contourite deposits are interpreted to form under the influence of a westward flowing proto-AABW. However, at the northernmost limit of the study area, an eastward contour current, interpreted as a proto-CDW is for the first time recorded.

Phase 3, middle Miocene (>17 Ma), the seafloor off the Wilkes Land is occupied by a proto-AABW towards the south, and a proto-CDW towards the north.





# Chapter 6

## General Discussion

Oligocene - Miocene ice sheet and  
paleoceanographic evolution off the  
Wilkes Land margin

---



## CHAPTER 6

### GENERAL DISCUSSION

#### OLIGOCENE-MIOCENE ICE SHEET AND PALEOCEANOGRAPHIC EVOLUTION OFF THE WILKES LAND MARGIN

The results from the work conducted in Oligocene to Miocene sediments from IODP site U1356 and in the grid of multichannel reflection seismic profiles off the eastern Wilkes Land margin provide insights into three main phases with different ice sheet and/or ocean configurations:

##### 6.1. PHASE 1 - EARLY OLIGOCENE (33.6 TO 28 MA)

Sediments recovered at IODP site U1356 show that deep-water deposition in the eastern Wilkes Land margin is characterized by the interaction between hemipelagic and gravity flows (i.e., turbidity currents and mass transport deposits-MTDs) with bottom currents (Escutia et al., 2011; 2014). Correlations with the MCS profiles show that, where site U1356 is located, early contourite deposits between unconformities WL-U3 and WL-U4 develop dominantly sheeted morphologies. These sheeted drifts infill the topographic depressions between the base of the continental slope and the Adélie Rift Block (ARB). Only where the Adélie Rift Block (ARB) and the structural highs to the north of the ARB outcrop, erosional and depositional contourite morphologies develop (Fig 6.1). This points to the topographic relieves in the abyssal plain as the main controls in bottom current deposition.

The distribution of the contourite moats and mounds around the ARB and the structural highs point to the presence of a westward flux that we interpret to correspond with a proto-AABW. The formation of Antarctic bottom waters off the eastern Wilkes Land has been already reported based on neodymium isotopic compositions measured in fish debris from the early Eocene to the Oligocene (Huck et al., 2007). In the absence of sea-ice for most of the Oligocene (Houben et al., 2013; Bijl et al., 2018), proto-ABBW formation in the Wilkes Land is inferred to form by density contrasts resulting from temperature and salinity changes in surface waters (Huck et al., 2017), similar processes were suggested for the formation of proto-AABW during the warm late Oligocene (Chapter 3, Salabarnada et al., 2018).

##### 6.2. PHASE 2 - LATE OLIGOCENE (28 TO ~23.4 MA)

Late Oligocene (26-25 Ma) sediments recovered from Site U1356 record glacial-interglacial deposition that is dominated by bottom current reworking of hemipelagic and gravity flow deposits (Escutia et al.,



2011; Salabarnada et al., 2018). Based in XRF current velocity proxy ( $Zr/Ti$ ; Chapter 3), glacial-interglacial changes in the bottom current velocity during the warm late Oligocene are driven by obliquity. The lack of ice rafted debris (IRD) in these sediments compared to older and younger sections, was taken to indicate that the EAIS was retreated to the continent and not reaching the coast (Salabarnada et al., 2018). In support of that, Bijl et al. (2018) reports at the same Site temperate waters with warm affinity dinocyst species existent today north of the Polar Front, the absence of sea-ice affinity dinocysts, and elevated sea surface temperatures (Hartman et al., 2018) are interpreted to represent ice-free and open oceanic conditions.

After peak warm conditions in the late Oligocene, climate deteriorated during the latest Oligocene (after 25 Ma to 23.4 Ma). The cooling resulted in ice sheet advances into the continental shelf and shelf edge as witnessed by large mass transport deposits (MTDs) deposited in the base of the slope and the basin and reaching site U1356. However, in situ sediments interbedded between glacial MTD in the continental rise have similar characteristics to those from before 25 Ma indicating that during interglacial times ice sheets continued to retreat to the continent and fronts migrated south. Calcareous nannofossils events within the in situ sediments also point to times of warmer interglacial conditions allowing the proto-CDW to reach site U1356 (see Fig 5.5 in Chapter 5). In addition, interbedded in situ sediments between MTDs record at least 8 times of EAIS advance and retreat during the latest Oligocene cooling trend leading to the Mi-1 event, which points to a highly dynamic EAIS during this time period.

Seismic stratigraphic analysis show how sediment drift morphologies above unconformity WL-U4 become more widespread but continue to mainly develop where bottom currents interact with the structural highs (Fig. 6.1). For the first time in this margin, contouritic moats associated with drift 3 suggest the existence of eastward flowing contour currents. Today, eastward flowing currents off the WL are part of the CDW and the ACC (Rintoul et al., 2001), which suggest drift 3 may record the establishment in this margin of a proto-CDW. This is in agreement with the presence of the carbonated sediments in late Oligocene (26-25 Ma) sediments at site U1356 previously mentioned. These deposits are interpreted to result from intrusions of a proto-CDW closer to the continental margin during warm interglacial periods (Chapter, X; Salabarnada et al., 2018). The intrusion of warmer waters is also recorded by neodymium isotopes measured in fish debris in late Oligocene sediments from DSDP site 269, which report similar values to the modern CDW (Evangelinos et al., submitted).

Previous studies have described a change in the paleoceanographic configurations during this time period. Scher et al. (2015) postulate the onset of the ACC to take place at around 30 Ma, with a Polar Front already active and placed around 60°S latitude. In the northern zone of the Tasman gateway and south of New Zealand, the Marshall paraconformity marks a shift, at around 28 Ma, in the sedimentary style from low to high energy environments with coarse-grained calcareous drifts produced by strong bottom currents (Carter et al., 2004). Based on this observation this unconformity has been interpreted to record the initiation of the ACC (Carter et al., 2004).

### 6.3. PHASE 3 - THE OLIGOCENE MIOCENE TRANSITION (~23.4 TO >17 MA)

Regarding ice sheet evolution, a sharp shift in sedimentation style on the continental rise (from dominant MTD deposition to turbidite and hemipelagic deposition) at around 23.4 Ma points to an important and irreversible change in the configuration of the EAIS in this margin sector (see Chapter 4). Sedimentation rates decrease sharply (Escutia et al., 2011), and this low sedimentation rates are also recorded throughout the Wilkes Land margin (De Santis et al., 2003; Escutia et al., 2005; Leitchenkov et al., 2007). We hypothesize that the erosion and overdeepening of the WSB by successive advances and retreats of the EAIS since the early Oligocene is responsible for this change. This is in agreement with topographic reconstructions and modelling studies that show a shift from a WSB occupied by low-lying lands at 34 Ma to an overdeepened basin by the Miocene (Gasson et al., 2016; Paxman et al., 2018, 2019). In addition, Paxman et al (2019) suggests this shift to take place during the Oligocene.

During the early middle Miocene (> 17 Ma) a shift to overall finer-grained sediments is interpreted to imply another landward change in depositional depocenters. We cannot however know at this time if this shift is related to overdeepening of the continental shelf. An additional explanation could be a decrease in supply of sediments caused either by the lack of available erodible materials or to a change in the thermal regime of the EAIS.

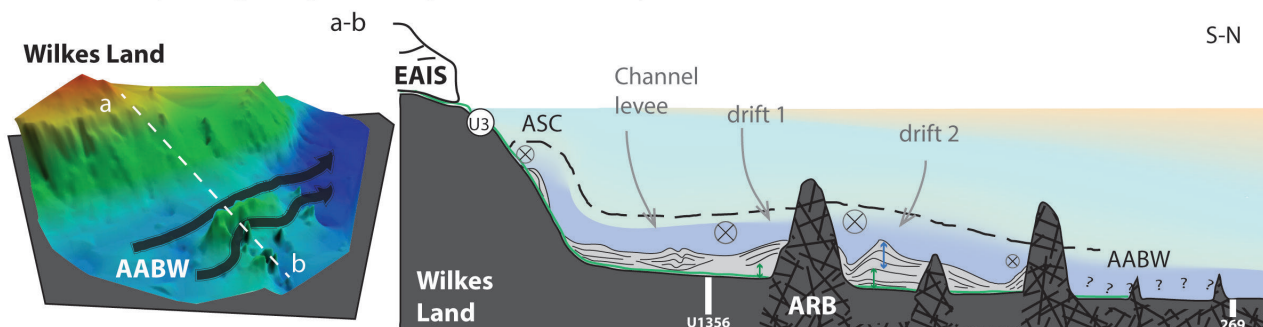
Regarding the paleoceanographic evolution in this margin, contouritic morphologies continue to become more widespread occupying the slope to the abyssal plain. In addition, drift morphologies become more complex in this phase (e.g., with the location of the moats and drifts 3 and 4) pointing to the existence of two cores of the eastward flowing proto-CDW. This contrasts with the present paleoceanographic configuration in the study area that is bathed by the westward flowing AABW (Fig. 5.2, Chapter 5). An ocean configuration different than the modern one is also reported by the presence of dinocysts that today are present to the north of the Polar Front (Bijl et al., 2018) and by warmer than present southern ocean surface temperatures (Hartmann et al., 2018). This different ocean configuration during the latest Oligocene-early Miocene characterized by two water masses reaching the seafloor is only found at present to the north of the study area.



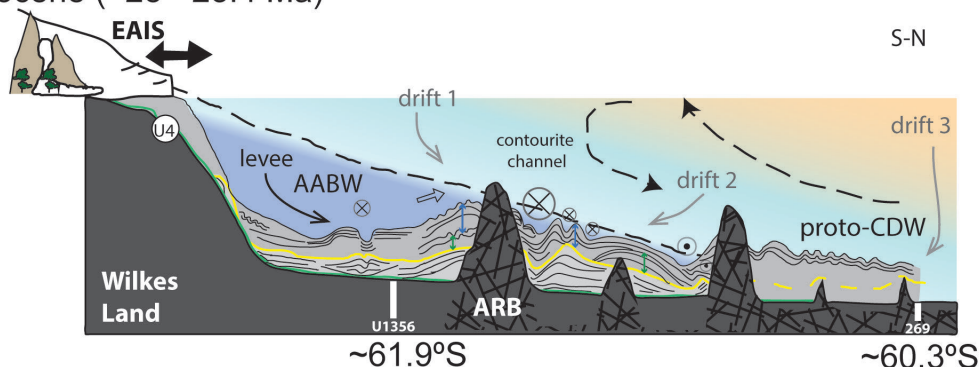


Contouritic stratigraphic evolution and paleoceanographic implications in Wilkes Land:

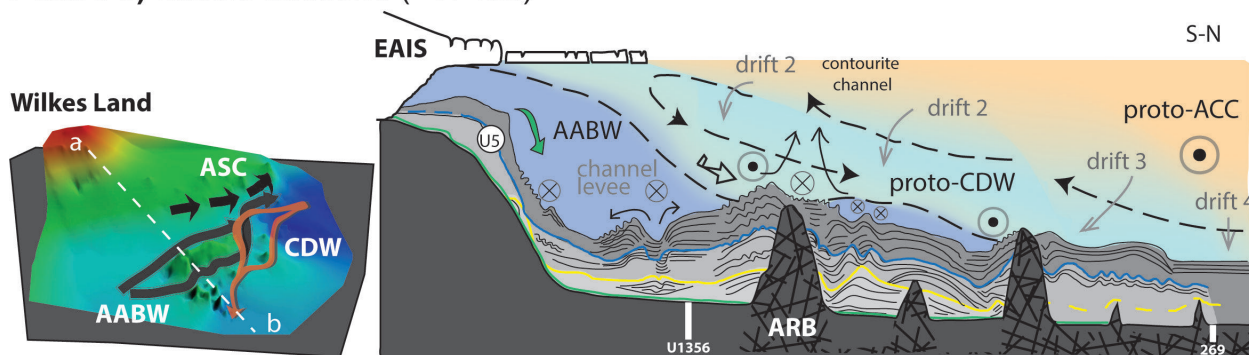
**Phase 1) Early Oligocene (~33.6 - 28 Ma)**



**Phase 2) Late Oligocene (~28 - 23.4 Ma)**



**Phase 3) Middle Miocene (>17 Ma)**



Wilkes Land margin seismic unconformities

- WL-U5
- WL-U4
- WL-U3



- 1st phase Build-up of small mounds and drifts
- 2nd phase Big drift development with drift crests moving landward in general

**Figure 6.1.** Long term and schematic evolution of the ice sheet, the paleoceanography, and the drift formation off the Wilkes Land margin. We separated three evolutive phases, coincident with the regional seismic unconformities in the Wilkes Land margin. 3-D bathymetries are based on the paleosurface reconstruction of Phase 1 and phase 3 (Chapter 5). The profile reconstructs an idealized section where all the processes occur linearly.

# Chapter 7

Summary and Conclusions

---



## SUMMARY AND CONCLUSIONS

To implement the three main objectives of this thesis (presented in the Context and Motivation section), we have conducted and integrated results from a suit of analyses in both sediment cores and seismic reflection profiles. Our study of sediment cores recovered at Site U1356 has allowed to determine ice sheet and ocean configuration variability at different temporal snapshots. This is because sediment recovery in these cores was not continuous although was very high for the late Oligocene section (80%). For this, the resolution of our reconstructions range between orbital resolution (tens of thousands of years) and millions of years. In addition, the correlation of results from Site U1356 with the grid of seismic profiles has allowed to extend the insights into ice sheet and paleoceanographic configurations at a regional scale.

In this way, the overarching aim of this thesis – to understand ice sheet and ocean configuration and dynamics in an unexplored margin of East Antarctica during the warm late Oligocene and the transient Mi-1 glaciation – has been addressed with the following conclusions related to each of the specific objectives:

### 1. *Ice sheet evolution and glacial-interglacial dynamics during the Oligocene and the OMT*

Chapters 2 and 3 provide new information on the ice sheet dynamics and configuration of the EAIS during the late Oligocene, the OMT, and the early middle Miocene. Because U1356 is in a deep-water setting we cannot provide direct insights into ice sheet grounding line advances and retreats but based on the inferred glacial-marine sedimentary processes and the presence/absence of IRD we conclude that:

- During the late Oligocene (26 – 25 Ma) the Wilkes Subglacial Basin was not overdeepened as it is today. Instead topographic and modelling reconstructions show it occupied by low-lands at near sea level. Based on the lack of IRD in late Oligocene sediments (compared with older and younger sections that contain IRDs) we conclude that ice sheets during this period were mainly continental-based and did not extend to the marine margin.
- After peak warm conditions in the late Oligocene climate deteriorated during the latest Oligocene (between approximately 24 and 23.4 Ma). The cooling resulted in repeated ice sheet advances into the continental shelf and shelf edge witnessed by stacked MTD deposits. The presence of in situ sediments interbedded between glacial mass transport deposits (MTDs) in the continental rise, point to at least 8 times of EAIS advance. However, the presence of calcareous nannofossils within the in situ sediments point to warm conditions prevailing during times of ice sheet retreat (similar to those reported between 26 and 25 Ma). Therefore, based on our observations, the EAIS was highly dynamic during this time period.



- A sharp shift in sedimentation style at site U1356 and regionally (from dominant MTD deposition to turbidite and hemipelagic deposition) at around 23.4 Ma points to an important and irreversible change in the configuration of the EAIS in this margin sector. This change is attributed to result from the EAIS in the WSB becoming marine-based as a consequence of erosion and overdeepening of the Wilkes Subglacial Basin by the repeated advances and retreats of the EAIS since it was formed in the early Oligocene (33.6Ma).
- During the early middle Miocene (> 17 Ma) an additional shift to overall finer-grained sediments is interpreted to imply a landward change in depositional depocenters. We cannot however know at this time if this overall decrease in sediment supply to the margin is related to the overdeepening of the continental shelf, to the lack of available erodible materials, or to a change in the thermal regime of the EAIS.

## 2. *Paleoceanographic evolution and polar front dynamics during the Oligocene and the Miocene*

Chapters 2 and 3 provide paleoceanographic reconstructions mostly based on the late Oligocene interval with high sediment recovery, which allowed for a detailed study of glacial-interglacial cyclicity at site U1356. Our interpretations are based on the sedimentological, geochemical and mineralogical imprint of deep bottom waters in sediments that were at the seafloor during the different studied periods. We conclude that:

- For the late Oligocene period (26-25 Ma), glacial cycles are characterized by reworking of the sediments delivered to the site by bottom-currents of varying strengths and by low-oxygenation conditions at the seafloor. This has been taken to indicate the presence of a proto-AABW bathing Site U1356. In contrast, interglacial cycles are characterized an increase in the strength of bottom-current and more oxygenated conditions at the sea floor related to times when the proto-AABW remained closer to the continent allowing the proto-CDW to reach the site.
- Our interpreted glacial-interglacial changes in paleoceanographic configurations during the late Oligocene (26-25 Ma) show for the first time that frontal systems were already active in this segment of the Southern Ocean. These late Oligocene frontal systems were however weaker when compared to modern ones.
- One of the evidences for a weaker frontal system during the late Oligocene is the preservation of carbonated nannofossils in some of the interglacial sediments. The presence of carbonated sediments is taken to indicate that the proto-CDW bathing U1356 is modified by warmer north component waters (i.e., NADW-like) intruding closer to the Antarctic continent. The modern strong frontal system does not allow for these intrusions to take place.
- In situ sediments preserved between the MTD beds (approximately between 24 and 23.4 Ma), are similar to those described for the 26 to 25 Ma interval, including the presence of carbonates beds.

This suggests that the paleoceanographic configuration described for the late Oligocene (26-25 Ma) persisted until just before the Mi-1 event.

In Chapter 4 we extend the results from drilling Site U1356 regionally using the grid of multichannel seismic profiles. The study of the erosional and depositional morphologies in this margin allows us to determine the presence of bottom-currents and their evolution through time. We also provide insights into the main controls in current paths off the Wilkes Land Margin. We conclude that:

- Between 33.6-28 Ma there is evidence for only one water mass bathing the study area seafloor. This bottom water has a westward flow that we interpret to correspond with a proto-AABW.
- The first evidence for the onset of a current flowing eastward is observed at 28 Ma. This deep water mass develops at around 62° latitude and is interpreted to be an expression of the proto-CDW. The proto-AABW dominates landward from the Adélie Rift Block (ARB) while the proto-CDW flows in the area and to the north of the ARB. This agrees with our previous conclusion of the existence of a polar front system at that time. Similar configurations in the modern Southern Ocean are only observed north from the study area with a single water mass (the AABW) occupying today the seafloor.
- A different ocean configuration is determined for the latest Oligocene-early Miocene when the eastward flowing currents become more widespread and two main cores for this proto-CDW are observed.

### 3. *Forcing mechanisms and thresholds that drive EAIS dynamics and paleoceanographic variability during the Oligocene and the Miocene*

Our findings in Chapters 2 and 3 allow us to provide insights into both: the mechanisms and thresholds driving the reported ice sheet dynamics and paleoceanographic configurations. We conclude that:

- Spectral analyses on late Oligocene (26-25 Ma) reveal that glacial-interglacial migrations of the Southern Ocean frontal systems are astronomical driven primarily by obliquity (40 kyr) timescales.
- The shift from MTD to turbidite-dominated deposition at Site U1356 at around 23.4 Ma is interpreted to represent a major threshold in the behaviour of the East Antarctic Ice Sheet in this sector of the east Antarctic margin. We interpret this threshold to correspond with the time when the EAIS became marine-based following erosion and overdeepening of the Wilkes Subglacial Basin during successive ice sheet expansions.



## UNSETTLED ISSUES AND FUTURE PERSPECTIVES

This thesis represents a step towards a better understanding of past environmental, ice sheet, and paleoceanographic changes during the Oligocene-early Miocene in the eastern Wilkes Land margin. However, new questions arise regarding to specific abrupt and transient environmental changes observed at Site U1356 and the regional multichannel seismic profiles.

Site U1356 provides one of the best records for the Oligocene in the East Antarctic area, because overall recovery of the Oligocene section was good (50%). However, recovery was very low (22%) for the latest Oligocene-Miocene. This low recovery, together with the presence of thick and coarse MTDs has not allowed a higher resolution age model as well as a better characterization of the environmental changes leading to one of the major transitions in Earth's climate, the Oligocene-Miocene transition (OMT). The recovery at site U1356 is typical of deep holes drilled close to the Antarctic margin given the presence of IRDs and coarse beds that prevent recovery of the full suite of sediments. In fact, a site drilled by the Deep Sea Drilling Program (DSDP) to the north of U1356, recovered sedimentary sections that are coeval to the ill-recovered MTD section at site U1356. Unfortunately, DSDP drilling took place by spot coring (i.e., not drilling continuously) and therefore the problem persists. To address this challenge a strategy put in place by the SCAR (Scientific Committee on Antarctic Research) Scientific Research Programme Past Antarctic Ice Sheet Dynamics (PAIS; Escutia et al., 2012; Escutia et al., 2019) need to be put in place in this margin. This strategy targets to obtain continental shelf to abyssal plain latitudinal records to obtain snapshots (but direct records) into different configurations of the ice sheet and the ocean from areas close to the continent and continuous datable records (albeit indirect) from areas further away from the continent (i.e., north of site U1356). Therefore further efforts to understand ice sheet and ocean behaviour in this margin should include targeting sites in the abyssal plain north of U1356 and sites closer to land. IODP Expedition 373, now in the schedule although pending dates, targets sedimentary sections on the continental shelf. In addition, a proposal has been submitted to collect a transect of sites from north of U1356 to close to the Australian margin. These programs, when implemented should help to obtain a better understanding of the EAIS and the Southern Ocean in front of the WSB.

There is a need for improvement of age models and the community is actively working on this. Well dated sections are needed in order to be able to make circum-antarctic comparisons of ice sheet evolution and paleoceanographic configurations. This is important because the ice sheet has not evolved uniformly throughout the entire margin, and the causes of these differences need to be addressed. For example, we need to better understand what are the vulnerable areas of the ice sheet and to inform the ice sheet models that the IPCC uses to make their future projections of global sea level change. In addition, this circum-Antarctic comparisons are also important to feed into paleoceanographic models to better understand links between the ice sheet and the SO and also the links between SO circulation and northern latitude circulation. In this regard, more studies are needed in order to understand the evolution of Southern

Ocean circulation and its links with the onset and past evolution of the North Atlantic Deep Water, its relation with AABW and with the global Thermohaline circulation. Lack of knowledge of these interactions in the past prevents a better understanding the shifts that we observe in our records.

Results from this thesis should be of interest to calibrate ice-ocean-atmosphere models that can then provide new insights into the mechanisms responsible for high dynamic ice sheets that existed in the eastern Wilkes Land margin to just prior de Mi-1 event.

After 10 years, the study of the sedimentary sections collected by the IODP Expedition 318 is still producing high-level science and providing valuable information in order to understand the dynamics and the evolution of the East Antarctic continent and the Southern Ocean off the eastern Wilkes Land. The future, IODP expedition 373 in the Wilkes Land will help to unravel proximal ice sheet dynamics as they target continental shelf sites ranging from the Eocene to present. In addition, last year Antarctic IODP expeditions 374, and 379 drilled in the Ross Sea and the Weddell Sea and will surely provide new and complementary information that will help close some of our outstanding questions and open new ones.







## References

---



## REFERENCES

- Abrahamsen, E. P., Meredith, M. P., Falkner, K. K., Torres-Valdes, S., Leng, M. J., Alkire, M. B., et al. (2009). Tracer-derived freshwater composition of the Siberian continental shelf and slope following the extreme Arctic summer of 2007. *Geophysical Research Letters*, *36*(7), 5. <https://doi.org/10.1029/2009GL037341>
- Agnihotri, R., Altabet, M. A., Herbert, T. D., & Tierney, J. E. (2008). Subdecadally resolved paleoceanography of the Peru margin during the last two millennia. *Geochemistry, Geophysics, Geosystems*, *9*(5), 15. <https://doi.org/10.1029/2007GC001744>
- Anderson, J., Kurtz, D., & Weaver, F. (1979). Sedimentation on the Antarctic continental slope. *SEPM Special Publication*, *27*, 265–283. Retrieved from [http://archives.datapages.com/data/sepm\\_sp/SP27/Sedimentation\\_on\\_the\\_Antarctic.pdf](http://archives.datapages.com/data/sepm_sp/SP27/Sedimentation_on_the_Antarctic.pdf)
- Anderson, J. B. (1999). *Antarctic Marine Geology*. Cambridge, UK: Cambridge University Press. Retrieved from [www.cambridge.org/9780521131681](http://www.cambridge.org/9780521131681)
- Arndt, J. E., Schenke, H. W., Jakobsson, M., Nitsche, F. O., Buys, G., Goleby, B., et al. (2013). The International Bathymetric Chart of the Southern Ocean (IBCSO) Version 1.0-A new bathymetric compilation covering circum-Antarctic waters. *Geophysical Research Letters*, *40*(12), 3111–3117. <https://doi.org/10.1002/grl.50413>
- Askin, R. A., & Raine, J. I. (2000). Oligocene and Early Miocene Terrestrial Palynology of the Cape Roberts Drillhole CRP-2/2A, Victoria Land Basin, Antarctica. *Terra Antarctica*, *7*, 493–501. Retrieved from <http://epic.awi.de/27369/1/Ask2000a.pdf>
- Bahr, A., Jiménez-Espejo, F. J., Kolasinac, N., Grunert, P., Hernández-Molina, F. J., Röhl, U., et al. (2014). Deciphering bottom current velocity and paleoclimate signals from contourite deposits in the Gulf of Cádiz during the last 140 kyr: An inorganic geochemical approach. *Geochemistry, Geophysics, Geosystems*, *15*(8), 3145–3160. <https://doi.org/10.1002/2014GC005356>
- Barker, P. F., & Kennett, J. P. (1988). Proceedings, initial reports, Ocean Drilling Program, Leg 113, Weddell Sea, Antarctica.
- Barrett, P. J. (1989). *Antarctic Cenozoic history from the CIROS-1 drillhole, McMurdo Sound*. DRIS Publishing.
- Barrett, P. J. (2007). Cenozoic Climate and Sea Level History from Glacimarine Strata off the Victoria Land Coast, Cape Roberts Project, Antarctica. In M. J. Hambrey, P. Christoffersen, N. Glasser, & B. Hubbard (Eds.), *Glacial Sedimentary Processes and Products* (pp. 259–287). Oxford: Blackwell Publishing. <https://doi.org/10.1002/9781444304435.ch15>
- Barron, J. A., Baldauf, J. G., Barrera, E., Caulet, J.-P., Huber, B. T., Keating, B. H., et al. (1991). Biochronologic and magnetostratigraphic synthesis of Leg 119 sediments from the Kerguelen Plateau and Prydz Bay, Antarctica. In *Barron, J., Larsen, B., et al., Proc. ODP, Sci. Results* (Vol. 119, pp. 813–847).
- Bart, P. J., & Iwai, M. (2012). The overdeepening hypothesis: How erosional modification of the marine-scape during the early Pliocene altered glacial dynamics on the Antarctic Peninsula's Pacific margin. *Palaeogeography, Palaeoclimatology, Palaeoecology*, *335–336*(2012), 42–51. <https://doi.org/10.1016/j.palaeo.2011.06.010>
- Bart, P., & De Santis, L. (2012). Glacial Intensification During the Neogene: A Review of Seismic Strati-

- graphic Evidence from the Ross Sea, Antarctica, Continental Shelf. *Oceanography*, 25(3), 166–183. <https://doi.org/10.5670/oceanog.2012.92>
- Beddow, H. M., Liebrand, D., Sluijs, A., Wade, B. S., & Lourens, L. J. (2016). Global change across the Oligocene-Miocene transition: High-resolution stable isotope records from IODP Site U1334 (equatorial Pacific Ocean). *Paleoceanography*, 31(1), 81–97. <https://doi.org/10.1002/2015PA002820>
- Beerling, D. J., & Royer, D. L. (2011). Convergent Cenozoic CO<sub>2</sub> history. *Nature Geoscience*, 4(7), 418–420. <https://doi.org/10.1038/ngeo1186>
- Bijl, P. K., Bendle, J. A. P., Bohaty, S. M., Pross, J., Schouten, S., Tauxe, L., et al. (2013). Eocene cooling linked to early flow across the Tasmanian Gateway. *Proceedings of the National Academy of Sciences*, 110(24), 9645–9650. <https://doi.org/10.1073/pnas.1220872110>
- Bijl, P. K., Houben, A. J. P., Bruls, A., Pross, J., & Sangiorgi, F. (2018). Stratigraphic calibration of Oligocene–Miocene organic-walled dinoflagellate cysts from offshore Wilkes Land, East Antarctica, and a zonation proposal. *Journal of Micropalaeontology*, 37(1), 105–138. <https://doi.org/10.5194/jm-37-105-2018>
- Bijl, P. K., Houben, A. J. P., Hartman, J. D., Pross, J., Salabarnada, A., Escutia, C., & Sangiorgi, F. (2018). Paleooceanography and ice sheet variability offshore Wilkes Land, Antarctica - Part 2: Insights from Oligocene-Miocene dinoflagellate cyst assemblages. *Climate of the Past*, 14(7), 1015–1033. <https://doi.org/10.5194/cp-14-1015-2018>
- Billups, K., Channell, J. E. T., & Zachos, J. (2002). Late Oligocene to early Miocene geochronology and paleoceanography from the subantarctic South Atlantic. *Paleoceanography*, 17(1), 4-1-4–11. <https://doi.org/10.1029/2000PA000568>
- Billups, K., & Schrag, D. P. (2003). Application of benthic foraminiferal Mg/Ca ratios to questions of Cenozoic climate change. *Earth and Planetary Science Letters*, 209(1–2), 181–195. [https://doi.org/10.1016/S0012-821X\(03\)00067-0](https://doi.org/10.1016/S0012-821X(03)00067-0)
- Bindoff, N. L., Rintoul, S. R., & Massom, R. (2000). Bottom Water formation and polynyas in Adélie Land, Antarctica. *Royal Society of Tasmania*, 133(3), 51–56.
- Bindoff, N. L., Rosenberg, M. a., & Warner, M. J. (2000). On the circulation and water masses over the Antarctic continental slope and rise between 80 and 150°E. *Deep Sea Research Part II: Topical Studies in Oceanography*, 47(12–13), 2299–2326. [https://doi.org/10.1016/S0967-0645\(00\)00038-2](https://doi.org/10.1016/S0967-0645(00)00038-2)
- Bohaty, S. M., & Harwood, D. M. (1998). Southern Ocean pliocene paleotemperature variation from high-resolution silicoflagellate biostratigraphy. *Marine Micropaleontology*, 33(3–4), 241–272. [https://doi.org/10.1016/S0377-8398\(97\)00037-6](https://doi.org/10.1016/S0377-8398(97)00037-6)
- Bouma, A. H. (1962). Sedimentology of some flysch deposits. *Agraphic Approach to Facies Interpretation*, 168.
- Brancolini, G., Cooper, A. K., & Coren, F. (1995). Seismic Facies and Glacial History in the Western Ross Sea (Antarctica). *Geology and Seismic Stratigraphy of the Antarctic Margin, AGU Antarctic Research Series*, 68, 209–233. Retrieved from <http://onlinelibrary.wiley.com/doi/10.1029/AR068p0209/summary>
- Bromley, R. G., & Ekdale, A. A. (1984). Chondrites: a trace fossil indicator of anoxia in sediments. *Science*, 224, 872–875. Retrieved from <http://go.galegroup.com/ps/anonymou?id=GALE%-7CA3279153&sid=googleScholar&v=2.1&it=r&linkaccess=fulltext&issn=00368075&p=A-ONE&sw=w&authCount=1&isAnonymousEntry=true>
- Brown, L. F., & Fisher, W. L. (1979). *Principles of Seismic Stratigraphic Interpretation: Interpretation of Dep-*

*ositional Systems and Lithofacies from Seismic Data*. AAPG.

- Busetti, M., Caburlotto, a., Armand, L., Damiani, D., Giorgetti, G., Lucchi, R. G., et al. (2003). Plio-Quaternary sedimentation on the Wilkes land continental rise: preliminary results. *Deep Sea Research Part II: Topical Studies in Oceanography*, 50(8–9), 1529–1562. [https://doi.org/10.1016/S0967-0645\(03\)00078-X](https://doi.org/10.1016/S0967-0645(03)00078-X)
- Caburlotto, A., Lucchi, R. G., Santis, L., Macrì, P., & Tolotti, R. (2009). Sedimentary processes on the Wilkes Land continental rise reflect changes in glacial dynamic and bottom water flow. *International Journal of Earth Sciences*, 99(4), 909–926. <https://doi.org/10.1007/s00531-009-0422-8>
- Calvert, S. E., & Pedersen, T. F. (1996). Sedimentary geochemistry of manganese; implications for the environment of formation of manganiferous black shales. *Economic Geology*, 91(1), 36–47. <https://doi.org/10.2113/gsecongeo.91.1.36>
- Calvert, S. E., & Pedersen, T. F. (2007). Chapter Fourteen Elemental Proxies for Palaeoclimatic and Palaeoceanographic Variability in Marine Sediments: Interpretation and Application. In *Developments in Marine Geology* (Vol. 1, pp. 567–644). [https://doi.org/10.1016/S1572-5480\(07\)01019-6](https://doi.org/10.1016/S1572-5480(07)01019-6)
- Campagne, P., Crosta, X., Houssais, M. N., Swingedouw, D., Schmidt, S., Martin, A., et al. (2015). Glacial ice and atmospheric forcing on the Mertz Glacier Polynya over the past 250 years. *Nature Communications*, 6, 6642. <https://doi.org/10.1038/ncomms7642>
- Carter, L., & McCave, I. N. (2002). Eastern New Zealand Drifts, Miocene-Recent. *Geological Society, London, Memoirs*, 22(1), 385–407. <https://doi.org/10.1144/GSL.MEM.2002.022.01.27>
- Carter, L., Mccave, I. N., & Williams, M. J. M. (2009). Circulation and Water Masses of the Southern Ocean: A Review, 9197(8), 4–9. [https://doi.org/10.1016/S1571-9197\(08\)00004-9](https://doi.org/10.1016/S1571-9197(08)00004-9)
- Carter, R. M., Mccave, I. N., & Carter, L. (2004). Leg 181 Synthesis: Fronts , Flows , Drifts , Volcanoes , and the Evolution of the Southwestern Gateway to the Pacific Ocean , Eastern New Zealand. In C. (Ed. . Richter (Ed.), *Proceedings of the Ocean Drilling Program, Scientific Results* (Vol. 181).
- Chase, T. E., Seekins, B. A., Young, J. D., & Eitrem, S. L. (1987). Marine topography of offshore Antarctica.
- Close, D. I., Watts, A. B., & Stagg, H. M. J. (2009). A marine geophysical study of the Wilkes Land rifted continental margin, Antarctica. *Geophysical Journal International*, 177(2), 430–450. <https://doi.org/10.1111/j.1365-246X.2008.04066.x>
- Cofaigh, C. Ó., Taylor, J., Dowdeswell, J. A., & Pudsey, C. J. (2003). Palaeo-ice streams, trough mouth fans and high-latitude continental slope sedimentation. *Boreas*, 32(1), 37–55. <https://doi.org/10.1080/03009480310001858>
- Colleoni, F., De Santis, L., Montoli, E., Olivo, E., Sorlien, C. C., Bart, P. J., et al. (2018). Past continental shelf evolution increased Antarctic ice sheet sensitivity to climatic conditions. *Scientific Reports*, 8(1), 11323. <https://doi.org/10.1038/s41598-018-29718-7>
- Colwell, J. B., Stagg, H. M. J., Direen, N. G., Bernardel, G., & Borissova, I. (2006). The Structure of the Continental Margin off Wilkes Land and Terre Adélie Coast , East Antarctica. *East*, 327–340.
- Contreras, L., Bijl, P. K., Greenwood, D. R., Bohaty, S. M., Schouten, S., Bendle, J. a, et al. (2012). Persistent near-tropical warmth on the Antarctic continent during the early Eocene epoch. *Nature*, 488(7409), 73–7. <https://doi.org/10.1038/nature11300>
- Cook, C. P., Hill, D. J., van de Flierdt, T., Williams, T., Hemming, S. R., Dolan, A. M., et al. (2014). Sea surface temperature control on the distribution of far-traveled Southern Ocean ice-rafted detritus

- during the Pliocene. *Paleoceanography*, 29(6), 533–548. <https://doi.org/10.1002/2014PA002625>
- Cook, C. P., van de Flierdt, T., Williams, T., Hemming, S. R., Iwai, M., Kobayashi, M., et al. (2013). Dynamic behaviour of the East Antarctic ice sheet during Pliocene warmth. *Nature Geoscience*, 6(9), 765–769. <https://doi.org/10.1038/ngeo1889>
- Cook, C. P., Hemming, S. R., van de Flierdt, T., Pierce Davis, E. L., Williams, T., Galindo, A. L., et al. (2017). Glacial erosion of East Antarctica in the Pliocene: A comparative study of multiple marine sediment provenance tracers. *Chemical Geology*, 466(January), 199–218. <https://doi.org/10.1016/j.chemgeo.2017.06.011>
- Coxall, H. K., Wilson, P. A., Pälike, H., Lear, C. H., & Backman, J. (2005). Rapid stepwise onset of Antarctic glaciation and deeper calcite compensation in the Pacific Ocean. *Nature*, 433(7021), 53–57. <https://doi.org/10.1038/nature03135>
- Cramer, B. S., Toggweiler, J. R., Wright, J. D., Katz, M. E., & Miller, K. G. (2009). Ocean overturning since the Late Cretaceous: Inferences from a new benthic foraminiferal isotope compilation. *Paleoceanography*, 24(4), 14. <https://doi.org/10.1029/2008PA001683>
- Croudace, I. W., Rindby, A., & Rothwell, R. G. (2006). ITRAX: description and evaluation of a new multi-function X-ray core scanner. *Geological Society, London, Special Publications*, 267(1), 51–63. Retrieved from <http://sp.lyellcollection.org/content/267/1/51.short>
- Damiani, D., Giorgetti, G., & Turbanti, I. M. (2006). Clay mineral fluctuations and surface textural analysis of quartz grains in Pliocene–Quaternary marine sediments from Wilkes Land continental rise (East-Antarctica): Palaeoenvironmental significance. *Marine Geology*, 226(3–4), 281–295. <https://doi.org/10.1016/j.margeo.2005.11.002>
- De Santis, L., Brancolini, G., & Donda, F. (2003). Seismo-stratigraphic analysis of the Wilkes Land continental margin (East Antarctica): influence of glacially driven processes on the Cenozoic deposition. *Deep Sea Research Part II: Topical Studies in Oceanography*, 50(8–9), 1563–1594. [https://doi.org/10.1016/S0967-0645\(03\)00079-1](https://doi.org/10.1016/S0967-0645(03)00079-1)
- De Santis, L., Brancolini, G., Donda, F., O'Brien, P., Santis, L. De, & Brien, P. O. (2010). Cenozoic deformation in the George V Land continental margin (East Antarctica). *Marine Geology*, 269(1–2), 1–17. <https://doi.org/10.1016/j.margeo.2009.12.001>
- De Santis, L., Anderson, J. B., Brancolini, G., & Zayatz, I. (2013). Seismic Record of Late Oligocene Through Miocene Glaciation on the Central and Eastern Continental Shelf of the Ross Sea. In *Geology and Seismic stratigraphy of the Antarctic margin. Antarctic Research Series*. (Vol. 68, pp. 235–260). <https://doi.org/10.1029/AR068p0235>
- DeCesare, M., Pekar, S. F., & DeCesare. (2013). Investigating a Middle to Late Miocene Carbonate Preservation Event in the Southern Ocean. *American Geophysical Union, Fall Meeting 2013, Abstract #PP43A-2072*, (1), 12–13. Retrieved from <http://adsabs.harvard.edu/abs/2013AGUFMP-P43A2072D>
- DeConto, R. M., & Pollard, D. (2003). A coupled climate–ice sheet modeling approach to the Early Cenozoic history of the Antarctic ice sheet. *Palaeogeography, Palaeoclimatology, Palaeoecology*, 198(1–2), 39–52. [https://doi.org/10.1016/S0031-0182\(03\)00393-6](https://doi.org/10.1016/S0031-0182(03)00393-6)
- DeConto, R. M., & Pollard, D. (2016). Contribution of Antarctica to past and future sea-level rise. *Nature*, 531(7596), 591–597. <https://doi.org/10.1038/nature17145>
- DeMaster, D. J. (2013). The Diagenesis of Biogenic Silica: Chemical Transformations Occurring in the Water Column, Seabed, and Crust. *Treatise on Geochemistry: Second Edition*, 9(Figure 1), 103–111.

<https://doi.org/10.1016/B978-0-08-095975-7.00704-X>

- Diekmann, B. (2007). Sedimentary patterns in the late Quaternary Southern Ocean. *Deep Sea Research Part II: Topical Studies in Oceanography*, 54(21–22), 2350–2366. <https://doi.org/10.1016/j.dsr2.2007.07.025>
- Diester-Haass, L. (1996). Late Eocene-Oligocene paleoceanography in the southern Indian Ocean (ODP Site 744). *Marine Geology*, 130(1–2), 99–119. [https://doi.org/10.1016/0025-3227\(95\)00128-X](https://doi.org/10.1016/0025-3227(95)00128-X)
- Dingle, R., Birch, G., Bremner, J., De Decker, R., Du Plessis, A., Engelbrecht, J., et al. (1987). Deep-sea sedimentary environments around southern Africa (south-east Atlantic and southwest Indian Oceans). *Annals of the South African Museum*, 98, 1–27.
- Direen, N. G., Stagg, H. M. J., Symonds, P. A., & Norton, I. O. (2013). Variations in rift symmetry: cautionary examples from the Southern Rift System (Australia-Antarctica). *Geological Society, London, Special Publications*, 369(1), 453–475. <https://doi.org/10.1144/SP369.4>
- Doebelin, N., & Kleeberg, R. (2015). Profex: a graphical user interface for the Rietveld refinement program BGMN. *Journal of Applied Crystallography*, 48(5), 1573–1580.
- Domack, E. W., & Powell, R. (2017). *Modern Glaciomarine Environments and Sediments: An Antarctic Perspective. An Antarctic Perspective. Past Glacial Environments: Second Edition*. Elsevier Ltd. <https://doi.org/10.1016/B978-0-08-100524-8.00030-0>
- Donda, F., Brancolini, G., De Santis, L., & Trincardi, F. (2003). Seismic facies and sedimentary processes on the continental rise off Wilkes Land (East Antarctica): evidence of bottom current activity. *Deep Sea Research Part II: Topical Studies in Oceanography*, 50(8–9), 1509–1527. [https://doi.org/10.1016/S0967-0645\(03\)00075-4](https://doi.org/10.1016/S0967-0645(03)00075-4)
- Donda, F., Brancolini, G., O'Brien, P. E., De Santis, L., & Escutia, C. (2007). Sedimentary processes in the Wilkes Land margin: a record of the Cenozoic East Antarctic Ice Sheet evolution. *Journal of the Geological Society*, 164(1), 243–256. <https://doi.org/10.1144/0016-76492004-159>
- Donda, F., O'Brien, P. E., De Santis, L., Rebesco, M., & Brancolini, G. (2008). Mass wasting processes in the Western Wilkes Land margin: Possible implications for East Antarctic glacial history. *Palaeogeography, Palaeoclimatology, Palaeoecology*, 260(1–2), 77–91. <https://doi.org/10.1016/j.palaeo.2007.08.008>
- Drewry, D. J. (1983). *Antarctica: glaciological and geophysical folio* (Vol. 2). University of Cambridge, Scott Polar Research Institute Cambridge, United ....
- Duliu, O. (1999). Computer axial tomography in geosciences: an overview. *Earth-Science Reviews*, 48(4), 265–281. [https://doi.org/10.1016/S0012-8252\(99\)00056-2](https://doi.org/10.1016/S0012-8252(99)00056-2)
- Dypvik, H., & Harris, N. B. (2001). Geochemical facies analysis of fine-grained siliciclastics using Th/U, Zr/Rb and (Zr + Rb)/Sr ratios. *Chemical Geology*, 181(1–4), 131–146. [https://doi.org/10.1016/S0009-2541\(01\)00278-9](https://doi.org/10.1016/S0009-2541(01)00278-9)
- Ehrmann, W. U., & Mackensen, A. (1992). Sedimentological evidence for the formation of an East Antarctic ice sheet in Eocene/Oligocene time. *Palaeogeography, Palaeoclimatology, Palaeoecology*, 93(1–2), 85–112. [https://doi.org/10.1016/0031-0182\(92\)90185-8](https://doi.org/10.1016/0031-0182(92)90185-8)
- Ehrmann, W., Setti, M., & Marinoni, L. (2005). Clay minerals in Cenozoic sediments off Cape Roberts (McMurdo Sound, Antarctica) reveal palaeoclimatic history. *Palaeogeography, Palaeoclimatology, Palaeoecology*, 229(3), 187–211. <https://doi.org/10.1016/j.palaeo.2005.06.022>
- Eittrheim, S. L., & Smith, G. L. (1987). Seismic sequences and their distribution on the Wilkes Land mar-



gin.

- Eittrheim, S. L., Cooper, A. K., & Wannesson, J. (1995). Seismic stratigraphic evidence of ice-sheet advances on the Wilkes Land margin of Antarctica. *Sedimentary Geology*, 96(1–2), 131–156. [https://doi.org/10.1016/0037-0738\(94\)00130-M](https://doi.org/10.1016/0037-0738(94)00130-M)
- Escutia, C., Eittrheim, S. L., Cooper, A. K., & NELSON, C. H. (1997). Cenozoic sedimentation on the Wilkes Land continental rise, Antarctica. In *The Antarctic Region: Geological Evolution and Processes. Proc. Int. Symp. Antarct. Earth Sci* (Vol. 7, pp. 791–795).
- Escutia, C., Eittrheim, S. L., Cooper, A. K., Nelson, C. H., Survey, U. S. G., Road, M., & Park, M. (2000). Morphology and acoustic character of the Antarctic Wilkes Land turbidite systems: ice-sheet-sourced versus river-sourced fans. *Journal of Sedimentary Research*, 70(1), 84–93.
- Escutia, C., Nelson, C. H., Acton, G. D., Eittrheim, S. L., Cooper, a. K., Warnke, D. a., & Jaramillo, J. M. (2002). Current controlled deposition on the Wilkes Land continental rise, Antarctica. *Geological Society, London, Memoirs*, 22(1), 373–384. <https://doi.org/10.1144/GSL.MEM.2002.022.01.26>
- Escutia, C., Warnke, D., Acton, G. ., Barcena, A., Burckle, L., Canals, M., & Frazee, C. . (2003). Sediment distribution and sedimentary processes across the Antarctic Wilkes Land margin during the Quaternary. *Deep Sea Research Part II: Topical Studies in Oceanography*, 50(8–9), 1481–1508. [https://doi.org/10.1016/S0967-0645\(03\)00073-0](https://doi.org/10.1016/S0967-0645(03)00073-0)
- Escutia, C., De Santis, L., Donda, F., Dunbar, R. B., Cooper, A. K., Brancolini, G., & Eittrheim, S. L. (2005). Cenozoic ice sheet history from East Antarctic Wilkes Land continental margin sediments. *Global and Planetary Change*, 45(1–3), 51–81. <https://doi.org/10.1016/j.gloplacha.2004.09.010>
- Escutia, C., Donda, F., Lobo, F. J., & Tanahashi, M. (2007). Extensive debris flow deposits on the eastern Wilkes Land margin : a key to changing glacial regimes. In U. A. K., Cooper and C. R. Raymond et al. (Ed.), *Online Proceedings of the 10th ISAES* (pp. 2000–2003). <https://doi.org/10.3133/of2007-1047.srp026>
- Escutia, C., Bárcena, M. A., Lucchi, R. G., Romero, O., Ballegeer, A. M., Gonzalez, J. J., & Harwood, D. M. (2009). Circum-Antarctic warming events between 4 and 3.5Ma recorded in marine sediments from the Prydz Bay (ODP Leg 188) and the Antarctic Peninsula (ODP Leg 178) margins. *Global and Planetary Change*, 69(3), 170–184. <https://doi.org/10.1016/j.gloplacha.2009.09.003>
- Escutia, C., Brinkhuis, H., & Klaus, A. (2011). Expedition 318 summary. <https://doi.org/10.2204/iodp.proc.318.101.2011>
- Escutia, C., Brinkhuis, H., Klaus, A., & Expedition 318 Scientists. (2011b). Site U1356. In C. Escutia, H. Brinkhuis, A. Klaus, & Expedition 318 Scientists (Eds.), *Proceeding of the Integrated Ocean Drilling Program, 318* (Vol. 318). Tokyo: Integrated Ocean Drilling Program Management International, Inc. <https://doi.org/10.2204/iodp.proc.318.104.2011>
- Escutia, C., & Brinkhuis, H. (2014). *From Greenhouse to Icehouse at the Wilkes Land Antarctic Margin: IODP Expedition 318 Synthesis of Results. Developments in Marine Geology* (Vol. 7). Elsevier. <https://doi.org/10.1016/B978-0-444-62617-2.00012-8>
- Etourneau, J., Ehlert, C., Frank, M., Martinez, P., Schneider, R., 2012. Contribution of changes in opal productivity and nutrient distribution in the coastal upwelling systems to Late Pliocene/Early Pleistocene climate cooling. *Clim. Past* 8, 1435–1445.
- Etourneau, J. (2014). Palaeoceanography: Tectonically driven upwelling. *Nature Geoscience*, 7(10), 698–699. <https://doi.org/10.1038/ngeo2258>
- Etourneau, J., Sgubin, G., Crosta, X., Swingedouw, D., Barbara, L., Houssais, M., et al. (2017). Ocean tem-

- perature impact on ice shelf instability along the eastern Antarctic Peninsula margin. *Nature Communications*, (December 2019), 2017. <https://doi.org/10.1038/s41467-018-08195-6>
- Etourneau, J., Sgubin, G., Crosta, X., Swingedouw, D., Willmott, V., Barbara, L., Houssais, M.N., Schouten, S., Damsté, J.S.S., Goosse, H., Escutia, C., Crespín, J., Massé, G., Kim, J.H., 2019. Ocean temperature impact on ice shelf extent in the eastern Antarctic Peninsula. *Nat. Commun.* 10, 8–15.
- Evans, M. E., Heller, F., Bloemendal, J., & Thouveny, N. (1997). Natural magnetic archives of past global change. *Surveys in Geophysics*, 18(2–3), 183–196. <https://doi.org/10.1023/A:1006583809200>
- Eynaud, F., Giraudeau, J., Pichon, J. J., & Pudsey, C. J. (1999). Sea-surface distribution of coccolithophores, diatoms, silicoflagellates and dinoflagellates in the South Atlantic Ocean during the late austral summer 1995. *Deep-Sea Research Part I: Oceanographic Research Papers*, 46(3), 451–482. [https://doi.org/10.1016/S0967-0637\(98\)00079-X](https://doi.org/10.1016/S0967-0637(98)00079-X)
- Faugères, J.-C., & Stow, D. A. V. (1993). Bottom-current-controlled sedimentation: a synthesis of the contourite problem. *Sedimentary Geology*, 82(1–4), 287–297. [https://doi.org/10.1016/0037-0738\(93\)90127-Q](https://doi.org/10.1016/0037-0738(93)90127-Q)
- Faugères, J.-C., Stow, D. A. V., Imbert, P., & Viana, A. (1999). Seismic features diagnostic of contourite drifts. *Marine Geology*, 162, 1–38.
- Faugères, J.-C., Zaragosi, S., Mezeraïs, M. L., & Masse, L. (2002). The Vema contourite fan in the South Brazilian Basin. *Deep-Water Contourite Systems: Modern Drifts and Ancient Series, Seismic and Sedimentary Characteristics*, 22, 209–222. <https://doi.org/10.1144/gsl.mem.2002.022.01.15>
- Faugères, J.-C., & Stow, D. A. V. (2008). Chapter 14 Contourite Drifts (pp. 257–288). [https://doi.org/10.1016/S0070-4571\(08\)10014-0](https://doi.org/10.1016/S0070-4571(08)10014-0)
- Ferraccioli, F., Coren, F., Bozzo, E., Zanolla, C., Gandolfi, S., Tabacco, I., & Frezzotti, M. (2001). Rifted(?) crust at the East Antarctic Craton margin: gravity and magnetic interpretation along a traverse across the Wilkes Subglacial Basin region. *Earth and Planetary Science Letters*, 192(3), 407–421. [https://doi.org/10.1016/S0012-821X\(01\)00459-9](https://doi.org/10.1016/S0012-821X(01)00459-9)
- Ferraccioli, F., Armadillo, E., Jordan, T., Bozzo, E., & Corr, H. (2009). Aeromagnetic exploration over the East Antarctic Ice Sheet: A new view of the Wilkes Subglacial Basin. *Tectonophysics*, 478(1–2), 62–77. <https://doi.org/10.1016/j.tecto.2009.03.013>
- Field, C. B., Barros, V. R., Dokken, D. J., Mach, K. J., Mastrandrea, M. D., Bilir, T. E., et al. (2014). *IPCC, 2014: Climate Change 2014: Impacts, Adaptation, and Vulnerability. Part A: Global and Sectoral Aspects. Contribution of Working Group II to the Fifth Assessment Report of the Intergovernmental Panel on Climate Change*. (C. B. Field, V. R. Barros, D. J. Dokken, K. J. Mach, M. D. Mastrandrea, T. E. Bilir, et al., Eds.). Cambridge, United Kingdom and New York, NY, USA: Cambridge University Press. Retrieved from <http://hdl.handle.net/20.500.11822/17771>
- Florindo, F., Roberts, A. P., & Palmer, M. R. (2003). Magnetite dissolution in siliceous sediments. *Geochemistry, Geophysics, Geosystems*, 4(7), 1–13. <https://doi.org/10.1029/2003GC000516>
- Foster, G. L., & Rohling, E. J. (2013). Relationship between sea level and climate forcing by CO<sub>2</sub> on geological timescales. *Proceedings of the National Academy of Sciences of the United States of America*, 110(4), 1209–14. <https://doi.org/10.1073/pnas.1216073110>
- Foubert, A., & Henriët, J.-P. (2009). *Nature and Significance of the Recent Carbonate Mound Record* (Vol. 126). Berlin, Heidelberg: Springer Berlin Heidelberg. <https://doi.org/10.1007/978-3-642-00290-8>
- Fouinat, L., Sabatier, P., Poulénard, J., Reyss, J.-L., Montet, X., & Arnaud, F. (2017). A new CT scan methodology to characterize a small aggregation gravel clast contained in a soft sediment matrix. *Earth*

- Surface Dynamics*, 5(1), 199–209. <https://doi.org/10.5194/esurf-5-199-2017>
- Fretwell, P., Pritchard, H. D., Vaughan, D. G., Bamber, J. L., Barrand, N. E., Bell, R., et al. (2013). Bedmap2: Improved ice bed, surface and thickness datasets for Antarctica. *Cryosphere*, 7(1), 375–393. <https://doi.org/10.5194/tc-7-375-2013>
- Fukamachi, Y., Wakatsuchi, M., Taira, K., Kitagawa, S., Ushio, S., Takahashi, A., et al. (2000). Seasonal variability of bottom water properties off Adélie Land, Antarctica. *Journal of Geophysical Research: Oceans*, 105(C3), 6531–6540. <https://doi.org/10.1029/1999JC900292>
- Fukamachi, Y., Rintoul, S. R., Church, J. A., Aoki, S., Sokolov, S., Rosenberg, M. A., & Wakatsuchi, M. (2010). Strong export of Antarctic Bottom Water east of the Kerguelen plateau. *Nature Geoscience*, 3(5), 327–331. <https://doi.org/10.1038/ngeo842>
- Gasson, E., DeConto, R. M., Pollard, D., & Levy, R. H. (2016). Dynamic Antarctic ice sheet during the early to mid-Miocene. *Proceedings of the National Academy of Sciences*, 113(13), 3459–3464. <https://doi.org/10.1073/pnas.1516130113>
- Gilbert, R., Nielsen, N., Desloges, J. R., & Rasch, M. (1998). Contrasting glacial marine sedimentary environments of two arctic fiords on Disko, West Greenland. *Marine Geology*, 147(1–4), 63–83. [https://doi.org/10.1016/S0025-3227\(98\)00008-5](https://doi.org/10.1016/S0025-3227(98)00008-5)
- Gonthier, E. G., Faugères, J.-C., & Stow, D. A. V. (1984). Contourite facies of the Faro drift, Gulf of Cadiz. *Geological Society, London, Special Publications*, 15(1), 275–292.
- Goodell, H. G. (1973). *Marine sediments of the Southern Oceans*. American Geographical Society.
- Govin, A., Michel, E., Labeyrie, L., Waelbroeck, C., Dewilde, F., & Jansen, E. (2009). Evidence for northward expansion of Antarctic Bottom Water mass in the Southern Ocean during the last glacial inception. *Paleoceanography*, 24(1), 14. <https://doi.org/10.1029/2008PA001603>
- Gradstein, F. M., Ogg, J. G., & Smith, A. G. (2004). *A Geologic Time Scale 2004*. Earth (Vol. 2004). Retrieved from <http://books.google.com/books?id=rse4v1P-f9kC&pgis=1>
- Grobe, H., & Mackensen, A. (1992). Late Quaternary climatic cycles as recorded in sediments from the Antarctic Continental margin. *The Antarctic Paleoenvironments: A Perspective on Global Change. Antarctic Research Series*, 56, 349–376. <https://doi.org/10.1029/10013/epic.11662.d001>
- Gruetzner, J., Uenzelmann-Neben, G., 2016. Contourite drifts as indicators of Cenozoic bottom water intensity in the eastern Agulhas Ridge area, South Atlantic. *Mar. Geol.* 378, 350–360.
- Hall, I. R., McCave, I. N., Zahn, R., Carter, L., Knutz, P. C., & Weedon, G. P. (2003). Paleocurrent reconstruction of the deep Pacific inflow during the middle Miocene: Reflections of East Antarctic Ice Sheet growth. *Paleoceanography*, 18(2). <https://doi.org/10.1029/2002PA000817>
- Hampton, M. A., Kravitz, J. H., & Luepke, G. (1987). Geology of sediment cores from the George V continental margin, Antarctica.
- Hannah, M. J., Wilson, G. J., & Wrenn, J. H. (2000). Oligocene and miocene marine palynomorphs from CRP-2/2A, Victoria Land Basin, Antarctica. *Terra Antarctica*, 7(4), 503–511.
- Hannah, M. J., Wrenn, J., & Wilson, G. (2001). Preliminary report on early Oligocene and latest Eocene marine palynomorphs from CRP-3 drillhole, Victoria Land Basin, Antarctica. *Terra Antarctica*, 8(4), 383–388. Retrieved from <http://epic.awi.de/27347/1/Han2001g.pdf>
- Harris, P. T. (2000). Ripple cross-laminated sediments on the East Antarctic Shelf: Evidence for episodic bottom water production during the Holocene? *Marine Geology*, 170(3–4), 317–330. [https://doi.org/10.1016/S0025-3227\(00\)00096-7](https://doi.org/10.1016/S0025-3227(00)00096-7)

- Hartman, J. D., Sangiorgi, F., Salabarnada, A., Peterse, F., Houben, A. J. P., Schouten, S., et al. (2018). Paleooceanography and ice sheet variability offshore Wilkes Land, Antarctica - Part 3: Insights from Oligocene-Miocene TEX86-based sea surface temperature reconstructions. *Climate of the Past*, 14, 1275–1297. <https://doi.org/10.5194/cp-14-1275-2018>
- Hauptvogel, D. W., Pekar, S. F., & Pincay, V. (2017). Evidence for a heavily glaciated Antarctica during the late Oligocene “warming” (27.8–24.5 Ma): Stable isotope records from ODP Site 690. *Paleoceanography*, 32(4), 384–396. <https://doi.org/10.1002/2016PA002972>
- Hauptvogel, D. W. (2015). *The State Of The Oligocene Icehouse World : Sedimentology , Provenance , And Stable Isotopes Of Marine Sediments From The Antarctic Continental Margin*. PhD Dissertation. University Of New York.
- Hayes, D. E., & Frakes, L. A. (1975). General Synthesis, Deep Sea Drilling Project Leg 28. In *Initial Reports of the Deep Sea Drilling Project*, 28 (Vol. 28). U.S. Government Printing Office. <https://doi.org/10.2973/dsdp.proc.28.136.1975>
- Hayes, D. E., & Barrett, P. J.: ODP Site 269, (January 1973).
- Heezen, B. C., Schneider, E. D., & Pilkey, O. H. (1966). Sediment transport by the Antarctic bottom current on the Bermuda Rise. *Nature*, 211(5049), 611–612.
- Hennekam, R., & de Lange, G. (2012). X-ray fluorescence core scanning of wet marine sediments: methods to improve quality and reproducibility of high-resolution paleoenvironmental records. *Limnology and Oceanography: Methods*, 10(12), 991–1003. <https://doi.org/10.4319/lom.2012.10.991>
- Hepp, D. A. (2007). *Late Miocene-Pliocene glacial cyclicity in a deep-sea sediment drift on the Antarctic Peninsula continental margin: Sedimentary and diagenetic processes*, Ph.D Thesis. Universität Bremen.
- Hepp, D. A., Mörz, T., Hensen, C., Frederichs, T., Kasten, S., Riedinger, N., & Hay, W. W. (2009). A late Miocene–early Pliocene Antarctic deepwater record of repeated iron reduction events. *Marine Geology*, 266(1–4), 198–211. <https://doi.org/10.1016/j.margeo.2009.08.006>
- Hernández-Molina, F. J., Larter, R. D., Rebesco, M., & Maldonado, A. (2006). Miocene reversal of bottom water flow along the Pacific Margin of the Antarctic Peninsula: Stratigraphic evidence from a contourite sedimentary tail. *Marine Geology*, 228(1–4), 93–116. <https://doi.org/10.1016/j.margeo.2005.12.010>
- Hesse, R., & Schacht, U. (2011). Chapter 9 Early Diagenesis of Deep-Sea Sediments. In H. HüNeke & T. Mulder (Eds.), *Developments in Sedimentology* (Vol. 63, pp. 557–713). Amsterdam and Oxford: Elsevier B.V. <https://doi.org/10.1016/B978-0-444-53000-4.00009-3>
- Hinnov, L. A. (2013). Cyclostratigraphy and its revolutionizing applications in the earth and planetary sciences. *Bulletin of the Geological Society of America*, 125(11–12), 1703–1734. <https://doi.org/10.1130/B30934.1>
- Hodell, D. A., Channell, J. E. T., Curtis, J. H., Romero, O. E., & Röhl, U. (2008). Onset of “Hudson Strait” Heinrich events in the eastern North Atlantic at the end of the middle Pleistocene transition (~640 ka)? *Paleoceanography*, 23(4). <https://doi.org/10.1029/2008PA001591>
- Holbourn, A., Kuhnt, W., Schulz, M., & Erlenkeuser, H. (2005). Impacts of orbital forcing and atmospheric carbon dioxide on Miocene ice-sheet expansion. *Nature*, 438(7067), 483–487. <https://doi.org/10.1038/nature04123>
- Houben, A. J. P., Bijl, P. K., Pross, J., Bohaty, S. M., Passchier, S., Stickley, C. E., et al. (2013). Reorganization of Southern Ocean Plankton Ecosystem at the Onset of Antarctic Glaciation. *Science*, 340(6130), 341–344. <https://doi.org/10.1126/science.1223646>

- Huber, M., & Sloan, L. C. (2001). Heat transport, deep waters, and thermal gradients: Coupled simulation of an Eocene greenhouse climate. *Geophysical Research Letters*, 28(18), 3481–3484. <https://doi.org/10.1029/2001GL012943>
- Huber, M., Brinkhuis, H., Stickley, C. E., Döös, K., Sluijs, A., Warnaar, J., et al. (2004). Eocene circulation of the Southern Ocean: Was Antarctica kept warm by subtropical waters? *Paleoceanography*, 19(4), n/a-n/a. <https://doi.org/10.1029/2004PA001014>
- Huck, C. E., van de Flierdt, T., Bohaty, S. M., & Hammond, S. J. (2017). Antarctic climate, Southern Ocean circulation patterns, and deep water formation during the Eocene. *Paleoceanography*, 32(7), 674–691. <https://doi.org/10.1002/2017PA003135>
- Jaccard, S. L., Galbraith, E. D., Martínez-García, A., & Anderson, R. F. (2016). Covariation of deep Southern Ocean oxygenation and atmospheric CO<sub>2</sub> through the last ice age. *Nature*, 530(7589), 207–210. <https://doi.org/10.1038/nature16514>
- Jacobs, S. S., Jenkins, A., Giulivi, C. F., & Dutrieux, P. (2011). Stronger ocean circulation and increased melting under Pine Island Glacier ice shelf. *Nature Geoscience*, 4(8), 519.
- Jamieson, S. S. R., Stokes, C. R., Ross, N., Rippin, D. M., Bingham, R. G., Wilson, D. S., et al. (2014). The glacial geomorphology of the Antarctic ice sheet bed. *Antarctic Science*, 26(6), 724–741. <https://doi.org/10.1017/S0954102014000212>
- Johnson, G. C. (2008). Quantifying Antarctic Bottom Water and North Atlantic Deep Water volumes. *Journal of Geophysical Research*, 113(C5), C05027. <https://doi.org/10.1029/2007JC004477>
- Jordan, T. a., Ferraccioli, F., Corr, H., Graham, a., Armadillo, E., & Bozzo, E. (2010). Hypothesis for mega-outburst flooding from a palaeo-subglacial lake beneath the East Antarctic Ice Sheet. *Terra Nova*, no-no. <https://doi.org/10.1111/j.1365-3121.2010.00944.x>
- Kemp, E. M., & Barrett, P. J. (1975). Antarctic glaciation and early Tertiary vegetation. *Nature*, 258(5535), 507–508. <https://doi.org/10.1038/258507a0>
- Kennett, J. P., Houtz, R. E., Andrews, P. B., Edwards, A. R., Gostin, V. A., Hajós, M., et al. (1975). Cenozoic paleoceanography in the southwest Pacific Ocean, Antarctic Glaciation, and the development of the Circum-Antarctic Current. *Deep Sea Drilling Project Initial Reports*, 29, 1155–1169.
- Kennett, J. P., & Shackleton, N. J. (1976). Oxygen isotopic evidence for the development of the psychrosphere 38 Myr ago. *Nature*, 260(5551), 513.
- Kennett, J. P. (1977). Cenozoic evolution of Antarctic glaciation, the circum-Antarctic Ocean, and their impact on global paleoceanography. *Journal of Geophysical Research*, 82(27), 3843–3860. <https://doi.org/10.1029/JC082i027p03843>
- Kisch, H. J. (1991). Illite crystallinity: recommendations on sample preparation, X-ray diffraction settings, and interlaboratory samples. *Journal of Metamorphic Geology*, 9(6), 665–670.
- Kominz, M. A., & Pekar, S. F. (2001). Oligocene eustasy from two-dimensional sequence stratigraphic backstripping. *Geological Society of America Bulletin*, 113(3), 291–304. [https://doi.org/10.1130/0016-7606\(2001\)113<0291:OEFTDS>2.0.CO;2](https://doi.org/10.1130/0016-7606(2001)113<0291:OEFTDS>2.0.CO;2)
- Korff, L., von Dobeneck, T., Frederichs, T., Kasten, S., Kuhn, G., Gersonde, R., & Diekmann, B. (2016). Cyclic magnetite dissolution in Pleistocene sediments of the abyssal northwest Pacific Ocean: Evidence for glacial oxygen depletion and carbon trapping. *Paleoceanography*, 31(5), 600–624. <https://doi.org/10.1002/2015PA002882>
- Kuhn, G., & Diekmann, B. (2002). Late Quaternary variability of ocean circulation in the southeastern

- South Atlantic inferred from the terrigenous sediment record of a drift deposit in the southern Cape Basin (ODP Site 1089). *Palaeogeography, Palaeoclimatology, Palaeoecology*, 182(3–4), 287–303. [https://doi.org/10.1016/S0031-0182\(01\)00500-4](https://doi.org/10.1016/S0031-0182(01)00500-4)
- Kuvaas, B., & Leitchenkov, G. (1992). Glaciomarine turbidite and current controlled deposits in Prydz Bay, Antarctica. *Marine Geology*, 108(3–4), 365–381. [https://doi.org/10.1016/0025-3227\(92\)90205-V](https://doi.org/10.1016/0025-3227(92)90205-V)
- Lambelet, M., van de Flierdt, T., Butler, E. C. V., Bowie, A. R., Rintoul, S. R., Watson, R. J., et al. (2018). The Neodymium Isotope Fingerprint of Adélie Coast Bottom Water. *Geophysical Research Letters*, 45(20), 11,247–11,256. <https://doi.org/10.1029/2018GL080074>
- Laskar, J., Robutel, P., Joutel, F., Gastineau, M., Correia, a. C. M., & Levrard, B. (2004). A long-term numerical solution for the insolation quantities of the Earth. *Astronomy and Astrophysics*, 428(1), 261–285. <https://doi.org/10.1051/0004-6361:20041335>
- Lear, C. H., Elderfield, H., & Wilson, P. A. (2000). Cenozoic deep-sea temperatures and global ice volumes from Mg/Ca in benthic foraminiferal calcite. *Science*, 287(5451), 269–272.
- Lear, C. H., Rosenthal, Y., Coxall, H. K., & Wilson, P. A. (2004). Late Eocene to early Miocene ice sheet dynamics and the global carbon cycle. *Paleoceanography*, 19(4). <https://doi.org/10.1029/2004PA001039>
- Lear, C. H., Bailey, T. R., Pearson, P. N., Coxall, H. K., & Rosenthal, Y. (2008). Cooling and ice growth across the Eocene-Oligocene transition. *Geology*, 36(3), 251–254.
- Leckie, R. M., & Webb, P.-N. (1983). Late Oligocene–early Miocene glacial record of the Ross Sea, Antarctica: Evidence from DSDP Site 270. *Geology*, 11(10), 578. [https://doi.org/10.1130/0091-7613\(1983\)11<578:LOMGRO>2.0.CO;2](https://doi.org/10.1130/0091-7613(1983)11<578:LOMGRO>2.0.CO;2)
- Leitchenkov, G. L., Gandyukhin, V. V., Guseva, Y. B., Raymond, C. editor, & International Symposium on Antarctic Earth, S. (2007). Cenozoic environmental changes along the East Antarctic continental margin inferred from regional seismic stratigraphy. *Open-File Report - U. S. Geological Survey*, Short Research Paper 005. <https://doi.org/10.3133/of2007-1047.srp005>
- Levy, R., Harwood, D., Florindo, F., Sangiorgi, F., Tripathi, R., von Eynatten, H., et al. (2016). Antarctic ice sheet sensitivity to atmospheric CO<sub>2</sub> variations in the early to mid-Miocene. *Proceedings of the National Academy of Sciences*, 113(13), 3453–3458. <https://doi.org/10.1073/pnas.1516030113>
- Levy, R. H., Meyers, S. R., Naish, T. R., Golledge, N. R., McKay, R. M., Crampton, J. S., et al. (2019). Antarctic ice-sheet sensitivity to obliquity forcing enhanced through ocean connections. *Nature Geoscience*, 1. <https://doi.org/10.1038/s41561-018-0284-4>
- Liebrand, D., Lourens, L. J., Hodell, D. a., de Boer, B., van de Wal, R. S. W., & Pälike, H. (2011). Antarctic ice sheet and oceanographic response to eccentricity forcing during the early Miocene. *Climate of the Past*, 7(3), 869–880. <https://doi.org/10.5194/cp-7-869-2011>
- Liebrand, D., Beddow, H. M., Lourens, L. J., Pälike, H., Raffi, I., Bohaty, S. M., et al. (2016). Cyclostratigraphy and eccentricity tuning of the early Oligocene through early Miocene (30.1–17.1 Ma): Cibicides mundulus stable oxygen and carbon isotope records from Walvis Ridge Site 1264. *Earth and Planetary Science Letters*, 450, 392–405. <https://doi.org/10.1016/j.epsl.2016.06.007>
- Liebrand, D., de Bakker, A. T. M., Beddow, H. M., Wilson, P. A., Bohaty, S. M., Ruessink, G., et al. (2017). Evolution of the early Antarctic ice ages. *Proceedings of the National Academy of Sciences*, 114(15), 3867–3872. <https://doi.org/10.1073/pnas.1615440114>
- Lisiecki, L. E., Raymo, M. E., & Curry, W. B. (2008). Atlantic overturning responses to Late Pleistocene climate forcings. *Nature*, 456(7218), 85–88. <https://doi.org/10.1038/nature07425>

- Liu, Z., Pagani, M., Zinniker, D., DeConto, R., Huber, M., Brinkhuis, H., et al. (2009). Global cooling during the Eocene-Oligocene climate transition. *Science*, 323(5918), 1187–1190.
- López-Quirós, A., Lobo, F. J., Escutia, C., García, M., Hernández-Molina, F. J., Pérez, L. F., et al. (2020). Geomorphology of Ona Basin, southwestern Scotia Sea (Antarctica): Decoding the spatial variability of bottom-current pathways. *Marine Geology*, 422(January), 106113. <https://doi.org/10.1016/j.mar-geo.2020.106113>
- Lowe, A. L., & Anderson, J. B. (2003). Evidence for abundant subglacial meltwater beneath the paleo-ice sheet in Pine Island Bay, Antarctica. *Journal of Glaciology*, 49(164).
- Lowe, D. R. (1982). Sediment gravity flows; II, Depositional models with special reference to the deposits of high-density turbidity currents. *Journal of Sedimentary Research*, 52(1), 279–297.
- Lucchi, R. G., & Rebesco, M. (2007). Glacial contourites on the Antarctic Peninsula margin: insight for palaeoenvironmental and palaeoclimatic conditions. *Geological Society, London, Special Publications*, 276(1), 111–127. <https://doi.org/10.1144/GSL.SP.2007.276.01.06>
- Lyle, M., Gibbs, S., Moore, T. C., & Rea, D. K. (2007). Late Oligocene initiation of the Antarctic Circumpolar Current: Evidence from the South Pacific. *Geology*, 35(8), 691. <https://doi.org/10.1130/G23806A.1>
- Mackensen, A., Grobe, H., Hubberten, H., Spiess, V., & Fütterer, D. (1989). Stable isotope stratigraphy from the Antarctic continental margin during the last one million years. *Marine Geology*, 87(2–4), 315–321. [https://doi.org/10.1016/0025-3227\(89\)90068-6](https://doi.org/10.1016/0025-3227(89)90068-6)
- Maldonado, A., Barnolas, A., Bohoyo, F., Escutia, C., Galindo-Zaldívar, J., Hernández-Molina, J., et al. (2005). Miocene to Recent contourite drifts development in the northern Weddell Sea (Antarctica). *Global and Planetary Change*, 45(1–3), 99–129. <https://doi.org/10.1016/j.gloplacha.2004.09.013>
- Mann, M. E., & Lees, J. M. (1996). Robust estimation of background noise and signal detection in climatic time series. *Climatic Change*, 33(3), 409–445. <https://doi.org/10.1007/BF00142586>
- Martín-Chivelet, J., Fregenal-Martínez, M. A., & Chacón, B. (2008). Chapter 10 Traction Structures in Contourites. In *Contourites* (pp. 157–182). [https://doi.org/10.1016/S0070-4571\(08\)10010-3](https://doi.org/10.1016/S0070-4571(08)10010-3)
- McKay, R., Browne, G., Carter, L., Cowan, E., Dunbar, G., Krissek, L., et al. (2009). The stratigraphic signature of the late Cenozoic Antarctic Ice Sheets in the Ross Embayment. *Geological Society of America Bulletin*, 121(11–12), 1537–1561. <https://doi.org/10.1130/B26540.1>
- McKay, R., Naish, T., Carter, L., Riesselman, C., Dunbar, R., Sjunneskog, C., et al. (2012). Antarctic and Southern Ocean influences on Late Pliocene global cooling. *Proceedings of the National Academy of Sciences*, 109(17), 6423–6428. <https://doi.org/10.1073/pnas.1112248109>
- Meyers, S. R., Sageman, B. B., & Hinnov, L. A. (2001). Integrated quantitative stratigraphy of the Cenomanian-Turonian Bridge Creek Limestone Member using evolutive harmonic analysis and stratigraphic modeling. *Journal of Sedimentary Research*, 71(4), 628–644.
- Meyers, S. R., Sageman, B. B., & Arthur, M. A. (2012). Obliquity forcing of organic matter accumulation during Oceanic Anoxic Event 2. *Paleoceanography*, 27(3). <https://doi.org/10.1029/2012PA002286>
- Meyers, S. R. (2014). Astrochron: An R Package for Astrochronology. Retrieved from <https://cran.r-project.org/package=astrochron>
- Milankovitch, M. M. (1941). Canon of insolation and the iceage problem. *Koniglich Serbische Akademie Beograd Special Publication*, 132.
- Miller, K. G., Wright, J. D., & Fairbanks, R. G. (1991). Unlocking the ice house: Oligocene-Miocene

- oxygen isotopes, eustasy, and margin erosion. *Journal of Geophysical Research*, 96(B4), 6829–6848. <https://doi.org/10.1029/90JB02015>
- Miramontes, E., Garreau, P., Caillaud, M., Jouet, G., Pellen, R., Hernández-Molina, F. J., et al. (2019). Contourite distribution and bottom currents in the NW Mediterranean Sea: Coupling seafloor geomorphology and hydrodynamic modelling. *Geomorphology*, 333, 43–60. <https://doi.org/10.1016/j.geomorph.2019.02.030>
- Moore, W. S., & Dymond, J. (1991). Fluxes of <sup>226</sup>Ra and barium in the Pacific Ocean: The importance of boundary processes. *Earth and Planetary Science Letters*, 107(1), 55–68. [https://doi.org/10.1016/0012-821X\(91\)90043-H](https://doi.org/10.1016/0012-821X(91)90043-H)
- Mudelsee, M., Bickert, T., Lear, C. H., & Lohmann, G. (2014). Cenozoic climate changes: A review based on time series analysis of marine benthic  $\delta^{18}\text{O}$  records. *Reviews of Geophysics*, 52(3), 333–374. <https://doi.org/10.1002/2013RG000440>
- Mulder, T., & Alexander, J. (2001). The physical character of subaqueous sedimentary density flows and their deposits. *Sedimentology*, 48(2), 269–299.
- Naish, T. R., Woolfe, K. J., Barrett, P. J., Wilson, G. S., Atkins, C., Bohaty, S. M., et al. (2001). Orbitally induced oscillations in the East Antarctic ice sheet at the Oligocene/Miocene boundary. *Nature*, 413(6857), 719–723. <https://doi.org/10.1038/35099534>
- Naish, T., Wilson, G. S., Dunbar, G. B., & Barrett, P. J. (2008). Constraining the amplitude of Late Oligocene bathymetric changes in western Ross Sea during orbitally-induced oscillations in the East Antarctic Ice Sheet: (2) Implications for global sea-level changes. *Palaeogeography, Palaeoclimatology, Palaeoecology*, 260(1–2), 66–76. <https://doi.org/10.1016/j.palaeo.2007.08.021>
- Naish, T., Powell, R., Levy, R., Wilson, G., Scherer, R., Talarico, F., et al. (2009). Obliquity-paced Pliocene West Antarctic ice sheet oscillations. *Nature*, 458(7236), 322–328. <https://doi.org/10.1038/nature07867>
- Nelson, C. H., Escutia, C., Damuth, J. E., & Twichell, D. C. (2011). Interplay of mass-transport and turbidite-system deposits in different active tectonic and passive continental margin settings: external and local controlling factors. In *Mass-Transport Deposits in Deepwater Settings* (Vol. 96, pp. 39–66). Society for Sedimentary Geology.
- Nelson, C. S., & Cooke, P. J. (2001). History of oceanic front development in the New Zealand sector of the southern ocean during the cenozoic - A synthesis. *New Zealand Journal of Geology and Geophysics*, 44(4), 535–553. <https://doi.org/10.1080/00288306.2001.9514954>
- Niemi, T. M., Ben-Avraham, Z., Hartnady, C. J. H., & Reznikov, M. (2000). Post-Eocene seismic stratigraphy of the deep ocean basin adjacent to the southeast African continental margin: a record of geostrophic bottom current systems. *Marine Geology*, 162(2–4), 237–258.
- O'Brien, P. E., Cooper, A. K., & Richter, C. (2001). Proc. ODP, Init. Repts., 188. College Station, TX (*Ocean Drilling Program*).
- O'Brien, P. E., Cooper, A. K., Florindo, F., Handwerger, D. A., Lavelle, M., Passchier, S., et al. (2004). Prydz channel fan and the history of extreme ice advances in Prydz Bay. In C. Cooper, A.K., O'Brien, P.E., and Richter (Ed.), *Proceedings of the Ocean Drilling Program, Scientific Results Volume 188* (Vol. 188, pp. 1–32). Proc. ODP, Sci. Results.
- O'Regan, M., John, K. St., Moran, K., Backman, J., King, J., Haley, B. A., et al. (2010). Plio-Pleistocene trends in ice rafted debris on the Lomonosov Ridge. *Quaternary International*, 219(1–2), 168–176. <https://doi.org/10.1016/j.quaint.2009.08.010>



- Orsi, A. H., Whitworth, T., & Nowlin, W. D. (1995). On the meridional extent and fronts of the Antarctic Circumpolar Current. *Deep Sea Research Part I: Oceanographic Research Papers*, 42(5), 641–673. [https://doi.org/10.1016/0967-0637\(95\)00021-W](https://doi.org/10.1016/0967-0637(95)00021-W)
- Orsi, A. H., Johnson, G. C., & Bullister, J. L. (1999). Circulation, mixing, and production of Antarctic Bottom Water. *Progress in Oceanography*, 43(1), 55–109. [https://doi.org/10.1016/S0079-6611\(99\)00004-X](https://doi.org/10.1016/S0079-6611(99)00004-X)
- Otto-Bliesner, B. L. (2002). Late Cretaceous ocean: Coupled simulations with the National Center for Atmospheric Research Climate System Model. *Journal of Geophysical Research*, 107(D2), 4019. <https://doi.org/10.1029/2001JD000821>
- Pagani, M., Zachos, J. C., Freeman, K. H., Tipple, B., & Bohaty, S. (2005). Marked Decline in Atmospheric Carbon Dioxide Concentrations During the Paleogene. *Science*, 309(5734), 600–603. <https://doi.org/10.1126/science.1110063>
- Paillard, D., Labeyrie, L., & Yiou, P. (1996). Macintosh Program performs time-series analysis. *Eos, Transactions American Geophysical Union*, 77(39), 379–379. <https://doi.org/10.1029/96EO00259>
- Pälike, H., Norris, R. D., Herrle, J. O., Wilson, P. a, Coxall, H. K., Lear, C. H., et al. (2006). The Heartbeat of the Oligocene Climate System. *Science*, 314(5807), 1894–1898. <https://doi.org/10.1126/science.1133822>
- Pardo, P. C., Pérez, F. F., Velo, A., & Gilcoto, M. (2012). Water masses distribution in the Southern Ocean: Improvement of an extended OMP (eOMP) analysis. *Progress in Oceanography*, 103, 92–105. <https://doi.org/10.1016/j.pocean.2012.06.002>
- Passchier, S., Bohaty, S. M., Jiménez-Espejo, F., Pross, J., Röhl, U., van de Flierdt, T., et al. (2013). Early Eocene to middle Miocene cooling and aridification of East Antarctica. *Geochemistry, Geophysics, Geosystems*, 14, n/a-n/a. <https://doi.org/10.1002/ggge.20106>
- Passchier, S., Ciarletta, D. J., Miriagos, T. E., Bijl, P. K., & Bohaty, S. M. (2017). An Antarctic stratigraphic record of stepwise ice growth through the Eocene-Oligocene transition. *Geological Society of America Bulletin*, 129(3–4), 318–330. <https://doi.org/10.1130/B31482.1>
- Passchier, S., State, M., Pleistocene-holocene, L., Sea, B., Pliocene, E., & Ice, A. (2018). Sedimentary processes and facies on a high- latitude passive continental margin , Wilkes, (December 2017).
- Patterson, M. O., McKay, R., Naish, T., Escutia, C., Jimenez-Espejo, F. J., Raymo, M. E., et al. (2014). Orbital forcing of the East Antarctic ice sheet during the Pliocene and Early Pleistocene. *Nature Geoscience*, 7(11), 841–847. <https://doi.org/10.1038/ngeo2273>
- Paxman, G. J. G., Jamieson, S. S. R., Ferraccioli, F., Bentley, M. J., Ross, N., Armadillo, E., et al. (2018). Bedrock erosion surfaces record former East Antarctic Ice Sheet extent. *Geophysical Research Letters*. <https://doi.org/10.1029/2018GL077268>
- Paxman, G. J. G., Jamieson, S. S. R., Ferraccioli, F., Bentley, M. J., Ross, N., Watts, A. B., et al. (2019). The Role of Lithospheric Flexure in the Landscape Evolution of the Wilkes Subglacial Basin and Transantarctic Mountains, East Antarctica. *Journal of Geophysical Research: Earth Surface*, 124(3), 812–829. <https://doi.org/10.1029/2018JF004705>
- Payne, R. R., Conolly, J. R., & Aabbott, W. H. (1972). Turbidite Muds within Diatom Ooze off Antarctica: Pleistocene Sediment Variation Defined by Closely Spaced Piston Cores. *GSA Bulletin*, 83(2), 481–486. Retrieved from [https://doi.org/10.1130/0016-7606\(1972\)83\[481:TMWDOO\]2.0.CO;2](https://doi.org/10.1130/0016-7606(1972)83[481:TMWDOO]2.0.CO;2)
- Peck, V. L., Allen, C. S., Kender, S., McClymont, E. L., & Hodgson, D. A. (2015). Oceanographic variability on the West Antarctic Peninsula during the Holocene and the influence of upper circumpolar deep

- water. *Quaternary Science Reviews*, 119, 54–65. <https://doi.org/10.1016/j.quascirev.2015.04.002>
- Pekar, S. F., DeConto, R. M., & Harwood, D. M. (2006). Resolving a late Oligocene conundrum: Deep-sea warming and Antarctic glaciation. *Palaeogeography, Palaeoclimatology, Palaeoecology*, 231(1–2), 29–40. <https://doi.org/10.1016/j.palaeo.2005.07.024>
- Penkrot, M. L., Jaeger, J. M., LeVay, L. J., & St-Onge, G. (2016). Multivariate Modeling of Glacimarine Lithostratigraphy Using Scanning Xrf and Multisensory Core Properties Validated With Ct Imagery. <https://doi.org/10.1130/abs/2016AM-282907>
- Pfuhl, H. a., & McCave, I. N. (2005). Evidence for late Oligocene establishment of the Antarctic Circumpolar Current. *Earth and Planetary Science Letters*, 235(3–4), 715–728. <https://doi.org/10.1016/j.epsl.2005.04.025>
- Pierce, E. L., van de Flierdt, T., Williams, T., Hemming, S. R., Cook, C. P., & Passchier, S. (2017). Evidence for a dynamic East Antarctic ice sheet during the mid-Miocene climate transition. *Earth and Planetary Science Letters*, 478, 1–13. <https://doi.org/10.1016/j.epsl.2017.08.011>
- Pliper, D. J. W., Deptuck, M. E., Mosher, D. C., Hughes Clarke, J. E., & Migeon, S. (2012). Erosional and Depositional Features of Glacial Meltwater Discharges on the Eastern Canadian Continental Margin. In *Application of the Principles of Seismic Geomorphology to Continental-Slope and Base-of-Slope Systems: Case Studies from Seafloor and Near-Seafloor Analogues* (pp. 61–80). SEPM (Society for Sedimentary Geology). <https://doi.org/10.2110/pec.12.99.0061>
- Pollard, D., & DeConto, R. M. (2009). Modelling West Antarctic ice sheet growth and collapse through the past five million years. *Nature*, 458(7236), 329–332. <https://doi.org/10.1038/nature07809>
- Posamentier, H. W., & Kolla, V. (2003). Seismic Geomorphology and Stratigraphy of Depositional Elements in Deep-Water Settings. *Journal of Sedimentary Research*, 73(3), 367–388. <https://doi.org/10.1306/111302730367>
- Powell, R., & Domack, G. W. (2002). Modern glaciomarine environments. In *Modern and Past Glacial Environments* (pp. 361–389). <https://doi.org/10.1016/b978-075064226-2/50015-5>
- Prebble, J. G., Raine, J. I., Barrett, P. J., & Hannah, M. J. (2006). Vegetation and climate from two Oligocene glacioeustatic sedimentary cycles (31 and 24 Ma) cored by the Cape Roberts Project, Victoria Land Basin, Antarctica. *Palaeogeography, Palaeoclimatology, Palaeoecology*, 231(1–2), 41–57. <https://doi.org/10.1016/j.palaeo.2005.07.025>
- Pritchard, H. D., Ligtenberg, S. R. M., Fricker, H. A., Vaughan, D. G., van den Broeke, M. R., & Padman, L. (2012). Antarctic ice-sheet loss driven by basal melting of ice shelves. *Nature*, 484(7395), 502–505. <https://doi.org/10.1038/nature10968>
- Pross, J., Contreras, L., Bijl, P. K., Greenwood, D. R., Bohaty, S. M., Schouten, S., et al. (2012). Persistent near-tropical warmth on the antarctic continent during the early eocene epoch. *Nature*, 488(7409), 73–77. <https://doi.org/10.1038/nature11300>
- Pudsey, C. J. (1992). Late quaternary changes in Antarctic bottom water velocity inferred from sediment grain size in the northern Weddell Sea. *Marine Geology*, 107(1–2), 9–33. [https://doi.org/10.1016/0025-3227\(92\)90066-Q](https://doi.org/10.1016/0025-3227(92)90066-Q)
- Pudsey, C. J., & Camerlenghi, A. (1998). Glacial–interglacial deposition on a sediment drift on the Pacific margin of the Antarctic Peninsula. *Antarctic Science*, 10(3), 286–308. <https://doi.org/10.1017/S0954102098000376>
- Pudsey, C. . (2000). Sedimentation on the continental rise west of the Antarctic Peninsula over the last three glacial cycles. *Marine Geology*, 167(3–4), 313–338.

3227(00)00039-6

- Pyle, K. M., Hendry, S. K. R., Meredith, M. P., Sherrell, R. M., & Hall, I. R. (2016). Barium cycling in Antarctic waters : interactions with oceanic and coastal processes, (July).
- R. M. Mitchum, J., Vail, P. R., & Thompson, S. (1977). Seismic Stratigraphy and Global Changes of Sea Level, Part 2: The Depositional Sequence as a Basic Unit for Stratigraphic. In *Seismic Stratigraphy - applications to hydrocarbon exploration* (pp. 53–62). Houston, Texas: Exxon Production Research Company.
- Raine, J., & Askin, R. (2001). Terrestrial palynology of Cape Roberts Project Drillhole CRP-3, Victoria Land Basin, Antarctica. *Terra Antartica*, 8(4), 389–400. Retrieved from <http://epic.awi.de/27346>
- Rebesco, M., Larter, R. D., Barker, P. F., Camerlenghi, A., & Vanneste, L. E. (1997). The history of sedimentation on the continental rise west of the Antarctic Peninsula. *Geology and Seismic Stratigraphy of the Antarctic Margin*, 2, 71, 29–49.
- Rebesco, M., & Camerlenghi, A. (Eds.). (2008). *Contourites, Volume 60*. Oxford, UK: Elsevier.
- Rebesco, M., Hernández-Molina, F. J., Van Rooij, D., & Wåhlin, A. (2014). Contourites and associated sediments controlled by deep-water circulation processes: State-of-the-art and future considerations. *Marine Geology*, 352, 111–154. <https://doi.org/10.1016/j.margeo.2014.03.011>
- Reid, J. L., Nowlin Jr, W. D., & Patzert, W. C. (1977). On the characteristics and circulation of the southwestern Atlantic Ocean. *Journal of Physical Oceanography*, 7(1), 62–91.
- Reinardy, B. T. I., Escutia, C., Iwai, M., Jimenez-Espejo, F. J., Cook, C., van de Flierdt, T., & Brinkhuis, H. (2015). Repeated advance and retreat of the East Antarctic Ice Sheet on the continental shelf during the early Pliocene warm period. *Palaeogeography, Palaeoclimatology, Palaeoecology*, 422, 65–84. <https://doi.org/10.1016/j.palaeo.2015.01.009>
- Renaudie, J. (2016). Quantifying the Cenozoic marine diatom deposition history: Links to the C and Si cycles. *Biogeosciences*, 13(21), 6003–6014. <https://doi.org/10.5194/bg-13-6003-2016>
- Richter, T. O., van der Gaast, S., Koster, B., Vaars, A., Gieles, R., de Stigter, H. C., et al. (2006). The Avaatech XRF Core Scanner: technical description and applications to NE Atlantic sediments. *Geological Society, London, Special Publications*, 267(1), 39–50. <https://doi.org/10.1144/GSL.SP.2006.267.01.03>
- Rignot, E., Jacobs, S., Mouginot, J., & Scheuchl, B. (2013). Ice-Shelf Melting Around Antarctica. *Science*, 341(6143), 266–270. <https://doi.org/10.1126/science.1235798>
- Rignot, E., Mouginot, J., Scheuchl, B., Van Den Broeke, M., Van Wessem, M. J., & Morlighem, M. (2019). Four decades of Antarctic ice sheet mass balance from 1979–2017. *Proceedings of the National Academy of Sciences of the United States of America*, 116(4), 1095–1103. <https://doi.org/10.1073/pnas.1812883116>
- Rintoul, S. (2000). Southern Ocean currents and climate. *Tasmania and the Southern Ocean*, 133(3), 41–50.
- Rintoul, S., Hughes, C., & Olbers, D. (2001). *The Antarctic Circumpolar Current System. Ocean Circulation and Climate*. <https://doi.org/10.1002/ajp.20122>
- Rintoul, S. R. (2007). Rapid freshening of Antarctic Bottom Water formed in the Indian and Pacific oceans. *Geophysical Research Letters*, 34(6), 1–5. <https://doi.org/10.1029/2006GL028550>
- Rintoul, S. R. (2018). The global influence of localized dynamics in the Southern Ocean. *Nature*, 558(7709), 209–218. <https://doi.org/10.1038/s41586-018-0182-3>

- Rintoul, S. R., & da Silva, C. E. (2019). Antarctic Circumpolar Current. In *Encyclopedia of Ocean Sciences* (pp. 248–261). Elsevier. <https://doi.org/10.1016/B978-0-12-409548-9.11298-9>
- Rodriguez, A. B., & Anderson, J. B. (2004). Contourite origin for shelf and upper slope sand sheet, offshore Antarctica. *Sedimentology*, *51*(4), 699–711. <https://doi.org/10.1111/j.1365-3091.2004.00645.x>
- Roeske, T. (2011). *Dissolved Barium and Particulate Rare Earth Elements as Tracers for Shelf-Basin Interaction in the Arctic Ocean*, Ph.D. Thesis. Universität Bremen. Retrieved from <http://epic.awi.de/26084/>
- Röhl, U., Brinkhuis, H., Stickley, C. E., Fuller, M., Schellenberg, S. a, Wefer, G., & Williams, G. L. (2004). Sea level and astronomically induced environmental changes in middle and late Eocene sediments from the East Tasman Plateau. *Geophysical Monograph Series*, *151*, 127–151.
- Rothwell, R. G., & Croudace, I. W. (2015). *Micro-XRF Studies of Sediment Cores*. (I. W. Croudace & R. G. Rothwell, Eds.), *Micro-XRF studies of sediment cores* (Vol. 17). Dordrecht: Springer Netherlands. <https://doi.org/10.1007/978-94-017-9849-5>
- Rydningen, T. A., Laberg, J. S., & Kolstad, V. (2015). Seabed morphology and sedimentary processes on high-gradient trough mouth fans offshore Troms, northern Norway. *Geomorphology*, *246*, 205–219. <https://doi.org/10.1016/j.geomorph.2015.06.007>
- Salabarnada, A., Escutia, C., Röhl, U., Nelson, C. H., McKay, R., Jiménez-Espejo, F. J., et al. (2018). Paleooceanography and ice sheet variability offshore Wilkes Land, Antarctica – Part 1: Insights from late Oligocene astronomically paced contourite sedimentation. *Climate of the Past*, *14*(7), 991–1014. <https://doi.org/10.5194/cp-14-991-2018>
- Salzmann, U., Strother, S., Sangiorgi, F., Bijl, P., Pross, J., Woodward, J., et al. (2016). Oligocene to Miocene terrestrial climate change and the demise of forests on Wilkes Land, East Antarctica. In *EGU General Assembly Conference Abstracts* (Vol. 18, p. EPSC2016-2717).
- Sangiorgi, F., Bijl, P. K., Passchier, S., Salzmann, U., Schouten, S., McKay, R., et al. (2018). Southern Ocean warming and Wilkes Land ice sheet retreat during the mid-Miocene. *Nature Communications*, *9*(1), 317. <https://doi.org/10.1038/s41467-017-02609-7>
- Sauermilch, I., Whittaker, J. M., Bijl, P. K., Totterdell, J. M., & Jokat, W. (2019). Tectonic, Oceanographic, and Climatic Controls on the Cretaceous-Cenozoic Sedimentary Record of the Australian-Antarctic Basin. *Journal of Geophysical Research: Solid Earth*, *124*(8), 7699–7724. <https://doi.org/10.1029/2018JB016683>
- Scher, H. D., & Martin, E. E. (2008). Oligocene deep water export from the North Atlantic and the development of the Antarctic Circumpolar Current examined with neodymium isotopes. *Paleoceanography*, *23*(1). <https://doi.org/10.1029/2006PA001400>
- Scher, H. D., Whittaker, J. M., Williams, S. E., Latimer, J. C., Kordesch, W. E. C., & Delaney, M. L. (2015). Onset of Antarctic Circumpolar Current 30 million years ago as Tasmanian Gateway aligned with westerlies. *Nature*, *523*(7562), 580–583. <https://doi.org/10.1038/nature14598>
- Schlitzer, R., Anderson, R. F., Dodas, E. M., Lohan, M., Geibert, W., Tagliabue, A., et al. (2018). The GEOTRACES Intermediate Data Product 2017. *Chemical Geology*, *493*, 210–223. <https://doi.org/10.1016/j.chemgeo.2018.05.040>
- Schneider, R. R., Price, B., Müller, P. J., Kroon, D., & Alexander, I. (1997). Monsoon related variations in Zaire (Congo) sediment load and influence of fluvial silicate supply on marine productivity in the east equatorial Atlantic during the last 200,000 years. *Paleoceanography*, *12*(3), 463–481. <https://doi.org/10.1029/96PA03640>

- Schnitker, D. (1980). Global Paleooceanography and Its Deep Water Linkage to the Antarctic Glaciation. *Earth-Science Reviews*, 16, 1–20.
- Shanmugam, G., Spalding, T. D., & Rofheart, D. H. (1993). Traction structures in deep-marine, bottom-current-reworked sands in the Pliocene and Pleistocene, Gulf of Mexico. *Geology*, 21(10), 929. [https://doi.org/10.1130/0091-7613\(1993\)021<0929:TSIDMB>2.3.CO;2](https://doi.org/10.1130/0091-7613(1993)021<0929:TSIDMB>2.3.CO;2)
- Shanmugam, G. (2008). Chapter 5 Deep-water Bottom Currents and their Deposits. In *Developments in Sedimentology* (Vol. 60, pp. 59–81). [https://doi.org/10.1016/S0070-4571\(08\)10005-X](https://doi.org/10.1016/S0070-4571(08)10005-X)
- Shanmugam, G. (2017). Contourites: Physical oceanography, process sedimentology, and petroleum geology. *Petroleum Exploration and Development*, 44(2), 183–216. [https://doi.org/10.1016/S1876-3804\(17\)30023-X](https://doi.org/10.1016/S1876-3804(17)30023-X)
- Shen, Q., Wang, H., Shum, C. K., Jiang, L., Hsu, H. T., & Dong, J. (2018). Recent high-resolution Antarctic ice velocity maps reveal increased mass loss in Wilkes Land, East Antarctica. *Scientific Reports*, 8(1), 4477. <https://doi.org/10.1038/s41598-018-22765-0>
- Shevenell, A. E., Kennett, J. P., & Lea, D. W. (2004). Middle Miocene Southern Ocean cooling and Antarctic cryosphere expansion. *Science (New York, N.Y.)*, 305(5691), 1766–70. <https://doi.org/10.1126/science.1100061>
- Shevenell, A. E., Kennett, J. P., & Lea, D. W. (2008). Middle Miocene ice sheet dynamics, deep-sea temperatures, and carbon cycling: A Southern Ocean perspective. *Geochemistry, Geophysics, Geosystems*, 9(2). <https://doi.org/10.1029/2007GC001736>
- Shimada, K., Aoki, S., Ohshima, K. I., & Rintoul, S. R. (2012). Influence of Ross Sea Bottom Water changes on the warming and freshening of the Antarctic Bottom Water in the Australian-Antarctic Basin. *Ocean Science*, 8(4), 419–432. <https://doi.org/10.5194/os-8-419-2012>
- Sijp, W. P., England, M. H., & Huber, M. (2011). Effect of the deepening of the Tasman Gateway on the global ocean. *Paleoceanography*, 26(4), 1–18. <https://doi.org/10.1029/2011PA002143>
- Sokolov, S., & Rintoul, S. R. (2002). Structure of Southern Ocean fronts at 140°E. *Journal of Marine Systems*, 37(1–3), 151–184. [https://doi.org/10.1016/S0924-7963\(02\)00200-2](https://doi.org/10.1016/S0924-7963(02)00200-2)
- Solomon, S., Qin, D., Manning, M., Chen, Z., Marquis, M., Averyt, K., et al. (Eds.). (2007). *IPCC, 2007: Climate Change 2007: The Physical Science Basis. Contribution of Working Group I to the Fourth Assessment Report of the Intergovernmental Panel on Climate Change. Climate Change 2013 - The Physical Science Basis*. Cambridge, United Kingdom and New York, NY, USA: Cambridge University Press. <https://doi.org/10.1017/CBO9781107415324.004>
- Spence, P., Holmes, R. M., Hogg, A. M., Griffies, S. M., Stewart, K. D., & England, M. H. (2017). Localized rapid warming of West Antarctic subsurface waters by remote winds. *Nature Climate Change*, 7(8), 595.
- St-Onge, G., & Long, B. F. (2009). CAT-scan analysis of sedimentary sequences: An ultrahigh-resolution paleoclimatic tool. *Engineering Geology*, 103(3–4), 127–133. <https://doi.org/10.1016/j.enggeo.2008.06.016>
- Stagg, H. M. J., Colwell, J. B., Direen, N. G., O'Brien, P. E., Brown, B. J., Bernardel, G., et al. (2004). Geological Framework of the Continental Margin in the region of the Australian Antarctic Territory. *Geoscience Australia Record*, 2004(25), 356.
- Stickley, C. E., Brinkhuis, H., Schellenberg, S. A., Sluijs, A., Röhl, U., Fuller, M., et al. (2004). Timing and nature of the deepening of the Tasmanian Gateway. *Paleoceanography*, 19(4), n/a-n/a. <https://doi.org/10.1029/2004PA001022>

- Stocchi, P., Escutia, C., Houben, A. J. P., Vermeersen, B. L. a., Bijl, P. K., Brinkhuis, H., et al. (2013). Relative sea-level rise around East Antarctica during Oligocene glaciation. *Nature Geoscience*, 6(5), 380–384. <https://doi.org/10.1038/ngeo1783>
- Stocker, T. F., Qin, D., Plattner, G.-K., Tignor, M., Allen, S. K., Boschung, J., et al. (2013). Climate Change 2013: The Physical Science Basis. Contribution of Working Group I to the Fifth Assessment Report of the Intergovernmental Panel on Climate Change. In C. U. Press (Ed.), *IPCC2014*. Cambridge, United Kingdom and New York.
- Stow, D. (Ed.). (2002). *Deep-water contourite systems: modern drifts and ancient series, seismic and sedimentary characteristics*. Geological Society of London.
- Stow, D. A. V., Faugères, J.-C., Howe, J. A., Pudsey, C. J., & Viana, A. R. (2002). Bottom currents, contourites and deep-sea sediment drifts: current state-of-the-art. In D. A. V. Stow, J.-C. Faugères, J. A. Howe, C. J. Pudsey, & A. R. Viana (Eds.), *Deep-Water Contourite Systems: Modern Drifts and Ancient Series, Seismic and Sedimentary Characteristics* (Vol. 22, pp. 7–20). London: The Geological Society of London. <https://doi.org/10.1144/GSL.MEM.2002.022.01.02>
- Stow, D. A. V., & Faugères, J.-C. (2008). Chapter 13 Contourite Facies and the Facies Model. In *Contourites* (pp. 223–256). [https://doi.org/10.1016/S0070-4571\(08\)10013-9](https://doi.org/10.1016/S0070-4571(08)10013-9)
- Strother, S. L., Salzmann, U., Sangiorgi, F., Bijl, P. K., Pross, J., Escutia, C., et al. (2017). A new quantitative approach to identify reworking in Eocene to Miocene pollen records from offshore Antarctica using red fluorescence and digital imaging. *Biogeosciences*, 14(8), 2089–2100. <https://doi.org/10.5194/bg-14-2089-2017>
- Tanahashi, M., Ishihara, T., Yuasa, M., Murakami, F., & Nishimura, A. (1997). Preliminary report of the TH95 geological and geophysical survey results in the Ross Sea and Dumont D’Urville Sea.
- Tauxe, L., Stickley, C. E., Sugisaki, S., Bijl, P. K., Bohaty, S. M., Brinkhuis, H., et al. (2012). Chronostratigraphic framework for the IODP Expedition 318 cores from the Wilkes Land Margin: Constraints for paleoceanographic reconstruction. *Paleoceanography*, 27(2). <https://doi.org/10.1029/2012PA002308>
- Team, R. C. (2017). R Core Team (2017). R: A language and environment for statistical computing. *R Found. Stat. Comput. Vienna, Austria*. URL [Http://www.R-Project.Org/](http://www.R-Project.Org/), Page R Foundation for Statistical Computing.
- Thorn, V. (2001). Oligocene and early Miocene phytoliths from CRP-2/2A and CRP-3, Victoria Land Basin, Antarctica. *Terra Antartica*, 8(4), 407–422. Retrieved from <http://epic.awi.de/27344/>
- Tjallingii, R., Röhl, U., Kölling, M., & Bickert, T. (2007). Influence of the water content on X-ray fluorescence core-scanning measurements in soft marine sediments. *Geochemistry, Geophysics, Geosystems*, 8(2). <https://doi.org/10.1029/2006GC001393>
- Toggweiler, J. R., Russell, J. L., & Carson, S. R. (2006). Midlatitude westerlies, atmospheric CO<sub>2</sub>, and climate change during the ice ages. *Paleoceanography*, 21(2), 1–15. <https://doi.org/10.1029/2005PA001154>
- Toggweiler, J. R., & Russell, J. (2008). Ocean circulation in a warming climate. *Nature*, 451(7176), 286–288. <https://doi.org/10.1038/nature06590>
- Tribouillard, N., Algeo, T. J., Lyons, T., & Riboulleau, A. (2006). Trace metals as paleoredox and paleoproductivity proxies: An update. *Chemical Geology*, 232(1–2), 12–32. <https://doi.org/10.1016/j.chemgeo.2006.02.012>
- Tripsanas, E. K., Piper, D. J. W., Jenner, K. a., & Bryant, W. R. (2007). Submarine mass-transport facies:

- new perspectives on flow processes from cores on the eastern North American margin. *Sedimentology*, (2008), 070916035251003-??? <https://doi.org/10.1111/j.1365-3091.2007.00894.x>
- Uenzelmann-Neben, G. (2001). Seismic characteristics of sediment drifts: An example from the Agulhas Plateau, southwest Indian Ocean. *Marine Geophysical Research*, 22(5–6), 323–343. <https://doi.org/10.1023/A:1016391314547>
- Uenzelmann-Neben, G. (2002). Contourites on the Agulhas Plateau, SW Indian Ocean: indications for the evolution of currents since Palaeogene times. *Geological Society, London, Memoirs*, 22(1), 271–288. <https://doi.org/10.1144/GSL.MEM.2002.022.01.20>
- Uenzelmann-Neben, G., Schlüter, P., Weigelt, E., 2007. Cenozoic oceanic circulation within the South African gateway: Indications from seismic stratigraphy. *South African J. Geol.* 110, 275–294.
- Van Daele, M., Cnudde, V., Duyck, P., Pino, M., Urrutia, R., & De Batist, M. (2014). Multidirectional, synchronously-triggered seismo-turbidites and debrites revealed by X-ray computed tomography (CT). *Sedimentology*, 61(4), 861–880. <https://doi.org/10.1111/sed.12070>
- van Hinsbergen, D. J. J., de Groot, L. V., van Schaik, S. J., Spakman, W., Bijl, P. K., Sluijs, A., et al. (2015). A Paleolatitude Calculator for Paleoclimate Studies. *PLOS ONE*, 10(6), e0126946. <https://doi.org/10.1371/journal.pone.0126946>
- van Wijk, E. M., & Rintoul, S. R. (2014). Freshening drives contraction of Antarctic Bottom Water in the Australian Antarctic Basin. *Geophysical Research Letters*, 41(5), 1657–1664. <https://doi.org/10.1002/2013GL058921>
- Vandenbergh, N., Hilgen, F. J., Speijer, R. P., Ogg, J. G., Gradstein, F. M., Hammer, O., et al. (2012). The Paleogene Period. In *The Geologic Time Scale* (pp. 855–921). Elsevier. <https://doi.org/10.1016/B978-0-444-59425-9.00028-7>
- Veldkamp, A., & Kroonenberg, S. B. (1993). Application of bulk sand geochemistry in mineral exploration and Quaternary research: a methodological study of the Allier and Dore terrace sands, Limagne rift valley, France. *Applied Geochemistry*, 8(2), 177–187. [https://doi.org/10.1016/0883-2927\(93\)90033-D](https://doi.org/10.1016/0883-2927(93)90033-D)
- Villa, G., & Persico, D. (2006). Late Oligocene climatic changes: Evidence from calcareous nannofossils at Kerguelen Plateau Site 748 (Southern Ocean). *Palaeogeography, Palaeoclimatology, Palaeoecology*, 231(1–2), 110–119. <https://doi.org/10.1016/j.palaeo.2005.07.028>
- Villa, G., Persico, D., Wise, S. W., & Gadaleta, A. (2012). Calcareous nannofossil evidence for Marine Isotope Stage 31 (1Ma) in Core AND-1B, ANDRILL McMurdo Ice Shelf Project (Antarctica). *Global and Planetary Change*, 96–97(2012), 75–86. <https://doi.org/10.1016/j.gloplacha.2009.12.003>
- Wanlu, F., Jiang, D., Montañez, I. P., Meyers, S. R., Motani, R., & Tintori, A. (2016). Eccentricity and obliquity paced carbon cycling in the Early Triassic and implications for post-extinction ecosystem recovery. *Scientific Reports*, 6(1), 27793. <https://doi.org/10.1038/srep27793>
- Weertman, J. (1974). Stability of the Junction of an Ice Sheet and an Ice Shelf. *Journal of Glaciology*, 13(67), 3–11. <https://doi.org/10.3189/S0022143000023327>
- Whitehead, J. M., & Bohaty, S. M. (2003). Pliocene summer sea surface temperature reconstruction using silicoflagellates from Southern Ocean ODP Site 1165. *Paleoceanography*, 18(3). <https://doi.org/10.1029/2002PA000829>
- Whitehead, J. M., Wotherspoon, S., & Bohaty, S. M. (2005). Minimal Antarctic sea ice during the Pliocene. *Geology*, 33(2), 137. <https://doi.org/10.1130/G21013.1>

- Wilhelms-Dick, D., Westerhold, T., Röhl, U., Wilhelms, F., Vogt, C., Hanebuth, T. J. J., et al. (2012). A comparison of mm scale resolution techniques for element analysis in sediment cores. *Journal of Analytical Atomic Spectrometry*, 27(9), 1574. <https://doi.org/10.1039/c2ja30148b>
- Williams, T., & Handwerger, D. (2005). A high-resolution record of early Miocene Antarctic glacial history from ODP Site 1165, Prydz Bay. *Paleoceanography*, 20(2). <https://doi.org/10.1029/2004PA001067>
- Wilson, D. S., & Luyendyk, B. P. (2009). West antarctic paleotopography estimated at the eocene-oligocene climate transition. *Geophysical Research Letters*, 36(16), 10–13. <https://doi.org/10.1029/2009GL039297>
- Wilson, G. S., Levy, R. H., Naish, T. R., Powell, R. D., Florindo, F., Ohneiser, C., et al. (2012). Neogene tectonic and climatic evolution of the Western Ross Sea, Antarctica — Chronology of events from the AND-1B drill hole. *Global and Planetary Change*, 96–97, 189–203. <https://doi.org/10.1016/j.gloplacha.2012.05.019>
- Witus, A. E., Braneky, C. M., Anderson, J. B., Szczuciński, W., Schroeder, D. M., Blankenship, D. D., & Jakobsson, M. (2014). Meltwater intensive glacial retreat in polar environments and investigation of associated sediments: example from Pine Island Bay, West Antarctica. *Quaternary Science Reviews*, 85(2014), 99–118. <https://doi.org/10.1016/j.quascirev.2013.11.021>
- Wouters, B., Bamber, J. L., van den Broeke, M. R., Lenaerts, J. T. M., & Sasgen, I. (2013). Limits in detecting acceleration of ice sheet mass loss due to climate variability. *Nature Geoscience*, 6(8), 613–616. <https://doi.org/10.1038/ngeo1874>
- Zachos, J. (2001a). Trends, Rhythms, and Aberrations in Global Climate 65 Ma to Present. *Science*, 292(5517), 686–693. <https://doi.org/10.1126/science.1059412>
- Zachos, J. C. (2001b). Climate Response to Orbital Forcing Across the Oligocene-Miocene Boundary. *Science*, 292(5515), 274–278. <https://doi.org/10.1126/science.1058288>
- Zachos, J., Kroon, D., Bloom, P., & Et, A. (2004). Initial Reports Leg 208. *Proceedings of the Ocean Drilling Program*, 208, 1–112. Retrieved from [http://www-odp.tamu.edu/Publications/208\\_IR/VOLUME/CHAPTERS/IR208\\_02.PDF](http://www-odp.tamu.edu/Publications/208_IR/VOLUME/CHAPTERS/IR208_02.PDF)
- Zachos, J. C., Dickens, G. R., & Zeebe, R. E. (2008). An early Cenozoic perspective on greenhouse warming and carbon-cycle dynamics. *Nature*, 451(7176), 279–83. <https://doi.org/10.1038/nature06588>
- Zeeden, C., Hilgen, F., Westerhold, T., Lourens, L., Röhl, U., & Bickert, T. (2013). Revised Miocene splice, astronomical tuning and calcareous plankton biochronology of ODP Site 926 between 5 and 14.4 Ma. *Palaeogeography, Palaeoclimatology, Palaeoecology*, 369, 430–451.
- Zhang, Y. G., Pagani, M., Liu, Z., Bohaty, S. M., & DeConto, R. (2013). A 40-million-year history of atmospheric CO<sub>2</sub>. *Philosophical Transactions of the Royal Society A: Mathematical, Physical and Engineering Sciences*, 371(2001), 20130096–20130096. <https://doi.org/10.1098/rsta.2013.0096>
- Ziegler, M., Jilbert, T., de Lange, G. J., Lourens, L. J., & Reichert, G.-J. (2008). Bromine counts from XRF scanning as an estimate of the marine organic carbon content of sediment cores. *Geochemistry, Geophysics, Geosystems*, 9(5). <https://doi.org/10.1029/2007GC001932>





# Appendices

---



## APPENDIX 1

### CO-AUTHORED PAPERS RELATED TO THE TOPIC OF THE THESIS

- **Salabarnada, A.**, Escutia, C., Röhl, U., Nelson, C. H., McKay, R., Jiménez-Espejo, F. J., Bijl, P. K., Hartman, J. D., Strother, S. L., Salzmann, U., Evangelinos, D., López-Quirós, A., Flores, J. A., Sangiorgi, F., Ikebana, M. and Brinkhuis, H.: *Paleoceanography and ice sheet variability offshore Wilkes Land, Antarctica – Part 1: Insights from late Oligocene astronomically paced contourite sedimentation*, *Clim. Past*, 14(7), 991–1014, doi:10.5194/cp-14-991-2018, 2018.

Q1, Impact Factor: 3.47

- López-Quirós, A., Lobo, F.J., Escutia, C., García, M., Hernández-Molina, F.J., Pérez, L.F., Boboyo, F., Evangelinos, D., **Salabarnada, A.**, Maldonado, A., Naveira Garabato, A.C., 2020. *Geomorphology of Ona Basin, southwestern Scotia Sea (Antarctica): Decoding the spatial variability of bottom-current pathways*. *Mar. Geol.* 422, 106113.

Q1, Impact Factor: 3.349

- López-Quirós, A., Escutia, C., Sánchez-Navas, A., Nieto, F., Garcia-Casco, A., Martín-Algarra, A., Evangelinos, D., **Salabarnada, A.**, 2019. *Glaucony authigenesis, maturity and alteration in the Weddell Sea: An indicator of paleoenvironmental conditions before the onset of Antarctic glaciation*. *Science Reports.* 9, 13580.

Q1, Impact Factor: 4.525

- Bijl, P. K., Houben, A. J. P., Hartman, J. D., Pross, J., **Salabarnada, A.**, Escutia, C. and Sangiorgi, F.: *Paleoceanography and ice sheet variability offshore Wilkes Land, Antarctica - Part 2: Insights from Oligocene-Miocene dinoflagellate cyst assemblages*, *Clim. Past*, 14(7), 1015–1033, doi:10.5194/cp-14-1015-2018, 2018.

Q1, Impact Factor: 3.47

- Hartman, J. D., Sangiorgi, F., **Salabarnada, A.**, Peterse, F., Houben, A. J. P., Schouten, S., Brinkhuis, H., Escutia, C. and Bijl, P. K.: *Paleoceanography and ice sheet variability offshore Wilkes Land, Antarctica - Part 3: Insights from Oligocene-Miocene TEX86-based sea surface temperature reconstructions*, *Clim. Past*, 14, 1275–1297, doi:10.5194/cp-14-1275-2018, 2018.

Q1, Impact Factor: 3.47

- Strother, S. L., Salzmann, U., Sangiorgi, F., Bijl, P. K., Pross, J., Escutia, C., **Salabarnada, A.**, Pound, M. J., Voss, J. and Woodward, J.: *A new quantitative approach to identify reworking in Eocene to Miocene pollen records from offshore Antarctica using red fluorescence and digital imaging*, *Biogeosciences*, 14(8), 2089–2100, doi:10.5194/bg-14-2089-2017, 2017.

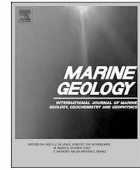
Q1, Impact Factor: 3.951





Contents lists available at ScienceDirect

Marine Geology

journal homepage: [www.elsevier.com/locate/margeo](http://www.elsevier.com/locate/margeo)

## Geomorphology of Ona Basin, southwestern Scotia Sea (Antarctica): Decoding the spatial variability of bottom-current pathways



Adrián López-Quirós<sup>a,\*</sup>, Francisco J. Lobo<sup>a</sup>, Carlota Escutia<sup>a</sup>, Marga García<sup>a</sup>,  
F. Javier Hernández-Molina<sup>b</sup>, Lara F. Pérez<sup>c</sup>, Fernando Bohoyo<sup>d</sup>, Dimitris Evangelinos<sup>a</sup>,  
Ariadna Salabarnada<sup>a</sup>, Andrés Maldonado<sup>a</sup>, Alberto C. Naveira Garabato<sup>e</sup>

<sup>a</sup> Instituto Andaluz de Ciencias de la Tierra, CSIC-Universidad de Granada, Avda. de las Palmeras 4, 18100 Armilla, Granada, Spain

<sup>b</sup> Department of Earth Sciences, Royal Holloway University of London, Egham, Surrey TW20 0EX, UK

<sup>c</sup> British Antarctic Survey (BAS), High Cross, Madingley Road, Cambridge CB3 0ET, UK

<sup>d</sup> Instituto Geológico y Minero de España, Ríos Rosas, 23, 28003 Madrid, Spain

<sup>e</sup> School of Ocean and Earth Science, National Oceanography Centre, Southampton SO14 3ZH, UK

### ARTICLE INFO

Editor: Michele Rebesco

#### Keywords:

Scotia Sea  
Ona Basin  
Seafloor morphology  
Contourites  
Bottom-current circulation  
Mass movements

### ABSTRACT

Ona Basin, the westernmost oceanic basin in the southern Scotia Sea, is affected by the opposite flows of Circumpolar Deep Water (CDW) and Weddell Sea Deep Water (WSDW); thus, it represents a key location for exploring seafloor morphologies influenced by bottom currents. The present study aims to capture the spatial arrangement of recent subsurface contourite features, assuming a latitudinal influence of water masses and the interactions between along- and downslope processes, in order to contribute to the knowledge of regional deepwater flow pathways and to the sedimentary model of small sediment-starved oceanic basins. To this end, the investigation combines an interpretation of multibeam bathymetry and parametric echo sounder seismic data complemented with hydrological data. The distribution of morpho-sedimentary features in Ona Basin reveals two major domains. The southern margin of the basin can be regarded as a mixed/hybrid system containing abundant sediment drifts with channels and contourite moats and a lateral continuity interrupted by downslope morphologies. In contrast, the northern abyssal setting comprises relatively homogeneous large sheeted drifts with superimposed sediment waves, mounded drifts, and several scattered erosive features, likely reflecting the more distinct influence of deepwater contourite processes. Our work demonstrates that tectonic features in the southern basin control the interaction between deepwater along- and downslope processes, as the westward flow of the WSDW is deflected, channelized, and intensified along its westward route. In the northern region, the study indicates an overall clockwise rotation of the WSDW flow, with the spatial and vertical variability of CDW and WSDW affecting the distribution of bottom-current features around seamounts and/or structural highs. The results underscore the importance of sloping interphases in the water mass vertical structure, the degree of basin confinement, and the influence of local bathymetric elevations in sedimentation models of small sediment-starved oceanic basins.

### 1. Introduction

The deep seafloor morphology can be shaped by bottom-current processes through erosion, sediment transport, and deposition (e.g., Rebesco et al., 2014). The resulting sediment bodies (i.e., ‘contourites’; Stow et al., 2002; Rebesco and Camerlenghi, 2008; Rebesco et al., 2014) are defined as sediments deposited or substantially reworked by the action of bottom currents. High-resolution geomorphological seafloor mapping, combined with recent distributed sedimentary units inferred from high-resolution sub-seafloor seismic data, can be used for

insights into the characterization of recent sedimentary processes sculpting contourite deposits in modern continental margins and adjacent abyssal plains (e.g., Trincardi et al., 2007; MacLachlan et al., 2008). More recent studies combine these seafloor acoustic data with oceanographic information about the water column in order to understand the relationship and links between geological and oceanographic processes (Preu et al., 2013; Hernández-Molina et al., 2014). Recent advances in contourite research further integrate geological and oceanographic datasets with numerical modeling (e.g., Zhang et al., 2016).

The combined interpretation of geological and oceanographic

\* Corresponding author.

E-mail address: [alquiros@iact.ugr-csic.es](mailto:alquiros@iact.ugr-csic.es) (A. López-Quirós).

<https://doi.org/10.1016/j.margeo.2020.106113>

Received 2 July 2019; Received in revised form 27 December 2019; Accepted 28 December 2019

Available online 13 January 2020

0025-3227/ © 2020 Elsevier B.V. All rights reserved.

OPEN

# Glaucony authigenesis, maturity and alteration in the Weddell Sea: An indicator of paleoenvironmental conditions before the onset of Antarctic glaciation

Received: 14 March 2019  
Accepted: 6 September 2019  
Published online: 19 September 2019

Adrián López-Quirós<sup>1</sup>, Carlota Escutia<sup>1</sup>, Antonio Sánchez-Navas<sup>2</sup>, Fernando Nieto<sup>2</sup>, Antonio García-Casco<sup>2</sup>, Agustín Martín-Algarra<sup>3</sup>, Dimitris Evangelinos<sup>1</sup> & Ariadna Salabarnada<sup>1</sup>

Three types of glaucony grains were identified in the late Eocene (~35.5–34.1 Ma) sediments from Ocean Drilling Program (ODP) Hole 696B in the northwestern Weddell Sea (Antarctica). The grains are K<sub>2</sub>O-rich (~7 wt%) and formed by smectite-poor interstratified ~10 Å glauconite-smectite with flaky/rosette-shaped surface nanostructures. Two glaucony types reflect an evolved (types 1 and 2 glaucony; less mature to mature) stage and long term glauconitization, attesting to the glaucony grains being formed *in situ*, whereas the third type (type 3 glaucony) shows evidences of alteration and reworking from nearby areas. Conditions for the glaucony authigenesis occurred in an open-shelf environment deeper than 50 m, under sub-oxic conditions near the sediment-water interface. These environmental conditions were triggered by low sedimentation rates and recurrent winnowing action by bottom-currents, leading to stratigraphic condensation. The condensed glaucony-bearing section provides an overview of continuous sea-level rise conditions pre-dating the onset of Antarctic glaciation during the Eocene-Oligocene transition. Sediment burial, drop of O<sub>2</sub> levels, and ongoing reducing (postoxic to sulphidic) conditions at Hole 696B, resulting in iron-sulphide precipitation, were a key limiting factor for the glauconitization by sequestration of Fe<sup>2+</sup>.

Glauconite is the iron-potassium hydrous phyllosilicate mineral typical of the glaucony green marine clay facies, which also includes Fe-rich, 2:1 dioctahedral specimens with expandable layers of randomly interstratified glauconite-smectite<sup>1</sup>. The term glaucony was defined first by Odin and Létolle<sup>2</sup> for marine green sediments formed by mixed layer glauconite-smectite minerals, which differ from the nonexpanding end-member glauconitic mica (i.e. the true glauconite mineral). Glaucony is commonly reported in low-latitude, shallow-marine settings at water depths <500 m, temperatures below 15 °C, and under sub-oxic, partially reducing conditions<sup>3</sup>. It is typically associated with low sedimentation rates and condensed intervals<sup>3</sup>. However, glaucony has also been reported in deep-sea (>2000 m), low-temperature (3–6 °C) environments<sup>4–6</sup>, and in very shallow marine, estuarine<sup>7–9</sup> and paleosol<sup>9</sup> settings. Most of the aforementioned settings share several post-depositional physicochemical conditions: (1) low accumulation rates of detrital sediment, (2) long residence times (10<sup>3</sup>–10<sup>6</sup> years for ancient records<sup>3</sup>, and alternatively <10<sup>4</sup> years for recent records<sup>10</sup>) of the detrital grains near to the sediment-water interface, (3) granular substratum (siliciclastic or carbonatic; including the muddy filling inside the cavities of carbonate bioclasts) with high permeability and porosity, (4) redox potential (Eh) ~0 mV, (5) seawater pH 7–8, and (6) organic matter-rich, semiconfined micro-environments. In summary, glaucony is a sensitive proxy of low sedimentation rates in the marine realm and constitutes a powerful tool for sedimentological and sequence stratigraphic interpretations, due to its association with well-defined trends of sea-level change<sup>11,12</sup>.

<sup>1</sup>Instituto Andaluz de Ciencias de la Tierra, CSIC-Universidad de Granada, Avda. las Palmeras 4, 18100, Armilla, Granada, Spain. <sup>2</sup>Department of Mineralogy and Petrology, University of Granada, 18071, Granada, Spain. <sup>3</sup>Department of Stratigraphy and Paleontology, University of Granada, 18071, Granada, Spain. Correspondence and requests for materials should be addressed to A.L.-Q. (email: alquiros@iact.ugr-csic.es)



Clim. Past, 14, 991–1014, 2018  
<https://doi.org/10.5194/cp-14-991-2018>  
 © Author(s) 2018. This work is distributed under  
 the Creative Commons Attribution 4.0 License.



Climate  
of the Past

Open Access

## Paleoceanography and ice sheet variability offshore Wilkes Land, Antarctica – Part 1: Insights from late Oligocene astronomically paced contourite sedimentation

Ariadna Salabarnada<sup>1,\*</sup>, Carlota Escutia<sup>1</sup>, Ursula Röhl<sup>2</sup>, C. Hans Nelson<sup>1</sup>, Robert McKay<sup>3</sup>, Francisco J. Jiménez-Espejo<sup>4</sup>, Peter K. Bijl<sup>5</sup>, Julian D. Hartman<sup>5</sup>, Stephanie L. Strother<sup>6</sup>, Ulrich Salzmann<sup>6</sup>, Dimitris Evangelinos<sup>1</sup>, Adrián López-Quirós<sup>1</sup>, José Abel Flores<sup>7</sup>, Francesca Sangiorgi<sup>5</sup>, Minoru Ikehara<sup>8</sup>, and Henk Brinkhuis<sup>5,9</sup>

<sup>1</sup>Instituto Andaluz de Ciencias de la Tierra, CSIC-Univ. de Granada, Armilla, 18100, Spain

<sup>2</sup>MARUM – Center for Marine Environmental Sciences, University of Bremen, Leobener Strasse 8, 28359 Bremen, Germany

<sup>3</sup>Antarctic Research Centre, Victoria University of Wellington, Wellington, 6140, New Zealand

<sup>4</sup>Department of Biogeochemistry, Japan Agency for Marine–Earth Science and Technology, Yokosuka, Kanagawa, 237-0061, Japan

<sup>5</sup>Department of Earth Sciences, Marine Palynology and Palaeoceanography, Faculty of Geosciences, Laboratory of Palaeobotany and Palynology, Utrecht University, Princetonlaan 8a, 3584 CB Utrecht, the Netherlands

<sup>6</sup>Department of Geography and Environmental Sciences, Faculty of Engineering and Environment, Northumbria University, Newcastle upon Tyne, NE1 8ST, UK

<sup>7</sup>Department of Geology, University of Salamanca, Salamanca, 37008, Spain

<sup>8</sup>Center for Advanced Marine Core research, Kochi University, Nankoku, Kochi, 783-8502, Japan

<sup>9</sup>NIOZ, Royal Netherlands Institute for Sea Research, and Utrecht University, Landsdiep 4, 1797SZ 't Horntje, Texel, the Netherlands

\*Invited contribution by Ariadna Salabarnada, recipient of the EGU Climate: Past, Present & Future Outstanding Student Poster and PICO Award 2016.

**Correspondence:** Ariadna Salabarnada (a.salabarnada@csic.es)

Received: 16 November 2017 – Discussion started: 5 December 2017

Revised: 2 May 2018 – Accepted: 21 June 2018 – Published: 10 July 2018

**Abstract.** Antarctic ice sheet and Southern Ocean paleoceanographic configurations during the late Oligocene are not well resolved. They are however important to understand the influence of high-latitude Southern Hemisphere feedbacks on global climate under CO<sub>2</sub> scenarios (between 400 and 750 ppm) projected by the IPCC for this century, assuming unabated CO<sub>2</sub> emissions. Sediments recovered by the Integrated Ocean Drilling Program (IODP) at Site U1356, offshore of the Wilkes Land margin in East Antarctica, provide an opportunity to study ice sheet and paleoceanographic configurations during the late Oligocene (26–25 Ma). Our study, based on a combination of sediment facies analysis, magnetic susceptibility, density, and X-ray fluorescence geochemical data, shows that glacial and interglacial sediments are continuously reworked by bottom currents, with maximum veloc-

ities occurring during the interglacial periods. Glacial sediments record poorly ventilated, low-oxygenation bottom water conditions, interpreted as resulting from a northward shift of westerly winds and surface oceanic fronts. Interglacial sediments record more oxygenated and ventilated bottom water conditions and strong current velocities, which suggests enhanced mixing of the water masses as a result of a southward shift of the polar front. Intervals with preserved carbonated nannofossils within some of the interglacial facies are interpreted as forming under warmer paleoclimatic conditions when less corrosive warmer northern component water (e.g., North Atlantic sourced deep water) had a greater influence on the site. Spectral analysis on the late Oligocene sediment interval shows that the glacial–interglacial cyclicality and related displacements of the Southern Ocean frontal

Clim. Past, 14, 1275–1297, 2018  
<https://doi.org/10.5194/cp-14-1275-2018>  
 © Author(s) 2018. This work is distributed under  
 the Creative Commons Attribution 4.0 License.



Climate  
of the Past

Open Access

## Paleoceanography and ice sheet variability offshore Wilkes Land, Antarctica – Part 3: Insights from Oligocene–Miocene TEX<sub>86</sub>-based sea surface temperature reconstructions

Julian D. Hartman<sup>1</sup>, Francesca Sangiorgi<sup>1</sup>, Ariadna Salabarnada<sup>2</sup>, Francien Peterse<sup>1</sup>, Alexander J. P. Houben<sup>3</sup>, Stefan Schouten<sup>4</sup>, Henk Brinkhuis<sup>1,4</sup>, Carlota Escutia<sup>2</sup>, and Peter K. Bijl<sup>1</sup>

<sup>1</sup>Marine Palynology and Paleoceanography, Laboratory of Palaeobotany and Palynology, Department of Earth Sciences, Utrecht University, Princetonlaan 8a, 3584CB Utrecht, the Netherlands

<sup>2</sup>Instituto Andaluz de Ciencias de la Tierra, CSIC/Universidad de Granada, Avenida de las Palmeras 4, 18100 Armilla, Granada, Spain

<sup>3</sup>Applied Geosciences Team, Netherlands Organisation for Applied Scientific Research (TNO), Princetonlaan 6, 3584CB Utrecht, the Netherlands

<sup>4</sup>NIOZ Royal Netherlands Institute for Sea Research, and Utrecht University, Landsdiep 4, 1797SZ 't Horntje, Texel, the Netherlands

**Correspondence:** Julian D. Hartman ([juulhartman@gmail.com](mailto:juulhartman@gmail.com))

Received: 27 November 2017 – Discussion started: 14 December 2017

Revised: 9 August 2018 – Accepted: 12 August 2018 – Published: 4 September 2018

**Abstract.** The volume of the Antarctic continental ice sheet(s) varied substantially during the Oligocene and Miocene (~ 34–5 Ma) from smaller to substantially larger than today, both on million-year and on orbital timescales. However, reproduction through physical modeling of a dynamic response of the ice sheets to climate forcing remains problematic, suggesting the existence of complex feedback mechanisms between the cryosphere, ocean, and atmosphere systems. There is therefore an urgent need to improve the models for better predictions of these systems, including resulting potential future sea level change. To assess the interactions between the cryosphere, ocean, and atmosphere, knowledge of ancient sea surface conditions close to the Antarctic margin is essential. Here, we present a new TEX<sub>86</sub>-based sea surface water paleotemperature record measured on Oligocene sediments from Integrated Ocean Drilling Program (IODP) Site U1356, offshore Wilkes Land, East Antarctica. The new data are presented along with previously published Miocene temperatures from the same site. Together the data cover the interval between ~ 34 and ~ 11 Ma and encompasses two hiatuses. This record allows us to accurately reconstruct the magnitude of sea surface temperature (SST) variability and trends on both million-year and glacial–interglacial timescales. On average, TEX<sub>86</sub> val-

ues indicate SSTs ranging between 10 and 21 °C during the Oligocene and Miocene, which is on the upper end of the few existing reconstructions from other high-latitude Southern Ocean sites. SST maxima occur around 30.5, 25, and 17 Ma. Our record suggests generally warm to temperate ocean offshore Wilkes Land. Based on lithological alternations detected in the sedimentary record, which are assigned to glacial–interglacial deposits, a SST variability of 1.5–3.1 °C at glacial–interglacial timescales can be established. This variability is slightly larger than that of deep-sea temperatures recorded in Mg / Ca data. Our reconstructed Oligocene temperature variability has implications for Oligocene ice volume estimates based on benthic  $\delta^{18}\text{O}$  records. If the long-term and orbital-scale SST variability at Site U1356 mirrors that of the nearby region of deep-water formation, we argue that a substantial portion of the variability and trends contained in long-term  $\delta^{18}\text{O}$  records can be explained by variability in Southern high-latitude temperature and that the Antarctic ice volume may have been less dynamic than previously thought. Importantly, our temperature record suggests that Oligocene–Miocene Antarctic ice sheets were generally of smaller size compared to today.





Clim. Past, 14, 1–19, 2018  
 https://doi.org/10.5194/cp-14-1-2018  
 © Author(s) 2018. This work is distributed under  
 the Creative Commons Attribution 4.0 License.



Climate  
of the Past

Open Access

## Paleoceanography and ice sheet variability offshore Wilkes Land, Antarctica – Part 2: Insights from Oligocene–Miocene dinoflagellate cyst assemblages

Peter K. Bijl<sup>1,\*</sup>, Alexander J. P. Houben<sup>2</sup>, Julian D. Hartman<sup>1</sup>, Jörg Pross<sup>3</sup>, Ariadna Salabarnada<sup>4</sup>, Carlota Escutia<sup>4</sup>, and Francesca Sangiorgi<sup>1</sup>

<sup>1</sup>Marine Palynology and Paleoceanography, Laboratory of Palaeobotany and Palynology, Department of Earth Sciences, Faculty of Geosciences, Utrecht University. P.O. Box 80.115, 3508 TC Utrecht, the Netherlands

<sup>2</sup>Geological Survey of the Netherlands, Netherlands Organisation for Applied Scientific Research (TNO), Princetonlaan 6, 3584 CB, Utrecht, the Netherlands

<sup>3</sup>Paleoenvironmental Dynamics Group, Institute of Earth Sciences, Heidelberg University, Im Neuenheimer Feld 234, 69120 Heidelberg, Germany

<sup>4</sup>Instituto Andaluz de Ciencias de la Tierra, CSIC-UGR, 18100 Armilla, Spain

\*Invited contribution by Peter K. Bijl, recipient of the EGU Arne Richter Award for Outstanding Early Career Scientists 2014.

**Correspondence:** Peter K. Bijl (p.k.bijl@uu.nl)

Received: 13 November 2017 – Discussion started: 5 December 2017

Revised: 9 May 2018 – Accepted: 21 June 2018 – Published:

**Abstract.** Next to atmospheric CO<sub>2</sub> concentrations, ice-proximal oceanographic conditions are a critical factor for the stability of Antarctic marine-terminating ice sheets. The Oligocene and Miocene epochs (~34–5 Myr ago) were time intervals with atmospheric CO<sub>2</sub> concentrations between those of present-day and those expected for the near future. As such, these past analogues may provide insights into ice-sheet volume stability under warmer-than-present-day climates. We present organic-walled dinoflagellate cyst (dinocyst) assemblages from chronostratigraphically well-constrained Oligocene to mid-Miocene sediments from Integrated Ocean Drilling Program (IODP) Site U1356. Situated offshore the Wilkes Land continental margin, East Antarctica, the sediments from Site U1356 have archived the dynamics of an ice sheet that is today mostly grounded below sea level. We interpret dinocyst assemblages in terms of paleoceanographic change on different timescales, i.e. with regard to both glacial–interglacial and long-term variability. Our record shows that a sea-ice-related dinocyst species, *Selenopemphix antarctica*, occurs only for the first 1.5 Myr of the early Oligocene, following the onset of full continental glaciation on Antarctica, and after the Mid-Miocene Climatic Optimum. Dinocysts suggest a weaker-than-modern sea-ice season for the remainder of the Oligocene and Miocene.

The assemblages generally bear strong similarity to present-day open-ocean, high-nutrient settings north of the sea-ice edge, with episodic dominance of temperate species similar to those found in the present-day subtropical front. Oligotrophic and temperate surface waters prevailed over the site notably during interglacial times, suggesting that the positions of the (subpolar) oceanic frontal systems have varied in concordance with Oligocene–Miocene glacial–interglacial climate variability.

### 1 Introduction

The proportion of the East Antarctic ice sheet that is presently grounded below sea level is much larger than originally interpreted (Fretwell et al., 2013). This implies that a larger part of the continental ice sheet is sensitive to basal melting by warm waters than previously thought (Shepherd et al., 2012; Rignot et al., 2013; Wouters et al., 2015), and that a higher amplitude and faster rate of sea-level rise is to be expected under future climate warming than previously acknowledged (IPCC, 2013). Studying the amount of and variability in Antarctic ice volume in periods with high atmospheric CO<sub>2</sub> concentrations (*p*CO<sub>2</sub>) provides addi-

Biogeosciences, 14, 2089–2100, 2017  
 www.biogeosciences.net/14/2089/2017/  
 doi:10.5194/bg-14-2089-2017  
 © Author(s) 2017. CC Attribution 3.0 License.



Biogeosciences  
 Open Access

## A new quantitative approach to identify reworking in Eocene to Miocene pollen records from offshore Antarctica using red fluorescence and digital imaging

Stephanie L. Strother<sup>1</sup>, Ulrich Salzmann<sup>1</sup>, Francesca Sangiorgi<sup>2</sup>, Peter K. Bijl<sup>2</sup>, Jörg Pross<sup>3</sup>, Carlota Escutia<sup>4</sup>, Ariadna Salabarnada<sup>4</sup>, Matthew J. Pound<sup>1</sup>, Jochen Voss<sup>5</sup>, and John Woodward<sup>1</sup>

<sup>1</sup>Department of Geography, Faculty of Engineering and Environment, Northumbria University, Ellison Building, Newcastle upon Tyne, NE1 8ST, UK

<sup>2</sup>Marine Palynology and Paleoceanography, Department of Earth Sciences, Faculty of Geosciences, Laboratory of Palaeobotany and Palynology, Utrecht University, Heidelberglaan 2, 3584CS Utrecht, the Netherlands

<sup>3</sup>Paleoenvironmental Dynamics Group, Institute of Earth Sciences, Heidelberg University, Im Neuenheimer Feld 234, 69120 Heidelberg, Germany

<sup>4</sup>Instituto Andaluz de Ciencias de la Tierra, CSIC-Universidad de Granada, Granada, Spain

<sup>5</sup>School of Mathematics, University of Leeds, Leeds LS2 9JT, UK

Correspondence to: Stephanie L. Strother (slstrother2@gmail.com)  
 and Ulrich Salzmann (ulrich.salzmann@northumbria.ac.uk)

Received: 15 September 2016 – Discussion started: 24 October 2016  
 Revised: 16 March 2017 – Accepted: 30 March 2017 – Published: 24 April 2017

**Abstract.** Antarctic palaeoclimate evolution and vegetation history after the formation of a continent-scale cryosphere at the Eocene–Oligocene boundary, 33.9 million years ago, has remained a matter of controversy. In particular, the reconstruction of terrestrial climate and vegetation has been strongly hampered by uncertainties in unambiguously identifying non-reworked as opposed to reworked sporomorphs that have been transported into Antarctic marine sedimentary records by waxing and waning ice sheets. Whereas reworked sporomorph grains over longer non-successive geological timescales are easily identifiable within younger sporomorph assemblages (e.g. Permian sporomorphs in Pliocene sediments), distinguishing non-reworked from reworked material in palynological assemblages over successive geological time periods (e.g. Eocene sporomorphs in Oligocene sediments) has remained problematic. This study presents a new quantitative approach to identifying non-reworked pollen assemblages in marine sediment cores from circum-Antarctic waters. We measured the fluorescence colour signature, including red, green, and blue fluorescence; brightness; intensity; and saturation values of selected pollen and spore taxa from Eocene, Oligocene, and Miocene sediments from the

Wilkes Land margin Site U1356 (East Antarctica) recovered during Integrated Ocean Drilling Program (IODP) Expedition 318. Our study identified statistically significant differences in red-fluorescence values of non-reworked sporomorph taxa against age. We conclude that red fluorescence is a reliable parameter for identifying the presence of non-reworked pollen and spores in Antarctic marine sediment records from the circum-Antarctic realm that are influenced by glaciation and extensive reworking. Our study provides a new tool to accurately reconstruct Cenozoic terrestrial climate change on Antarctica using fossil pollen and spores.

### 1 Introduction

Antarctica plays a key role in understanding past and future global climate change due to the impact its large ice sheets exert on sea level as well as on oceanic and atmospheric circulation. Throughout the last 65 million years, the Antarctic continent has undergone a drastic change from a greenhouse environment in the early Paleogene towards an icehouse world in the late Paleogene and Neogene (e.g. Askin

Published by Copernicus Publications on behalf of the European Geosciences Union.





## APPENDIX 2

### DATASETS FROM CHAPTER 3 AND 4

1. Chapter 3 late Oligocene XRF scanner from IODP Site 318-U1356 Wilkes Land Margin, Antarctica is published in the open Access scientific repository of PANGAEA:

*Salabarnada, A.; Escutia, C.; Röhl, U.; Nelson, C. H.; McKay, R.; Jiménez-Espejo, F.J.; Bijl, P.K.; Hartman, J.D.; Ikehara, M.; Strother, S.L.; Salzmann, U.; Evangelinos, D.; López-Quirós, A.; Flores, J.A.; Sangiorgi, F.; Brinkhuis, H. (2018): Late Oligocene XRF scanner data from IODP Site 318-U1356 Wilkes Land Margin, Antarctica. <https://doi.org/10.1594/PANGAEA.892208>.*

2. Chapter 4 discrete X-Ray fluorescence dataset from the late Oligocene to early middle Miocene transition analyzed on IODP Site U1356 Expedition 318 off the Wilkes Land margin:

*Salabarnada et al., unpublished: Discrete X-Ray fluorescence dataset from the late Oligocene to early middle Miocene transition analyzed on IODP Site U1356 Expedition 318 off the Wilkes Land margin.*

| Hole  | Sample                             | depth bsf | SiO2 (%) | CaO (%) | TiO2 (%) | Zr (PPM) | Ba (PPM) |
|-------|------------------------------------|-----------|----------|---------|----------|----------|----------|
|       | <b>Core-section-top cm/base cm</b> |           |          |         |          |          |          |
| U1356 | 42R-1-42.5/45                      | 392.825   | 61.838   | 1.913   | 0.71     | 244      | 773      |
| U1356 | 42R-1-108/110                      | 393.48    | 63.489   | 1.803   | 0.695    | 220      | 785      |
| U1356 | 42R-2-11.5/14                      | 393.825   | 75.718   | 1.034   | 0.453    | 139      | 438      |
| U1356 | 42R-CC-3/6                         | 394.32    | 63.46    | 1.827   | 0.693    | 214      | 621      |
| U1356 | 43R-1-30/32                        | 402.3     | 57.542   | 4.341   | 0.738    | 198      | 783      |
| U1356 | 43R-1-87/89                        | 402.87    | 71.365   | 3.242   | 0.431    | 116      | 392      |
| U1356 | 43R-1-124/126                      | 403.24    | 59.597   | 3.112   | 0.719    | 187      | 660      |
| U1356 | 43R-2-39/41                        | 403.89    | 74.246   | 1.85    | 0.419    | 103      | 419      |
| U1356 | 43R-2-87/89                        | 404.37    | 54.923   | 4.047   | 0.751    | 184      | 857      |
| U1356 | 43R-CC-16/18                       | 404.79    | 76.92    | 1.05    | 0.495    | 134      | 443      |
| U1356 | 44R-1-17/19                        | 411.77    | 76.302   | 0.791   | 0.414    | 100      | 376      |
| U1356 | 45R-1-30/32                        | 421.5     | 75.31    | 0.962   | 0.418    | 95       | 485      |
| U1356 | 45R-1-68/69                        | 421.88    | 61.563   | 1.914   | 0.631    | 193      | 766      |
| U1356 | 46R-1-59/61                        | 431.39    | 61.299   | 3.892   | 0.671    | 159      | 649      |
| U1356 | 46R-1-91/92                        | 431.71    | 68.899   | 2.127   | 0.513    | 181      | 1171     |
| U1356 | 46R-1-95/96                        | 431.75    | 68.663   | 1.444   | 0.558    | 111      | 806      |
| U1356 | 46R-2-84/85                        | 433.08    | 65.955   | 1.4     | 0.599    | 138      | 649      |
| U1356 | 46R-2-90.5/92.5                    | 433.145   | 69.553   | 2.285   | 0.586    | 215      | 980      |
| U1356 | 46R-3-24/26                        | 433.96    | 60.723   | 1.862   | 0.721    | 187      | 710      |
| U1356 | 46R-3-71/73                        | 434.43    | 62.416   | 2.258   | 0.632    | 155      | 734      |



| Hole  | Sample                             | depth bsf | SiO2 (%) | CaO (%) | TiO2 (%) | Zr (PPM) | Ba (PPM) |
|-------|------------------------------------|-----------|----------|---------|----------|----------|----------|
|       | <b>Core-section-top cm/base cm</b> |           |          |         |          |          |          |
| U1356 | 47R-1-57/58.5                      | 440.97    | 61.022   | 1.911   | 0.777    | 209      | 734      |
| U1356 | 47R-1-122/124                      | 441.62    | 60.206   | 3.001   | 0.711    | 189      | 780      |
| U1356 | 47R-2-65/67                        | 442.51    | 58.99    | 3.121   | 0.727    | 186      | 815      |
| U1356 | 47R-2-124/126                      | 443.1     | 60.941   | 2.031   | 0.685    | 166      | 828      |
| U1356 | 47R-3-14/16                        | 443.46    | 59.409   | 1.721   | 0.671    | 156      | 722      |
| U1356 | 47R-3-71/73                        | 444.03    | 54.724   | 7.095   | 0.669    | 169      | 595      |
| U1356 | 47R-4-1/3                          | 444.63    | 48.397   | 13.172  | 0.566    | 136      | 527      |
| U1356 | 47R-4-43/46                        | 445.05    | 51.387   | 13.489  | 0.521    | 135      | 410      |
| U1356 | 47R-4-92/94                        | 445.54    | 49.193   | 11.405  | 0.614    | 158      | 592      |
| U1356 | 47R-4-120,5/122                    | 445.825   | 62.897   | 2.305   | 0.629    | 148      | 721      |
| U1356 | 48R-1-46/48                        | 450.36    | 61.271   | 2.374   | 0.682    | 177      | 928      |
| U1356 | 48R-2-35/37                        | 451.75    | 62.974   | 1.731   | 0.677    | 175      | 1063     |
| U1356 | 48R-3-49/51                        | 453.39    | 63.35    | 1.784   | 0.666    | 160      | 871      |
| U1356 | 50R-1-33/35                        | 469.327   | 66.23    | 2.579   | 0.629    | 229      | 761      |
| U1356 | 51R-1-68/71                        | 479.28    | 69.249   | 2.536   | 0.439    | 197      | 790      |
| U1356 | 51R-1-114.5/117                    | 479.745   | 62.726   | 2.628   | 0.678    | 215      | 869      |
| U1356 | 51R-1-144/147                      | 480.04    | 67.687   | 1.353   | 0.591    | 180      | 458      |
| U1356 | 51R-2-41/44                        | 480.51    | 67.409   | 1.837   | 0.59     | 141      | 598      |
| U1356 | 53R-1-141/143                      | 499.21    | 64.114   | 1.876   | 0.579    | 199      | 719      |
| U1356 | 54R-1-57.5/60                      | 507.975   | 67.397   | 1.803   | 0.634    | 214      | 593      |
| U1356 | 54R-3-60/63                        | 510.69    | 64.554   | 2.417   | 0.6      | 176      | 682      |
| U1356 | 55R-1-5/7                          | 517.05    | 31.782   | 28.35   | 0.29     | 81       | 219      |
| U1356 | 55R-1-45/47                        | 517.45    | 66.665   | 3.201   | 0.641    | 163      | 557      |
| U1356 | 56R-1-13/15                        | 526.63    | 54.232   | 1.072   | 0.657    | 118      | 583      |
| U1356 | 57R-1-10.5/12                      | 535.905   | 63.251   | 1.399   | 0.612    | 175      | 683      |
| U1356 | 57R-1-33/35.5                      | 536.13    | 65.257   | 2.19    | 0.656    | 177      | 446      |
| U1356 | 57R-1-89/92                        | 536.69    | 70.842   | 1.619   | 0.543    | 207      | 652      |
| U1356 | 57R-1-112/114                      | 536.92    | 64.165   | 1.657   | 0.667    | 157      | 600      |
| U1356 | 57R-2-31/33                        | 537.42    | 69.02    | 1.17    | 0.567    | 133      | 390      |
| U1356 | 57R-2-77/79.5                      | 537.88    | 60.877   | 1.962   | 0.733    | 202      | 671      |
| U1356 | 58R-1-14/17                        | 545.54    | 61.212   | 3.433   | 0.689    | 218      | 535      |
| U1356 | 58R-1-33/37                        | 545.73    | 64.872   | 1.587   | 0.66     | 197      | 822      |
| U1356 | 58R-CC-3.5/7                       | 546.025   | 59.387   | 6.616   | 0.628    | 192      | 506      |
| U1356 | 59R-1-91.5/93.5                    | 555.915   | 65.383   | 2.123   | 0.599    | 206      | 666      |
| U1356 | 59R-1-131.5/133,5                  | 556.315   | 73.14    | 1.477   | 0.473    | 145      | 418      |
| U1356 | 60R-1-37/39                        | 564.97    | 70.205   | 1.317   | 0.511    | 146      | 451      |
| U1356 | 60R-1-70.5/72.5                    | 565.305   | 62.158   | 1.801   | 0.65     | 177      | 652      |
| U1356 | 60R-2-21.5/23,5                    | 565.825   | 45.976   | 17.418  | 0.367    | 89       | 344      |
| U1356 | 62R-CC-29/31                       | 584.09    | 31.899   | 28.643  | 0.407    | 164      | 255      |
| U1356 | 63R-1-20/22                        | 593.6     | 66.128   | 2.1     | 0.56     | 209      | 918      |
| U1356 | 63R-1-43/45                        | 593.83    | 64.547   | 1.759   | 0.703    | 280      | 609      |
| U1356 | 63R-1-91/93 sand                   | 594.31    | 67.115   | 1.905   | 0.606    | 378      | 1168     |
| U1356 | 63R-1-91/93 mud                    | 594.31    | 59.049   | 1.45    | 0.756    | 167      | 829      |
| U1356 | 63R-2-33/36                        | 595.11    | 57.651   | 1.718   | 0.602    | 151      | 756      |

| Hole  | Sample                             | depth bsf | SiO2 (%) | CaO (%) | TiO2 (%) | Zr (PPM) | Ba (PPM) |
|-------|------------------------------------|-----------|----------|---------|----------|----------|----------|
|       | <b>Core-section-top cm/base cm</b> |           |          |         |          |          |          |
| U1356 | 63R-3-63/65                        | 596.72    | 48.944   | 13.101  | 0.621    | 266      | 468      |
| U1356 | 63R-3-96/98                        | 597.041   | 57.995   | 5.215   | 0.679    | 204      | 499      |
| U1356 | 63R-4-33/35.5                      | 597.67    | 62.212   | 1.875   | 0.669    | 167      | 682      |
| U1356 | 64R-1-83/85                        | 603.83    | 60.551   | 3.11    | 0.722    | 193      | 570      |
| U1356 | 64R-2-48/50                        | 604.98    | 63.337   | 1.707   | 0.655    | 157      | 716      |
| U1356 | 64R-3-35.5/38                      | 606.215   | 63.462   | 1.608   | 0.639    | 189      | 588      |
| U1356 | 64R-3-67/70                        | 606.53    | 63.069   | 1.457   | 0.627    | 150      | 739      |
| U1356 | 66R-1-46/48                        | 622.76    | 60.386   | 1.505   | 0.775    | 157      | 958      |
| U1356 | 66R-1-117/119                      | 623.47    | 60.54    | 1.312   | 0.77     | 172      | 641      |
| U1356 | 67R-1-38/40                        | 632.28    | 60.189   | 3.285   | 0.678    | 193      | 569      |
| U1356 | 67R-1-82/84                        | 632.72    | 63.526   | 1.177   | 0.713    | 179      | 742      |
| U1356 | 67R-1-111/113                      | 633.01    | 62.747   | 1.232   | 0.731    | 188      | 640      |
| U1356 | 67R-2-17/19                        | 633.37    | 62.778   | 1.251   | 0.746    | 190      | 592      |
| U1356 | 67R-2-58.5/60.5                    | 633.785   | 61.349   | 1.287   | 0.742    | 174      | 797      |
| U1356 | 67R-2-80/82                        | 634       | 63.011   | 1.119   | 0.698    | 166      | 676      |
| U1356 | 68R-1-13/15                        | 641.53    | 55.707   | 9.453   | 0.611    | 220      | 542      |
| U1356 | 68R-1-59/61                        | 641.99    | 65.004   | 1.381   | 0.666    | 250      | 599      |
| U1356 | 68R-2-3/6                          | 642.93    | 64.518   | 1.228   | 0.72     | 191      | 648      |
| U1356 | 68R-2-72/74.5                      | 643.62    | 63.222   | 1.231   | 0.716    | 222      | 597      |
| U1356 | 68R-2-128/129                      | 644.18    | 66.093   | 1.351   | 0.665    | 179      | 685      |
| U1356 | 68R-3-67/69                        | 644.95    | 62.418   | 1.239   | 0.748    | 174      | 712      |
| U1356 | 68R-4-33/35                        | 645.78    | 64.046   | 1.432   | 0.69     | 259      | 550      |
| U1356 | 69R-1-38,5/41                      | 651.385   | 64.216   | 1.211   | 0.684    | 219      | 507      |
| U1356 | 69R-2-18.5/21                      | 652.535   | 62.197   | 1.372   | 0.79     | 192      | 719      |
| U1356 | 69R-5-50/53                        | 657.1     | 64.079   | 1.047   | 0.656    | 162      | 594      |
| U1356 | 69R-6-37/39,5                      | 658.448   | 62.864   | 1.191   | 0.659    | 160      | 582      |
| U1356 | 70R-1-79.5/82                      | 661.395   | 65.552   | 1.444   | 0.653    | 252      | 501      |
| U1356 | 70R-2-130/133                      | 663.35    | 64.042   | 1.152   | 0.653    | 175      | 690      |
| U1356 | 70R-3-120/122,5                    | 664.65    | 60.595   | 3.692   | 0.693    | 189      | 532      |
| U1356 | 70R-4-80/83                        | 665.7     | 66.68    | 0.976   | 0.577    | 164      | 498      |
| U1356 | 71R-2-70/72                        | 672.05    | 62.877   | 2.106   | 0.649    | 166      | 705      |
| U1356 | 71R-2-140/142                      | 672.75    | 53.363   | 11.427  | 0.602    | 218      | 487      |
| U1356 | 71R-4-100/102                      | 675.116   | 54.071   | 9.477   | 0.64     | 192      | 499      |
| U1356 | 71R-5-70/72                        | 676.21    | 57.663   | 7.622   | 0.626    | 203      | 553      |
| U1356 | 72R-1-80/82                        | 680.6     | 64.511   | 4.823   | 0.565    | 214      | 558      |
| U1356 | 72R-1-130/132                      | 681.26    | 64.857   | 1.024   | 0.62     | 203      | 652      |
| U1356 | 72R-2-130/132                      | 682.56    | 64.094   | 1.469   | 0.703    | 187      | 690      |
| U1356 | 72R-4-80/82                        | 684.63    | 63.073   | 2.569   | 0.671    | 232      | 619      |
| U1356 | 72R-5-20/22                        | 685.44    | 65.361   | 1.084   | 0.609    | 160      | 638      |
| U1356 | 72R-6-60/62                        | 687.53    | 58.441   | 6.751   | 0.6      | 157      | 514      |







## PROFESSIONAL EXPERIENCE

---

- January – July 2018 Contract of works and services at IACT-CSIC (Spain), project-bound: TASMANDRAKE – Studying the formation and evolution of the Antarctic Circumpolar current (ACC).
- February 2013 – March 2016 Pre-Doc contract at IACT-CSIC (Spain), project-bound: CAGES - Cenozoic East Antarctic Glacial Evolution from Sediments Collected by Ocean Drilling in the Wilkes Land Margin.
- January 2012 – January 2013 Pre-Doc Fellowship UCM-REPSOL at Repsol Technology Centre (CTR) Madrid (Spain). Commissioning and development of analytical techniques of mineralogy, petrology and geochemistry studies of upstream rock-fluid interaction.
- 2009 – 2010 SOTASÒL-AT Serveis de geologia s.l.p. Barcelona (Spain)  
Geotechnical studies, geological cartography for the Geological Survey of Catalonia, Spain.
- 2008 – 2009 Geological Survey from Catalonia, IGC Barcelona (Spain)  
Natural Hazards area. Avalanche cartography, nivometeorological studies.

## EDUCATION

---

- 2013 - present: Current academic status: Ph.D., March 2020.  
Ph.D. thesis: "Oligocene - Miocene Ice Sheet And Paleooceanographic Evolution Of The Eastern Wilkes Land Margin"  
Supervisor: Prof. Dr. Carlota Escutia Dotti
- 2010-2012: M.Sc. in Global Change  
Spanish Research Council (CSIC)-Universidad Internacional Menéndez Pelayo (UIMP)  
Diploma thesis (M.Sc.): Recent depositional evolution of a high altitude, alpine lake: Marboré Lake (Ordesa-Monte Perdido National Park, Spanish Pyrenees). Supervisor: Prof. Dr. Blas Valero Garcés.
- February 2010: Bachelor degree in Geology, University of Barcelona (UB), Spain.  
Erasmus in Perugia, Italy.  
Diploma thesis (B.Sc.): Comparison and validation of three snow avalanche numerical models in Raspes Roies mountain (Boí-Taüll, Western Pyrenees, Spain).

## INTERNSHIPS

---

- 2013 (August): 7-day stay at the IODP in the Gulf Coast Core Repository in College Station Texas A&M (USA). Re-describing and sampling sediment cores from Expedition 318 Site U1356.
- 2013 (6-9 May): 4-day stay at the IODP Bremen Core Repository (Germany). CT-scan acquisition of the deglaciation section from IODP Expedition 318 Site 1357.
- 2014 (October-December): 4 month stay in the Antarctic Research Center, University of Victoria in Wellington (NZ). Work with Rob MacKay and Tim Naish on data from Sites U1356 and U1361.
- 2015 (July-October): 3 month stay in JAMSTEC (Japan) and the IODP Kochi Core Repository. Geochemical data interpretation-IODP Site 1356. Analytical work: CT-scans and Geochemical mapping of the Oligocene-Miocene transition sediments.
- 2016: 10-day stay in the IODP in the Gulf Coast Core Repository in College Station Texas A&M. Re-describing and sampling sediment cores from DSDP Leg 28 and 29 (Sites 269, 274 and 278) and ODP Leg 113 (Site 696). Focusing on Eocene-Oligocene and Oligocene-Miocene Transitions.

## SCIENTIFIC OCEANOGRAPHIC EXPEDITIONS

---

- January – February 2018 BIO Hesperides, DRAKE2018, Antarctica  
PI: Carlota Escutia, Fernando Bohoyo 6 weeks duration
- June 2013 RV Marion Dufresne, MD194 "EuroFLEETS GATEWAY" Ghent University (Belgium).  
PI: Dr. David Van Rooij. 11 days duration
- May 2010 RV García del Cid, "COSTEM" Institut de Ciències del Mar (ICM) Barcelona (Spain).  
PI: Dr. Pere Puig. 6 days duration
- April 2010 RV Sarmiento de Gamboa, "MEDOC" Institut de Ciències del Mar (ICM) Barcelona (Spain).  
PI: Dr. César R. Ranero. 20 days duration



**RELATED COURSES**

---

- May 2016 “Avizo Training” software for post-processing of CT-Scans. By FEI VSG Company. (<http://www.vsg3d.com/>).
- May 2015 “Shortcourse on XRD methods for study of clays & clay minerals” taught by Ray E. Ferrell Jr. (Louisiana State University Professor Emeritus).
- May 2015 Theoretical-practical course on ICP-MS, ICTJA-CSIC, in Barcelona, Spain.
- April 2014 “Messinian Salinity Crisis: Budgets, Balances, and Diagenesis”, IACT-CSIC, Spain. Taught by: Prof. Emeritus Dr. Gert J. De Lange.
- Sep. 2013 ECORD Summer School. MARUM, Bremen, Germany. “Deep-Sea Sediments: From Stratigraphy to Age Models”

**AWARDS**

---

2018: Best earth science poster at IX Simposio de Estudios Polares SEP 2108, Madrid, Title: “Origin And Evolution Of Bottom Current Deposition In The Antarctic Wilkes Land Margin During The Oligocene And Miocene”.

2016: Outstanding Student Poster (OSPP) Award for poster presentation in the International Conference EGU, Viena, for: Obliquity paced contourite cyclicity in Antarctic sediments from the Wilkes Land (Site U1356) during Late Oligocene. Ariadna Salabarnada et al.

**GRANTS**

---

2013 (9-20 September): ECORD Scholarship to participate in the ECORD Summer School “Deep-Sea Sediments: From Stratigraphy to Age Models” (ECORD awardee).

2104 (October-December): Ministry of Science and Competitively awardee for a 4-month stay in the Antarctic Research Centre-Victoria Univ. of Wellington (NZ).

2015 (13-17 July 2015): PAIS travel funding to attend the ISAES XII in Goa (India).

2015 (July-October): Ministry of Science and Competitively awardee for a 3-month stay in JAMSTEC (Japan).

2016: PAIS (Past Antarctic Ice Sheet) travel funding to attend IODP “Antarctica’s Cenozoic ice and climate history: New Science and new challenges of drilling in Antarctic waters” Workshop.

2017: PAIS (Past Antarctic Ice Sheet) travel and conference fee funding for attending PAIS conference in Trieste (Italy) September 2017.

2018: APECS-Spain conference fee funding for attending IX Simposio de Estudios Polares, Madrid (Spain) in September 2018.

**PUBLICATIONS**

---

**Salabarnada, A.**, Escutia, C., Röhl, U., Nelson, C. H., McKay, R., Jiménez-Espejo, F. J., Bijl, P. K., Hartman, J. D., Strother, S. L., Salzmann, U., Evangelinos, D., López-Quirós, A., Flores, J. A., Sangiorgi, F., Ikehara, M. and Brinkhuis, H.: Paleoceanography and ice sheet variability offshore Wilkes Land, Antarctica – Part 1: Insights from late Oligocene astronomically paced contourite sedimentation, *Climate of the Past*, 14(7), 991–1014, doi:10.5194/cp-14-991-2018, 2018.

López-Quirós, A., Lobo, F. J., Escutia, C., García, M., Hernández-Molina, F. J., Pérez, L. F., Bohoyo, F., Evangelinos, D., **Salabarnada, A.**, Maldonado, A. and Naveira Garabato, A. C.: Geomorphology of Ona Basin, southwestern Scotia Sea (Antarctica): Decoding the spatial variability of bottom-current pathways, *Mar. Geol.*, 422(January), 106113, doi:10.1016/j.margeo.2020.106113, 2020.

López-Quirós, A., Escutia, C., Sánchez-Navas, A., Nieto, F., Garcia-Casco, A., Martín-Algarra, A., Evangelinos, D. and **Salabarnada, A.**: Glaucony authigenesis, maturity and alteration in the Weddell Sea: An indicator of paleoenvironmental conditions before the onset of Antarctic glaciation, *Sci. Rep.*, 9(1), 1–12, doi:10.1038/s41598-019-50107-1, 2019.

Hartman, J. D., Sangiorgi, F., **Salabarnada, A.**, Peterse, F., Houben, A. J. P., Schouten, S., Brinkhuis, H., Escutia, C. and Bijl, P. K.: Paleoceanography and ice sheet variability offshore Wilkes Land, Antarctica - Part 3: Insights from Oligocene-Miocene TEX86-based sea surface temperature reconstructions, *Climate of the Past*, 14, 1275–1297, doi:10.5194/cp-14-1275-2018, 2018.

Bijl, P. K., Houben, A. J. P., Hartman, J. D., Pross, J., **Salabarnada, A.**, Escutia, C. and Sangiorgi, F.: Paleoceanography and ice sheet variability offshore Wilkes Land, Antarctica - Part 2: Insights from Oligocene-Miocene dinoflagellate cyst assemblages, *Climate of the Past*, 14(7), 1015–1033, doi:10.5194/cp-14-1015-2018, 2018.

Oliva-Urcia, B., Moreno, A., Leunda, M., Valero-Garcés, B., González-Sampériz, P., Gil-Romera, G., Mata, M. P., Adsuar, A., Aranbarri, J., Barreiro, F., Bartolomé, M., Bueno, B., García-Prieto, E., García, B., Larrasoña, J. C., Parés, J. M., Pérez, A., Rico, M., **Salabarnada, A.**, Salazar, Á., Sevilla-Callejo, M. and Tarrats, P.: Last deglaciation and Holocene environmental change at high altitude in the Pyrenees: the geochemical and paleomagnetic record from Marboré Lake (N Spain), *J. Paleolimnol.*, 59(3), 349–371, doi:10.1007/s10933-017-0013-9, 2018.

Strother, S. L., Salzmann, U., Sangiorgi, F., Bijl, P. K., Pross, J., Escutia, C., **Salabarnada, A.**, Pound, M. J., Voss, J. and Woodward, J.: A new quantitative approach to identify reworking in Eocene to Miocene pollen records from offshore Antarctica using red fluorescence and digital imaging, *Biogeosciences*, 14(8), 2089–2100, doi:10.5194/bg-14-2089-2017, 2017.

Valero-Garcés, B.L., Oliva-Urcia, B., Moreno Caballud, A., Rico Herrero, M.T., Mata-Campo, P., Salazar-Rincón, A., Rieradevall, M., García-Ruiz, J.M., Chueca Cía, J., González-Sampériz, P., Pérez Sanz, A., **Salabarnada, A.**, Pardo, A., Sancho, C., Barreiro-Lostres, F., Bartolomé, M., García-Prieto, E., Gil-Romera, G., López Merino, L., Sevilla-Callejo, M., Tarrats, P., 2014. Dinámica glacial, clima y vegetación en el Parque Nacional de Ordesa y Monte Perdido durante el Holoceno. Organismo Autónomo Parques Nacionales. ISBN: 978-84-8014-853-5.

## PUBLICATIONS AT SCIENTIFIC MEETINGS (as 1<sup>st</sup> author)

---

**Salabarnada, A.**, Escutia, C., Nelson, H.C., Evangelinos, D., López, A., Castro, S. De, 2017. Bottom current deposition in the Antarctic Wilkes Land margin during the Oligocene, in: EGU General Assembly 2017 Geophysical Research Abstracts. EGU General Assembly 2017, p. Vol. 19, EGU2017-12464-1.

**Salabarnada, A.**, Escutia, C., Nelson, H.C., Evangelinos, D., López-Quirós, A., Castro, S. de, 2017. Bottom current deposition in the Antarctic Wilkes Land margin during the Oligocene, in: Past Antarctic Ice Sheet Dynamics (PAIS) Conference.

**Salabarnada, A.**, Escutia, C., Nelson, H.C., Roehl, U., Jimenez-Espejo, F.J., Evangelinos, D., McKay, R., Ikehara, M., López-Quirós, A., 2017. Late Oligocene contourite sedimentation in the Antarctic Wilkes Land margin: IODP Site U1356, in: Past Antarctic Ice Sheet Dynamics (PAIS) Conference.

**Salabarnada, A.**, Escutia, C., Nelson, C.H., Roehl, U., Jiménez-Espejo, F., Evangelinos, D., Ikehara, M., McKay, R., López-Quirós, A. Late Oligocene contourite sedimentation in the Antarctic Wilkes Land margin: IODP Site U1356. IX Congreso Geológico de España, 2016.

**Salabarnada, A.**, Escutia, C., Nelson, C.H., Roehl, U., Jimenez-Espejo, F.J., Evangelinos, D., Ikehara, M., McKay, R., and Lopez-Quiros, A. (2016). Obliquity paced contourite cyclicity in Antarctic sediments from the Wilkes Land (Site U1356) during Late Oligocene. *Geophysical Research Abstracts* Vol. 18, EGU2016-14854, 2016. EGU General Assembly 2016 (Vienna).

**Salabarnada, A.**, Escutia, C., Nelson, C.H., Damuth, J.E., and Jiménez-Espejo F.J. (2015). East Antarctic Ice Sheet Dynamics during the Oligocene-miocene Transition: Insights from IODP Site 1356 Drilling off the Wilkes Land Margin. XII International Symposium on Antarctic Earth Sciences (Goa, India). Abstracts Vol S15-477.

**Salabarnada A.**, Escutia C., Nelson H., Damuth J., Jimenez-Espejo F.J. (2015). The Oligocene-Miocene transition at the East Antarctic Wilkes Land margin: IODP Site 1356. European Geophysical Union (EGU) General Assembly 2015 (Vienna), *Geophysical Research Abstracts*, Vol. 17, EGU2015-15698-1, 2015

**Salabarnada, A.**, Escutia, C., Nelson H.C., Damuth, L., and Brinkhuis, H. (2014). Varying depositional environments across the Oligocene-Miocene boundary and their relevance for East Antarctic ice sheet history: IODP Site U1356, Wilkes Land margin. European Geophysical Union (EGU) 2014 (Vienna), *Geophysical Research Abstracts*, Vol. 16, EGU2014-13705, 2014.

## OUTREACH

---

November 2015, 2016, 2017 Science week in Andalusia (Spain): “Antarctica and the oceanic basins around it”, IACT-CSIC.

October 2015 PIISA – Introduction of science and research to High-School students in Andalusia, Spain.

## SOFTWARE

---

Kingdom, Avizo Fire (CT-Scans)  
R for Astrochron, Analyseries  
ArcGis, Microstation, CAD  
Profex XRD processing software  
Microsoft Office, Adobe Pack (Illustrator, Photoshop, Indesign)

## LANGUAGES

---

Spanish: Native  
Catalan: Native  
English: Very good oral, written and communication skills.  
Italian: Good oral and communications skills.  
French: A1 – learning in progress

